Università degli Studi di Padova
Centro Ricerche Fusione

Ghent University

JOINT RESEARCH DOCTORATE IN FUSION SCIENCE AND ENGINEERING
Cycle XXXIV

Power exhaust and plasma divertor interaction study by means of a 2D edge numerical code

Coordinator: Prof. Fabio Villone

Supervisor at Università degli Studi di Padova (Home University):
Dr. Paolo Innocente

Supervisor at Università degli Studi di Padova (Home University):
Prof. Piero Martin

Supervisor at Ghent University (Host University): Prof. Kristel Crombé

Ph.D. student: Luca Balbinot

Padova, January 2022

Ai miei nonni,
il mio ponte tra passato e futuro.

Abstract

Finding an abundant, safe, continuous and reliable source of energy is one of the main challenges for mankind in the 21^{st} century. The exploitation of energy from nuclear fusion is one of the possibilities to meet the ever-growing energy demand. To reach high fusion rates, a hot dense plasma must be confined for a sufficiently long time, the higher temperature, density and confinement time, the higher the performance. One of the strategies for obtaining and containing the fusion fuel, which is in plasma state at such high temperatures, is magnetic confinement. Even with a strong magnetic confinement, the heat and particle flux coming from the main plasma to the internal wall of a fusion machine is extremely high to be handled by current materials. To mitigate this problem, a magnetic configuration called *divertor* is used to split the plasma region into a hot and dense core and a colder region called scrape-off layer SOL which is in between the main plasma and the wall. The divertor configuration is properly designed to menage and dissipate the incoming energy and particle flux.

The exhaust of a huge amount of power to the divertor targets is considered to be one of the most critical aspects of the Demonstration power plant (DEMO). DEMO is presently based on a H-mode single null (SN) tokamak configuration. The elevated particle and power exhaust to the divertor targets foreseen in fusion-relevant machines can provoke degradation, cracking and even melting of the plasma-facing components (PFC). For this reasons, alternative magnetic divertor configurations (ADCs) and the use of liquid metal as PFC are currently studied to access the reliability and feasibility of future reactor machines.

This Ph.D. thesis focuses on the study of Scrape-Off Layer (SOL) and divertor plasma on existing and future fusion machines by means of the 2D-edge numerical code SOLEDGE2D-EIRENE.

The first topic presented is the study of power exhaust in current experiments by means of SOLEDGE2D-EIRENE. To achieve this goal, the available measurements and the physical processes included or missing in the code were investigated in order to allow an accurate description of the experiments and to understand which of the possible discrepancies between the simulations and the measurements could be attributed to limitations of the code. The second major aim was to predict transport profiles and plasma-wall interaction coefficients which could be scaled to future fusion devices.

Transport and plasma-wall interaction parameters derived from the modelling of present experiments were the basis for predictive modelling of plasma scenarios of the Japanese Tokamak JT-60SA and the Divertor Test Tokamak facility DTT. Modelling of JT-60SA inductive high input power scenarios defined an operative range in terms of input power, plasma density and impurity concentration for both seeded and unseeded plasmas. Modelling of DTT also aimed at defining an operative range with different seeded impurities which had to be compatible with core performances. The study of the effect on power exhaust of divertor closure and connection length aimed at analyzing the possible advantages in term of power handling that could be gained with these geometries. The outcome of the modelling of JT-60SA and DTT scenarios (plasma and neutral density, temperature an radiation) were used to test synthetic diagnostics like spectrometer and interferometer and were used to test the effects on the plasma of ECRH aperture during rump-up of DTT. Lastly, an hysteretical-like behaviour of cooling performances was observed in both machines, was described and theoretically justified.

The last topic presented is the study of liquid metal as plasma-facing components, focusing on the possible implementation for DTT operations. A self-consistent module for the evaluation of the sputtered and evaporated particles from the liquid metal was added to SOLEDGE2D-EIRENE. The module, reading the incoming energy and particle flux, estimates liquid metal surface temperature taking into account different target configurations or cooling methods. The module self-consistently estimate particle evaporation and sputtering and use them as sources in SOLEDGE2D-EIRENE. When the model was applied to DTT, it was found that the maximum input power flux to obtain sustainable conditions at the divertor could be doubled with respect to the unseeded case. The corresponding lithium concentration in the main plasma was acceptable, but alternative solutions were also studied to lower the impurity concentration caused by the high power and particle flux to the targets.

Sommario

Trovare una fonte di energia abbondante, sicura, continua e affidabile è una delle principali sfide per l'umanità nel 21^{st} secolo. Lo sfruttamento dell'energia da fusione nucleare è una delle possibilità per soddisfare la sempre crescente domanda di energia. Per raggiungere alti tassi di fusione, un plasma caldo e denso deve essere confinato per un tempo sufficientemente lungo, maggiore è la temperatura, la densità e il tempo di confinamento, maggiore è il rendimento. Una delle strategie per ottenere e contenere il combustibile di fusione, che si trova allo stato di plasma a temperature così elevate, è il confinamento magnetico. Anche con un forte confinamento magnetico, il calore e il flusso di particelle provenienti dal plasma principale verso la parete interna di una macchina a fusione sono estremamente elevati per essere gestiti dai materiali attuali. Per mitigare questo problema, viene usata una configurazione magnetica chiamata "divertore" per dividere la regione del plasma in un nucleo caldo e denso e una regione più fredda chiamata "scrape-off layer" (letteralmente strato di raschiamento) che si trova tra il plasma principale e la parete. La configurazione del divertore è adeguatamente progettata per gestire e dissipare l'energia in entrata e il flusso di particelle.

Lo scarico di un'enorme quantità di energia verso il divertore è considerato uno degli aspetti più critici della reattore Dimostrativo (DEMO). DEMO è attualmente basato su una configurazione tokamak a singolo divertore (SN) e alto confinamento. L'elevato scarico di particelle e di potenza divertore previsto nelle macchine rilevanti per la fusione può provocare la degradazione, la rottura e persino la fusione dei componenti rivolti al plasma (PFC). Per questo motivo, configurazioni magnetica alternative del divertore (ADCs) e l'uso di metallo liquido come PFC sono attualmente studiati per analizzare l'affidabilità e la fattibilità delle future macchine a fusione.

Questa tesi di dottorato si concentra sullo studio dello Scrape-Off Layer (SOL) e del plasma del divertore sulle macchine a fusione esistenti e future per mezzo del codice numerico 2D: SOLEDGE2D-EIRENE.

Il primo argomento presentato è lo studio dello scarico di potenza negli esperimenti attuali per mezzo di SOLEDGE2D-EIRENE. Per raggiungere questo obiettivo, le misurazioni disponibili e i processi fisici inclusi o mancanti nel codice sono stati studiati per permettere una descrizione accurata degli esperimenti e per capire quali delle possibili discrepanze tra le simulazioni e le misurazioni potrebbero essere attribuite alle limitazioni del codice. Il secondo obiettivo principale era quello di prevedere i profili di trasporto e i coefficienti di interazione plasma-parete che potessero essere scalati ai futuri dispositivi di fusione.

I parametri di trasporto e di interazione plasma-parete derivati dalla modellizzazione dei presenti esperimenti sono stati la base per la modellizzazione predittiva degli scenari di plasma del Tokamak giapponese JT-60SA e della struttura Divertor Test Tokamak DTT. La modellizzazione degli scenari induttivi ad alta potenza di ingresso di JT-60SA ha definito una gamma operativa in termini di potenza di ingresso, densità di plasma e concentrazione di impurità per plasmi con e senza impurità. Anche la modellazione di DTT mirava a definire un intervallo operativo con diverse impurità che dovevano essere compatibili con le prestazioni del plasma principale. Lo studio dell'effetto della chiusura del divertore e della lunghezza di connessione sulla potenza depositata aveva lo scopo di analizzare i possibili vantaggi in termini di gestione della potenza che si potevano ottenere con queste geometrie. I risultati della modellazione degli scenari JT-60SA e DTT (densità, temperatura e radiazione del plasma e dei neutri) sono stati utilizzati per testare

la diagnostica sintetica come spettrometro e interferometro e sono stati utilizzati per testare gli effetti sul plasma dell'apertura dei condotti dell' ECRH durante il rump-up di DTT. Infine, un comportamento di isteresi delle prestazioni di raffreddamento è stato osservato in entrambe le macchine, è stato descritto e giustificato teoricamente.

L'ultimo argomento presentato è lo studio del metallo liquido come prima componente di fronte al plasma, concentrandosi sulla possibile implementazione per le operazioni DTT. A SOLEDGE2D-EIRENE è stato aggiunto un modulo auto-consistente. Il modulo, leggendo l'energia in entrata e il flusso di particelle, stima la temperatura della superficie del metallo liquido tenendo conto di diverse configurazioni del target o metodi di raffreddamento utilizzati. Il modulo stima in modo auto-consistente l'evaporazione delle particelle e lo sputtering e li usa come termini di sorgente in SOLEDGE2D-EIRENE. Quando il modello è stato applicato a DTT, è stato trovato che il massimo flusso di potenza in ingresso per ottenere condizioni sostenibili al deviatore potrebbe essere raddoppiato rispetto all'analogo caso in tungsteno. La concentrazione di litio corrispondente nel plasma principale era accettabile, ma sono state studiate anche soluzioni alternative per abbassare la concentrazione di impurità causata dall'alta potenza e dal flusso di particelle verso i target.

Samenvatting

Het vinden van een overvloedige, veilige, continue en betrouwbare energiebron is een van de belangrijkste uitdagingen voor de mensheid in de 21^{st} eeuw. De exploitatie van energie uit kernfusie is een van de mogelijkheden om aan de steeds groeiende vraag naar energie te voldoen. Om hoge fusiesnelheden te bereiken moet een heet, dicht plasma gedurende een voldoende lange tijd worden opgesloten; hoe hoger de temperatuur, de dichtheid en de opsluitingstijd, hoe hoger de prestaties. Een van de strategieën om de fusiebrandstof, die zich bij zulke hoge temperaturen in plasmatoestand bevindt, te verkrijgen en op te sluiten, is magnetische opsluiting. Zelfs met een sterke magnetische opsluiting zijn de warmte en de deeltjesflux die van het hoofdplasma naar de binnenwand van een fusiemachine komen, extreem hoog om door de huidige materialen te worden verwerkt. Om dit probleem op te lossen wordt een magnetische configuratie gebruikt die "divertor" wordt genoemd, om het plasma te splitsen in een hete en dichte kern en een kouder gebied, de zogenaamde schraaplaag SOL, dat zich tussen het hoofdplasma en de wand bevindt. De divertorconfiguratie is goed ontworpen om de inkomende energie en deeltjesflux te doseren en af te voeren.

De afvoer van een enorme hoeveelheid energie naar de divertor-doelen wordt beschouwd als een van de meest kritische aspecten van de demonstratie-energiecentrale (DEMO). DEMO is momenteel gebaseerd op een H-mode single null (SN) tokamakconfiguratie. De hoge deeltjes- en vermogensuitstoot naar de divertor-targets, zoals voorzien in fusie-relevante machines, kan degradatie, scheuren en zelfs smelten van de plasma-geconfronteerde componenten (PFC) veroorzaken. Om deze redenen worden alternatieve magnetische divertor configuraties (ADCs) en het gebruik van vloeibaar metaal als PFC momenteel bestudeerd om de betrouwbaarheid en haalbaarheid van toekomstige reactormachines te benaderen.

Deze Ph.D. thesis richt zich op de studie van Scrape-Off Layer (SOL) en divertor plasma op bestaande en toekomstige fusiemachines door middel van de 2D-edge numerieke code: SOLEDGE2D-EIRENE.

Het eerste onderwerp dat wordt gepresenteerd is de studie van de vermogensafvoer in de huidige experimenten met behulp van SOLEDGE2D-EIRENE. Om dit doel te bereiken werden de beschikbare metingen en de fysische processen die in de code zijn opgenomen of ontbreken onderzocht om een nauwkeurige beschrijving van de experimenten mogelijk te maken en om te begrijpen welke van de mogelijke discrepanties tussen de simulaties en de metingen kunnen worden toegeschreven aan beperkingen van de code. Het tweede hoofddoel was het voorspellen van transportprofielen en plasma-wand interactiecoëfficiënten die opgeschaald kunnen worden naar toekomstige fusie-installaties.

Transport en plasma-wand interactie parameters afgeleid uit de modellering van deze experimenten vormden de basis voor voorspellende modellering van plasmascenario's van de Japanse Tokamak JT-60SA en de Divertor Test Tokamak faciliteit DTT. Modellering van JT-60SA inductieve scenario's met hoog ingangsvermogen definieerde een operatief bereik in termen van ingangsvermogen, plasmadichtheid en onzuiverheidsconcentratie voor zowel seeded als unseed plasma's. Modellering van DTT was ook gericht op het definiëren van een operatief bereik met verschillende bezaaide onzuiverheden die verenigbaar moesten zijn met de prestaties van de kern. De studie van het effect van de sluiting van de divertor en de lengte van de verbinding op de vermogensafgifte was gericht op het analyseren van de mogelijke voordelen in termen van vermogensafgifte die met deze geometrieën zouden kunnen worden verkregen. De resultaten van

de modellering van JT-60SA- en DTT-scenario's (plasma en neutrale dichtheid, temperatuur en straling) werden gebruikt om synthetische diagnostiek zoals spectrometer en interferometer te testen en werden gebruikt om de effecten op het plasma van de ECRH-opening te testen tijdens het opstijgen van DTT. Tenslotte werd een hysteretisch gedrag van de koelprestaties waargenomen in beide machines, beschreven en theoretisch verantwoord.

Het laatste onderwerp dat werd gepresenteerd is de studie van vloeibaar metaal als plasma-gerichte componenten, met de nadruk op de mogelijke implementatie voor DTT-operaties. Een zelfconsistente module voor de evaluatie van de gesputterde en verdampte deeltjes uit het vloeibaar metaal werd toegevoegd aan SOLEDGE2D-EIRENE. De module, die de inkomende energie en deeltjesflux leest, schat de oppervlaktetemperatuur van het vloeibare metaal, rekening houdend met verschillende doelconfiguraties of koelmethoden. De module schat zelfconsistent deeltjesverdamping en sputtering in en gebruikt deze als bronnen in SOLEDGE2D-EIRENE. Toen het model werd toegepast op DTT, bleek dat de maximale ingangsstroom om duurzame condities bij de divertor te verkrijgen kon worden verdubbeld ten opzichte van het niet-gezaaide geval. De corresponderende lithiumconcentratie in het hoofdplasma was aanvaardbaar, maar er werden ook alternatieve oplossingen bestudeerd om de onzuiverheidsconcentratie als gevolg van de hoge vermogens- en deeltjesflux naar de doelen te verlagen.

Contents

List of Figures

List of Tables

Chapter 1

Introduction

1.1 Global energy demand

It is typical among the physicist community to examine a problem considering its energy, how it produced and how it changes. If the human society and its need are examined considered its energy demand and production, some interesting results can be obtained. The energy consumption has been constantly increasing throughout human history, but in the last decades a major acceleration occurred (figure 1.1) and new energy source were added to the energy mix to meet the energy demand [8].

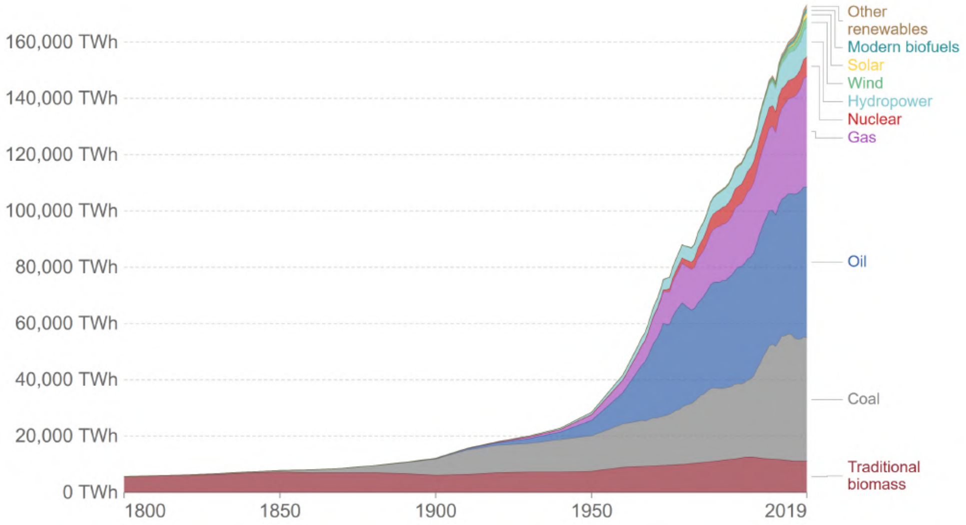

Figure 1.1: Total global energy consumption per year.

It is also evident that in order to achieve a Human Development Index (HDI) high enough to be considered a highly developed country, a certain amount of energy per capita is required; figure 1.2 shows a strong correlation between human development index and energy consumption [9]. Picture 1.2 shows only an instantaneous view of the correlation between measures. The hypothesis that this behaviour will remain in the future comes from the analysis of the catch-up path of different nations to HDI they possess currently possess, which is shown in figure 1.3a[1]. Figure 1.3b shows the analogous plot for HDI and electricity consumption with respect of the nowadays values.

These two results are sufficient to conclude that the energy consumption in the future won't decrease. The constantly increasing Earth population will cause the energy demand to increase, countries will use more energy, specifically electric energy, in order to achieve better human conditions.

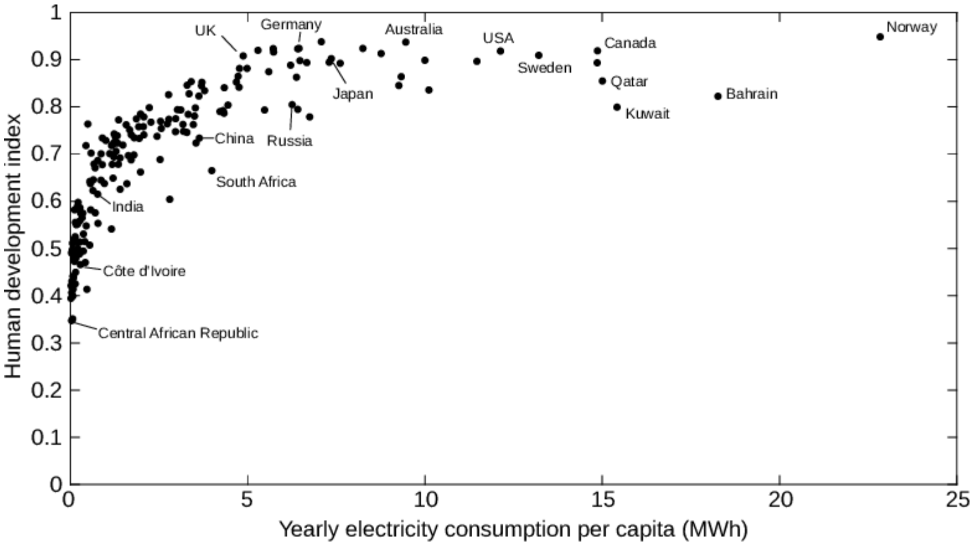

Figure 1.2: Energy consumption per capita in each nation vs human development index.

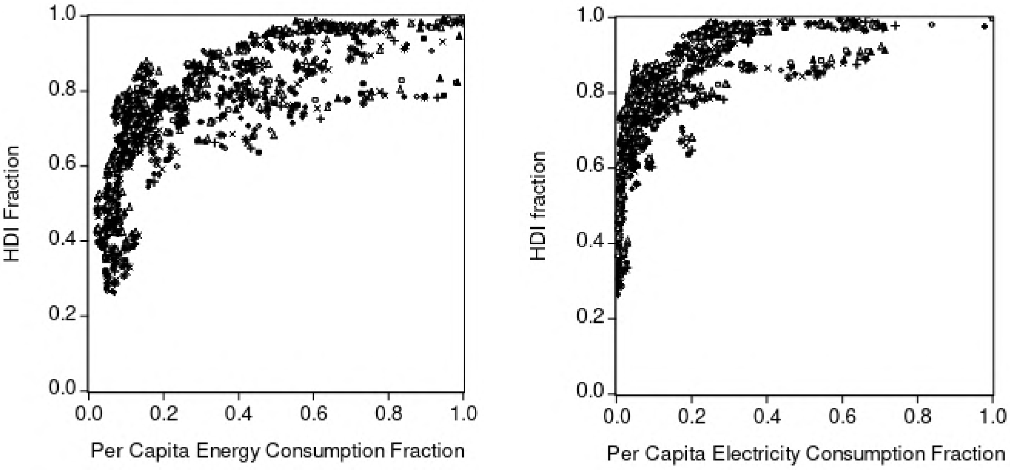

(a) HDI and energy consumption fractions correlate.

(b) HDI and electricity production fractions correlate.

Figure 1.3: HDI and its correlation to total energy consumption and electricity consumption fraction with respect to nowadays values [1].

1.2 Global energy production and climate change

To meet the increasing electrical energy demand, a mix of primary energy sources is used, some are continuous: fossil combustibles (coal, oil, natural gas), nuclear fission, hydro-energy and geothermal energy, some other are aleatory like solar power plants, wind, etc. Figure 1.4a shows that in 2019 the electric energy production was still highly dominated by fossil fuels. Fossil fuels are strong greenhouse gas emitters; figure 1.4b shows that the carbon footprint of fossil fuels per unit of energy produced is orders of magnitude higher than that of other sources. It is estimated that around 75% of the overall CO_2 production by human activity is given by electric energy production. The concentration of CO_2 in the atmosphere have influenced the climate patterns over the last million years. The rapid increase of CO_2 concentration during the last century has already caused an increase of the global energy temperature of 1° with respect to the pre-industrial age. The temperature increase is causing melting of arctic ice, shifting of temperature regimes, acidification of the oceans, shortage of water supplies and the increase of energy and frequency of catastrophic meteorological events. The objective of the Paris agreement is to counteract the increase of global temperature and limit the average temperature increase by 2° with respect to the pre-industrial age. To do so, carbon neutrality (the net 0 between carbon emission and re-absorption by human activity) must be reached between 2050 and 2070.

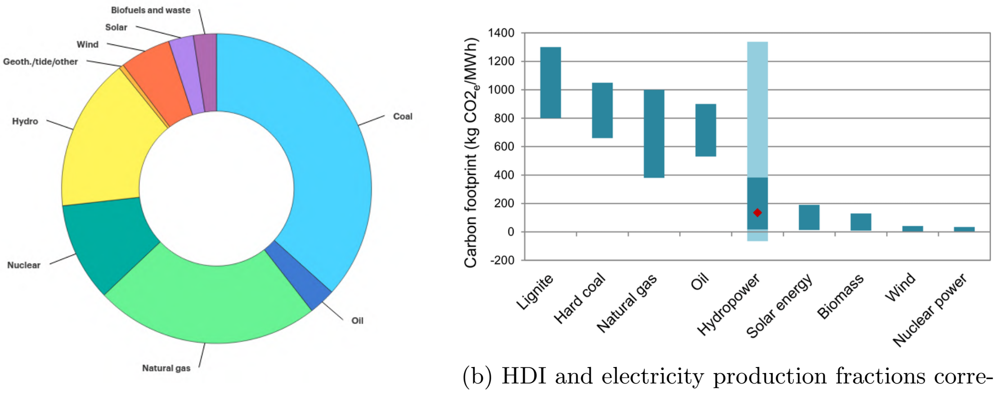

(a) Global electrical energy source mix in 2019 [10]

(b) HDI and electricity production fractions correlate.

Figure 1.4: Electric energy production ratio and carbon footprint of electric energy sources.

New policies are being applied and it is clear that de-carbonization of electric energy production will play a crucial role. On top of the energetic and environmental problem, the de-carbonization process should avoid possible social problems and inequalities generated by the changing of the electricity mix.

1.3 Nuclear Fusion

Nuclear fusion is a clean continuous abundant and safe energy source and could be a solution for global energy demand. Nuclear fusion is the opposite reaction of nuclear fission, it consist in fusing two lighter atoms into a heavier one. If the two starting atoms are lighter than iron, the nuclear energy bound of their fusion product is higher than the sum of the nuclear energy bounds of the starting nuclei; the energy difference between the two states of the reaction is converted into kinetic energy of the fusion products. On the contrary, if an element is heavier than iron, the reaction that transfer nuclear bounding energy to the kinetic energy of the particles is nuclear fission.

The fusion of two atoms is first avoided by the electrons; to make the nuclei interact it is first necessary to remove all the electrons from the atoms, the fuel is now in a state called plasma. The fusion of two nuclei face a major problem which is Coulomb repulsion force: the positive charge of the nuclei would repulse the ions. If the atoms collide with enough energy, it is possible that the two nuclei get so close to make the strong nuclear force prevail over the Coulomb force and fuse the nuclei. This is the reason why the rate coefficient of nuclear reaction normally increase with the increasing of particle energy (or temperature if particles thermalize).

Deuterium-tritium reaction (DT) is the most promising nuclear reaction to be used in a nuclear fusion power plant due to its higher rate coefficient ($\langle\sigma v\rangle$) at lower temperature (figure 1.5). DT reaction fuse the two hydrogen isotopes into an α particle and a free neutron:

$$\mathrm{D} + \mathrm{T} \rightarrow^{4} He(3.5MeV) + n(14.1MeV). \tag{1.1}$$

The mass energy difference of the two states is 17.6 MeV. distributed between the helium particle and the neutron.

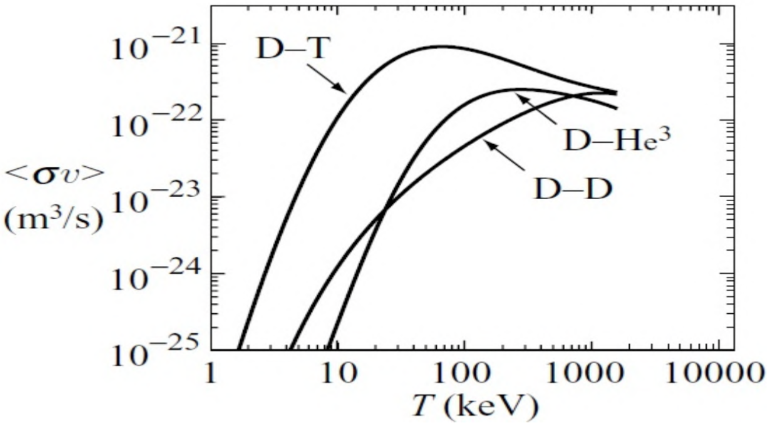

Figure 1.5: Rate coefficient of principal fusion-relevant hydrogen isotope reactions. DT reaction as a higher rate coefficient at lower temperature with respect to other nuclear reactions.

The 17 MeV produced by a single reaction, make nuclear fusion an extremely dense energy source. Energy density can be calculated as the quantity of energy released by a reaction per unit of mass. The same amount of energy produced by burning 100 tons of fossil fuel, is produced by 0.75 tons of uranium by nuclear fission of 0.13tons of DT mix by nuclear fusion; this make nuclear fusion 900 times more dense than fossil fuel.

It is not possible to generate nuclear energy by nuclear fusion by simply hitting a deuterium target with a tritium beam (or vice-versa) because the small cross section of the nuclear reaction, would make the majority of the beam particle simply deflect without producing any nuclear interaction and making the process not energetically convenient.

There are two different solution to the problem posed by the low cross section of the nuclear reaction. The first is to increase the fusion rate by simply increasing the fuel density, this is the path of inertial fusion that is not discussed in this work. The second method is that of making the particles interact multiple times after the first scattering. If particles are confined with a magnetic field, the scattered particles are not lost and can interact multiple times, thus it is needed to accelerate (heat up) the particles only once to make them interact multiple times. This is the principle of magnetic confined fusion.

Before proceeding to the description of magnetically confined fusion, a mention should be made of the method the fuel will be obtained in a fusion reactor. Deuterium is an abundant hydrogen isotope, with an abundance of 0.016% with respect to protium and it can simply be extracted from water. Tritium is an in-stable isotope with a half life of about 15 years so we must produce it. Future nuclear fusion power plant will be able to produce their own tritium in-situ by transmuting lithium. The idea is that of utilizing the fission of ^{6}Li by impact with a slow neutron to produce tritium:

$$^6\mathrm{Li} + n(slow) \rightarrow ^4\mathrm{He} + \mathrm{T} + \mathrm{energy}. \tag{1.2}$$

The slow neutron are produced by the fast fusion neutrons escaping the main chamber which are slowed down and multiplied by the interactions with ^{7}Li:

$$^7\mathrm{Li} + n(fast) \rightarrow ^4\mathrm{He} + \mathrm{T} + n - \mathrm{energy}, \tag{1.3}$$

Reaction 1.3 acts as both neutron slower and neutron multiplier. Thanks to lithium breading blanked enveloping the main chamber of a fusion device, the reactor will be able to produce its fuel utilizing the fusion products themselves.

1.3.1 Magnetically confined fusion

The principle of magnetically confined fusion is that of confining particles by means of magnetic field. Confined particles interact multiple times and produce fusion events if they have a reactor relevant temperature, dozens of keV according to figure 1.5. To be able to exploit nuclear fusion as a energy source, the power produced by fusion must be higher than that spent to heat up the particles and keep them confined, this is obtained by optimizing the triple product:

$$T_p = n_e T_e \tau, \tag{1.4}$$

where n_e is the electron density, T_e the electron temperature and τ the energy confinement time. The meaning of this product is that the fusion rate is proportional to the plasma density, the temperature of the plasma which increase the fusion cross-section, and the longer the particles interact, the most likely they produce a fusion reaction. Figure 1.6 shows the temporal succession of the triple product achieved by magnetically confined fusion machines and that required for a reactor.

The first scheme to magnetically confine plasma particles was the plasma bottle, an axial magnetic field which could confine the plasma at the two direction perpendicular to the magnetic

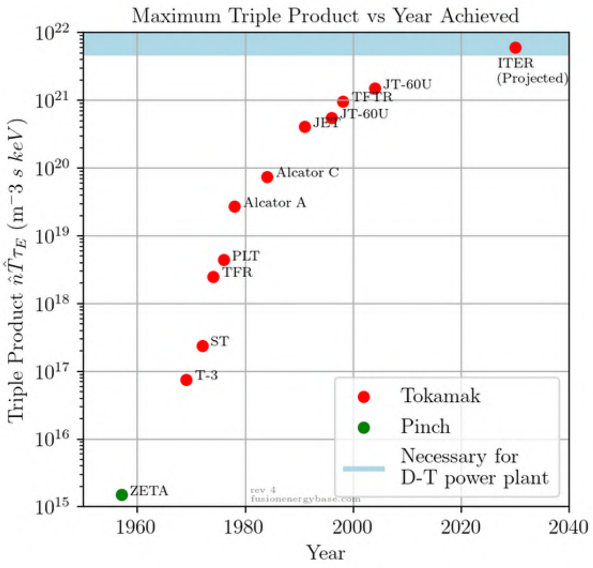

Figure 1.6: Temporal succession of triple product obtained by fusion machines in the last 60 years. The projection for ITER is included.

field field, the particle losses at the two 'sides' of the bottle, even if contained by magnetic mirrors, were still too high for a reactor-scalable machine.

The consequent idea was that of closing the magnetic field lines forming a toroidaly shaped magnetic configuration. In toroidal devices the toroidal magnetic field alone won't provide a sufficient particle confinement time due to particle drifts given by magnetic field curvature, thus a poloidal magnetic field is needed as well. There are three magnetic configurations that produce this kind of magnetic fields:

- the *tokamak* is a device where external magnetic coils produce the toroidal field, while the poloidal field in produced by the current induced in the plasma. The principle is the same used in the transformers: the current in the plasma (secondary winding) is produces by the variation of current in the central solenoid (primary winding);
- the *stellarator* is a magnetic device where both poloidal and toroidal field are made by external coils and no current flows in the plasma. It is extremely stable but also extremely complex due to the shape of the external coils required to produce the helical magnetic field;
- the *reversed-field pinch* is a magnetic configuration where majority of the magnetic field is generated by the current flowing in the plasma itself, instead of using a strong external toroidal field. The toroidal and poloidal components are similar to each other and the toroidal component of the magnetic field changes direction at the plasma boundary.

Currently the tokamak is the main path to the realization of a fusion power plant, with the stellarator being considered an alternative research path. This work will focus on tokamak plasma.

The next step towards the realization of a fusion power plant will be accomplished by the experiment ITER. ITER is the result of an international collaboration between EU, USA, Russia, Japan, India, China, South Korea and, with major radius $R = 6.2\,\mathrm{m}$ and a minor radius $a = 2\,\mathrm{m}$, will be the biggest tokamak ever built. The main objectives of ITER are to solve some plasma physics/performance as well as to test technological solutions in a reactor-relevant environment. The step following ITER will be the Demonstrative fusion reactor (DEMO) currently in conceptual design phase. Within the EUROfusion framework towards DEMO, two machines are under construction is support to ITER: JT-60SA which is ongoing the commissioning phase and the Divertor Test Tokamak facility (DTT) under construction in Italy. These two machine are smaller machines which will focus on testing specific areas of the tokamak in reactor-relevant regimes.

1.4 Work structure

This work focuses on SOL and divertor simulations by means of the edge numerical code SOLEDGE2D-EIRENE.

The goal of the project is studying edge and divertor plasma of present and future fusion devices. The project also aims at contributing to the scenario development of present and future machines and proposing optimization or alternative solutions to mitigate power exhaust to the divertor region.

Two purse these objectives the work was divided in four parts which will be described in four chapters:

In **chapter 2**, the principles of plasma edge physics and the most simple yet accurate models are presented. Subsequently edge numerical codes are described, particularly focusing on SOLEDGE2D-EIRENE. Lastly, the principle of liquid metal plasma facing components and the reason why they are considered an alternative solution to standard divertors are described.

In **chapter 3** the modelling of present experiments with SOLEDGE2D-EIRENE is presented. The comparison of modelling results with experimental data can give many information on edge plasma, it also provides a solid base for further modelling activity. In this work, the modelling of JET pulses with SOLEDGE2D-EIRENE (and the comparison with modelling with other codes or of different machines) was used to defined a validated set of transport parameters to be used for the predictive modelling of future machines.

In **chapter 4**, the information and experience gained by modelling present experiments, was used to model future scenarios of the Japanese tokamak JT-60SA and the Italian Divertor Tokamak Test facility (DTT). In both JT-60SA and DTT, an operative range of plasma density and purity was found to obtain sustainable power and particles fluxes to the divertor with different impurity seeding. For DTT case, a study was made on the effect of divertor geometry on detachment onset.

Chapter 5 describes the implementation and test of a module for the self-consistent modelling of liquid metal plasma facing components in SOLEDGE2D-EIRENE. The model was implemented and was tested in some DTT cases. The advantages and disadvantages of such solution with respect to standard divertor composition are described.

Chapter 2

Plasma edge physics and modelling

This work focuses on the plasma edge and plasma wall interaction physics. A definition and a brief discussion of plasma edge configurations is given in section 2.1.1. In section 2.1.2 plasma edge physics is introduced; a description is made of the most simple yet effective models and scaling currently used in plasma edge studies. Section 2.2 describes the 2D edge numerical code that was used in this work: SOLEDGE2D-EIRENE. Section 2.3 describes liquid metal PFCs, why they are considered as an alternative to current standard PFCs and why SOLEDGE2D-EIRENE meets the typical requirement of plasma modelling with liquid metal PFCs.

2.1 Plasma edge and divertor physics

2.1.1 Edge plasma configurations

The edge of magnetically confined plasmas can be defined as the portion of the plasma around the first magnetic surface that intersect an external wall, the volume within the last-closed-flux-surface (LCFS) is the core, the volume outside is the Scrape-Off-Layer. There are two possible edge configuration in a tokamak: the limiter and the divertor configuration.

Limiter configuration

In a limiter configuration a wall component called limiter intersect the magnetic flux surface separating the volume into core and SOL (see figure 2.1a. Since in a magnetically confined plasma $v_{rad} \ll v_{\|}$, where v_{rad} is the radial velocity, the particles that cross the $r = a$ surface hit the limiters before they have time to diffuse far in SOL. This is evident in figure 2.1b.

It is possible to estimate the width of the SOL from simple assumptions. In equation 2.1 the diffusive perpendicular transport equation is approximated as the fraction between plasma density and the width of the SOL.

$$\Gamma_{\perp} = -D_{\perp} \left.\frac{dn}{dr}\right|_{r=a} \sim -D_{\perp} \frac{n}{\lambda_{SOL}} \tag{2.1}$$

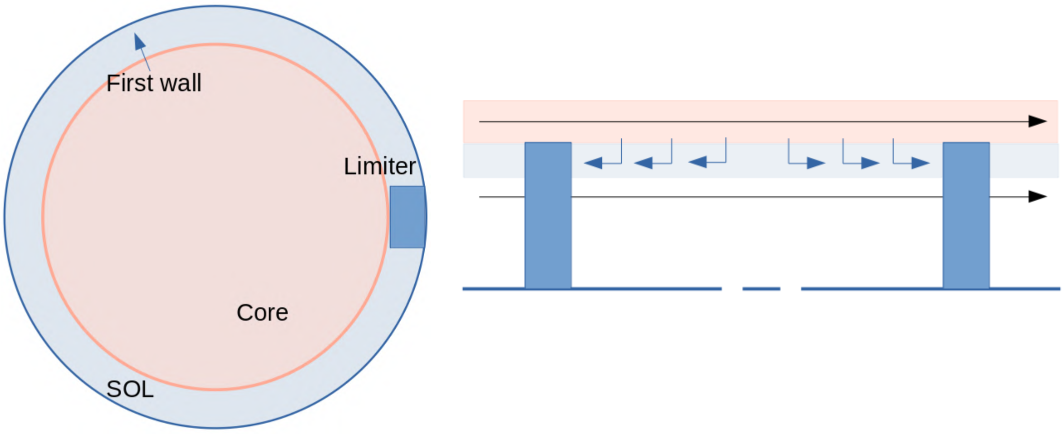

(a) Poloidal section of a limiter configuration.

(b) Representation of the SOL straightened out. Particle and energy flux diffuse from the core to the SOL and are transported to the limiter due to the higher speed parallel to the magnetic lines

Figure 2.1: Representation of a limiter configuration.

The particle flux perpendicular to the magnetic field lines can also be written as:

$$\Gamma_\perp = n v_\perp . \tag{2.2}$$

By substituting equation 2.1 into 2.2, equation is derived:

$$v_\perp = \frac{D_\perp}{\lambda_{SOL}} . \tag{2.3}$$

The average time spent to cross the SOL along the magnetic field line is estimated as:

$$\tau_{\|} = L/v_{\|} \simeq L/c_s , \tag{2.4}$$

where L is the connection length and $v_{\|}$ the particle velocity along the magnetic field line that can be approximated as the sound speed which is the particle entrance speed in the Debay sheath. The time spent in the SOL can also be calculated accordingly to velocity and space in the direction perpendicular to the magnetic field lines and by substituting we obtain:

$$\tau_\perp = \lambda_{SOL}/v_\perp \qquad \tau_\perp = \lambda^2/D_\perp \tag{2.5}$$

By equaling equation 2.4 and 2.5, equation 2.6 is obtained:

$$\lambda_{SOL} = \left(D_\perp L/c_s\right)^{1/2} . \tag{2.6}$$

Divertor configuration

The divertor configuration is the most used in fusion-relevant recent experiments because it decouples the main plasma from the plasma interacting with the wall. The divertor configuration is obtained by flowing an external current I_D parallel to the plasma current I_P. This current diverges the poloidal field in two directions: the inner divertor and the outer divertor, as shown in the figure 2.2. The two parallel currents I_P and I_D form a point called the *X-point* where the poloidal field cancels out (the X-point is a *point* if we look at the poloidal section of the plasma as in the figure 2.2, since the configuration is toroidally symmetric, the X-point is actually a circle.). The magnetic surface to which the X-point belongs is called *separator*, the surface immediately inside is the LCFS analogous to that of the configuration and limiter. The separatrix delimits the closed magnetic surfaces from the open ones; as in the limiter configuration, the zone outside the separatrix (in that case it was the LCFS) is called SOL because the charged particles entering this zone are scrapped-off from the plasma and led to the divertor targets due to the difference between parallel and orthogonal transport to the field lines. The same consideration that were done for the limiter configuration can be done for the divertor configuration by assuming the connection length to be half of the length to go from the inner to the outer divertor target along the magnetic field lines. A spaced is defined in the divertor configuration which is the volume below the X-point between the two divertor leg which is called *private region*; it is normally a low temperature low density region given that particles generally reach this region diffusion from the divertor leg or after being recycled by the wall and not directly from the main plasma.

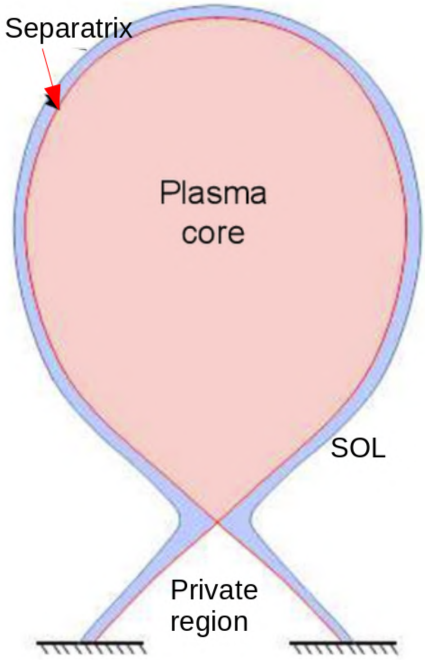

Figure 2.2: Representation of the divertor configuration.

The main advantage of the divertor configuration is that of de-coupling the main plasma from the wall not exposing directly a portion of the wall to the main plasma; it also allows to to direct the particle and power coming from the main plasma to specifically designed targets.

The addition of an X-point in the magnetic configuration introduces some complication like the reconstruction of the magnetic configuration and the location of the X-point and of the separatrix.

2.1.2 Plasma edge models

In this section I will introduce the basis of SOL and divertor physics describing one of the simplest effective models: the *2-point model* [11].

The power arriving in the SOL can be define as the difference between the total discharge power, P_{in}, and the power radiated in the main plasma by bremsstrahlung, high-Z line and low-Z impurities radiation, $P_{rad,core}$:

$$P_{SOL} = P_{in} - P_{rad,core} = P_{aux} + P_{Ohm} - P_{rad,core} \tag{2.7}$$

here the auxiliary power P_{aux} and the ohmic power P_{Ohm} contribute to the total one.
Considering the power balance in the SOL and diverted region, the two-point model divides the flux tube from the upstream to the plate in two different parts: the “conduction” region and the “recycling” one. To do that it is necessary to make some assumptions and simplifications. First of all, it is assumed to have an *opaque* divertor and that the heat is exhausted into the SOL by cross-field conduction and to the divertor by parallel conduction along field lines. It is also considered that there be significant sinks for energy, momentum and charged particles near the divertor due to line radiation by fuel species and impurities, friction between plasma ions and neutrals, and surface recombination at the target plate respectively. With all these assumptions, the plasma flux tube can be divided as in figure 2.3: the “conduction” region consists in the most of the SOL and it is considered to be almost free of sink and sources; the “recycling” region is close to the plate and it has a strong ionisation particle source and possibly sink of energy and momentum. Thanks to all this assumptions and adding simplifications of constant temperature in the recycling region, i.e. the volumetric energy losses are small respect with the plasma kinetic power deposited on the plate due to strong parallel convection, and of $T_i = T_e = T$ along the flux tube, the heat conduction along the SOL can be written in terms of the plasma temperature T and heat conductivity coefficient k_0[1] according to Spitzer and Härm:

$$q = -k_0 T^{5/2} \frac{dT}{dx} \tag{2.8}$$

It is to notice that, putting $T_e = T_i$, the ion conduction is negligible compared to the electron one. Assuming also that all the power enters in the SOL at a specific point, i.e. upstream of the divertor x=0, the integration of equation 2.8, leads to the following equality

$$T_u^{7/2} \simeq T_r^{7/2} + \frac{7 q_u L_r}{2 k_0} \tag{2.9}$$

---

[1] $k_0 = \frac{(4\pi\varepsilon_0)^2}{m_e^{1/2} ln\Lambda e^4 Z}$, where ε_0 is the permittivity, m_e and e the electric mass and charge, $ln\Lambda$ is the Coulomb logarithm and Z the effective charge.

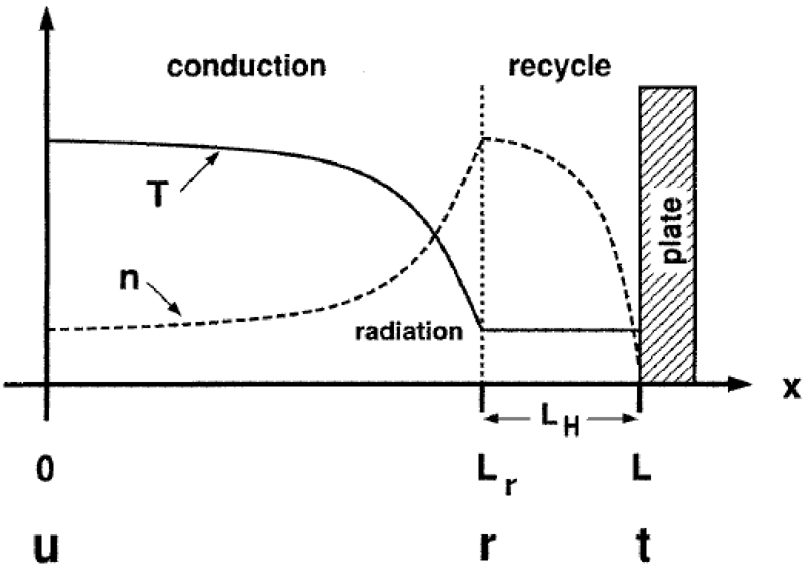

Figure 2.3

in which T_u and q_u are the temperature and the parallel power density at the upstream, T_r is the temperature of the plasma when enters in the recycling region, which can be assumed to be equal to the target one T_t, and L_r is the connection length from the upstream point to the recycling region, which can be considered equal to the connection length L itself.
The power density q_t that can be convected at the target plate through the electrostatic sheat at the target place surface is determined by the boundary "sheat condition" which involves the kinetic enthalpy of the flux of charged particles q_K and the potential enthalpy q_P that is convected by hydrogenic ions:

$$q_t = q_K + q_P = n_t c_{St} \gamma T_t + n_t c_{St} \varepsilon_{pot} \tag{2.10}$$

here there are the sheat heat transmission coefficient, $\gamma \approx 7$, the density and ion acoustic speed at the target, n_t and $c_{St} = (2T_t/m)^{1/2}$ respectively, and the potential energy per incident ion ε_{pot}. In the particular case in which the plasma has a supersonic flow towards the target plate, considering that without friction processes the pressure at the target would be about half of the upstream one and introducing the friction loss term f_m, it can be written

$$2n_t T_t = f_m n_u T_u = f_m n_r T_r \tag{2.11}$$

One of the most important term to understand the power dispersal is the *radial power decay length* in the SOL λ_P, which depends on the cross-field conduction of heat from the main plasma and on the parallel heat conduction to the divertor. In order to estimate λ_P, the following qualities of the P_{SOL} and of the upstream parallel conducted power q_u are used:

$$P_{SOL} = A_p n_u \chi_\perp \left(\frac{T_u}{\lambda_T} \right) \tag{2.12}$$

where A_p is the area of the plasma, $\chi_\perp$ is the anomalous cross-field heat conduction coefficient and λ_T is the radial temperature e-folding distance at the LCFS;

$$q_u = \frac{q_{95} P_{SOL}}{4\pi a k^{1/2} N \lambda_P} \tag{2.13}$$

where q_{95} is the safety factor at the 95% flux surface and N is the number of nulls in the poloidal field. Using the following relation between λ_T and λ_r, which is valid if $T_r << T_u$,

$$\frac{\lambda_P}{\lambda_T} = \frac{2}{7} \tag{2.14}$$

and combining equations 2.12 and 2.13, the radial power decay length can be expressed as

$$\lambda_P^2 = \left(\frac{2\pi R_0 q_{95}}{7N}\right) \frac{n_u \chi_\perp T_u}{q_u} \tag{2.15}$$

Depending on the relation between λ_P and T_u, i.e. on the ability of the SOL to sustain a significant temperature difference between the upstream and the target, it is possible to define two different plasma conditions: the *attached condition* and the *detached* one.
The attached condition is when the temperature at the divertor is sufficient high, $T_t > 10$ eV and $T_t \approx T_u$. The detached condition presents a sufficient low temperature in the SOL that results in a significant temperature gradient between the upstream temperature and the plate one. For the attached condition with a moderate density and the detached case with high density, it is possible to derive the same power e-folding distance:

$$\lambda_P = \left(\frac{6.4 R_0 a^{5/9} k^{5/18}}{k_0^{2/9} N^{4/9}}\right) \frac{q_{95}^{4/9} n_u^{7/9} \chi_\perp^{7/9}}{P_{SOL}^{5/9}} \tag{2.16}$$

It is to notice the strong dependence on the machine parameters R_0 and a, the major and minor radius of the camera respectively.

2.2 2D edge modelling with SOLEDGE2D-EIRENE

SOLEDGE2D-EIRENE[12][13][14] is a multi fluid coupled code used for the study of SOL and divertor plasma. SOLEDGE2D is a fluid code which solves the dynamic of plasma species and EIRENE is a Montecarlo code for neutrals. SOLEDGE2D solves fluid plasma equations and provides plasma background and source terms for the Montecarlo simulation, Eirene calculates neutral quantities and source and sink terms for SOLEDGE2D. A set of routine called STYX is used as a interface between the two codes. SOLEDGE2D can alternatively be coupled to a set of routines that evaluates neutral parameters with a fluid treatment which is faster but less accurate. This option was not used in this work and is not discussed here.

2.2.1 SOLEDGE2D

SOLEDGE2D description of the SOL and divertor plasma is based on mass, momentum and energy balances derived from the Braginskii's[15] or Zhdanov's[16] equations. Zhdanov closure was derived for multi-element plasma and is consequently more accurate for multi-component simulations[17]. Quasi-neutrality condition is assumed, meaning that mass and momentum conservation equations are solved for main and impurities ions only, electron density is derived from quasi neutrality and matching the ambipolar flux we obtain that electron and ion parallel velocity is equal: $u_e = u_i = u$. The energy balance is solved for each ion specie and for electrons. Partial differential equations solved by SOLEDGE2D are listen in [13] and [17].

Cross-field transport of particles,momentum and energy is treated with diffusive models, a possible convective term for particle transport can be simulated by a cross field pinch velocity. The diffusion coefficient D, μ, $\chi_{i/e}$ and the pinch velocity are set by the user. There is no self-consistent model that evaluates transport parameters from plasma parameters such as density, temperature, etc... For this reason, transport parameters are chosen to fit experimental data, scalings or expected profiles. Cross flied transport profiles have a major impact on SOLEDGE2D-EIRENE results, in this work a relevant focus will be given on the determination of accurate transport profiles. This treatment of perpendicular transport is analogous to that used in other similar 2D-edge numerical codes such as SOLPS5.2[18], SOLPS-ITER[19], UEDGE[20] and EDGE2D[21].

The main difference between SOLEDGE2D and the upper mentioned codes is the geometrical. By using a penalization technique, it is possible to extend SOLEDGE2D to the entire wall surface, differently similar codes like B2.5 where the grid extension is limited to no intersect the first wall anywhere but at the divertor targets. This means that in SOLEDGE2D there is no plasma particle loss at the external boundary of the grid, since the external boundary is always the wall surface. These particle losses were proven to influence numerical results in codes with finite grid extension [22]. The extension of the simulation domain to the external wall is obtained by extending SOLEDGE2D beyond the geometrical boundary of the first wall. The domain is split in to zones: the internal zone and the zone external to the first wall. Penalization parameters are applied to the cells belonging to the external zone, extra terms are inserted in the balances equations into the wall domain without generating extra source terms in the plasma. As a consequence, boundary conditions at the plasma-wall interfaces are recovered. This numerical scheme has been tested for limiter[14] and divertor[12] configurations. A view of a SOLEDGE2D grid and the corresponding map of the penalization parameter χ is shown in figure 2.4.

Boundary conditions at SOLEDGE2D inner boundary are given by the used on particle flux or density and on energy flux or temperature. Power or temperature boundary conditions are given for each species simulated, density or particle flux boundary conditions are given for all species but electrons. Zero momentum transfer boundary condition is hard-coded.

Given the characteristics of SOLEDGE2D code, combined with the possibility to adopt EIRENE for the neutral description, it is particularly suited for the simulation of different edge plasma scenarios. The code is particularly suitable for the simulation of closed divertor geometry such as corner-corner strike-point configuration in JET (that will be analyzed in this work) or TCV scenarios with buffles of alternative divertor configurations such as MAST-U Super-X.

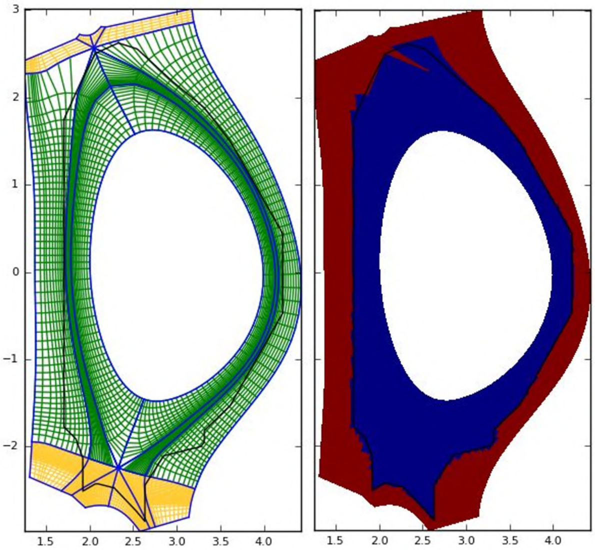

Figure 2.4: Example of SOLEDGE2D grid (a), the grid is extended beyond the first wall; the cell were the penalization technique is applied and those where it is not are shown in blue and red (b).

2.2.2 Eirene

Neutral dynamics is solved by Eirene. In high neutral density regimes, like high recycling or detachment, the analytical and fluid models are not suited to describe the neutral dynamics since the typical collisional mean free is shorter than the geometrical scale.

EIRENE is a code which gives a kinetic description of the neutral behaviour and transport [23]. It uses a Montecarlo method to solve the Boltzmann's equation for neutral particles. Since neutral transport is faster than plasma transport, Eirene always solves stationary equations. The Boltzmann's equation can be written in terms of the collision density $\psi(x) = \sigma_t(x)vf$, where $\sigma_t(x)$ is the macroscopic cross section. The kinetic equation in the integral form is:

$$\psi(x) = S(x) +^{'} \psi(x^{'})(x^{'}), \qquad (2.17)$$

where $S(x)$ is the initial distribution, K is the transition kernel, which represents the probability to evolve from a pre-collision state x' to the post-collision state x.

The Montecarlo method consists in launching multiple test particles from neutral sources location. The velocity, intensity of the source and collision rate for each test particle are retrieved from input parameters and atomic data. EIRENE is usually coupled with a fluid plasma code, which provides the plasma background which is considered stationary. Particle cross section are derived from ADAS [2], AMJUEL [24] and HYDHEL [25] database.

The use of a kinetic Monte Carlo codes allows to perform an accurate description of the neutral dynamics by tracking directly the neutrals trajectories; in turn, this feature allows to take into account the actual geometry of the divertor and vessel wall. As a results, the EIRENE code is able to perform a deep analysis on the effect related to a change in the vessel or magnetic configuration, e.g. to study the effect of the increase of the divertor closure. However, the greatest drawback stems in the high computational time which is much longer than the one required by the analytical and fluid model treatment.

These features, especially the latter point, are very interesting for the purpose of the PhD research activity. However, a validation phase is necessary and a benchmark of the results with experimental data is required. This is the focus of the chapter 4, where the results obtained with SOLEDGE2D-EIRENE code on a JET experiment are compared with the corresponding experimental data.

2.2.3 Numerical details

On the numerical side, a few precautions are taken when running SOLEDGE2D-EIRENE.

The adequacy of the radial grid is ensured by securing that the radial width of the grid is shorter than the typical radial phenomena. The region were the cell width is the shortest is around the separatrix. At the separatrix the heat flux decay length in some of the H-mode discharges analysed in this work, is as low as 1 mm. This king of phenomena are taken into account when making the grid for each pulse, it is ensured that at least 2/3 cells are contained outside of the separatrix within one heat flux decay length. The limitation on cell width largely reduces the maximum time-step in each iteration of SOLEDGE2D; this slows down the simulations which can be extremely slow when seeding impurities are introduced. A compromise was made between spatial resolution and reasonable modelling time scales. Similar same precaution was ensured inside the separatrix, the cell width is always shorter than the variation length of the main physical magnitudes, i.e.: $(\delta_r \ll T/\nabla_r T) \cup (\delta_r \ll n/\nabla_r n)$, where n and T are ion or electron temperature.

Similar precautions were taken when evaluating the poloidal resolution of the grid. Poloidal transport is much faster thus implying that lower spatial resolution is required. The area where the highest spatial resolution is required is the divertor region. At the divertor plates, thermal neutrals are emitted by recycling, and are immediately ionized. The typical mean free path of a wall temperature neutral in divertor plasma environment is typically withing few centimeters. The typical length of the first cells was set to about 0.3 cm.

Simulations convergence is evaluated according to two parameters: the convergence of global parameters like total energy and particle balance and, for simulations with impurities, the overall convergence of each ion specie profile.

2.3 Liquid metals as plasma facing components

Liquid metal-based divertors (LMDs) are a considered as an option to standard tungsten divertors of future high performance machines such as DEMO [26].

The most promising LMDs target models are based on the capillary porous system (CPS) technology. Liquid metals are electrical conductors, if a relevant current is induced in the metal, the $\mathbf{j} \times \mathbf{B}$ force can extract the liquid metal from the surface. This force can be counteracted by the capillary force of liquid metals. The component (typically made of tungsten) on top of which liquid metal are posed are porous to better exploit the high porosity of liquid metals. The porous surface also increase liquid metal mobility on the surface replenishing the area were the metals are extracted by sputtering or evaporation. The CPSs normally have an internal reservoir that is connected to the porous surface by a capillary system. Liquid metal flow from the reservoir to the CPS surface was tested to reach up to 10^{24}part/sm^2.

(a) Surface of the molybdenum CPS tested in FTU after (a) and before (b) being filled with lithium[?].

(b) Picture of the CPS used as a limiter in FTU testing[?].

(c) Picture of the CPS tested in the linear device MAGNUM-PSI[27].

Figure 2.5: Picture of tested CPS.

LMD have a higher robustness against transient loading (e.g. disruptions) with respect to tungsten divertors. The higher robustness level is achieved via vapor shielding. Vapor shielding act as a passive feedback scheme which is described in picture 2.6. When transient heat flux peak reaches the divertor, the increasing liquid metal temperature increase evaporation and sputtering, increasing impurity concentration and plasma radiation, consequently decreasing the power deposition to the PFC.

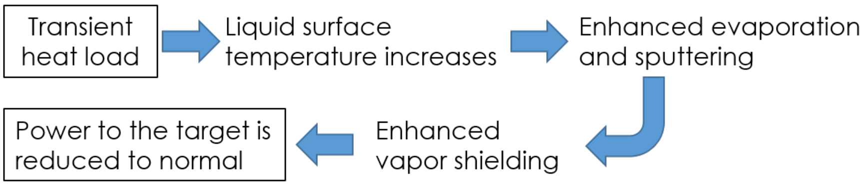

Figure 2.6: Sketch of the passive control scheme of liquid metal PFC

Transient loads provoke constant degradation, edge sharpening, deformation, cracking, melting and re-crystallization in standard tungsten divertor[28]. Although the all component is not invulnerable to all those phenomena, the liquid surface of LMD won't suffer from many of those. The surface is already melted, its shape depends on the shape of the underneath porous system and wherever liquid metal is removed, the surface is replenished by the CPS.

Due to the elevate liquid conductivity of liquid metals, plasma facing components can be smaller than those foreseen in DEMO and ITER baseline scenarios and can also sustain higher steady state heat loads [29]. This property may help with dimensions[30]: ARC tokamak, which aims at delivering the same fusion power as ITER (500 MW) in a device with half the major radius (3.3 m compared to 6.2 m) [31].

Tungsten monoblock and more generally tungsten PFC have been tested for year in linear devices, limiters and divertors. On the contrary, LMD haven't been tested yet in a fusion relevant scenario. This kind of experiments are required to test whether LMD can be suitable for a reactor-relevant environment avoiding metal sprays or CPS degradation.

Other downsides depend on the metallic element which is chosen and are discussed next section

2.3.1 Lithium and tin as liquid metal PFC

Lithium and tin are considered the best candidates as metallic element for a LMD because of their high capillarity and the value and width of the temperature range in which they are liquid.

Lithium is a low-Z element which is optimal since it is completely ionized in the temperature range of the core of a fusion device. Tin as $Z = 50$, a relatively high Z and can radiate much more in the plasma core which is not ideal. On the other hand, tin has an evaporation rate order of magnitude lower than lithium [32]. Due to the different Z of the two element the have opposing advantages and disadvantages. On one side tin may cause high radiation in the core, on the other side lithium may cause fuel dilution due to its high evaporation and sputtering rates. These two phenomena must be mitigated towards possible LMD-based fusion machines.

Tin has a further advantage over lithium which is the width of the temperature range the two elements are in liquid state. The temperature range is between 505and 2875 K for tin ($\Delta_T = 2370\,\mathrm{K}$) and between 454 and 1615 K for lithium ($\Delta_T = 1161\,\mathrm{K}$), making tin's twice as wide as lithium's. This temperature range can be interpreter as the operational range of a LMD since above the fusion temperature bubbles of the liquid metal element would enter the plasma.

The elevate chemical affinity of lithium with hydrogen may be a problem in a reactor-relevant environment due to the formation of LiT (lithium hydride made of tritium instead of protium). Lithium may absorb high quantity tritium, which is a radioactive element whose re-circulation and accumulation in the machine must be controlled.

2.3.2 Models of liquid metal PFC and present experiments

LMD concept should first be developed for testing at intermediate stages such as a Divertor Test Tokamak, (DTT) which foresees LMD as a possible furure divertor configuration. Presently, concept designs are needed with the potential to fulfill the requirements for DEMO, that can eventually be tested as thoroughly as the solid divertors.

Current design of liquid metal PFC are being tested for multiple reason:

- to test LM surface stability [33] and the effectiveness of slashing suppression by CPS [34][35][36]
- to demonstrate vapor shielding effectiveness[37][38][39];
- to test the vapor-box geometry, which is designed to reduce liquid metal concentrations in the core plasma [40];
- to test dissipate heat through convection[41][42]
- to estimate liquid metal loss in the CPS and the consequent fuel dilution [27][43]

2.3.3 Existing modelling of LMDs

Many models are currently used for modelling plasma scenarios with LMDs. Some use a predefined concentration of impurities [43], others used fixed temperature target [44][45] other utilized a self consistent code [46][47] but utilized a simpler transport code.

SOLEDGE2D-EIRENE is a particularly suitable code for simulating plasma scenarios with LMDs, which is mainly due to three factors:

- The penalisation technique used makes it particularly suitable for simulating very closed divertor geometries such as LMDs;
- The simulation of neutrals using Monte Carlo code makes it suitable for simulating scenarios with a high density of neutrals;
- The separate treatment of each ionised state of the impurities makes it particularly accurate in calculating the radiated power.

Chapter 3

Modelling of present machines

One of the main objectives of this thesis is the careful modelling and definition of realistic divertor scenarios of future fusion devices. The description of future machines is particularly challenging because, as described in the previous chapter, SOLEDGE2D-EIRENE is a complex code that requires several input parameters that must be properly set in order to obtain a realistic output. Some of the input parameters are directly derived from the plasma scenario (magnetic field, input power, puffing, pumping etc...); some others, like transport or plasma-wall interaction parameters, are determined by modelling well-diagnosed discharges.

In plasma-edge numerical codes such as SOLEDGE2D-EIRENE or SOLPS-ITER, cross-field transport parameters are not self consistently calculated, transport parameters are assigned and fixed before running the codes, the codes are 2-dimensional consequently there is no turbulent model which can calculate transport parameters from plasma profiles. Nevertheless, transport values are one of the input parameters that influence modelling results the most, so a careful guess of such parameters must be done when performing predictive modelling[48][49]. In the same way, plasma-wall interaction is determined by a set of key input parameters such as recombination coefficients and sputtering yield which were described in chapter 2. These are particularly important when modelling C-wall machines since carbon sputtering and redeposition are the main impurity source and sink [50].

The approach that was used in this work is to estimate the upper mentioned parameters by deriving them from modelling of comparable pulses of existing machines through comparison with experimental data. Another instrument that is used to determine transport parameter values is the Eich scaling which was described in the previous chapter.

In this chapter, the modelling activity of existing machines towards predictive modelling is described. In section 3.1 the modelling of tungsten-wall machine to validate input parameters to be used in DTT modelling is described; in chapter 3.2 the modelling activity on carbon-wall JET towards JT-60SA modelling is presented. In both sections, the available edge-plasma-relevant diagnostics are described first, then the modelling activity, the comparison to the experimental data and the main outcome are presented.

3.1 Modelling of W-wall machines towards DTT modelling

This section describes the modelling activity performed with the scope of determining a correct set of input parameters towards the modelling of the medium-density full-power single-null scenario of the Divertor-Test-Tokamak facility (DTT) under construction in Frascati (Italy)[4]. DTT is a machine specifically designed to test standards and alternative divertor configurations solutions such as the standard single null divertor, the double null, the snowflake and the X-divertor[51] and possibly technological solution like the liquid metal divertor. The feasibility and the compatibility of these solution with core performance (high energy and particle confinement, low fuel dilution etc..) will be tested with power-exhaust-relevant parameters as P_{aux}/R (the ratio between the auxiliary input power and the major radius of the machine) and collisionality similar to DEMO's parameters.

The first divertor that will equip DTT will be based on the tungsten mono-block technology. For this reason, the machines chosen to estimate the input parameters to be used for DTT modelling should also be equipped with metallic walls. The possibility of using different divertor technologies and divertor shapes is foreseen for later DTT experiments.

JET with the ITER-like wall (JET-ILW) and Alcator C-MOD (C-MOD) pulses were modelled to define and validate a set of transport parameters for DTT. JET was chosen because of the high plasma current, dimensions, temperature and above all the available auxiliary input power that is comparable to that foreseen in DTT. C-MOD was chosen for the high magnetic field (up to 8 T), plasma density and neutral opacity similar to that foreseen for DTT. JET modelling was performed with SOLEDGE2D-EIRENE and SOLPS-ITER. C-MOD modelling was performed with SOLEDGE2D-EIRENE, but it was not performed by the author of this work. For this reason, C-MOD modelling results are used in comparison to JET modelling results, the modelling activity is not analyzed in detail.

Tungsten itself is not included in SOLEDGE2D-EIRENE simulations due to the high atomic number that would require 74 fluid species to be simulated[52]; more often tungsten is treated with bundles that can reduce the number of tungsten species using collision rates averaged on multiple ionization states[53]. Nevertheless, the vast majority of tungsten-wall edge modelling is performed without including tungsten in the simulations and subtracting tungsten radiation from the input power to compensate for the radiative energy sink. In the SOL, due to the low temperature, tungsten radiation is negligible due to the low cooling rate of high-Z atoms at low temperature and the low sputtering yield of tungsten. These are the reason why this approximation was also used in this work.

To extend the validity of this modelling activity, a selection of JET pulses were also modelled with the edge numerical code SOLPS-ITER. This choice was made to compare the two codes, to confirm the validity of the transport coefficient found and to validate transport parameters for the considered DTT scenario which are realistic for multiple codes. The modelled DTT scenario is the full power inductive scenario, a better description of this scenario will be given in the next section and in chapter 4.2. Four JET pulses were modelled; out of those four, only the two with vertical-vertical target configuration were modelled with SOLPS-ITER; The two corner-corner cases could not be modelled with such code due to the closure of divertor geometry around the strike points. SOLPS-ITER modelling was not performed by the author of this work, which only focused on the comparison with SOLEDGE2D-EIRENE modelling results.

3.1.1 JET Pulse selection

The DTT scenario that will be simulated is the single-null scenario with the maximum nominal auxiliary input power: $P_{aux} = 45\,\mathrm{MW}$. The main characteristic of the scenario are listed in table 3.1. The scenario has high plasma current ($I_p = 5.5\,\mathrm{MA}$) and a strong toroidal magnetic field at the central axis ($B_T = 5.85\,\mathrm{T}$). The strike-point position will be on the vertical targets both at the inner and outer target, similarly to ITER. The scenario will be probably seeded with neon or argon. The major radius of the machine is $R = 2.19\,\mathrm{m}$ and the minor radius $a = 0.7\,\mathrm{m}$. The main plasma parameters that influence transport are: the magnetic field that is inversely proportional to the Larmor radius, input power, which influence thermal gradients and L-H transition and plasma density which is linked to plasma collisionality. DTT relevance of selected fusion machines and pulses was determined accordingly to this principle.

For transport parameter validation, JET equipped with the ILW was mainly chosen for the high auxiliary input power available. Pulses with the maximum available power flux were selected, in JET case it corresponds to $P_{aux} \gtrsim 32\,\mathrm{MW}$ compared to the $45\,\mathrm{MW}$ available in DTT. In DTT the power fraction crossing the separatrix is expected to be lower than in JET, due to the higher plasma density of DTT pulses and the possible higher impurity concentration that will be required. Greenwald density limit [54] of DTT full power high current scenario is more than twice as big as the density limit of the ITER-reference scenario in JET. As to obtain the maximum compatibility with DTT, JET pulses were selected with high plasma current as it is shown in table 3.1. JET pulses also have q_{cyl} similar to DTT full power single null scenario.

To have a more complete and unbiased analysis, JET pulses were selected with different seeding impurities. Out of the four chosen pulses, two were selected with neon seeding, one with nitrogen seeding and one deuterium-only case. For the same reason, one of the two neon-seeded cases also utilizes pellet injection for the ELM pacing, while the other does not. The position of the strike points is also different: in two of the considered pulses the strike points are in the vertical targets (vertical-vertical configuration as foreseen for DTT) and in the other two cases the strike points are in the low horizontal targets (corner-corner).

C-MOD was modelled because its scenarios better match DTT density and toroidal field as it is shown in table 3.1. In C-MOD particle density is sustained by neutral puffing, similarly to what will happen in DTT. JET is equipped with a system of two positive NBI that, when operated at full power, guarantees a particle flux in the order of $10^{21}\mathrm{D/s}$, while in DTT full-power scenario the NBI particle flux will be one order of magnitude lower[1], C-MOD is equipped with no NBI. It could seem that the DTT case is more similar to the JET case, but in reality, it is exactly the opposite. In the JET case, the particle flux from NBI is of the same order of magnitude of neutral particle penetration through the separatrix, thus the plasma density is sustained by both core flux from NBI (and pellets if available) and puffing. On the other hand, in DTT the NBI particle flux is negligible compared to the expected neutral penetration[2] similarly to C-MOD

---

[1] DTT will be equipped with a $500\,\mathrm{KeV}$ neutral beam injector while the energy of JET NBI is $50\,\mathrm{keV}$. If DTT neutral beam current is one order of magnitude lower than in JET, the energy deposited to the plasma is the same.

[2] The expected neutral penetration in DTT is estimated in chapter 4 to be about $10^{21}\mathrm{D/s}$, one order of magnitude higher than NBI particle flux; it was also predicted in [55]

Machine Pulse		JET 96482	JET 96139	JET 95946	JET 92436	C-Mod 1160729008	DTT
time	[s]	51.5	55.0	55.0	50.2	-	-
B_t	[T]	3.29	2.7	2.65	2.8	7.8	5.85
I_P	[MA]	3.5	2.5	2.5	3.0	1.42	5.5
q_{cyl}		2.7	2.4	2.4	2.3	3.97	2.2
R	[m]	2.97	3.03	3.04	3.05	0.68	2.19
a	[m]	0.92	0.85	0.90	0.95	0.22	0.7
b	[m]	1.60	1.40	1.40	1.45	-	1.16
k		1.73	1.65	1.56	1.53	-	1.66
Paux	[MW]	33.3	28.5	28.6	32.8	5	45
Te,core	[keV]	7.4	3.6	4.2	7.3	1	20
f_G		0.77	1.0	1.0	0.90		0.5
n_{core}	$[10^{19}m^{-3}]$	9.4	9.0	8.8	8.0	35	15.0
n_{sep}	$[10^{19}m^{-3}]$	1.9	5.6	4.7	1.7	10	8.0
n_c/n_s		4.9	1.6	1.9	4.7	3.5	1.9
$f_{pellets}$	[Hz]	25	-	-	-	-	tbd
Str. points		h-h	v-v	v-v	h-h		v-v
Seeding		Ne	-	N	Ne	-	Ne/Ar

Table 3.1: Main flat-top JET pulse plasma parameters and relative parameters at the flat-top for the full-power single-null DTT scenario as from [4].

where the NBI particle flux is absent. This consideration implies that C-MOD modelling will hardly provide information on particle transport parameter (D) within the pedestal given the zero particle flux from the core. The difficulty of matching density profiles within the pedestal top of C-MOD may indicate the presence of pinches that were not considered in this work.

In table 3.1 the main parameters of selected pulses are shown. As it is shown in the table, JET pulses can better match DTT, plasma current, machine dimensions, input power and electron temperature; on the other hand, C-MOD is a machine that operates with a high magnetic field, higher density and plasma opacity, more similar to DTT ones.

3.1.2 Pulse analysis and modelling methodology

Input power P_{in} is one of the main input parameters in SOLEDGE2D-EIRENE. The input power at the SOLEDGE2D-EIRENE inner boundary has to match the power that flows through the corresponding flux surface in the experiment; SOLEDGE2D-EIRENE inner boundary was set inside the pedestal top, for these pulses around the flux coordinate $\rho_{tor,norm} \approx 0.85 \pm 0.05$. To calculate the power flowing through the volume modelled by SOLEDGE2D-EIRENE, the power radiated within the code inner boundary has to be subtracted from the auxiliary input power coupled to the plasma. We are not modelling the time evolution of the pulse but we are interested in modelling the steady-state inter-ELM phase, for this reason, the power that increases diamagnetic energy and feeds the ELMs has also to be subtracted, a better explanation and an estimation of this power will be given later in this paragraph. The input power crossing the inner boundary can be calculated as:

$$P_{in} = P_{aux,tot} - P_{\mathrm{ELM}} - P_{rad,in}, \tag{3.1}$$

where $P_{rad,in}$ is the power radiated within the SOLEDGE2D-EIRENE inner boundary and P_{ELM} is the power dissipated by ELMs. This equation is explained in the following paragraphs.

The auxiliary input power $P_{aux,tot}$ is the sum of ICRH power absorbed by the plasma (ICRH/PTOT in the JET database and in the legend of the following images[3]), the NBI power deposited to the electrons (NBIP/GET) and the NBI power deposited to the ions (NBIP/GIT). In all of these cases, the diagnostic signal relative to the power absorbed by the plasma was used rather than that relative to the emitted energy. Figure 3.1 shows the time trace of such signals. The uncertainty on the input power values can be estimated as the variance of each value in the considered time interval which is highlighted in figures 3.1a-3.1d. The uncertainty on $P_{aux,tot}$ is calculated case-by-case and is about 1.5 MW. An elaboration of diagnostic signals estimates the D^+ flux from NBI absorbed by the plasma (NBI/EFLX in figures 3.1a-3.1d); the estimated NBI particle flux is fixed as the inner boundary condition of particle flux in SOLEDGE2D-EIRENE, this can be done because we are modelling steady-state conditions. It should be noted that this leads to a slight over-estimation of the particle flux coming from the core since part of the NBI flux is deposited outside of SOLEDGE2D-EIRENE inner boundary; the approximation is good since the NBI is optimized to deposit the particle as much as possible in the plasma centre.

Total and core plasma radiation is derived from bolometer LOSs shown in figure 3.3. A high time resolution reconstruction of core radiation is made in JET and is shown in figure 3.2 with the diagnostic name BOLO/TOPI. The high-time-resolution signal is very noisy due to ELM radiation and has an estimated error of 10% according to the JET database. A higher-quality bolometer reconstruction was requested for each analysed pulse at the required time; the time resolution of the bolometer is higher than the ELM frequency and it allows to filter bolometer signals between the ELM events, the so-called *inter-ELM* phase.

Bolometric reconstructions of power dissipation of each pulse are shown in figure 3.2a-, signals are plotted using the same energy scale in each pulse. The yellow contour represents the flux coordinate of the SOLEDGE2D-EIRENE inner boundary of each simulation relative to the respective pulse; the integration of the radiation within the contour is an estimation of $P_{rad,in}$ which has an estimated error of 5%. Figures 3.2a and 3.2d show a high radiation zone at the outer mid-plane; typically the source of such radiation is tungsten which is sputtered by heavy particles, pulse #92436 and #96482 are the neon seeded pulses and is neon itself that causes tungsten sputtering because the outer target is detached. If more neon was inserted and the target was detached, tungsten sputtering and radiation would have been much lower. Since tungsten is not included in the simulations, in these two cases, it was chosen to keep the SOLEDGE2D-EIRENE inner boundary outside of the tungsten radiating volume. It is then assumed that tungsten does not radiate in the SOLEDGE2D-EIRENE simulated domain, this is a reasonable assumption given the low tungsten radiation at small temperatures. On the contrary, in the nitrogen seeded case (pulse #95946), radiation is very strong at the x-point and the inner target since the inner target is detached and the outer target is partially detached.

---

[3] For simplicity the name of each set of data will be listed with the same name it has in the JET database.

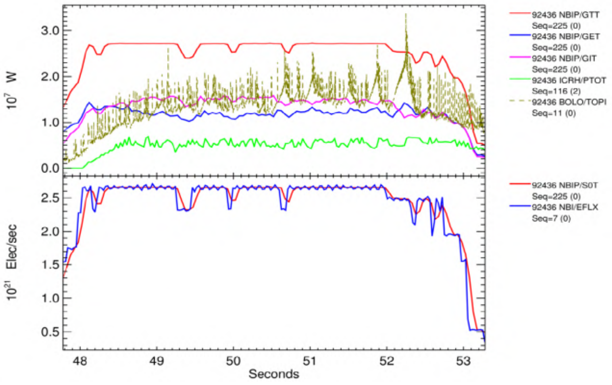

(a) JET #*92436*

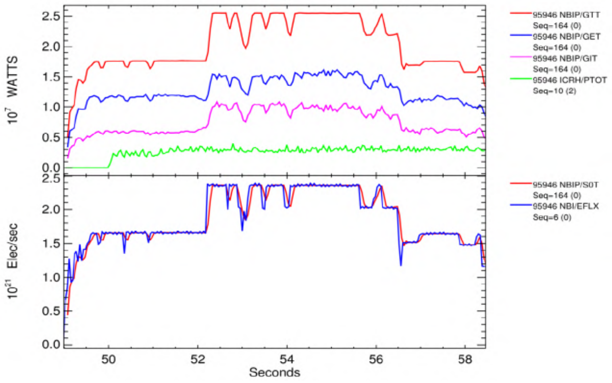

(b) JET #*95946*

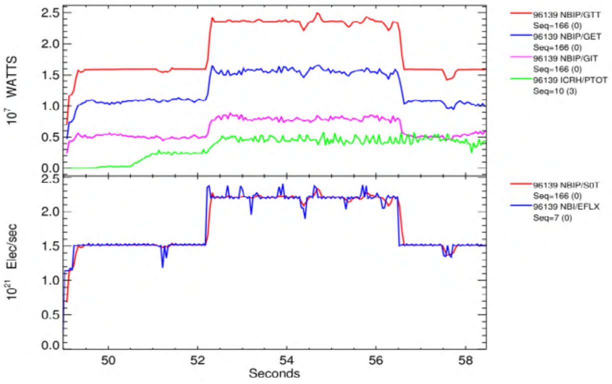

(c) JET #*96139*

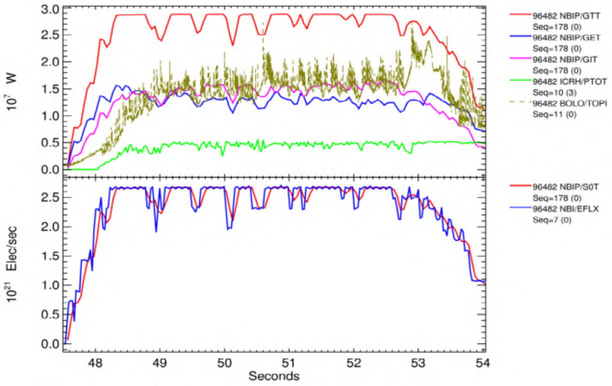

(d) JET #*96482*

Figure 3.1: Time-traces of considered JET pulses.

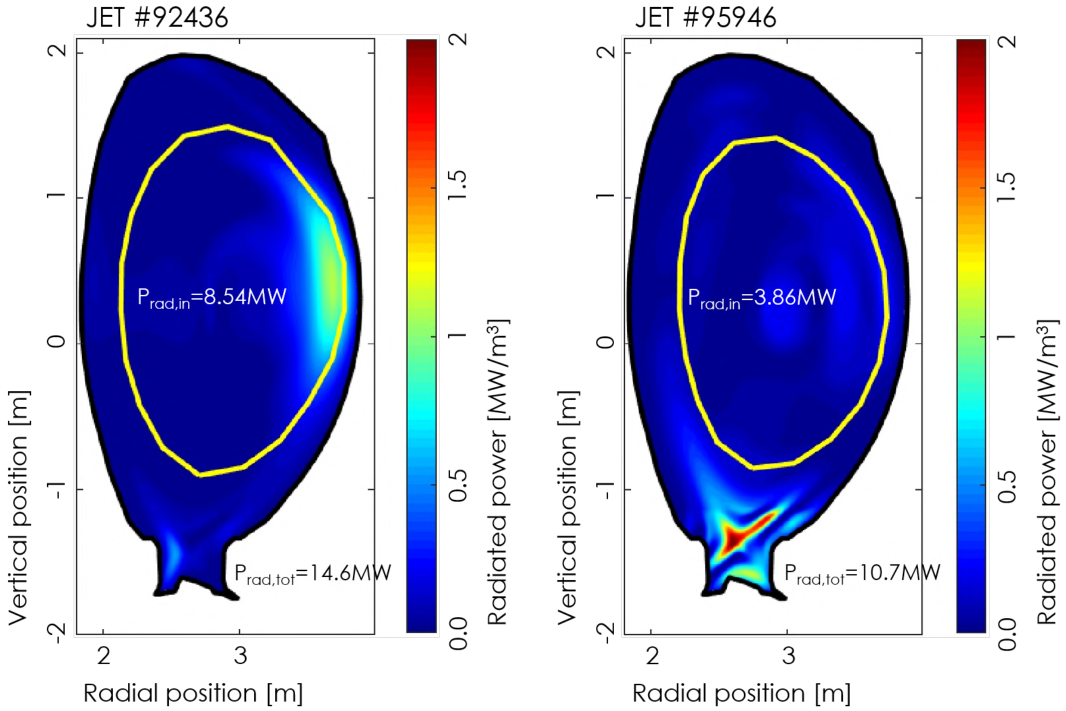

(a) Tomographic reconstruction of power dissipation by radiation of JET#92139 $t = 51.5\,\mathrm{s}$. The pulse is seeded with neon.

(b) Tomographic reconstruction of power dissipation by radiation of JET#95946 $t = 55.0\,\mathrm{s}$. The pulse is seeded with nitrogen.

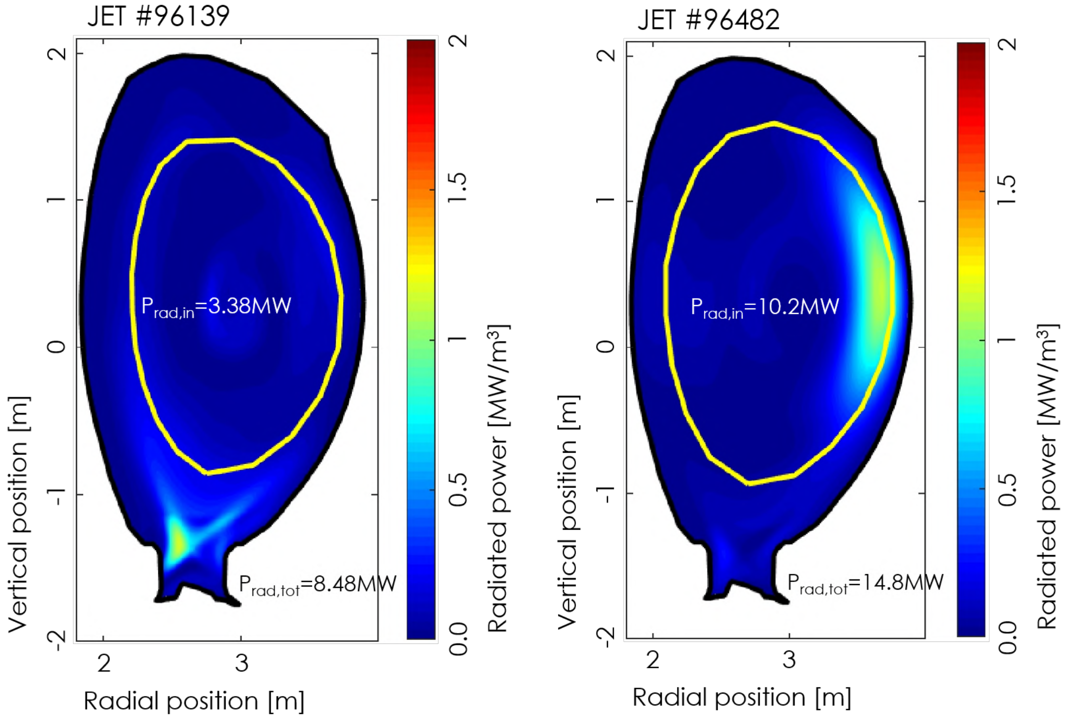

(c) Tomographic reconstruction of power dissipation by radiation of JET#96139 $t = 55.0\,\mathrm{s}$. The pulse is unseeded.

(d) Tomographic reconstruction of power dissipation by radiation of JET #96482 $t = 50.2\,\mathrm{s}$. The pulse is seeded with neon.

Figure 3.2: Tomographic reconstruction of considered JET pulses.

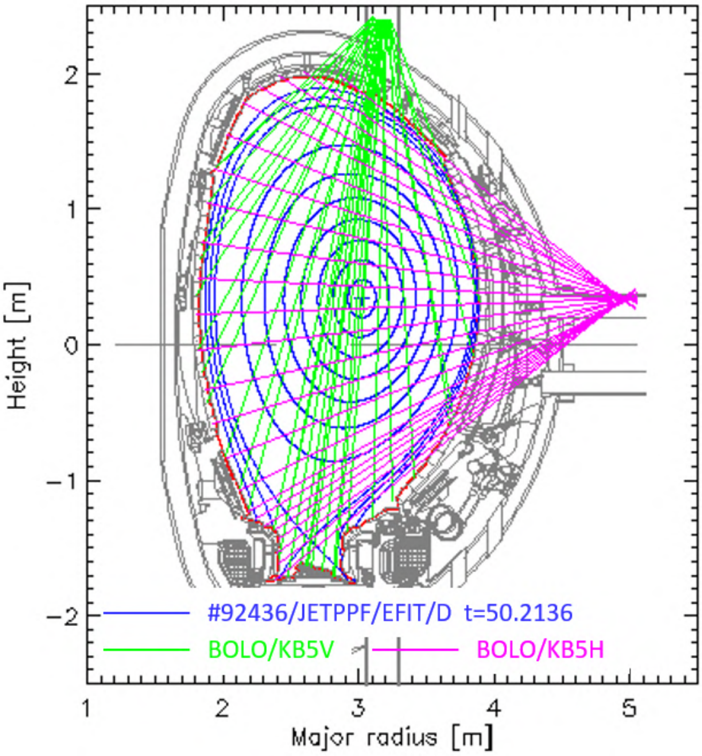

Figure 3.3: Bolometry line of sight available in JET.

The reduced temperature at the strike points lowers tungsten sputtering, tungsten concentration and subsequently tungsten radiation; radiation at the X-point is given by nitrogen itself.

In the inter-ELM phase the diamagnetic energy of the plasma increases[56][57], although, this phase can be approximated as a steady state using a simple technique. Since the power which increases the diamagnetic energy does not flow through the SOL, when performing inter-ELM modelling, this contribution (P_{ELM}) must be subtracted from the input when calculating P_{IN}. In JET, diamagnetic energy evolution is derived from JET *Equilibrium Reconstruction* EFIT or the *High Time Resolution Equilibrium Reconstruction* EHTR [58]; EHTR has a higher spatial and temporal resolution, much higher than typical ELM frequency.

Figure 3.4 shows the time trace of the diamagnetic energy of the considered JET pulses. For pulse #92436 and #96482, the signal from Be^{+2} is available and is shown in the lower part of figure 3.4a and 3.4d respectively. In those images, TBEI and TBEO refer to the sum over spectroscopy line of sights (LOSs) signal from inner and outer target respectively. Beryllium is one of the components of JET-ILW, it is deposited to the divertor and extracted again from it the during the ELMs [59][60][61], thus it can be used as a trigger signal for the ELMs; figures 3.4a and 3.4d show a clear correspondence between Be^{+2} signal peaks and diamagnetic energy variation.

P_{ELM} is calculated as the temporal derivative of diamagnetic energy in the inter-ELM phase. The derivative was calculated by considering the increase of diamagnetic energy signal from the high-resolution equilibrium reconstruction (EHTR/WP) over many ELM cycles in the flat-top phase of each of the considered pulses. The considered ELM-cycles are shown in yellow in figure

Pulse	P_{ELM} [MW]
JET #*92436*	8.8 ± 1.3
JET #*95946*	7.9 ± 1.4
JET #*96139*	10.0 ± 0.6
JET #*96482*	8.5 ± 0.4

Table 3.2: Power flux increasing diamagnetic energy derived from JET dataset.

Machine		JET	JET	JET	JET	C-Mod	DTT
Pulse		96482	96139	95946	92436		
P_{ECRH}	[MW]	0.0	0.0	0.0	0.0	3.0	26-36
P_{ICRH}	[MW]	4.5	4.7	3.1	5.5	2.0	3-9
P_{NBI}	[MW]	29.5	24.1	26.0	27.7	0.0	7.5-15
$P_{aux,tot}$	[MW]	33.3	28.5	28.6	32.8	5.0	~ 45.0
P_{ELM}	[MW]	8.5	10.0	7.9	8.8	-	5.0
$P_{rad,in}$	[MW]	10.2	3.4	3.9	8.6	-	10.0
$P_{rad,tot}$	[MW]	14.8	8.5	10.7	14.6	-	-
$\Gamma_{D,NBI}$	$[10^{20} s^{-1}]$	26.7	22.1	23.6	26.5	0.0	1.1
$\lambda^E_{q,att.}$	[mm]	0.9	1.2	1.3	1.1	0.9	0.4
$\lambda^E_{q,det.}$	[mm]	2.2	2.8	3.0	2.7	1.8	1.7

Table 3.3: Input power parameters for the considered JET pulses and DTT full power SN scenario as from [4]. Heat flux decay length for each pulse/scenario in attached and detached cases are calculated according to [5] and [6] respectively.

3.4. Table 3.2 show the calculated P_{ELM} values. The uncertainty is calculated as the distribution variance.

Calculating the uncertainty of each of the input parameters leads to a lower-boundary estimation of the precision limit of this modelling. When calculating the input power for each simulation with equation 3.1, an estimation is made of the uncertainty of each factor and by error propagation of P_{in}. The typical uncertainty is about $1.5-2$MW which is typically $10-15\%$ of P_{in}. A $10-15\%$ uncertainty on P_{in} directly correlates to a similar uncertainty on energy transport parameter $\chi_{e,i}$.

Table 3.3 shows the derived values that were previously described for each considered pulse; the values are also compared to the DTT full-power parameters derived from [4]. Estimations on radiated power are derived from [55] and it will be better described in chapter 4. In the table, data derived from Alcator C-MOD are also reported.

SOLEDGE2D-EIRENE has a separate treatment of electron and ion temperature, for this reason, the input power at the SOLEDGE2D-EIRENE inner boundary has to be split between electrons and ions. At the time of this work, there was no estimation of the power split between the electronic and ionic channels; furthermore, the spacial resolution of the ionic temperature diagnostic (charge exchange) was not sufficient for the validation of modelling results. The split between the two channels would directly influence the estimation of the heat transport energy parameters χ_i and χ_e. The methodology used in this work was using the same energy transport (i.e. $\chi_e = \chi_i$) and splitting the energy between electrons and ions so to obtain similar

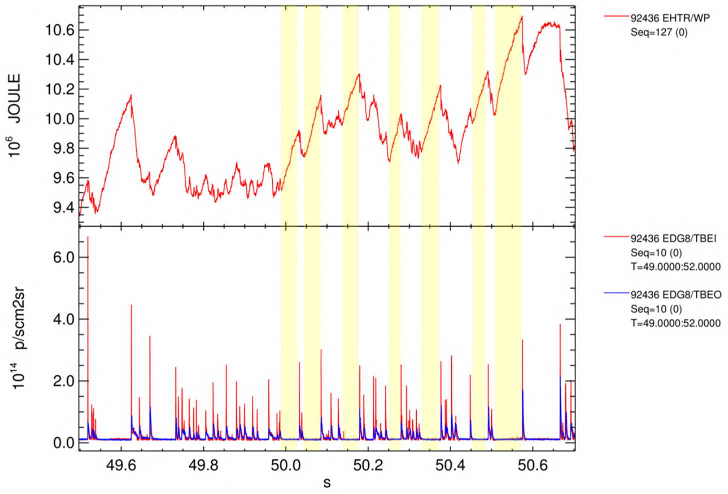

(a) JET#*92436* time-trace of diamagnetic energy and Be^{+2} signal.

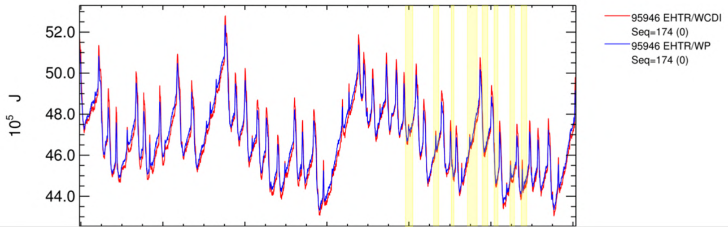

(b) JET#*95946* time-trace of diamagnetic energy.

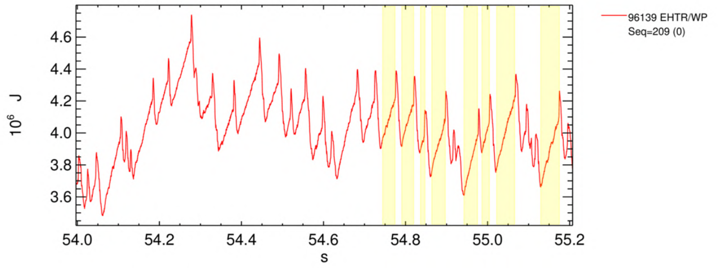

(c) JET#*96139* time-trace of diamagnetic energy.

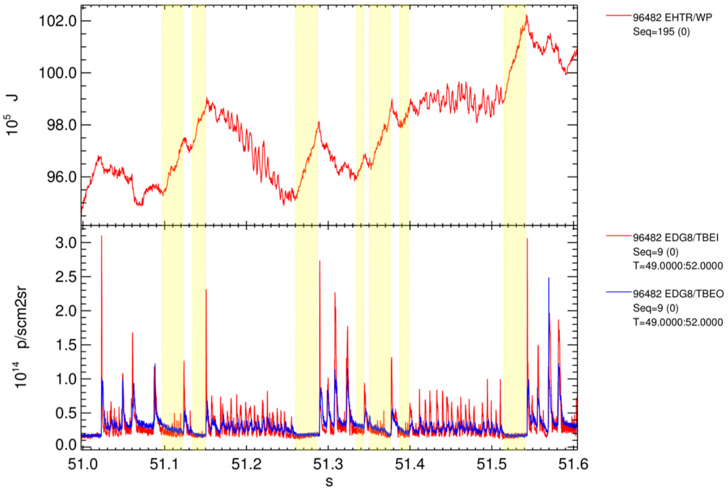

(d) JET#*96482* time-trace of diamagnetic energy and Be^{+2} signal.

Figure 3.4: Time-traces of considered JET pulses.

temperatures at the pedestal top. This choice is justified by the evidence that electron and ion temperature are similar in the selected JET pulses at the pedestal top. Measurements of ion temperature are given by the charge exchange diagnostic which does not have the spatial resolution of the HRTS to obtain the temperature profile in the pedestal.

Diagnostic data to be compared with modelling results are: electron density and temperature from high-resolution Thompson scattering (HRTS), total plasma radiation from bolometry, D-α emission from spectroscopy and electron density temperature saturation current and power deposition to the target from Langmuir probes. Since the modelling is steady-state, only inter-ELM data from the upper mentioned diagnostics are considered. This is done using a filter that uses beryllium data to determine intra-ELM intervals and exclude data relative to those intervals. This filter is necessary because data from intra-ELM intervals have much higher radiation and high power deposition to the targets than those from the inter-ELM phase that I am modelling.

For each selected pulse, a time of the discharge in which global parameters are stationary was chosen. Equilibria relative to those times was used, diagnostic data instead are derived from a time interval around the selected time removing intra-ELM interval data. After ELM data cleaning, data from the selected time intervals are averaged, the error is calculated as the variance of the signal values in the considered time.

Contribution of the HRTS is particularly important to estimate transport parameters in the near-SOL and pedestal region thanks to its high spatial resolution. A more refined fit of HRTS data was derived with EPED to reconstruct the pedestal taking only temperature and density within the last 10% of the ELM cycle, so just before the ELM occurs; this reconstruction corresponds to the time in which the maximum height of the pedestal is obtained. Plasma profiles at the outer mid-plane obtained with SOLEDGE2D-EIRENE and SOLPS are compared to the experimental data and the derived fit in the following sections.

Synthetic diagnostics of bolometer and spectrometer implemented to analyse SOLEDGE2D-EIRENE output and to be compared with experimental data are 1D integration along the plasma path of the total radiation emission or the line emission. The bolometer line of sights (LOSs) available in JET are shown in figure 3.3. Only data from vertical lines (in green in the picture) are analysed when comparing experimental data to synthetic diagnostic data from modelling; horizontal lines mainly measure radiation from the core given by tungsten and other high-Z impurities which are not modelled.

Figure 3.5 shows divertor details of magnetic surface, Langmuir probes and bolometer LOSs. Figure 3.5a shows the magnetic surface at the selected time during the flat top of a corner-corner and a vertical-vertical target pulse and the position of available Langmuir probes. In the corner-corner case, only one Langmuir probe is available near the strike point, this severely limits the estimation of target density and temperature profiles. Vertical-vertical divertor plasma is slightly better diagnosed with three Langmuir probes around the inner strike-point and two around the outer one. In all of the considered pulses, a strong sweeping is applied to spread the heat flux to a larger part of the divertor; this had the indirect effect of continuously changing the relative distance of the probes to the strike points, thus producing the target plasma profiles even with a limited number of probes. Vertical bolometer LOSs give a detailed analysis of divertor plasma emission in both vertical-vertical and corner-corner configuration due to their

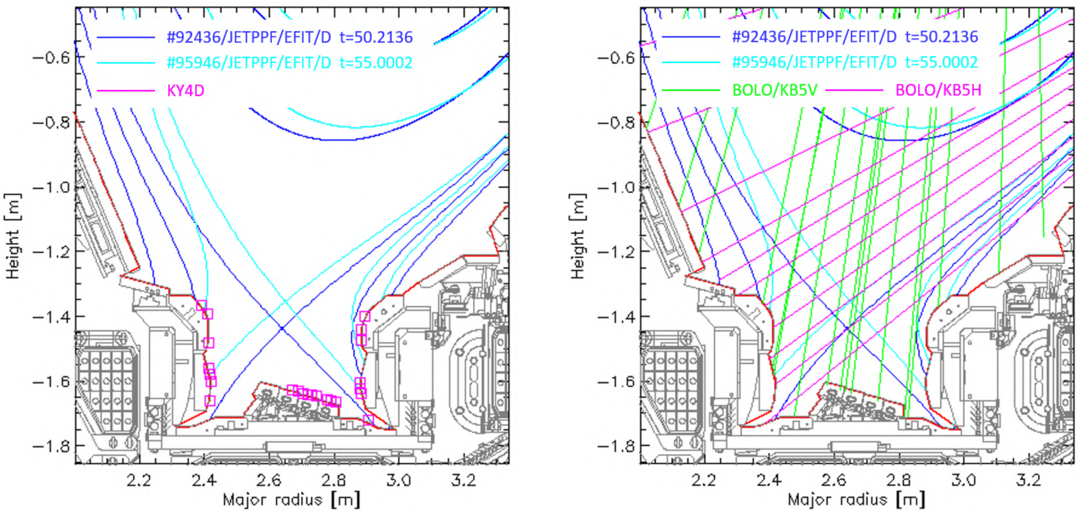

(a) JET *#92436* and *#95946* magnetic surface details in the divertor volume and position of the active Langmuir probes.

(b) JET *#92436* and *#95946* magnetic surface details in the divertor volume and position of the bolometer LOSs.

Figure 3.5: Details of a corner-corner and a vertical-vertical pulse and position of divertor-relevant diagnostics.

high spatial resolution, see figure 3.5b.

In this modelling, JET wall is divided in two parts, a *"cold wall"* and *"hot wall"* as it is shown in figure 3.6. In the cold wall, temperature (T_{wall}) is fixed at 500 K, in the hot part the T_{wall} = 1000 K[4]; this has an impact on the energy distribution of recycled neutral particles. Pumping surfaces are shown in red in figure 3.6, corresponding to the openings of the ducts that lead to the pumps. In this modelling for simplicity and numerical reason, it was decided to fix the albedo of the pumping surfaces instead of the pumping speed. The starting albedo in the simulations was set to R = 0.92 that approximately match the nominal 100 m^3/s according to the estimation made by Wiesen [62]. Minor adjustments in each simulation were made to the albedo to correctly match the separatrix density measured by HRTS. D_2, Ne and N puffed particles are added in the simulation at the specific puffing location (see figure 3.6); particles puffing rate in the simulation is set equal to the experimentally measured puffing rate.

---

[4] This approximation corresponds to the typical wall temperatures measured by infrared cameras in JET

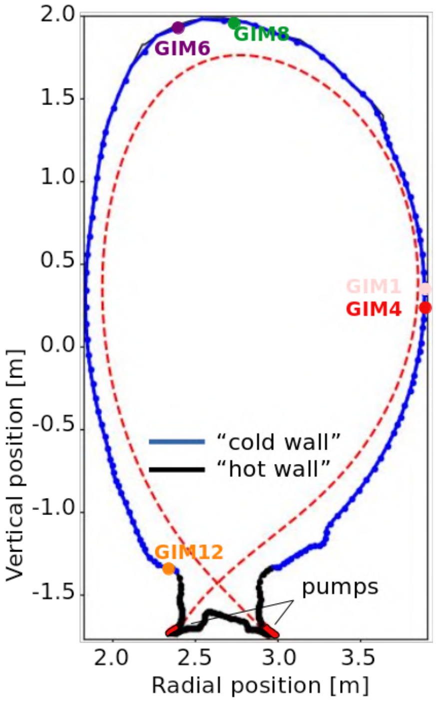

Figure 3.6: Sketch of the wall geometry, puffing locations and pumping surfaces of JET implemented in SOLEDGE2D-EIRENE simulations. The hot wall is represented in black, the cold wall in blue. Puffing is located at the Gas In-Mission locations (GIMs).

3.1.3 Edge modelling

The methodology and the input parameters described and calculated in section 3.1.2 were applied to each of the considered JET pulses. The modelling activity aims at finding the set of transport parameters that could reproduce experimental data from HRTS, pedestal reconstruction, bolometer, spectrometer and Langmuir probes the best. Results from SOLEDGE2D-EIRENE modelling are described in this section, the comparison with SOLPS modelling and the modelling of C-MOD with SOLEDGE2D-EIRENE is analysed in section 3.1.5.

Figure 3.7 shows the synthetic diagnostic LOSs. Bolometer LOSs are numbered from 1 to 24 clockwise from the poloidal projection shown in figure 3.7a. The first four and the last seven LOSs are not relevant for divertor modelling purposes: the first four LOSs intersect the volume not included in SOLEDGE2D-EIRENE simulations where tungsten radiation is localized, the last seven LOSs does not intersect the divertor volume where plasma radiation is localized. Spectrometer LOSs are numbered from 1 to 20, the first ten cross the inner divertor plasma and the last ten the outer divertor plasma, from left to right in the poloidal projection shown in figure 3.7b and 3.7d. The divertor-relevant LOSs are from 4 to 17, the first and the last 3 LOSs look at the upper corner of the divertor the zone that is usually more difficult to model given that SOLEDGE2D-EIRENE mesh is not perpendicular to the wall in that volume. Figure 3.7c shows the position of HRTS.

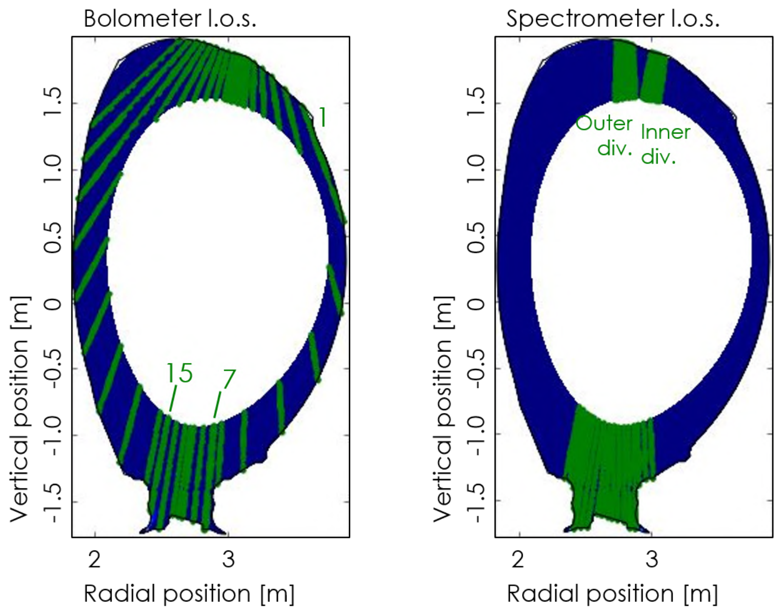

(a) SOLEDGE2D-EIRENE bolometer synthetic diagnostics.

(b) SOLEDGE2D-EIRENE spectrometer synthetic diagnostics.

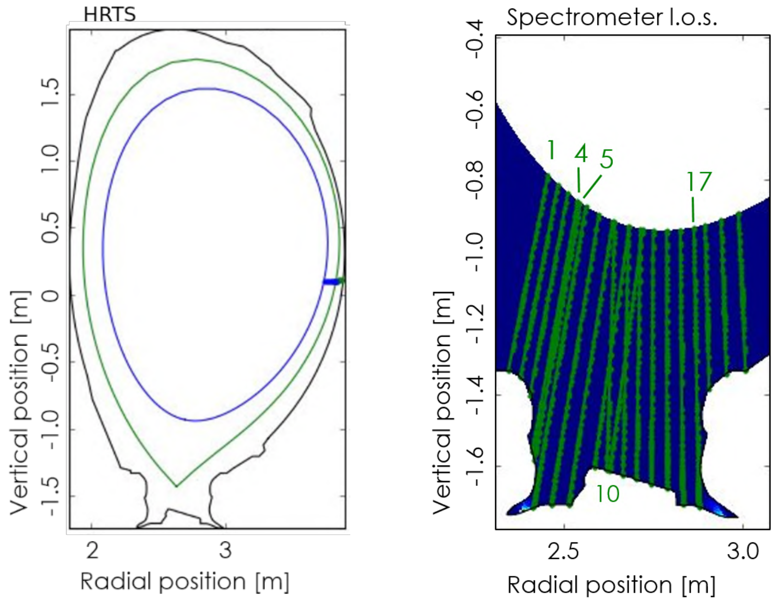

(c) SOLEDGE2D-EIRENE HRTS synth. diagn.

(d) SOLEDGE2D-EIRENE spectrometer synt. diagn. detail.

Figure 3.7: SOLEDGE2D-EIRENE synthetic diagnostics

JET *#96139*

Pulse *#96139* is a deuterium only pulse. In this pulse P_{ELM} reaches the higher value out of the four considered pulses (table 3.3). In this case, The input power is calculated by subtracting the total radiation instead of the power radiated inside the inner boundary of the modelling domain. The bolometer data are not analysed since power is mainly radiated by impurities extracted from the wall that are not modelled.

Radial transport profiles and section of transport profiles are shown in figure 3.8. Again, to match experimental data it was necessary to increase transport parameters below the X-point, also in this case the transport parameters below the X-point are equal to the transport parameters in the far SOL.

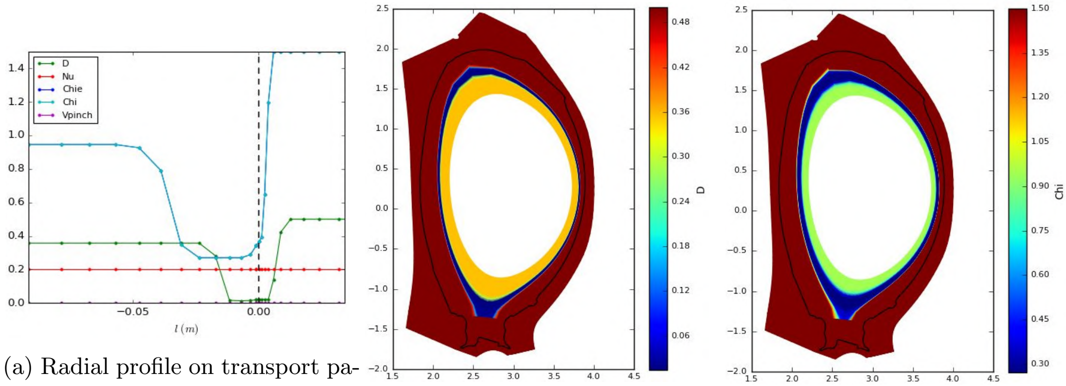

(a) Radial profile on transport parameters.

(b) Poloidal projection of particle transp. parameter D.

(c) Poloidal projection of energy transp. parameter χ.

Figure 3.8: Radial and poloidal projection of transport parameters used to match experimental data in pulse #96139.

Radial profiles of electron density and electron temperature are shown in figure 3.9a and 3.9b respectively. In this case, HRTS density data are noisy, density is higher at the pedestal top and lowers within the pedestal top, this is probably a nonphysical behaviour.

Figure 3.10 shows the comparison between D_α signal measured by spectroscopy and that from modelling. The matching with experimental data is particularly good at the outer target. Also in this case, data at the divertor corners are not matched.

There is a good agreement with available Langmuir probes data on the outer strike point in terms of density, saturation current and power deposition. Electron temperature is also matched in terms of absolute value, but in the simulation outcome it peaks farther from the separatrix than in experimental data.

Generally there is a good agreement with all the available experimental data but for the slight underestimation of electron density at the inner target. The heat flux decay length of the simulations is calculated by making an exponential fit of the mid-plane profile of the product $n_e \times T_e^{3/2}$, this method estimates $\lambda_q = 2.1$ which is higher that that predicted by the Eich scaling and shown in table 3.1.

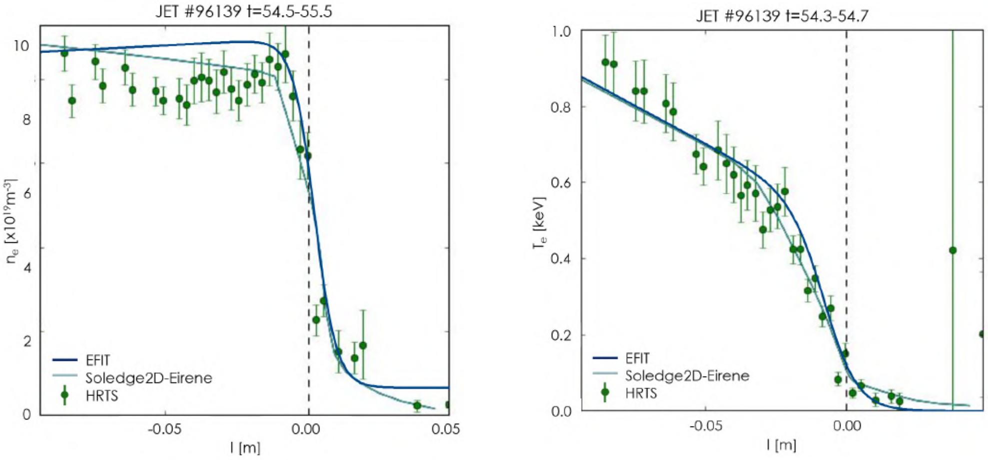

(a) Electron density at midplane.

(b) Electron temperature at midplane.

Figure 3.9: HRTS data from JET *#96139*, modelling results and EFIT profiles at 95% of ELM-cycle.

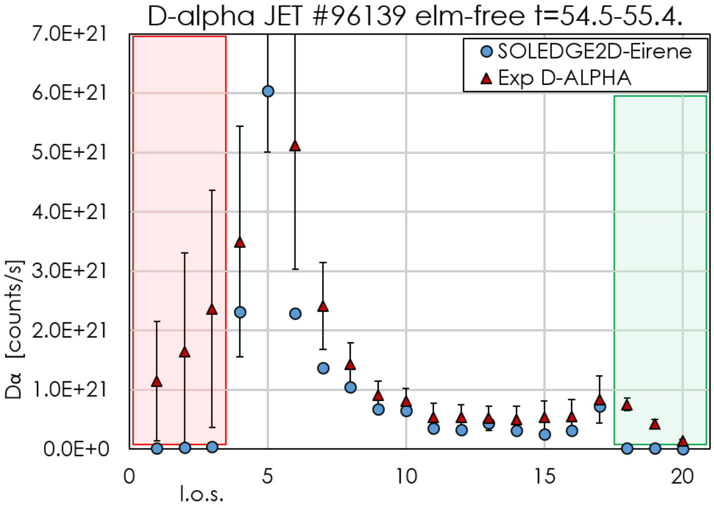

Figure 3.10: D_α emission as from SOLEDGE2D-EIRENE modelling results, obtained with the relative synthetic diagnostic, and experimental data from JET *#96139* spectroscopy. Red and green bands represent the inner divertor upper corner LOSs and the outer divertor upper corner LOSs respectively.

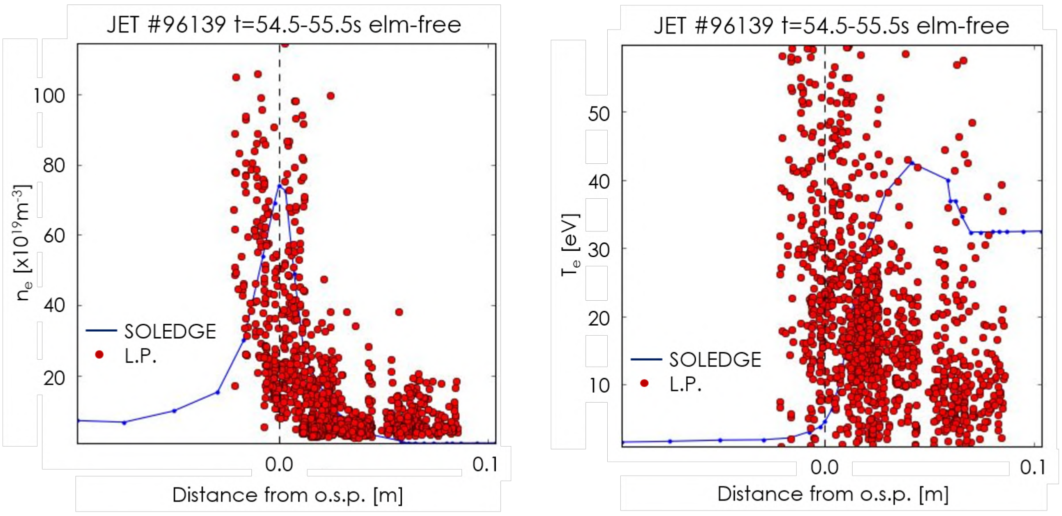

(a) Electron density at outer strike-point.

(b) Electron temperature at outer strike-point.

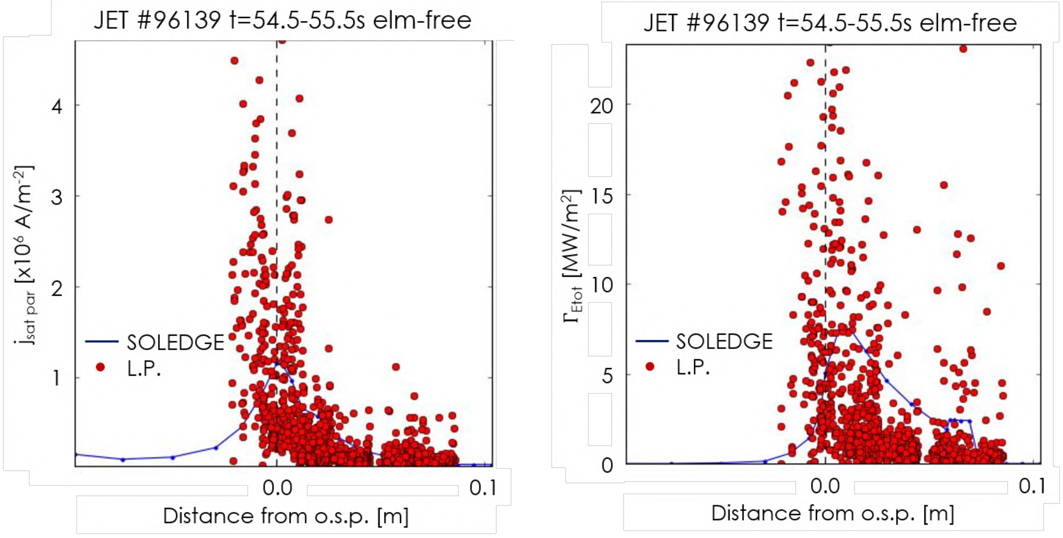

(c) Ionic saturation current at outer strike-point.

(d) Power flux at outer strike-point.

Figure 3.11: Langmuir probes data from JET # *96139* and modelling results. Experimental data are derived from a time interval of 1 s around the selected time, the data were not averaged over time because of the strong sweeping used for this pulse, only data referring to the ELMs interval were omitted.

JET *#96482* and JET *#92436*

Pulse #96482 and #92436 are two similar pulse, both have corner-corner target configuration, neon seeding, strong tungsten radiation and similar input power. The modelling was performed separately but results are similar and are presented together to avoid redundancy.

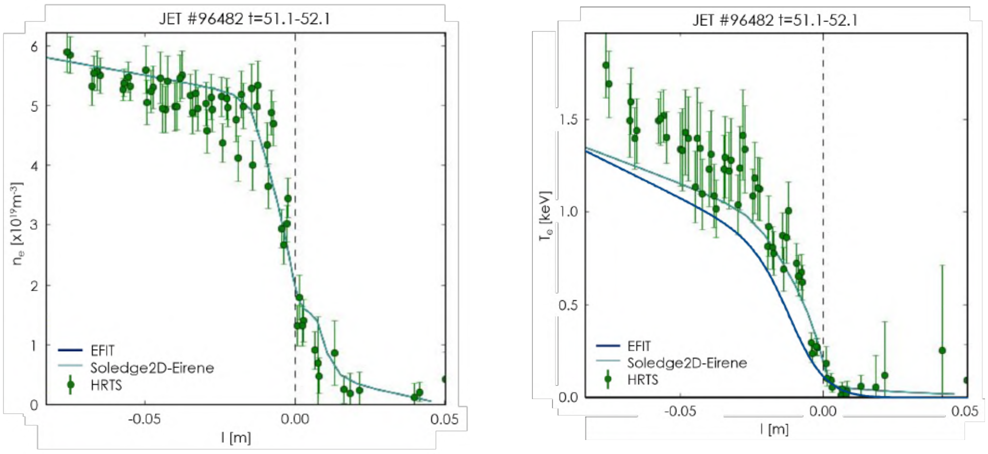

(a) Electron density at midplane.

(b) Electron temperature at midplane.

Figure 3.12: HRTS data from JET # *96482*, SOLEDGE2D-EIRENE modelling results and EPED profiles at 95% of ELM-cycle.

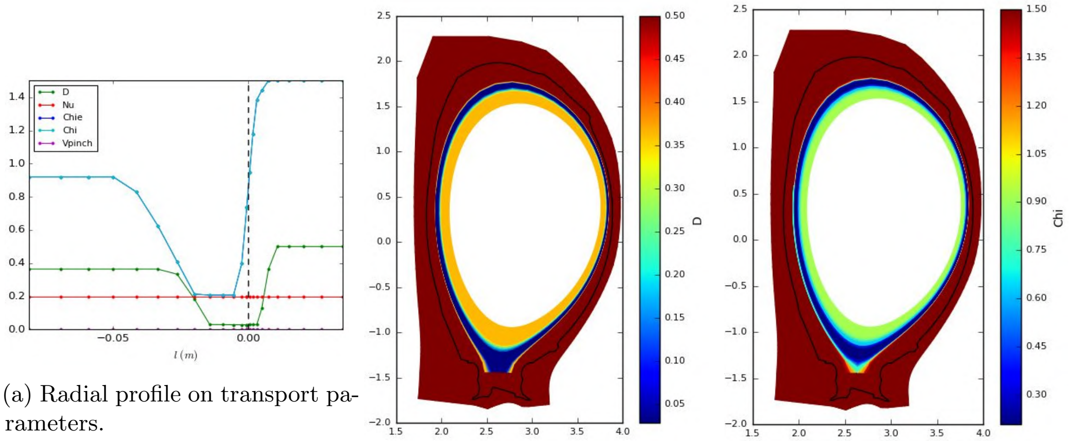

(a) Radial profile on transport parameters.

(b) Poloidal projection of particle transp. parameter D.

(c) Poloidal projection of energy transp. parameter χ.

Figure 3.13: Radial and poloidal projection of transport parameters used to match experimental data in pulse #96482.

Figure 3.12 shows a good agreement between experimental data for mid-plane temperature and density from HRTS and SOLEDGE2D-EIRENE simulations. Upstream density and temperature profiles were matched with the transport profiles whose radial section is shown in figure 3.13a. The electron density at the separatrix is obtained imposing an albedo at the pumping surface R= 0.955 which corresponds to a pumping speed $v_p = 95\,\mathrm{m}^3/\mathrm{s}$, very close to the nominal

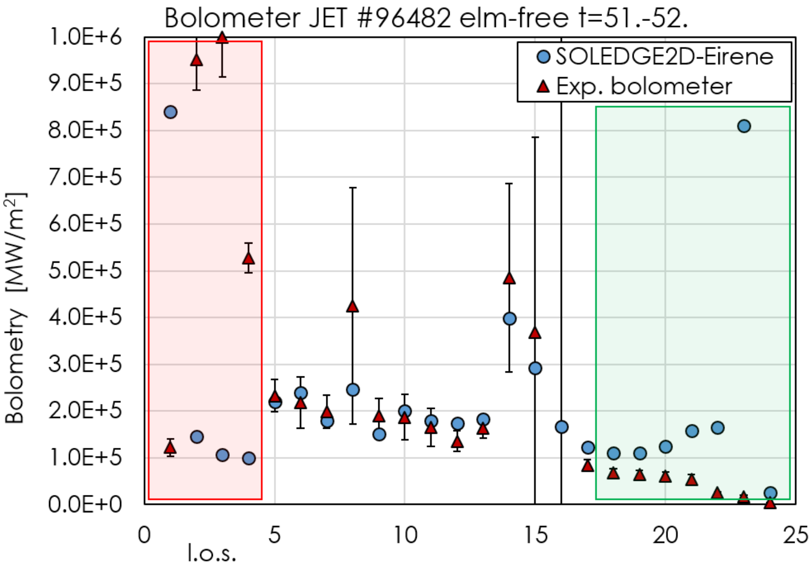

Figure 3.14: Radiated power as from modelling, obtained with the relative synthetic diagnostic, and experimental data from JET *#96482* vertical bolometer.

pumping speed $v_p^{nom} = 100\,\mathrm{m}^3/\mathrm{s}$. Far SOL and divertor transport parameters were set equal as in figure 3.13b and 3.13c with: $D_{\mathrm{div}} = D_{\text{far-SOL}} = 0.5\,\mathrm{m}^2/\mathrm{s}$ and $\chi_{\mathrm{div}} = \chi_{\text{far-SOL}} = 1.5\,\mathrm{m}^2/\mathrm{s}$.

Transport parameters shown in figure 3.13 also allow to match the D_α emission line measured by the spectrometer LOS as shown in figure 3.15. Also in these cases, as in the D-only case, a slight underestimation of electron density at the inner target emerges, even though synthetic diagnostic data are within the error bars of experimental data.

To match experimental data from the bolometer, neon pumping was set to obtain a total radiation equal to that estimated by tomographic reconstruction within the modelling domain which is calculated as $P_{rad,tot} - P_{rad,in}$ which is equal to 4.6 MW for pulse #96482 and to 6 MW for pulse #92436. The output of modelling is compared to the data from bolometer LOS in figure 3.14. The resulting pumping speed is similar to that of deuterium.

Figure 3.13a shows that the transport parameter χ at the separatrix is not equal to that at the pedestal but is increased. This is a common practice in edge modelling[63]. In this case it was necessary to reproduce temperature and density from Langmuir probes; if χ_{sep} was not increased, the temperature at the strike-points was over-estimated. The downside of this method is that by increasing χ_{sep}, also λ_q is increased. Figure 3.16a shows the transport parameters χ that was used to match the experimental data (blue line) and the estimation of the heat flux decay length[5]. The estimation of the λ_q relative to the blue transport profiles is twice as big as that predicted by the Eich scaling. To reproduce the λ_q predicted by the Eich scaling, the pedestal value of χ should be extended to the near-SOL as in the green line in figure 3.16a. If the Eich scaling is respected, the electron temperature measured by the Langmuir probes is not reproduced (figure 3.16b); on the contrary, with larger λ_q, the electron temperature is reproduced better (figure 3.16c).

---

[5] The heat flux decay length in the simulations was calculated with an exponential fit of the radial profile of the product $n \times T_e^{3/2}$ which is proportional to the heat flux.

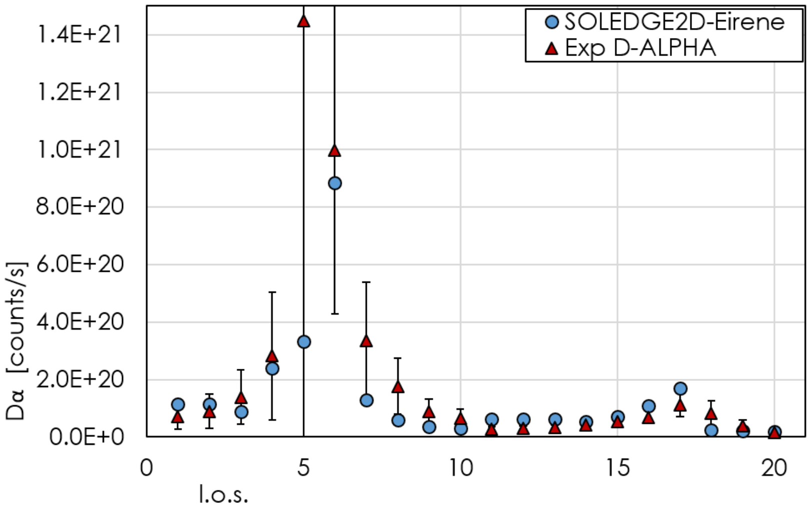

Figure 3.15: D_α emission as from modelling obtained with the relative synthetic diagnostic, and experimental data from JET *#96482* spectroscopy.

This difficulty to reproduce both upstream and downstream profiles indicates that probably some dissipating phenomena are missing in the simulations, this absence is counter-acted by increasing the heat flux decay length that enlarges the wetted area and lowers $q_{\parallel}$. One of the possible causes was identified in the set of reactions considered for EIRENE in SOLEDGE2D-EIRENE modelling. In this modelling activity, the particle reaction included is the same standard set used form SOLPS-ITER modelling, the so-called Kotov model [64], but for two reactions involving molecular deuterium which are missing. The two reactions are:

$$\begin{aligned} &D^+ + D_2 \rightarrow D^+ + D_2 \quad && \text{Elastic collision} \\ &D^+ + D_2 \rightarrow D + D_2^+ \quad && \text{Charghe exchange} \end{aligned} \tag{3.2}$$

It will be shown in the next section that the same behaviour is found in SOLPS-ITER modelling of these discharges. This implies that the difficulty to match up-stream profiles, down-stream profiles and heat flux decay length predicted by the Eich scaling is common between the two codes and does not depend on the two reaction which are missing in SOLEDGE2D-EIRENE.

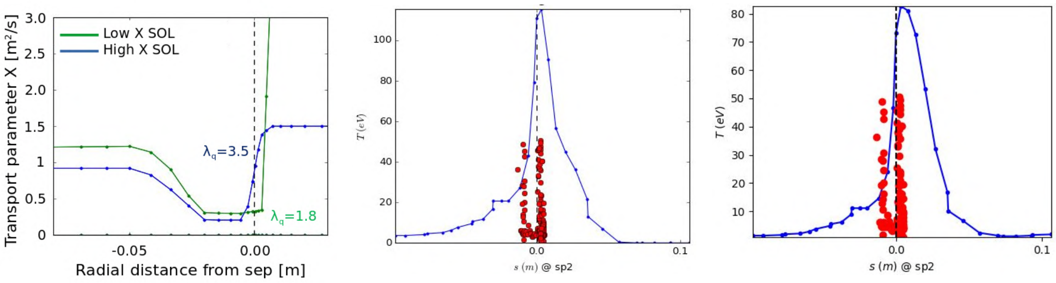

(a) Chi profile with larger or shorter λ_q depending on $\chi_{near,SOL}$.

(b) Temperature profile at the outer target with λ_q that reproduces Eich scaling.

(c) Temperature profile at the outer target with λ_q twice as large as that from Eich scaling.

Figure 3.16: Comparison between transport profiles with higher and lower λ_q.

3.1.4 Comparison with SOLPS modelling

In this section, the modelling results obtained with SOLPS of two of the four selected pulses are described.

To keep SOLEDGE2D-EIRENE and SOLPS-ITER simulations similar, as many input parameters as possible were kept equal between the two codes, even when some were hard-coded. Momentum transport parameter ν, which is not possible to easily evaluate, was kept uniform in all the simulations with both codes: $\nu = 0.2\text{m}^2/\text{s}$ similarly to value used in ITER modelling; the flux limiter coefficients for electrons, ions and viscosity were fixed equal to 0.2, 2.0 and 0.5 respectively; the secondary electron emission emission was suppressed; the ion sheath transmission coefficient is equal to 3 as hard-coded in SOLPS-ITER; no pinch velocities or drifts were used and parallel viscosity was not activated in both codes. Lastly, SOLPS mesh was extended as much as possible in order to avoid any influence of the finite extension of the grid [22]. SOLPS modelling was performed and has a good agreement with the transport profiles that had been previously obtained modelling a similar JET pulse [65].

Figure 3.17 shows SOLPS modelling results of JET pulse *#96139*. Also in SOLPS case it is possible to match temperature and density profile, as well as the absolute temperature value at the outer mid-plane, but not the temperature profile; also in SOLPS case the temperature peak is moved a couple of centimeters in SOL. Similar results are shown in figure 3.18.

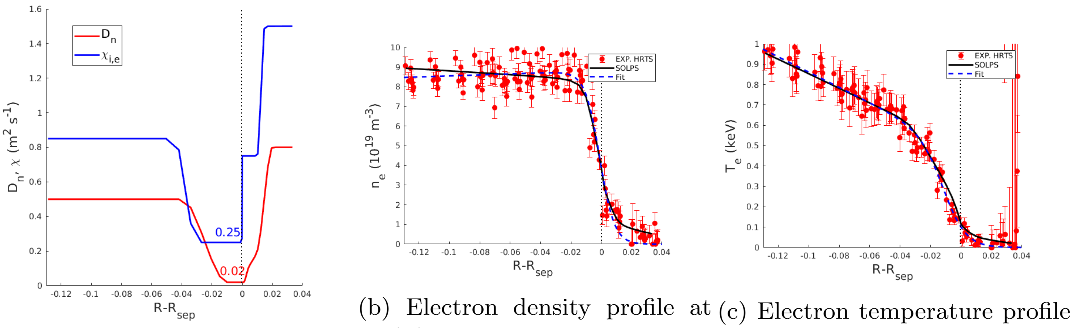

(a) Transport profiles derived with SOLPS.

(b) Electron density profile at midplane

(c) Electron temperature profile at midplane

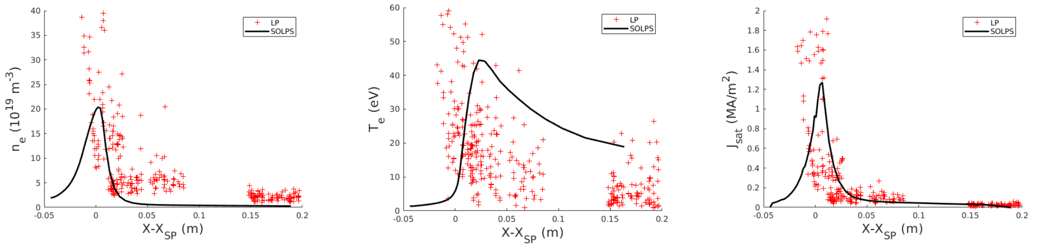

(d) Electron density at outer target.

(e) Electron temperature at outer target.

(f) Saturation current at outer target.

Figure 3.17: *#96139* SOLPS

The most important outcome from these simulation is the confirmation of the transport parameters found with SOLEDGE2D-EIRENE. The required transport parameters are compatible to those shown in the previous sections within a 50% factor. For the validation of transport

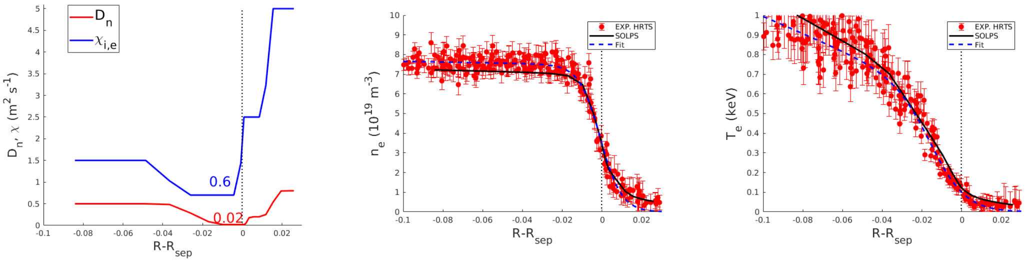

(a) SOLPS transp. prof. for *JET#95946*

(b) Electron density profile at midplane

(c) Electron temperature profile at midplane

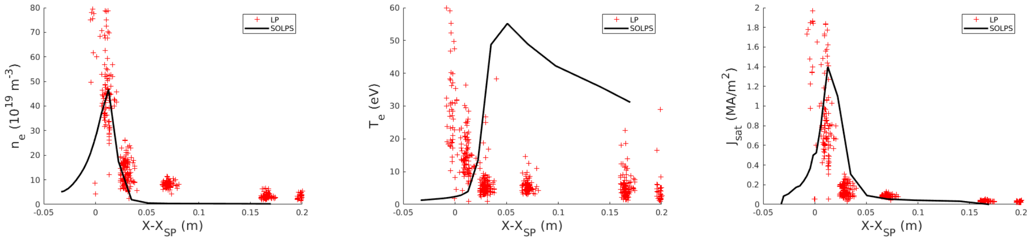

(d) Electron density at outer target.

(e) Electron temperature at outer target.

(f) Saturation current at outer target.

Figure 3.18: *#95946* SOLPS

parameters for DTT modelling, the 50% agreement between the two codes is enough to extend the validity of DTT transport parameters, that will be defined in section 3.1.6, to both codes.

To match Langmuir probes data, energy transport parameter in the near-SOL were increased with respect to the value at the pedestal (see figures 3.17a and 3.18a) as it was done for SOLEDGE2D-EIRENE modelling. This implies that there is a limit in both codes that does not allow to match both upstream and downstream profiles while having the expected heat flux decay length. Another common behaviour is the fact that the absolute temperature peak measured by the Langmuir probes is matched by the modelling, but in the results, electron temperature peaks further from the strike points than in experimental data.

Also in SOLPS, as in SOLEDGE2D-EIRENE simulations, transport parameters are increased in the far-SOL, χ is generally increased to $\chi_{\text{far-SOL}} \sim 1\,\text{m}^2/\text{s}$ and $D_{\text{far-SOL}} \sim 0.5\,\text{m}^2/\text{s}$. The same parameters are also used in the divertor region similarly to what was don in SOLEDGE2D-EIRENE and shown in figure 3.8b and 3.8c.

3.1.5 Comparison with C-MOD modelling

Simulation of edge CMOD plasma was performed with SOLEDGE2D-EIRENE, the modelling activity and results are described in [66]. The characteristic of the modelled pulse were listed in table 3.1.

Figures 3.19a and 3.19b show the transport profiles derived from SOLEDGE2D-EIRENE modelling of this C-MOD pulse. The comparison between density and temperature profiles at mid-plane and experimental data from Thompson scattering is shown in figure 3.20.

The transport profiles derived from the modelling of C-MOD are compatible to those found with SOLEDGE2D-EIRENE and SOLPS modelling of JET case. In those simulation

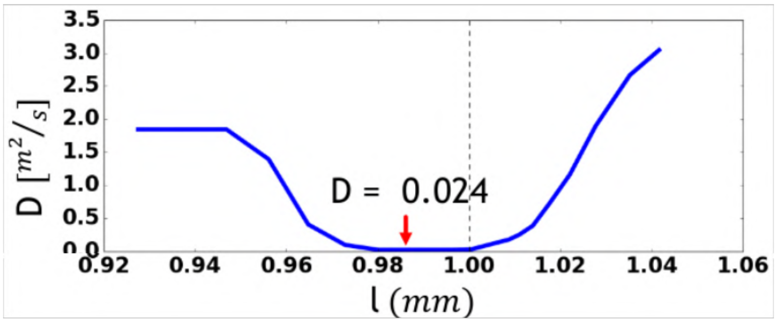

(a) Particle transport profile derived from C-MOD modelling.

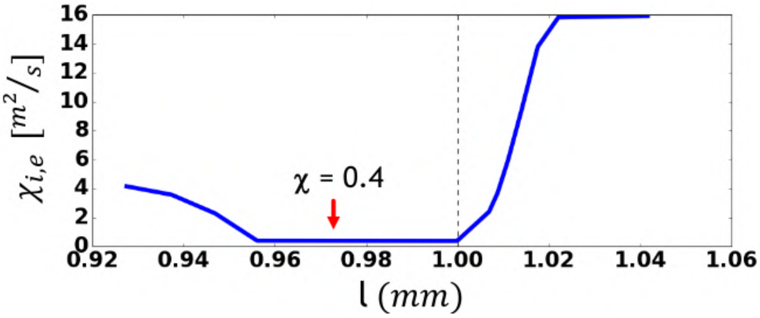

(b) Temperature transport profile derived from C-MOD modelling.

Figure 3.19: Transport profiles derived from C-MOD modelling.

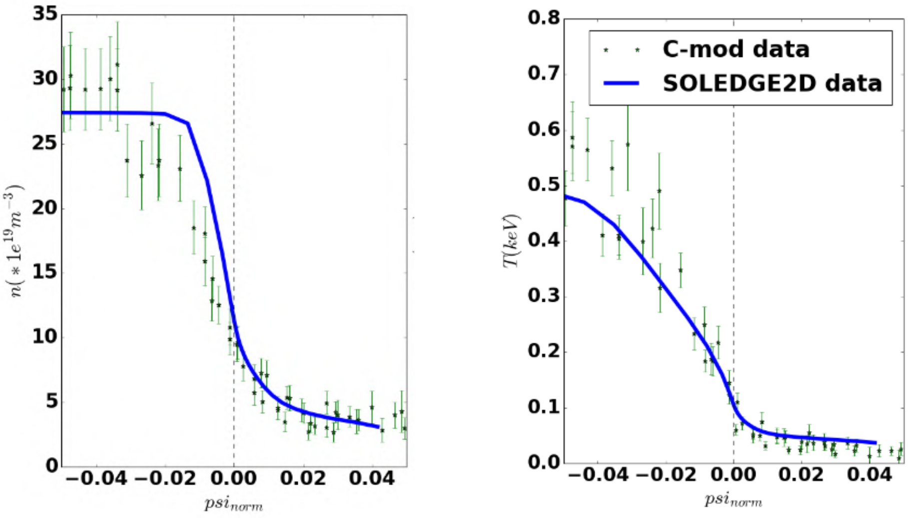

(a) Radial density profiles at mid-plane from SOLEDGE2D-EIRENE modelling and experimental data.

(b) Radial temperature profiles at mid-plane from SOLEDGE2D-EIRENE modelling and experimental data.

Figure 3.20: Radial profiles at mid-plane.

$0.02\,\mathrm{m^2/s} \lesssim \mathrm{D} \lesssim 0.04\,\mathrm{m^2/s}$ and $0.2\,\mathrm{m^2/s} \lesssim \chi \lesssim 0.4\,\mathrm{m^2/s}$. The calculated λ_q also respects the Eich scaling.

In the next section I'll show that the transport coefficient derived from JET and those derived from C-MOD when scaled to DTT single-null full-power scenario, will be even more compatible.

3.1.6 Proposed transport profiles for DTT

To have a more exhaustive analysis of what transport parameters could look like in DTT, they were also derived from core simulations of DTT full power scenario. Core modelling was performed with the JETTO suite which has the main advantage of being a first-principles code. The simulation domain was extended to the separatrix using a feedback method on neutral influx to reproduce pedestal profiles derived with the pedestal code E-PED and using the quasi-linear code QuaLiKiz to evaluate turbulent transport. The modelling activity and main results are described in [55]. The second advantage of core modelling is that it can distinguish between ionic and electronic power channels and so provide a different estimation of χ_i and χ_e.

The downside of this approach is that the simulation domain is extended only to the separatrix and consequently, transport parameters are derived by QuaLiKiz only inside the separatrix. Furthermore, JETTO is a poloidally symmetric code and can not take into account some strong poloidal asymmetry as neutral penetration which peaks in the vicinity of the puffing location. Neutral flux is a boundary condition that can influence the estimation of transport parameters near the separatrix.

Figure 3.21 shows the comparison between a set of transport parameters from SOLEDGE2D-EIRENE and SOLPS modelling of JET and from JETTO modelling of DTT full power scenario. Since the transport parameters are derived from different machines and pulses, profiles at mid-plane are drawn as a function of the toroidal normalized flux coordinate $\rho_{tor,norm}$ or simply ρ in the following pictures.

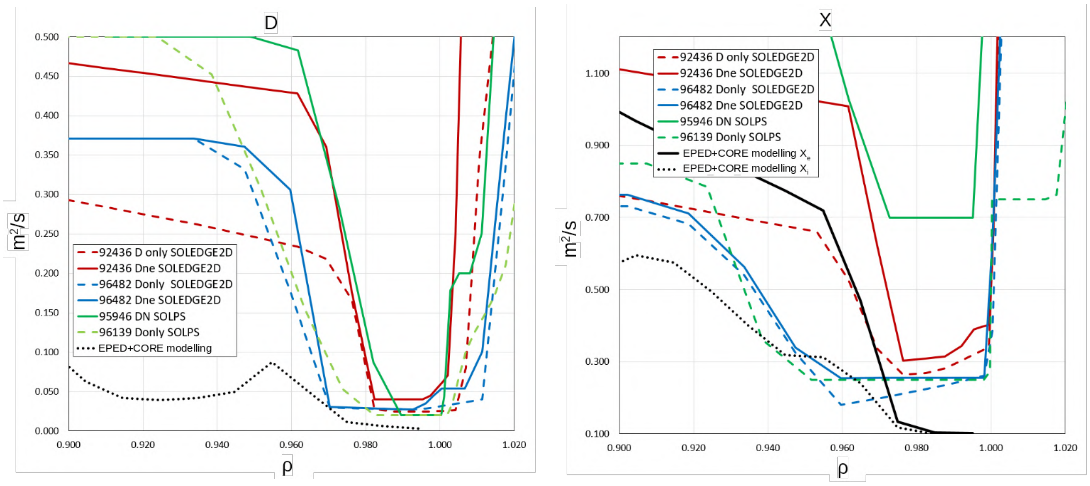

(a) Particle transport parameter D

(b) Energy transport parameter χ

Figure 3.21: Resume of transport profiles derived by SOLEDGE2D-EIRENE and SOLPS-ITER modelling of JET pulse and transport parameters derived by core modelling of DTT.

Outer mid-plane radial profile of particle transport parameter D is shown in figure 3.21a. All the modelling performed with edge codes, also including C-MOD modelling, predict a particle transport parameter at the pedestal between 0.2 and $0.4\,\mathrm{m}^2/\mathrm{s}$. Transport parameters derived from core modelling of DTT at the pedestal predict $D = 0.1\,\mathrm{m}^2/\mathrm{s}$ down to $D = 0.05\,\mathrm{m}^2/\mathrm{s}$ closer to the separatrix. As previously said, the estimation of particle transport parameters by core modelling inside the separatrix tends to be more inaccurate due to the influence of boundary conditions given by neutral particle penetration. There is instead a good agreement withing a factor 3 between D estimated by edge codes for JET and C-MOD and that estimated by JETTO for DTT. Inside the pedestal top, DTT particle transport is predicted to be lower than in JET case, this can be given by the lower particle flux from the core, the same behaviour was also found in C-MOD modelling.

Energy transport parameter(s) χ from edge modelling and $\chi_{e/i}$ from core modelling of DTT are shown in figure 3.21b. All the edge modelling performed in JET and C-MOD with both codes predicted a pedestal χ between 0.2 and $0.4\,\mathrm{m}^2/\mathrm{s}$. The transport profiles evaluated in JET and C-MOD must be re-scaled to be applied to DTT to take into account the different constructive and scenario parameters. According to the 2-point model and specifically to equation2.16:

$$\chi \propto \frac{1}{n_e}\left(\frac{P_{SOL}^5 \lambda_q^9}{R^9 a^5 k^{5/2} q_{95}^4}\right)^{1/7}, \tag{3.3}$$

to scale transport coefficients from modelled machines to DTT, the χ obtained by modelling JET and C-MOD was multiplied by the ration of the right-hand-side of equation 3.3 calculated with DTT parameters and JET or C-MOD parameters. Values used for this calculation are in table 3.1. The scaling factor is 0.44 from JET to DTT and 0.34 from c-MOD to DTT. From JET modelling $\chi_{ped}^{JET} \simeq 0.3\,\mathrm{m}^2/\mathrm{s}$ which re-scaled gives $\chi_{ped}^{DTT} \simeq 0.13\,\mathrm{m}^2/\mathrm{s}$, from C-MOD modelling $\chi_{ped}^{C-MOD} \simeq 0.4\,\mathrm{m}^2/\mathrm{s}$ which re-scaled gives $\chi_{ped}^{DTT} \simeq 0.135\,\mathrm{m}^2/\mathrm{s}$; the two estimations show great agreement between each other. The estimated value of χ_{ped} obtained with this scaling is in goods agreement with that obtained with core and pedestal modelling which estimated $\chi_{e,ped} \sim \chi_{i,ped} \sim 0.1\,\mathrm{m}^2/\mathrm{s}$.

Standardized transport parameters for DTT modelling were defined as follows. At the pedestal, transport parameters derived from edge modelling are re-scaled by the above mentioned factor resulting in $\chi_{ped} = 0.14\,\mathrm{m}^2\mathrm{s}$ and $_{ped} = 0.02\,\mathrm{m}^2/\mathrm{s}$. Inside the pedestal top, transport profiles are taken from core modelling, this is necessary especially for particle transport parameters given the low particle flux from the core; consequently, particle transport profile inside the pedestal top are more similar to those derived from edge modelling o C-MOD. In order to respect Eich scaling, pedestal transport parameters are extended to the near-SOL; before increasing it to the far-SOL values, low-χ region is extended to the near-SOL for a λ_q at the outer mid-plane, the same is done for D profile. The radial profile of transport parameters at mid-plane are shown in figure 3.22a and 3.22b; as a comparison, example of edge modelling transport profiles and core modelling transport profiles are also shown in the pictures. In the far SOL as well as in the divertor region below the X-point $\chi_i = \chi_e = 1.2\,\mathrm{m}^2/\mathrm{s}$ and $D = 0.5\,\mathrm{m}^2/\mathrm{s}$ as it was found by SOLEDGE2D-EIRENE and SOLPS modelling.

Some open question remains on the transport parameters set determined for DTT.

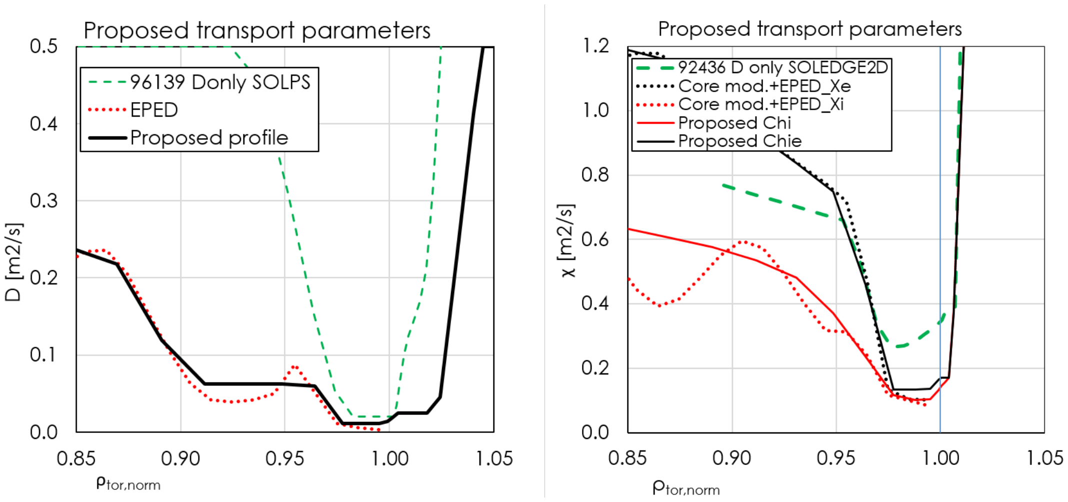

(a) D (b) χ

Figure 3.22: Derived transport profiles.

- The extension of pedestal profiles in the near-SOL is hardly predictable both in absolute value and spatial extension is the SOL. The extension is predicted by Eich scaling, while edge simulation could match better Langmuir probes data when transport parameters were increased at the separatrix without respecting the predicted heat flux decay length. Data from infra-red cameras are better estimators of power deposition than Langmuir probes; they could give on estimation of the heat flux profile on the target and consequently of λ_q
- The existence of possible pinch effect is not studied in this work but could play a role especially within the pedestal top.
- Impurities transport parameters are unknown and hardly measurable, in this work they were kept equal to those of deuterium.
- divertor plasma state could affect mid-plane transport profiles[6].

Test on DTT

The set of transport parameters defined in the previous section was applied to a DTT single null case in order to test the validity of such parameters. The aims of this test are two: first, to check whether the expected pedestal predicted by the Europed (E-PED) code[67]; second, if near-SOL behaviour are reproduced. The equilibria, boundary conditions and pumping are described in detail in chapter 4.2.3 to avoid redundancy.

The pedestal produced by EPED has a separatrix density $\langle \mathrm{n_e} \rangle_{\mathrm{sep}} = 5.0 \times 10^{19} \mathrm{m}^{-3}$, thus the separatrix density was fixed to the desired values by adjusting puffing in SOLEDGE2D-EIRENE simulation. The radial density profile of produced by the standard set of transport parameter in DTT and the pedestal predicted by EPED are shown in figure 3.23. The two profiles share a good agreement until the pedestal top. Similar results are for the scenario with $\langle \mathrm{n_e} \rangle_{\mathrm{sep}} = 8.0 \times 10^{19} \mathrm{m}^{-3}$. It was found that the pedestal top density in SOLEDGE2D-EIRENE was not much influenced by the separatrix density but rather by the divertor plasma state. In

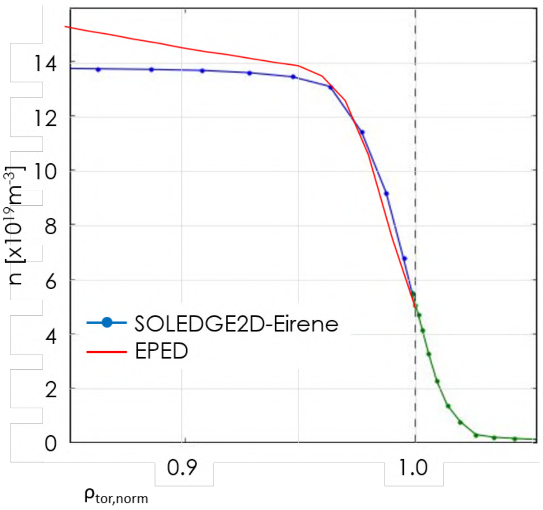

Figure 3.23: Application of selected transport profiles on DTT and comparison with EPED density profile.

detached condition the puffing to sustain the scenario separatrix density was much higher than in attached condition, consequently the neutral penetration and the pedestal top density were higher. Furthermore, the heat flux decay length measured at the outer mid-plane is equal to 1.1 mm similarly to the Eich scaling.

3.2 Modelling of C-wall JET discharge towards JT-60SA modelling

This section describes the modelling activity performed with the scope of determining a correct set of input parameters towards the modelling of the inductive full-power single-null scenario of the tokamak JT-60SA which will start its operation this year in Japan[7]. JT-60SA was designed and built in a collaboration between the EU and Japan. It will be one of the machines that will support ITER and will provide experimental evidence that will be crucial for DEMO designing. The device will be able to operate long-lasting inductive scenarios as well as pursue fully non-inductive steady-state operations in DEMO-relevant regimes.

During the initial research phases, and partially during the integrated research phase, the JT-60SA divertor will be made of carbon tiles. The entire first wall will be covered by carbon. For this reason, the machines chosen to estimate the input parameters to be used for JT-60SA modelling should also be equipped with a carbon wall.

The most similar existing machine (or machine that had existed) in terms of plasma temperature, collisionality, size and composition was JET equipped with carbon wall and is the ideal candidate to test and validate the input parameters for the edge modelling of the JT-60SA scenario. Simulation of JET diagnosed pulses was already used as a benchmark for JT-60SA core simulation by Garcia[68].

Since carbon is a low-Z element whose sputtering rate by deuterium bombardment is much higher than that of tungsten and whose contribution to SOL radiation is higher, its distribution in the SOL can not be simply ignored. Contrarily to what was done in the previous section, in this activity, the sputtering of wall material by plasma interaction is considered. Carbon radiation in the core is negligible since it is completely ionized at JET or JT-60SA core temperatures and radiates only by bremsstrahlung. In this case, the input parameters that describe plasma-wall interaction are also tested in JET before being applied for predictive modelling.

The JT-60SA scenario that will be modelled is named *”scenario 2”* in the research plan and I will refer to this scenario as such. JT-60SA scenario 2 is the full-inductive full-power scenario that will be tested with carbon wall during the initial research phase two of the machine. The characteristics of this scenario will be better described in chapter 4.1, here I will briefly discuss its main plasma characteristics which are listed in table 3.4 and that led to the choice of a comparable JET pulse.

Table 3.4 shows plasma parameters the JET pulse that was chosen to be modelled to test and validate input parameters for JT-60SA modelling (JET#69890) and those of JT-60SA scenario 2. The two scenarios have a very similar magnetic field (which is a key parameter for plasma transport), a similar major radius and density and Greenwald density fraction, both scenarios are in h-mode. The JET pulse is unseeded while JT-60SA will operate both with and without seeding. The main power exhaust-relevant parameter which is different between the two scenarios is the auxiliary input power which was 28.5 MW for the JET pulse and will be 41 MW for JT-60SA. The data relative to JET is the power coupled to the plasma, those relative to JT-60SA is the nominal input power from the auxiliary heating systems, the power coupled to the plasma will be slightly lower. Plasma current in JT-60SA will be double that in JET and

Machine Pulse		JT-60SA Scenario 2	JET 69890	diff.
time	[s]	-	-	-
B_t	[T]	2.25	2.18	3%
I_P	[MA]	5.5	2.0	64%
β_N		3.1	2.3	26%
q_{95}		3	3.5	16%
R	[m]	2.96	3.0	1%
a	[m]	1.18	0.9	31%
b	[m]	2.20	1.44	34%
k		1.86	1.6	14%
f_G		0.5	0.6	20%
n_{core}	$[10^{19} m^{-3}]$	6	7	17%
n_{sep}	$[10^{19} m^{-3}]$	1/2	3	4.7%
n_c/n_s		6/3	2.3	50%
mode		H	H	-
$P_{aux,tot}$	[MW]	41	28.5	28.6
$\Gamma_{D,NBI}$	$[10^{20} s^{-1}]$	30	14	-
S.P. pos.		2 vert.	1 vert 1 hor.	-
wall comp.		full C	full C	-
seeding		Ne/Ar	-	-
Pump. speed	[m^3/s]	up to 100	-	-

Table 3.4: Main flat-top JET pulse plasma parameters and relative parameters of the flat-top for the JT-60SA scenario #2 as from [7].

consequently the poloidal magnetic field and β will differ from JET.

3.2.1 Methodology and available diagnostics

The pulse analysis and the modelling methodology are analogous to those applyed for the modelling of JET pulses with ILW or C-MOD with some differences given by the availability of experimental data.

To determine the simulation input power, each member of the r.h.s. of equation 3.1 should be determined. The auxiliary input power is derived from the time-traces of the power coupled to the plasma from NBI and ICRH shown in figure 3.24. Magnetic field is derived at $t = 57\,\mathrm{s}$, the experimental data are derived from a time window of $2\,\mathrm{s}$ around $t = 57\,\mathrm{s}$.

The tomographic reconstruction was not available for this dated JET pulse, although, the power radiated within SOLEDGE2D-EIRENE inner boundary was retrieved with the less accurate estimation given by a less sophisticated bolometry data analysis. It was estimated $\mathrm{P}_{rad,in} = 3.4\,\mathrm{MW}$

I attempted to apply the same methodology to evaluate to power coupled to the ELMs, but it was not possible do to it precisely due to the low temporal resolution of the Thompson scattering available. When JET was equipped with carbon wall, the HRTS system was not available and the estimation of diamagnetic energy which relies on the estimation of the plasma profiles was based on the LIDAR Thompson scattering. The frequency of LIDAR data is only slightly higher than the ELM frequency and is not adequate to estimate the variation of diamagnetic energy during the ELM cycles as it is shown in figure 3.25.

To estimate P_{ELM} a similar more recent JET pulse was chosen, with a similar temperature, density, plasma shape, and input power and without pellet injection which are the plasma parameters that influence the ELM power and frequency the most. The selected pulse was JET#92141 which was analyzed with the same methodology used in the first section of this chapter. It was estimated that $\mathrm{P}_{\mathrm{ELM}} = 5 \pm 0.5\,\mathrm{MW}$. Table 3.5 list the quantities that leads to the determination of the input power in the analyzed JET pulse and in JT-60SA scenario 2.

Mid-plane radial electron e density profile are also measured by LIDAR T.s. which does not have the same spatial resolution of the HRTS. Consequently the stiff profiles of the pedestal are not well diagnosed as in the previous section and the EPED reconstruction will not be available. The determination of the position of the separatrix is always difficult and normally a bias on the radial position of the T.s. measurements is needed to correctly position the experimental data with respect to the separatrix. In the previous section the bias was set accurately to obtain $T_{e,sep} = 100/110\,\mathrm{eV}$ which is a common practice at JET. For this pulse the determination of the bias is less accurate because of the lower spatial resolution of LIDAR data. This introduces an error on the radial position of the experimental data that was ignored (because it was negligible) in the previous section. The uncertainty on separatrix position induces an uncertainty on plasma density at the separatrix.

Lastly, it was not possible to obtain validated Langmuir probes data, so the plasma condition at the divertor target will be mainly given by bolometric and spectroscopy data whose LOS are shown in figure 3.26a and 3.26b. The high spatial resolution of these two diagnostics was exploited so to obtain the maximum amount of information due to the lack of other experimental data.

The analysed pulse is unseeded and the only impurity in the plasma is carbon. The Bohdanski

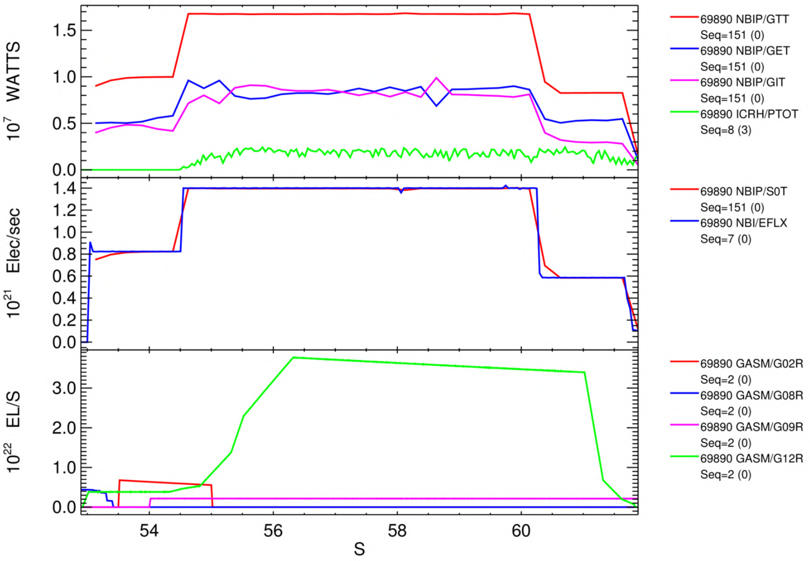

Figure 3.24: JET #*69890* time-trace of input power, NBI power flux and deuterium particle puffing flux

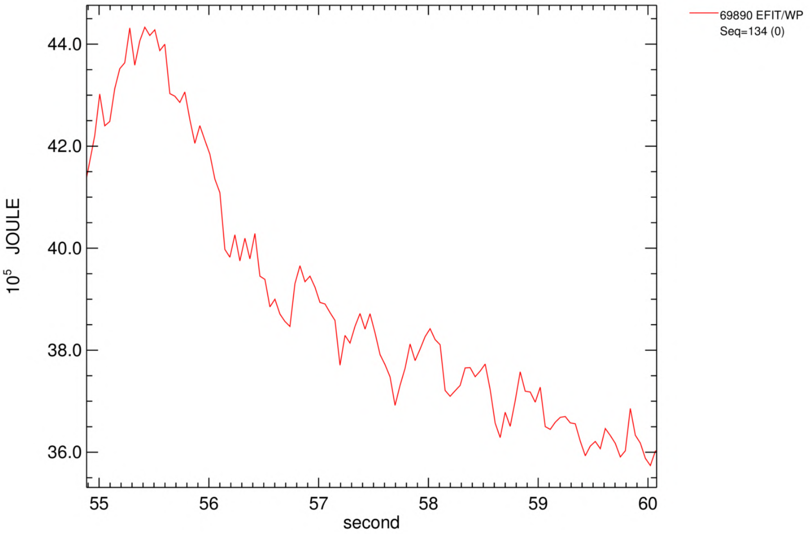

Figure 3.25: JET #*69890* time-trace of diamagnetic energy.

Machine		JT-60SA	JET	diff.
Pulse		Scenario 2	69890	
P_{ECRH}	[MW]	7	0.0	0.0
P_{ICRH}	[MW]	0	4.7	3.1
P_{NBI}	[MW]	34	24.1	26.0
$P_{aux,tot}$	[MW]	41	28.5	28.6
P_{ELM}	[MW]	5/10	5	25%
$P_{rad,in}$	[MW]	-	3.4	-
$P_{rad,tot}$	[MW]	-	8.5	-
$\Gamma_{D,NBI}$	$[10^{20}s^{-1}]$	30	14	-
$\lambda^{E}_{q,att.}$	[mm]	0.7	1.65	-

Table 3.5: Input power parameters for the considered JET pulse and JT-60SA scenario # as from [7]. Heat flux decay length for each pulse/scenario in attached and detached cases are calculated according to [5] and [6] respectively.

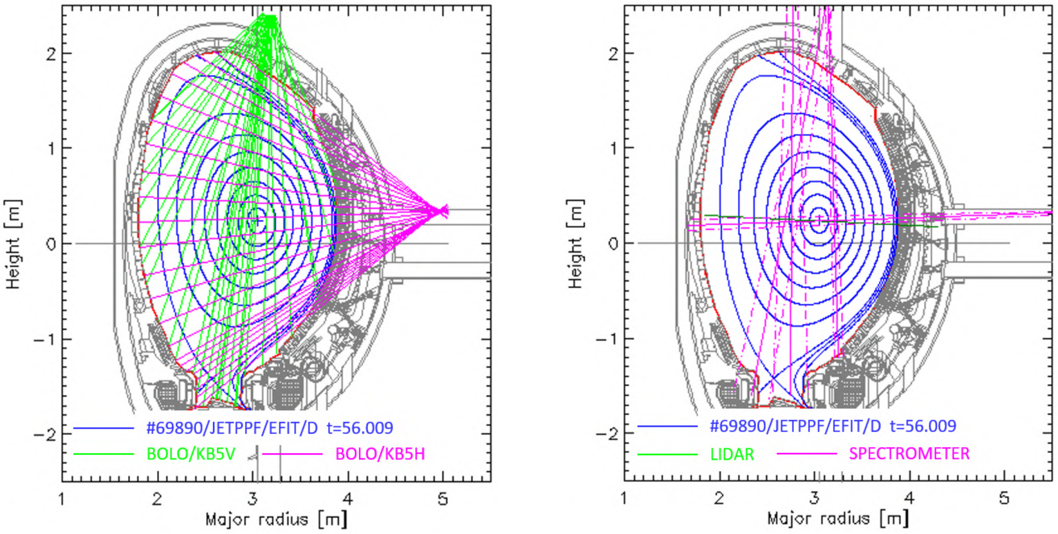

(a) Bolometer available line of sights for the considered JET pulse.

(b) Spectrometer line of sights and LIDAR Thompson scattering position.

Figure 3.26: Line of sights of available SOL-relevant diagnostics.

model was chosen to estimate carbon entry and recycling in the plasma. The validity of the model in this analysis and the possible additional need of a recycling coefficient is studied in section 3.2.2.

Electron density and temperature radial profiles from LIDAR for pulse JET#69890 are shown in figure 3.27. A 3 cm bias was used for radial positioning of the separatrix, as I discussed in the previous section the uncertainty on such quantity produces the uncertainty on radial density and temperature profiles and on separatrix density, from previous JET modelling, it is already known that the electron temperature at the separatrix will be in the range 100/150 eV. From the electron temperature data outside of the separatrix in figure 3.27b, it is also clear that the accuracy of electron temperature measurements is low in plasma region with low plasma density. From these data it is possible to conclude that the electron density at the separatrix is $3.5 \pm 0.6 \times 10^{19}\mathrm{m}^{-3}$, this uncertainty will be addressed using other sets of data like the D-α line from the spectrometer which is used to estimate deuterium density.

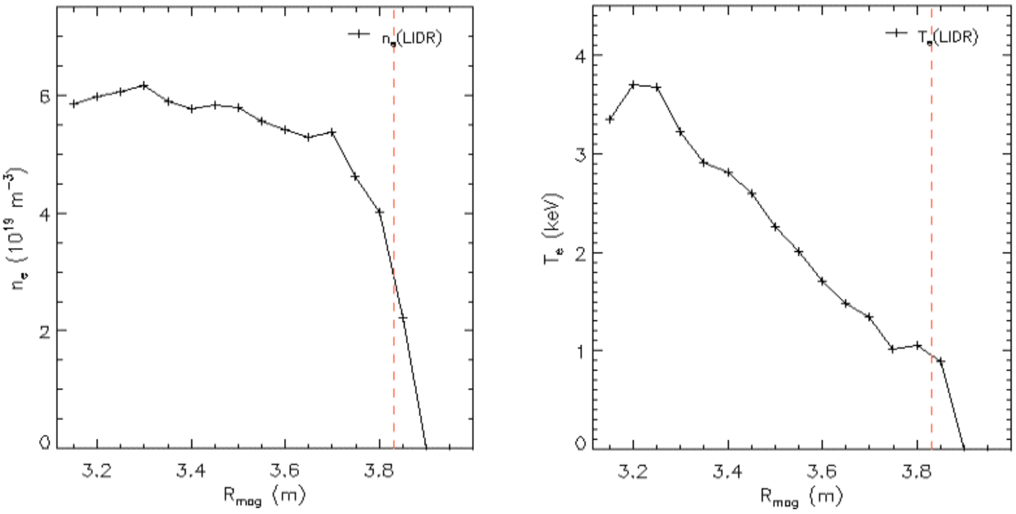

(a) Electron density radial profile.

(b) Electron temperature radial profile.

Figure 3.27: Mid-plane temperature and density profiles from LIDAR.

Figure 3.28 shows the experimental data from bolometer LOSs that were shown in figure 3.26a and look at four different plasma regions: the outer divertor strike point, the outer divertor leg, the X-point and the inner divertor strike point. With a good set of transport and recycling parameters, the experimental divertor plasma conditions would be reproduced and so the radiation distribution and the total radiation measured by the bolometer.

An initial guess on transport parameter at the pedestal/separatrix can be derived with the Eich scaling and the 2-point model. According to the Eich scaling, the estimated heat flux decay length for this pulse is $\lambda_q = 1.7\,\mathrm{mm}$. According to equation 2.16, with the plasma parameters listed in table 3.5, the estimated heat transport parameter is $\chi_{ped/sep} \sim 0.3\,\mathrm{m}^2/\mathrm{s}$.

In the next section, the comparison with the experimental data will be used to determine and validate some input and plasma parameters: electron density at the separatrix will be better determined through the comparison with spectrometer data, transport parameters at mid-plane and in the divertor region are tuned to reproduce data from bolometer and spectrometer,

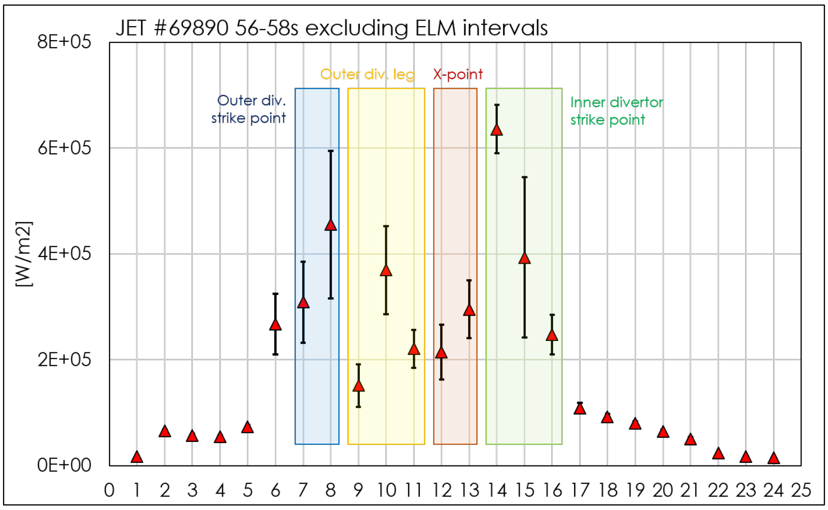

Figure 3.28: Experimental data and position of the vertical line of sight.

spectrometer emission lines from CII and CIII as well as the estimation of Z_{eff} will be used to validate carbon content and carbon species distribution.

3.2.2 Modelling results and analysis

A set of different plasma and transport profiles were tested against the experimental data, a selection of tested parameters are indicated in table 3.6. Bolometric and and Dα emission from modelling results of these runs are shown in figure 3.29. The runs have different transport coefficients at the separatrix (in the previously estimated), different transport coefficient in the divertor region (as shown in table 3.6, the transport coefficients in the divertor were a factor 4 to 6 larger with respect to those at the pedestal), and the usage of a ballooning coefficient proportional to $1/B_T$ was also tested.

Figure 3.29a shows that the runs with higher separatrix electron density or higher transport parameters, like run #37 (which was not shown for simplicity) or #39, have high radiation in the divertor leg and X-point region. These simulations are completely detached and the radiation zone moves farther away from the target. The radiation distribution in the experimental data instead is lower along the divertor leg and is higher at the targets. In the detached cases, the D_α signal from the outer divertor LOS was higher than from the inner divertor LOS, contrarily

run #	$\langle n_e \rangle_{sep}$ $[\times 10^{19} m^{-3}]$	D_{sep} $[m^2/s]$	χ_{sep} $[m^2/s]$	χ_{div}/χ_{ped}	factor $\propto 1/B_T$
32	3.0	0.16	0.28	4	No
33	3.0	0.16	0.35	6	Yes
36	3.0	0.18	0.35	4	No
37	4.0	0.18	0.30	4	No
38	3.0	0.18	0.35	6	No
39	3.5	0.20	0.35	6	Yes

Table 3.6: List of parameters used for modelling of JET#69890; results are shown in figure 3.29.

to what experimentally observed (figure 3.29b). From this comparison between experimental data and modelling, it can be excluded that the outer target is detached, thus excluding every set of input parameters which results in a detached outer divertor.

On the contrary, runs like #36 or #38 are too attached, neutral density is underestimated as shown by the D_α signal (figures 3.29b and 3.29d). The radiation is also entirely localized at the divertor targets and is much lower than the experimental data elsewhere (figures 3.29a and 3.29c). The set of input parameters that fits the experimental data the best is that of run #32 which uses the ballooning factor and has a χ slightly higher than that estimated by the Eich scaling. The behaviour at the outer target is better reproduced than at the outer target; in the simulations, the outer target is slightly more detached than in the experiment. I will show in the next chapter that in JT-60SA scenario 2 the outer target is much more concerning than the inner one for power-exhaust mitigation, so reproducing the realistic behaviour at the outer target is much more important.

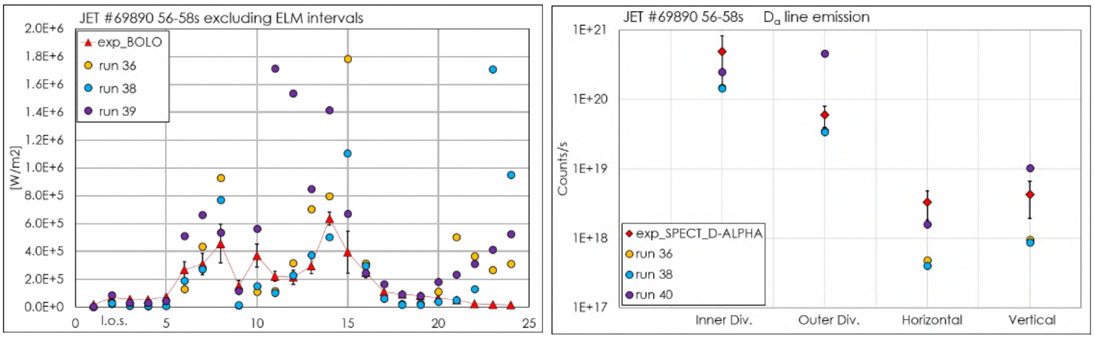

(a) Bolometer experimental signal and synthetic diagnostic signals.

(b) D_α experimental signal and synthetic diagnostic signals.

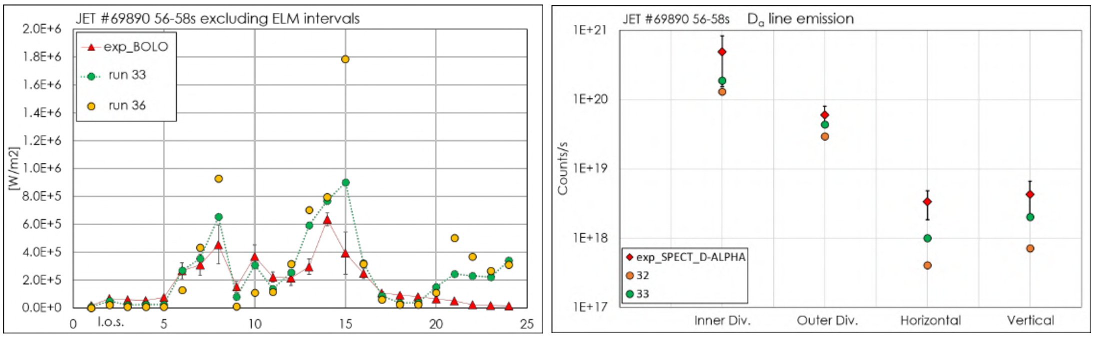

(c) Bolometer experimental signal and synthetic diagnostic signals.

(d) D_α experimental signal and synthetic diagnostic signals.

Figure 3.29: Bolometer and spectroscopy data and how they are used to evaluate JET transport parameters

The set of transport parameters that better fits the experimental data is that of run #33 whose transport profiles are shown in figure 3.30 and were applied in JT-60SA scenario 2 modelling that will be described in the next chapter.

The main limit of this modelling activity is given by the low spatial definition of Thompson scattering which is not enough to diagnose accurately the pedestal region, for this reason, pedestal profiles, especially density may not be accurately reproduced.

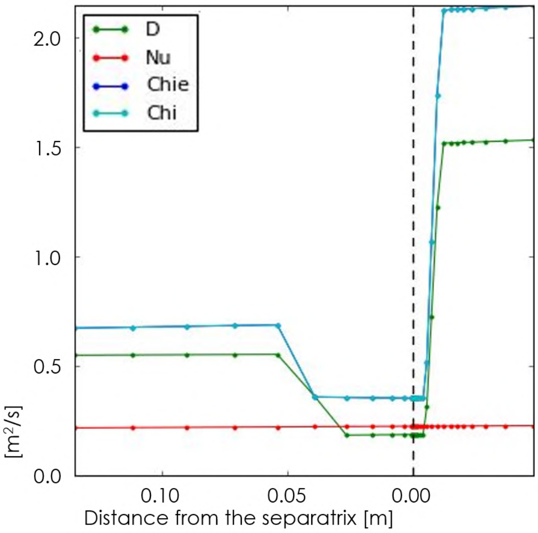

Figure 3.30: Transport parameter validated through JET #*69890* modelling.

Recycling factors on carbon wall

The sputtering model implemented in SOLEDGE2D-EIRENE estimates the sputtering yield through the Bohdanski formula. Normally the recycling coefficient for carbon is set to 0, meaning that when a carbon particle hits the carbon wall, it is always absorbed, a carbon source by self sputtering is calculated according to the Bohdanski formula. If the sputtering model is correct, there is no need neither for an additional recycling coefficient nor for carbon pumping. To test the validity of the sputtering and recycling model, a scan was made on the carbon recycling coefficient, from 0 to 0.8. The comparison of modelling results with CII and CIII spectroscopic lines proved that total carbon content is well-matched when the recycling coefficient is set to 0. The horizontal and vertical LOSs are very important to estimate the carbon content because they intersect the main plasma and are not directly influenced by divertor conditions. Again, it was difficult to reproduce the emission profile as the inner divertor, the carbon emission from the outer divertor instead is well matched.

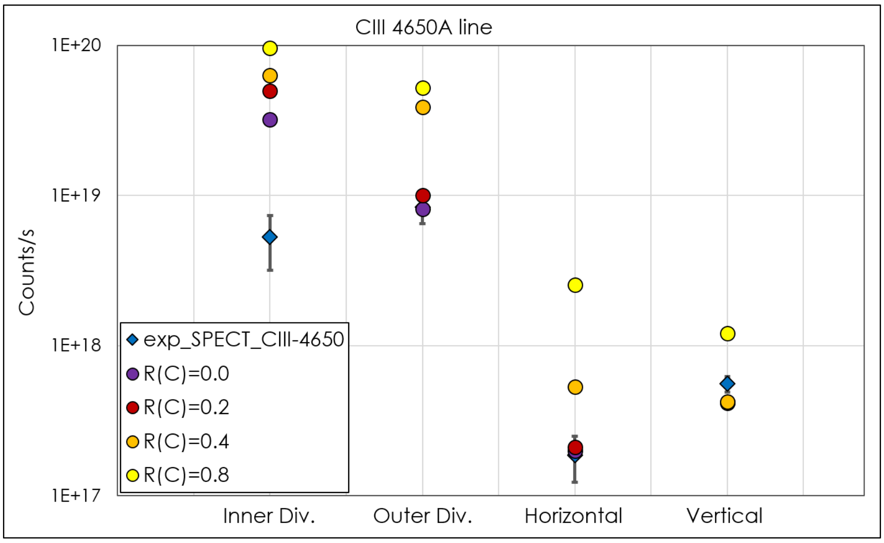

Figure 3.31: JET #*69890* C^{+2} 4650 A signal and modelling results.

Chapter 4

Predictive modelling towards future machines

This chapter is divided in three parts: in the first one, the modelling towards the experimental campaign of JT-60SA is described (section 4.1); in the second one, the modelling of DTT is presented (section 4.2.4); in the third one, an hysteretical-like behaviour found in the first two sections is analysed and studied (section 4.3)

4.1 Modelling towards the experimental campaigns of JT-60SA

JT-60SA aims to contribute and support the exploitation of ITER and by complementing ITER, to resolve key physics and engineering issues for the DEMO reactor. The objective of JT-60SA device is to confine break-even-equivalent high-temperature deuterium plasmas lasting for a duration longer than the time scales characterizing key plasma processes such as current diffusion and particle recycling, the goal is to obtain 100 s discharges[7]. The machine is equipped with superconducting toroidal and poloidal field coils. The maximum plasma current is 5.5 MA. The device is designed to study non-inductive steady-state operations with high values of the plasma pressure exceeding the no-wall ideal MHD stability limits. The target regimes of JT-60SA compared to those of present machines, ITER and DEMO are shown in figure 4.1a. The JT-60SA experiments should explore ITER and DEMO-relevant plasma regimes in terms of non-dimensional plasma parameters at high densities in the range of $1 \times 10^{20}\mathrm{m}^{-3}$. In the first two operational phases, JT-60SA will be equipped with a carbon wall, so the first test of high-β steady-state operations in JT-60SA will be firstly achieved in carbon wall environment. In the so-called *initial research one*, only about 20 MW of input power will be available, in the *initial research phase two* the maximum auxiliary input power will be 41 MW. After maturing integrated plasma control systems, in the later phase of the project, the divertor target and the first wall will be fully replaced by tungsten-coated carbon. The final mission of JT-60SA in support for ITER and DEMO will be investigated in a metallic wall environment.

To satisfy these requirements, JT-60SA can realize a wide range of diverted plasma equilibrium configurations covering a high plasma shaping factor ($S = q_{95}I_p/(aB_t) - 7$) and low aspect ratio. Figure 4.1b shows that the shape parameter of JT-60SA is equivalent to that of the Slim-CS DEMO that has the highest shape parameter among the DEMO designs. The major radius of JT-60SA is about half of ITER and the Slim CS DEMO. The plasma size of JT-60SA locates between ITER and other non-circular cross-section superconducting tokamaks (figure 4.1c).

A section of the carbon divertor for the first two operational phases is shown in figure 4.2. The divertor is mainly designed to operate in vertical-vertical configuration and has a cooled dome. The pumping system is located right below the dome and has a nominal pumping speed of 100 m^3/s.

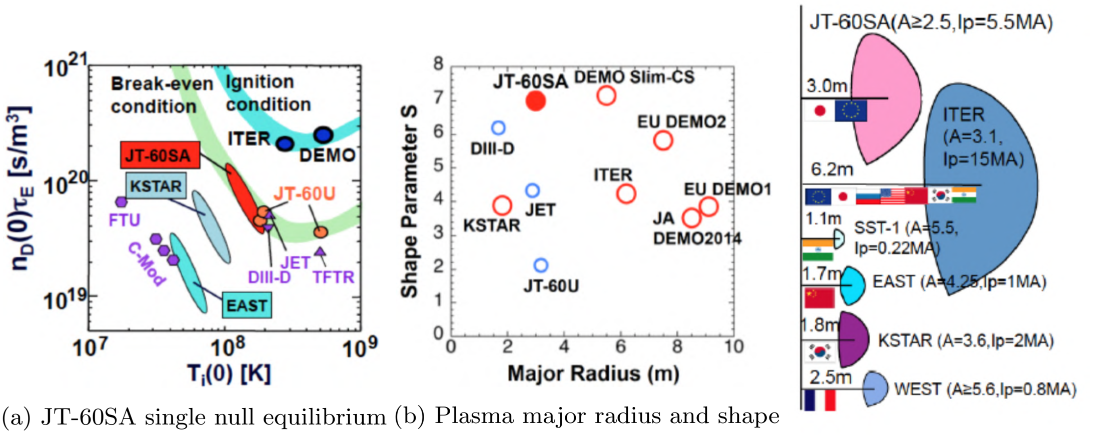

(a) JT-60SA single null equilibrium with 5.5MA.

(b) Plasma major radius and shape parameters.

(c) Plasma cross-section of superconductive tokamaks.

Figure 4.1: JT-60SA parameters and comparison with present machines, ITER and DEMO. Pictures derived from JT-60SA research plan.

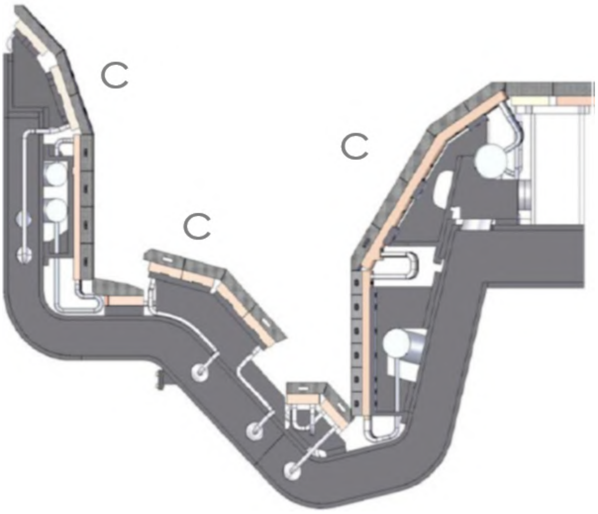

Figure 4.2: JT-60SA carbon divertor details.

Quantity	Unit	JT-60SA(#2)	JT-60SA(#3)
B$_t$	T	2.25	2.25
I$_p$	MA	5.5	5.5
kx		1.87	1.86
dx		0.5	0.5
β_N		3.1	2.6
dens$_{core}$	$10^{19}\ m^{-3}$	6	10
dens$_{sep}$	$10^{19}\ m^{-3}$	1	2
G. dens.	$10^{19}\ m^{-3}$	13	13
G. fract.		0.5	0.8
Power in.	MW	41	30
	MW	41	30
Magn. conf.		high el. SN	DN
q at sep.		5	5
H mode		H	H
Strike point		2 vertical	2 vertical
Seeding		Ne/Ar possible	Ne/Ar possible
div pump	m^3/s	100	100

Table 4.1: Main characteristics of the two full-inductive scenarios.

4.1.1 Scenario characteristics

The scenario analysed in this work is the so called *Scenario* #2 which is a single-null inductive scenario with the maximum foreseen plasma current ($I_p = 5.5\,\mathrm{MA}$). This scenario is the most challenging in terms of power exhaust; it has the maximum available auxiliary input power for the machine ($P_{aux} = 45\,\mathrm{MW}$) and a relatively low density with $\langle \mathrm{n_e} \rangle_{\mathrm{sep}} = 1 \times 10^{19}\mathrm{m}^{-3}$ and $\langle n_e \rangle_{core} = 6.0 \times 10^{19}\mathrm{m}^{-3}$. The main characteristics of the two full-inductive scenarios are shown in table 4.1. The scenario is modelled with carbon wall as mentioned in chapter 3.2.

The poloidal section of *scenario 2* equilibrium is shown in figure 4.3a. The strike points are located at the two vertical divertor plates next to the corners to maximize neutral compression. In the figure, the location of the absorbing surface is indicated in red. D$_2$ fueling is located at the outer mid-plane to optimize neutral penetration, while impurity puffing was located at the dome or on top of the outer divertor. The large dimensions of the machine, combined with the small predicted decay lengths, require a very detailed grid for SOLEDGE2D-EIRENE modelling, in this case, the grid is 110 × 30 cells large (figure 4.3b).
The main objectives of this modelling activity were:

- to test the scenario with realistic and validated transport parameters;
- to test if the predicted plasma regimes meet both the physical requirements of core performances and the technological need of mitigated power flux to the divertor targets
- to estimate carbon sputtering flux and carbon concentration
- to compare the cooling capabilities of different impurities and to investigate the impurity concentration required to obtain sustainable condition at the divertor and if it is compatible to that predicted in the scenario given in the research plan.

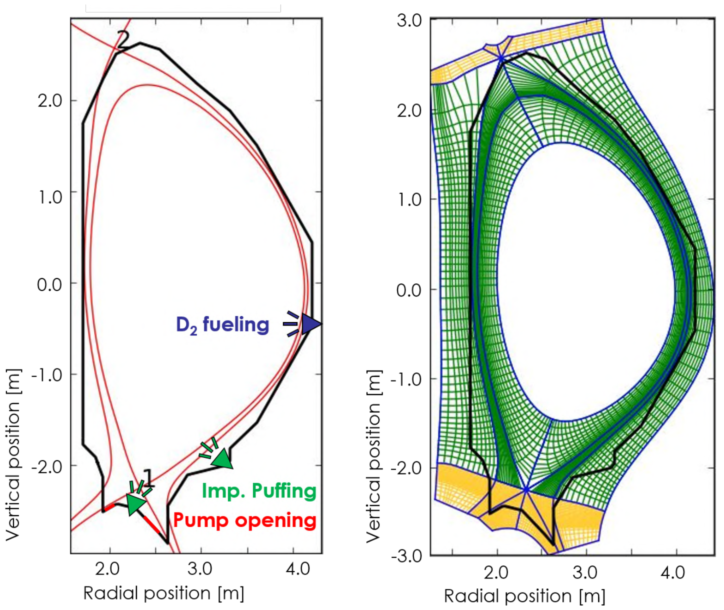

(a) JT-60SA equilibrium, pumping and puffing locations

(b) Implemented grid for JT-60SA scenario 2 modelling

Figure 4.3: Poloidal section of JT-60SA scenario 2 equilibrium, first wall shape, puffing, pumping locations and grid.

4.1.2 Modelling without impurity seeding

The first objective was to calculate the maximum input power that would provide sustainable conditions at the divertor targets and so to keep the power flux below 10 MW/m^2[7] in unseeded simulations, so considering only deuterium and carbon.

The transport parameters validated in 3.5 were used, and carbon sputtering was estimated using the Bodhanski model that was previously tested in JET.

Deuterium puffing was fixed to $\Gamma_{\mathrm{D2}} = 1 \times 10^{22} s^{-1}$, similarly to [69] and [70], and the albedo at the absorbing surfaces was tuned to obtain $\langle \mathrm{n_e} \rangle_{\mathrm{sep}} = 2 \times 10^{19} m^{-3}$. The initial scenario characteristics would have required $\langle \mathrm{n_e} \rangle_{\mathrm{sep}} = 1 \times 10^{19} m^{-3}$ but during this modelling campaign it was found that it was not possible to operate with such low separatrix density an input power that was compatible to that predicted for the scenario. This will be confirmed later on when impurities are added to the modelling.

A relevant asymmetry in terms of electron temperature and power deposition was found between the inner and outer divertor, as it is shown in figure 4.4. Because of this asymmetry, in this section and in the following I will refer to the attachment, detachment condition and power deposition referring only to the outer target.

The maximum input power to obtain sustainable conditions at the divertor plates was found to be $\mathrm{P_{in,max}}$ =18 MW according to the input power scan shown in figure 4.5. In the unseeded scenarios, $\mathrm{P_{rad,in}}$ is negligible since there is no high-Z impurities that can radiate in the core. The maximum sustainable input power was obtain by increasing the . For the $P_{in} = 18\,\mathrm{MW}$ case, the total radiation is $P_{rad} = 7\,\mathrm{MW}$. Impurity concentration increases with the increase of

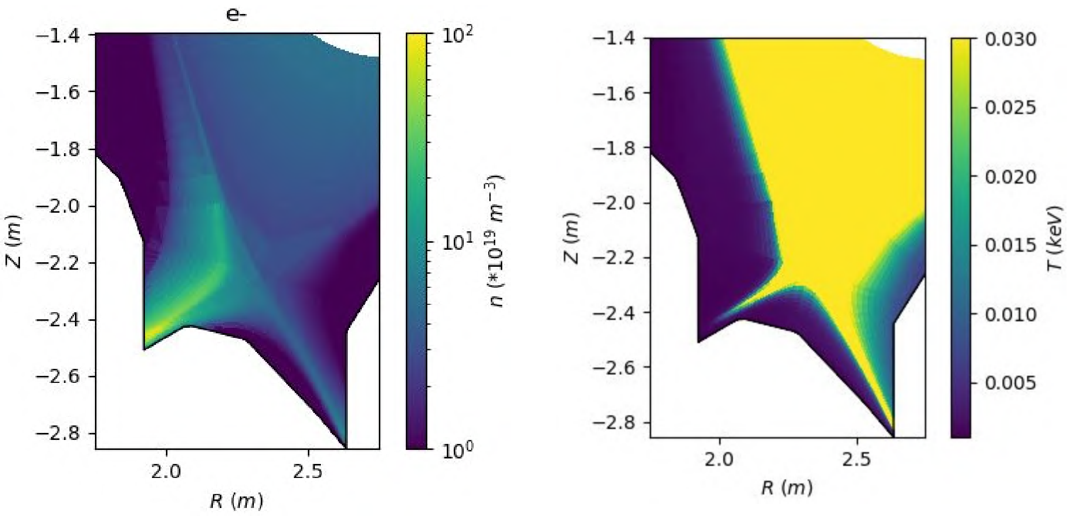

(a) Detail of divertor plasma electron density for the case with $P_{in} = 18\,\mathrm{MW}$

(b) Detail of divertor plasma electron temperature saturated at 30 eV case with $P_{in} = 18\,\mathrm{MW}$

Figure 4.4: Strong asymmetry between inner and outer divertor temperature and density.

input power because carbon sputtering yield increases with the increase of electron temperature, Z_{eff} at the pedestal top is also shown in figure 4.5 referring to the secondary axis.

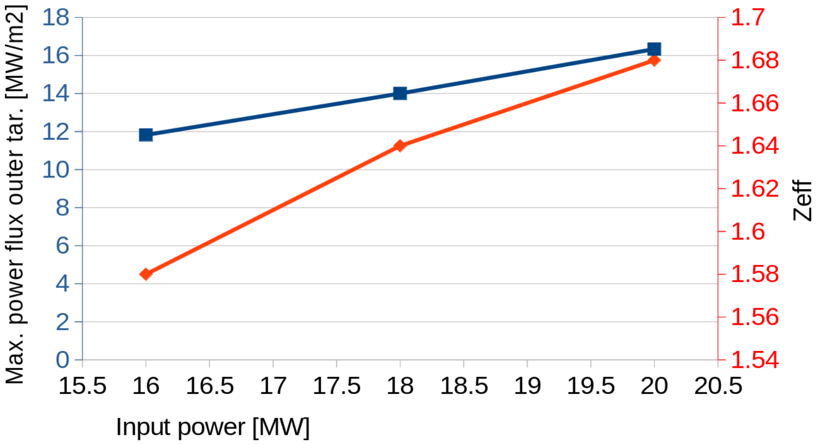

Figure 4.5: Power flux peak to the outer target and Z_{eff} in unseeded simulations.

Since total radiation within SOLEDGE2D-EIRENE inner boundary is negligible, the maximum auxiliary input power cal be estimated as: $\mathrm{P_{aux,max}} = \mathrm{P_{in,max}} + \mathrm{P_{ELM}} \simeq 24\,\mathrm{MW}$. The assumption that was made on P_{ELM} is reasonable since this scenario has similar input power, plasma density and plasma volume to the JET pulse analyzed.

4.1.3 Modelling of seeded discharges

The second objective was to find the operative window that allows sustainable power loads to the divertor in seeded simulations.
First, from lower density simulations with Pin=31MW, it was found that, it was not possible to obtain sustainable conditions at the divertor with reasonable $\langle \mathrm{Z_{eff}} \rangle_{\mathrm{sep}}$ if $\langle \mathrm{n_e} \rangle_{\mathrm{sep}} \leqslant 2.0 \times 10^{19}$ as in the unseeded cases.

Impurity seeding comparison

In the previous sections it was found that impurity seeding is required to obtain sustainable power deposition to the divertor target. A strong asymmetry between the power flowing to the inner and outer divertor was also found; in the scenarios with impurity seeding the asymmetry will become even larger.

The control parameter for impurity concentration is the plasma purity. The scenario has a plasma purity $\eta = 0.8$ where the plasma purity is defined as:

$$\eta = \left\langle \frac{n_D}{n_e} \right\rangle_{core} . \tag{4.1}$$

Since SOLEDGE2D-EIRENE modelling is extended only to the pedestal top, the plasma purity is calculated at the pedestal top. The modelling is performed with fixed fueling and puffing, similarly to what was done by Kawashima [69] and [70] with the edge code SONIC, puffing values are listed in table 4.2. Fueling level was tuned to obtain the wanted separatrix density with approximately the nominal pumping speed $v_s \simeq 100\,\mathrm{m^3/s}$. The deuterium fueling level is similar to that used by Kawashima. In SONIC simulations, impurities were not treated separately from deuterium, impurity densities were calculated as fixed fractions of deuterium's and their temperature was set equal to the electron temperature. The albedo of the absorbing surfaces was modulated to obtain $2.0 \times 10^{19}\mathrm{m^{-3}} \leq \langle \mathrm{n_e} \rangle_{\mathrm{sep}} \leq 2.5 \times 10^{19}\mathrm{m^{-3}}$ and to obtain the required plasma purity $\eta \simeq 0.8$.

Element	Puffing [part./s]
D	$1{\times}10^{22}$
Ne	$2{\times}10^{20}$
Ar	$1{\times}10^{20}$

Table 4.2: Puffing and fueling of the seeded simulations, neon and argon are alternative to each other.

The relation between the input power in SOLEDGE2D-EIRENE simulation P_{in} and the auxiliary input power P_{aux} is given by:

$$P_{in} = P_{aux} - P_{ELM} - P_{rad,in}, \tag{4.2}$$

where P_{ELM} is the ELM power and $P_{rad,in}$ is the power radiated within SOLEDGE2D-EIRENE inner boundary. An estimation of P_{in} is given by Zagorski's modelling with COREDIV[71]. For scenario #2 with neon seeding, slightly lower density and $\langle \mathrm{Z_{eff}} \rangle_{\mathrm{sep}} = 3.0$ the total power radiated inside the separatrix was estimated $P_{rad,sep} = 8\,\mathrm{MW}$. I assumed that 5 MW were radiated within the inner boundary and 3 MW between the inner boundary and the separatrix. P_{ELM} was estimated to be 5 MW as in the analogous JET case; this can be seen as a lower limit for P_{ELM} since the larger plasma volume and higher input power of JT-60SA may lead to higher P_{ELM}. With these two assumptions, the input power for SOLEDGE2D-EIRENE modelling relative to the full-power case was $P_{in} == 31\,\mathrm{MW}$. For the upper mentioned reasons, this can be considered the upper limits for P_{in}.

Both neon and argon are foreseen as seeding impurities for JT-60SA. An input power scan was performed in simulations with neon or argon. The scan was performed to compare the cooling performances of the two impurities and to find the maximum input power at SOLEDGE2D-EIRENE inner boundary which guarantees sustainable condition at the outer divertor; by inverting equation 4.1.3 it is possible to calculate the relative $P_{aux,max}$. The input power was scanned from 15 to 36 MW.

Results, in terms of maximum power flux and temperature at the outer divertor are shown in figure 4.6. Argon is generally a better cooling impurity for this scenario due to the higher cooling efficiency at high temperature which results in higher radiated power (figures 4.6c. Figure 4.6d shows the radiated power fraction which is calculated as $(P_{rad}^{SOLEDGE} + P_{rad,in})/P_{aux}$. Figure 4.6a and 4.6b show the power flux and electron temperature peak at the outer target; the red continuous lines represent the maximum values of those quantities sustainable by the target in steady state conditions, the red dashed line represent the input power that can be sustained for some transients. The maximum input power for neon and argon is estimated: $\mathrm{P}_{in,max}\,(Ar) \simeq 23\,\mathrm{MW}$ and $\mathrm{P}_{in,max}\,(Ne) \simeq 20\,\mathrm{MW}$. By inverting equation , the maximum auxiliary input power with $\eta = 0.8$ is $\mathrm{P}_{aux,max}\,(Ar) \simeq 33\,\mathrm{MW}$ and $\mathrm{P}_{aux,max}\,(Ne) \simeq 30\,\mathrm{MW}$.

The estimation of $P_{aux,max}$ is susceptible to the uncertainties on P_{ELM} and $P_{rad,in}$,but the modelling clearly indicated that the condition on plasma purity must be relaxed to obtain sustainable power flux to the outer divertor with $P_{aux} = 41\,\mathrm{MW}$.

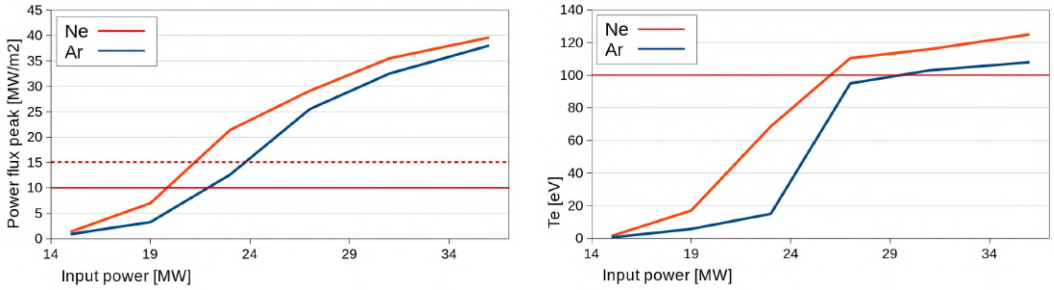

(a) Power flux peak at outer target. The dark red lines represent the nominal limits given by the applied divertor technologies.

(b) Temperature peak at outer target. The dark red lines represent the nominal limits given by the applied divertor technologies.

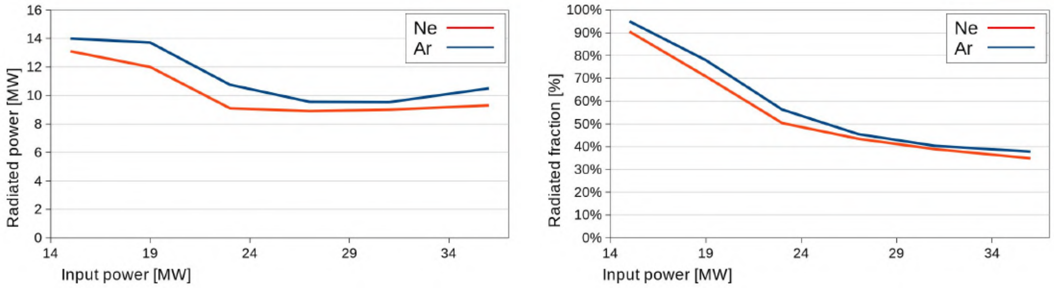

(c) Total radiated power for the input power scan with argon and neon.

(d) Radiated power fraction for the input power scan with argon and neon.

Figure 4.6: scan on input power with neon or argon as seeding impurities.

Scan on Argon content

A scan on impurity content was performed by varying argon influx in four different simulations, the albedo for argon at the pump entrance was kept constant as well as that for deuterium. $\langle n_e \rangle_{sep}$ was kept constant by tuning Γ_{D2}. The input power was set to P_{in} =31 MW to correspond to P_{aux} =41 MW, the foreseen auxiliary input power for the scenario. The scan was performed with argon as seeding impurity since in provides the best cooling performances.

Figure 4.7 shows the result of this scan. By relaxing the condition on plasma purity by 10%, it is possible to obtain sustainable condition at the outer divertor with $\langle n_e \rangle_{sep} = 2 \times 10^{19} m^{-3}$ and $P_{in} = 31$ MW.

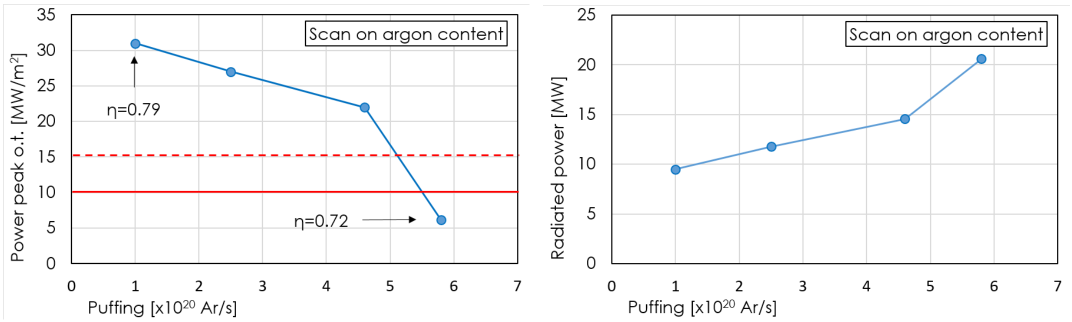

(a) Power peak at the outer target.

(b) Total radiated power.

Figure 4.7: scan on argon content.

Effect of sub-divertor modelling

The consistent modelling of sub-divertor neutral dynamics was made by using SOLEDGE2D-EIRENE together with the Montecarlo code AVOCADO. The reason of this work was to understand whether the strong asymmetry between inner and outer divertor was lowered by neutral transport below the dome. The neutral pressure difference between inner and outer target should be lowered by sub.divertor transport.

In previous simulations an albedo was used for deuterium and for the other impurities which was equal at the inner and outer divertor apertures indicated by the two red arrows in figure 4.8a. In that modelling activity, it was assumed that a particle was reflected or absorbed by those two surfaces with a fixed probability. In this work I also include the possibility for particles to flow from the inner to the outer divertor or vice-versa. The sub-divertor geometry shown in green in figure 4.8a, is schematized in figure 4.8b. Figure 4.8b shows the poloidal view of the sub-divertor geometry implemented in AVOCADO, while the full 3D geometry is shown in figure 4.8c. The sub-divertor geometry is modelled assuming toroidal symmetry with three surfaces that can be crossed by neutral particles, surface #1 and #2 correspond to the inner and outer divertor aperture which are the absorbing surfaces in SOLEDGE2D-EIRENE, surface #3 is the pump surface where it is predicted a nominal pumping speed of $100\,\mathrm{m}^3/\mathrm{s}$.

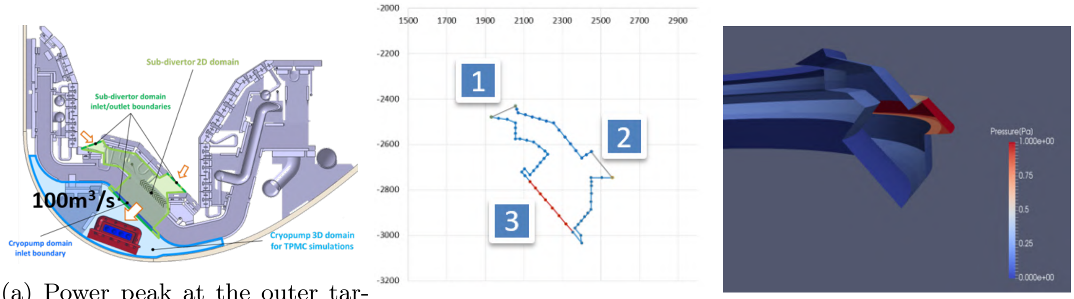

(a) Power peak at the outer target with and without sub-divertor modelling.

(b) Total radiated power with and without sub-divertor modelling.

(c) Total radiated power with and without sub-divertor modelling.

Figure 4.8: Effect of sub-divertor modelling on power exhaust.

The gas flow trough a conductance (C) (a tube, an aperture etc.) is linked to the pressure in the conductance by the equation:

$$Q[\mathrm{Pam}^3/\mathrm{s}] = C[\mathrm{m}^3/\mathrm{s}]P[\mathrm{Pa}]. \tag{4.3}$$

In molecular regime the conductance does not depend on pressure, this makes equation 4.3 a linear equation on pressure. According to equation 4.3, in the system described in section in figure 4.8b, the neutral flow through surface #1 can be calculated as:

$$Q_1 = C_{1,1}P_1 + C_{1,2}P_2 + C_{1,1}P_3, \tag{4.4}$$

where P_n is the neutral pressure at the n surface and $C_{1,n}$ is the conductance from surface n to surface 1. Let's define positive the flow entering the system and negative the flow exiting the system., equation 4.4 can be written for all the three surfaces:

$$\begin{bmatrix} C_{1,1} & C_{1,2} & C_{1,3} \\ C_{2,1} & C_{2,2} & C_{2,3} \\ C_{3,1} & C_{3,2} & C_{3,3} \end{bmatrix} \begin{bmatrix} P_1 \\ P_2 \\ P_3 \end{bmatrix} = \begin{bmatrix} Q_1 \\ Q_2 \\ Q_3 \end{bmatrix}. \tag{4.5}$$

Pressure P_1 and P_2 are given by edge modelling, Q_3 is given by the pump specifics[1], if the conductances are known, equation 4.1.3 becomes a system of three equations with three unknowns: Q_1, Q_2 and P_3.

Avocado[72] is a code that estimates the conductances $C_{n,m}$ in molecular regimes using a Montecarlo method. The conductances depend on the temperature distribution at the conductance entrance so, given t_m the temperature at the aperture m:

$$C_{n,m} = C_{n,m}\left(t_m\right). \tag{4.6}$$

Avocado was used making an assumption on neutral temperature at the three surfaces $t^0_{1,2,3}$, and a matrix $\left[C^0\right]$ was calculated. Each conductance of the matrix $\left[C^0\right]$ can be related to the probability $F_{m,n}$ of a particle to flow from a the surface n to the surface m by the equation:

$$C_{m,n} = \frac{1}{4}\left\langle v_t\right\rangle A_m F_{m,n}, \tag{4.7}$$

where $\left\langle v_{0tn}\right\rangle$ is the thermal speed of a particle with of temperature t^0_n, and A_m is the area of the m surface. Equation 4.7 is inverted to map each element of the matrix $\left[C^0\right]$ to the matrix of the probabilities of flowing from a surface to another $[F]$. Equation 4.7 is used again co calculate the matrix of the conductances with the temperatures at the surfaces given by SOLEDGE2D-EIRENE modelling $\left[C^T\right]$, calculated from $[F]$.

Using neural temperature and pressure from modelling, equation 4.1.3 can be solved on the three unknowns. Neutral flow across a surface and the surface pumping speed s are linked by equation:

$$Q_n = s_n P_n, \tag{4.8}$$

which is used to calculate the pumping speed of both surface #1 and #2. The calculated s_1 and s_2 are used as input parameters of SOLEDGE2D-EIRENE runs iteratively.

Due to the high asymmetry between inner and outer divertor, usually $P_1 \gg \P_2$, and consequently Q_2 is usually negative. Negative Q_2 implies that there is a net flux from the sub-divertor to the outer divertor region. Negative particle flow corresponds to a negative pumping speed that in SOLEDGE2D-EIRENE can be simulated with a puffing from the outer divertor pump surface. If $Q_2 < 0$, the puffing rate corresponding to the net particle flow was calculated as:

$$\Gamma_{puff} = \frac{s_2}{k_B T_{puff}} = \frac{Q_2}{k_B T_{puff} P_2} \tag{4.9}$$

This method was used iteratively on JT-60SA simulation to quantify the impact of sub-divertor neutral flow on divertor plasma. The simulations made the argon content scan without

---

[1] the flow through the pump surface is calculated as $Q_3 = c_s P_3$ where $c_s = 100\,\mathrm{m}^3/\mathrm{s}$ is the nominal pumping speed

sub-divertor modelling were used as a comparison.

Figure 4.9 shows the comparison between modelling results with and without sub-divertor modelling in terms of power flux peak to the outer divertor and total radiated power. The figures show that detachment onset at the outer target is slightly favoured when sub-divertor modelling is included. Minor differences in terms of power deposition and radiated power appear in the cases when the outer divertor is completely detached of attached, in the partially detached case with $\Gamma_{Ar} = 4.6 \times 10^{20}\,\mathrm{Ar/s}$, the effect of neutral flow from the inner to the outer divertor is more evident. Figure 4.10 shows the neutral pressure and the molecular density in the divertor region in the cases with $\Gamma_{Ar} = 4.6 \times 10^{20}\,\mathrm{Ar/s}$ without and with sub-divertor modelling. In the standard simulation the pumping speed from the inner pumping surface was $40\,\mathrm{m^3/s}$ and that from the outer pumping surface was $30\,\mathrm{m^3/s}$. In the case with sub.divertor modelling, the pumping speed at the inner divertor pumping surface, derived from equations and was $120\,\mathrm{m^3/s}$; at the outer divertor there was a net deuterium flux from the sub-divertor to the divertor region in the $\Gamma^{o.d.}_{D2} \simeq 1 \times 10^{22}\,\mathrm{D_s/s}$. The sub-divertor flow from the inner to the outer target sensibly reduces neutral pressure at the inner target and increases it at the outer target; this leads to an increase of friction and radiated power inducing a positive feedback that enhances detachment. The asymmetry between inner and outer divertor is reduced but still evident.

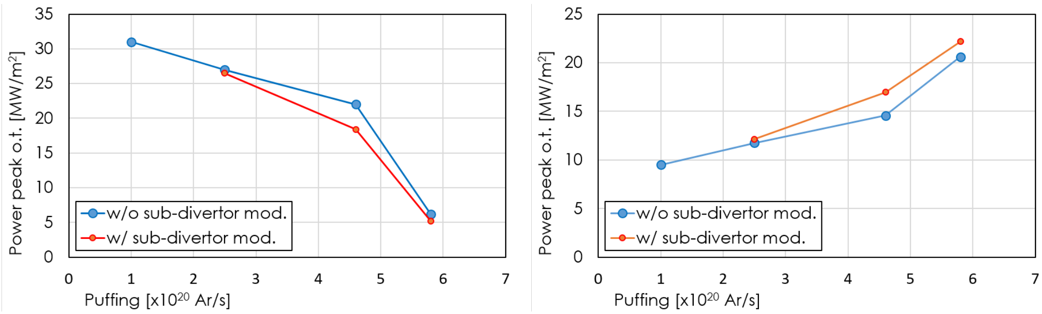

(a) Power peak at the outer target with and without sub-divertor modelling.

(b) Total radiated power with and without sub-divertor modelling.

Figure 4.9: Effect of sub-divertor modelling on power exhaust.

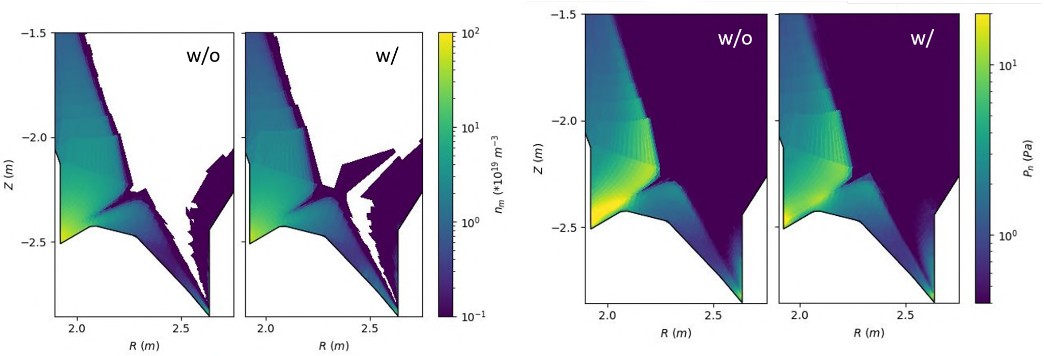

(a) D_2 density without sub-divertor modelling.

(b) Neutral pressure without sub-divertor modelling.

Figure 4.10: Comparison of neutral density and pressure with or without sub-divertor modelling for the case with $\Gamma_{Ar} = 4.6 \times 10^{20}\,\mathrm{Ar/s}$

4.1.4 An application: VUV spectrometer designing

Given the utilization of an imaging VUV spectrometer on JT-60SA[7][73] aiming at the divertor, a synthetic version of the diagnostic was prepared to explore the potential of the spectrometer in helping the investigation of the divertor physics and as a means to validate the results of complex simulation codes. Besides the qualification of the impurity content in the various scenarios, the spectrometer will be particularly useful, together with other systems, to investigate the physics of the plasma detachment.

The diagnostic instrument was described in [74]. It consists of a double imaging spectrometer coupled to the divertor employing two toroidal mirrors. The slit is contained in the poloidal plane to view across the divertor from the inner to the outer striking points. The distribution of the Lines Of Sight (LOS) is defined by the partition of the 2D CCD sensors in the sagittal direction; a view of the VUV spectrometer geometry is shown in figure 4.11. A bolometer array with analogous LOS will be available in a different toroidal section and, in principle, visible spectroscopy along the same LOS of the VUV system will be possible by intercepting the zero-order of the VUV spectrometer(s) and forwarding it to a visible spectrometer. The two spectrometers cover two different wavelength regions of $10-48$ and $44-125$nm respectively by means of custom-designed gratings [75], so that the resonance emission of low and medium Z elements can be captured with adequate wavelength resolution.

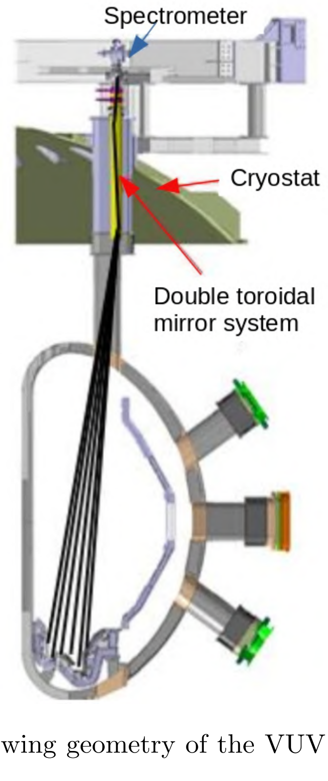

Figure 4.11: Overview of the viewing geometry of the VUV spectrometer to be installed on JT-60SA.

Recombination processes are a key flag of detachment onset, recombination may be highlighted by examining the relative intensities of lines from different ionization states and different transitions within the same ionization state as in [76] where the role of recombining vs ionizing plasma was determined using both VUV and visible C^{3+} spectra. In [77] n=7 to n=6 or n=6 to n=5 C^{3+} transitions were recognized as a signature of charge exchange recombination of C^{4+}.

To simulate the measurements, the output of SOLEDGE2D-EIRENE simulations carried out as described in section 4.1.2 and 4.1.3 was used. Spectral emission are integrated along a few LOS in cases with and without seeding with Ar or Ne and comparing situations with and without detachment. The spectral emission has been computed knowing at each point along with the LOS electron density and temperature and the densities of the specific ionization states as calculated in the simulation and making use of the ADAS database [2] where the emission rates resulting from a collisional radiative model are available for several transitions. The spectrum is then plotted considering for each grating the predicted FWHM. The calibration curve of the spectrometer has been neglected and the integral emission has been calculated along an ideal LOS with no finite transverse dimension. The final aim is for the exercise to be limited to the edge and divertor emission outside, the innermost radius considered in the simulations. The contribution of the emission from the core will be added in the future by including 1D simulations of the plasma core.

Edge simulations were performed using the 2D coupled code SOLEDGE2D-EIRENE. In the simulations 31 MW were assumed to cross the $\rho_{\mathrm{tor,norm}} = 0.8$ surface in steady-state conditions, assuming 10 MW radiated inside the $\rho_{\mathrm{tor,norm}} = 0.8$ surface. Deuterium fueling and impurity seeding were chosen to obtain $\langle \mathrm{n_e} \rangle_{\mathrm{sep}} = 2 \times 10^{19} \mathrm{m}^{-3}$ and the required impurity concentration. A detached and an attached case for both Ne and Ar seeded simulations were selected to help test the synthetic diagnostic. The right hand sides of figure 4.12a and 4.12b show the simulated radiated power at the edge for two cases with (bottom) and without (top) outer target detachment. Also in this section *detached* state refers to the outer target plasma.

Samples of the obtained synthetic spectra are shown in figures 4.13a-4.13c, for D^+C only, H + Ne and H + Ar respectively, comparing detached and attached cases along three LOS intercepting the inner divertor leg, the X-point region and the outer leg respectively. The LOS geometry is indicated by the poloidal sections on the first column on the left of figures 4.13a-4.13c. The spectra are very reach in information and some differences can be identified in the spectra between the two plasma scenarios as well as among the three LOS as a result of the different temperatures and densities in the various positions and scenarios. A simple consideration is the ratio between two carbon transitions, namely CIII 97.7 nm and CII 90.4 nm in the two cases of attached and detached plasma, with detachment reached by injecting Neon. It is seen in figure 4.14 that the ratio of the emissivities integrated along the three LOS is lower for all of the three LOS in the detachment case, as expected. This is not always the case. For other transitions related to higher ionization states the ratio of high to low states emissivities can be inverted when moving from attached to detached phase detachment, as the result of the different spatial distribution of the ionized states along the LOS. Figure 4.12 shows for reference the contour plots of the CII and CIII density populations in the attached and detached and the corresponding contour plots for n_e and T_e. Future work will explore the sensitivity of the instrument to variations of the plasma conditions possibly including visible spectra to further expand the potential in the study of a recombining plasma as done for instance in [76].

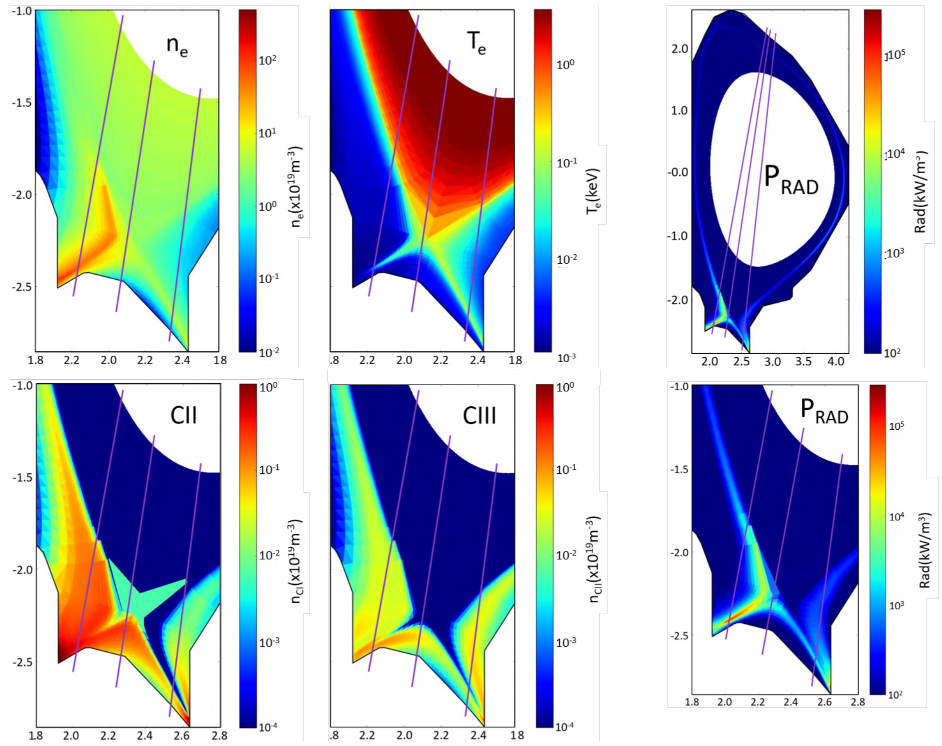

(a) Divertor plasma details for the attached case

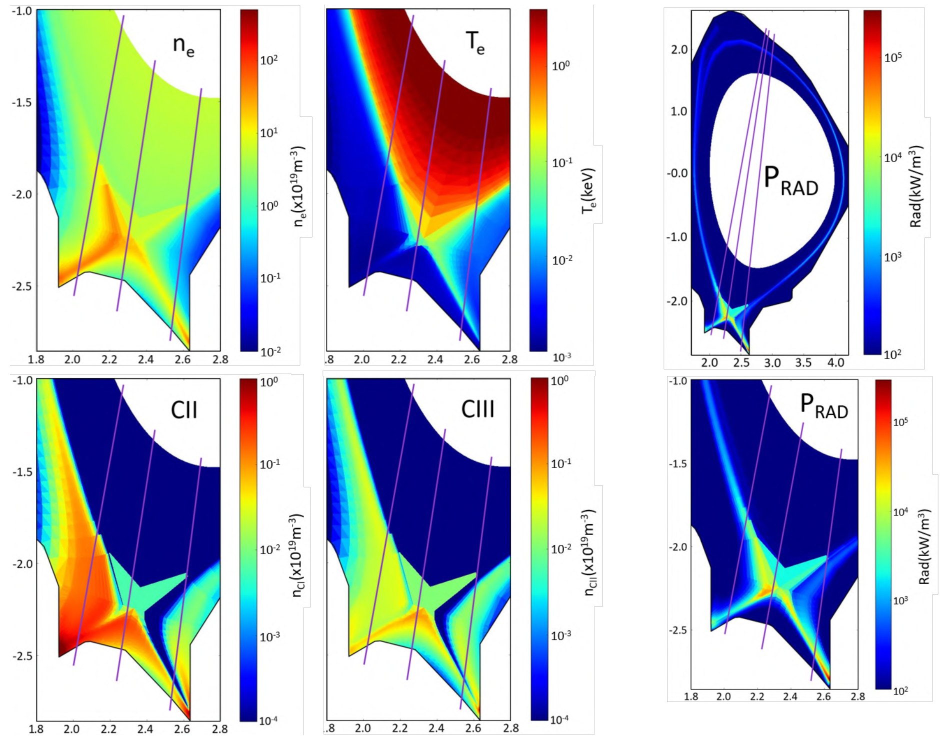

(b) Divertor plasma details for the detached case

Figure 4.12: Contour plots of n_e, T_e, radiation emission and CII and CIII populations for an attached and a detached argon seeded case. Centroids of the line of sights are in purple.

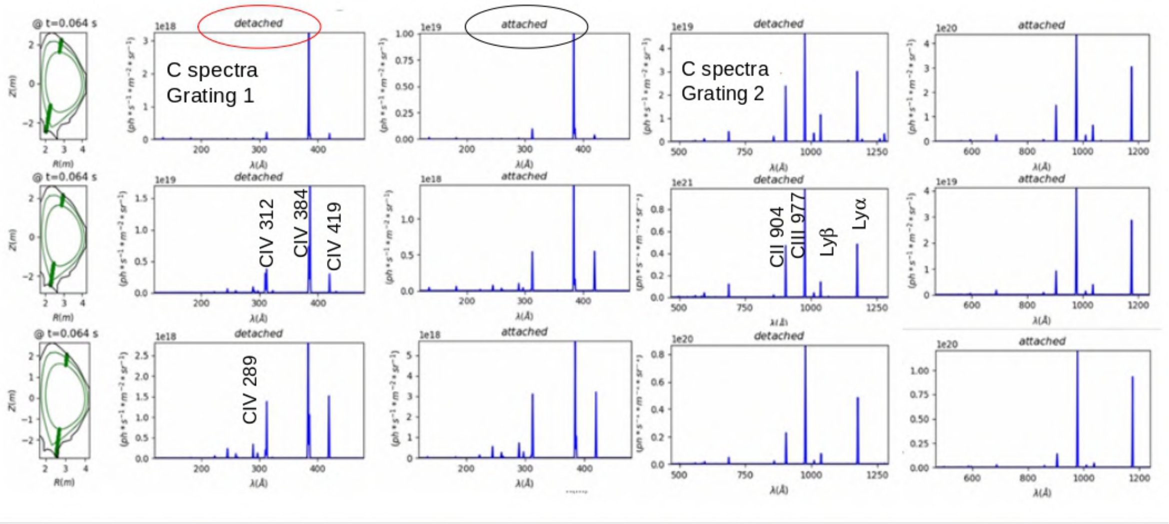

(a) Deuterium and carbon emission spectra for and attached and detached case.

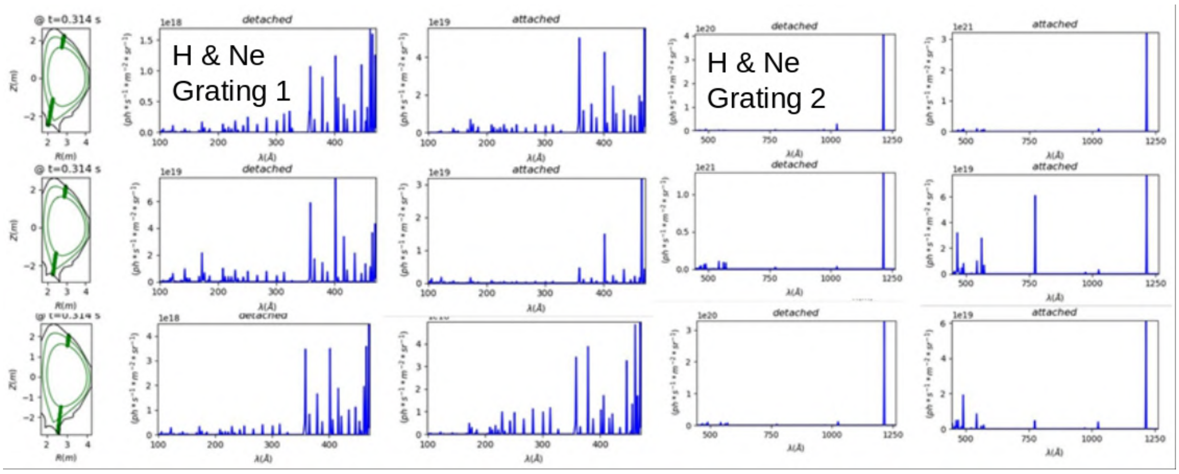

(b) Deuterium and neon emission spectra for and attached and detached case.

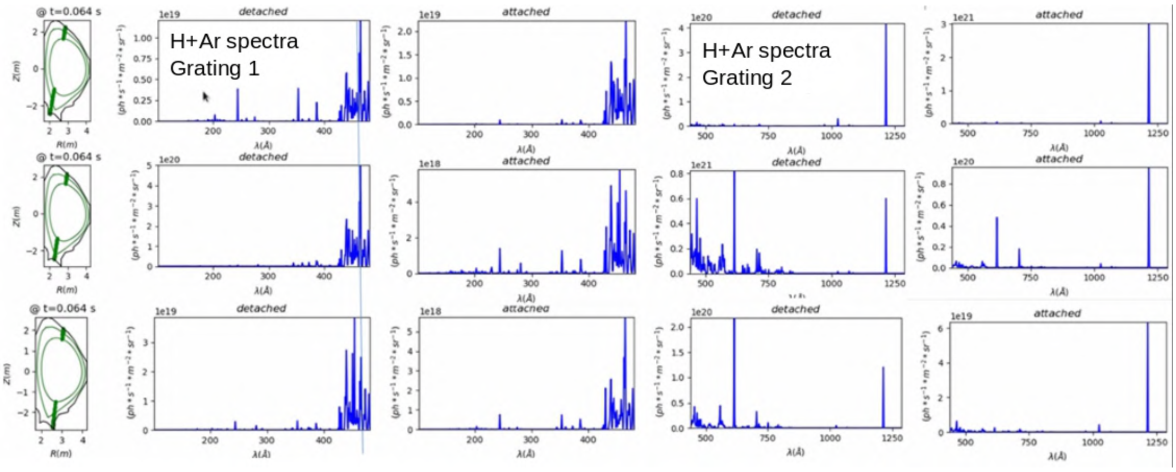

(c) Deuterium and argon emission spectra for and attached and detached case.

Figure 4.13: Spectra from for each of the two gratings simulated from an attached and a detached case in each of the impurity content combination considered.

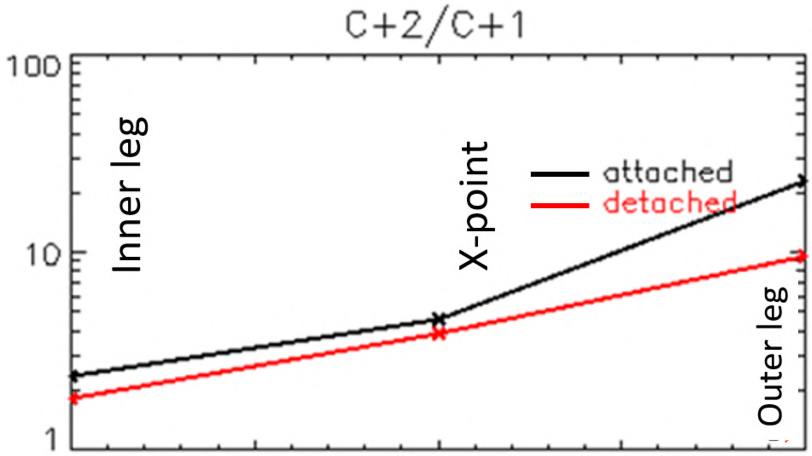

Figure 4.14: Ratios of CIII 97.7 to CII 90.4 nm line-integrated emissivities for the three LOS in the attached (black) and detached (red) cases at the inner divertor, dome and outer divertor. A sensible drop at the outer divertor of the ratio C^{+2}/C^{+1} is seen when outer divertor detaches. Minor changes appears at the inner divertor because it is always detached.

4.2 Modelling for DTT designing

In this chapter, the modelling activity of DTT full power single null scenario is described. First, a brief discussion of DTT main parameters is made in section 4.2.1. In section 4.2.2 the modelling activity of DTT single-null scenario with constant transport profiles is described. The aims of this modelling activity were: to define an operative scenario in terms of impurity seeding and plasma density with sustainable power loads to the divertor and to provide a plasma background for pumping system and diagnostic designing. In section 4.2.3 the modelling of DTT single-null scenario with the transport profiles validated in section 3.1 is described. The scope of this modelling activity is to further define an operational window for single-null full-power operation, compatible with core performances and to contribute to the divertor designing by studying the effect on detachment of divertor closure. In section 4.2.4 the application of modelling outcome to the designing of the ECRH launching system and the interferometer is described.

4.2.1 DTT scope and characteristics

The idea of constructing a divertor test facility comes from the observation that the solution to adopt a conventional divertor (which will be tested in ITER) may not be suitable for extrapolation to DEMO. In order to explore different possible routes, alternative solutions must be tested. The DTT facility is designed to test divertor solutions in regimes relevant for ITER and DEMO. Alternative divertor solutions such as the cooled liquid lithium limiter in FTU [35], the Super-X divertor in MAST-U [78] or the Snowflake divertor in TCV [79] are being tested, but the extrapolation from present devices to DEMO is considered not reliable]. The specific role of the DTT facility is to bridge the gap between today's proof-of-principle experiments and the DEMO reactor conditions. The main objectives of DTT can be summarized as follows:

- test whether the alternative divertor solutions can be technically integrated and are able to withstand the strong thermal loads in the DEMO device if the fraction of radiated power turns out to be lower than expected;

- improve the experimental knowledge in the heat exhaust at parameter ranges that cannot be addressed by present devices;
- To assess whether the alternative divertor magnetic configurations are viable in terms of the exhaust problems without compromising plasma bulk performances;
- to test whether the various possible divertor concepts are compatible with the technological constraints of DEMO, both under constructive and physical point of views;
- to test the divertors based on the use of liquid metals and test the compatibility with the parameters of the edge of a thermonuclear plasma.

DTT is a high toroidal field ($B_T = 6\,\mathrm{T}$) machine, with a high nominal plasma current 5.5 MA and a relatively small major radius. These characteristics will allow to operate with a high plasma density ($n_{e,core} 10^{20}\mathrm{m}^{-3}$), and with power-exhaust-relevant parameters similar to DEMO's such as collisionality and the ratio between input power and major radius of about 15 MW/m.

The designing phase of the first DTT divertor has not been finalised yet. Currently, a conventional divertor is integrated in the DTT conceptual design within the EUROFusion framework. In the following sections of this chapter, the divertor geometry that will be assumed will be that of the proposed FAST tokamak[80][81], which was proved able to operate with both single-null and quasi-snowflake configuration. It will be referred to that divertor geometry as the *FAST-like geometry* that will be shown in the next sections of this chapter.

4.2.2 Modelling of DTT with uniform transport parameters

The initial modelling of DTT SN full-power scenario is performed using uniform transport parameters. Although, as discussed in chapter 3, transport is one of the key input parameters that influence modelling results the most, even the more *"simplistic"* modelling made using uniform transport parameters could give plenty of information on the analyzed scenario. Modelling with uniform parameters is used to investigate differences between neutral distribution in attached or detached conditions for pumping system designing purposes, it is useful to compare cooling effectiveness of different seeding impurities, it is used to investigate the sensitivity required by a diagnostic to identify different divertor plasma state as it is done in chapter 4.2.4, it is applied to study the power share between inner and outer divertor, and also, if transport coefficients are wisely chosen, to find an approximate working range of a scenario in terms of plasma density and impurity concentration.

Lastly, this modelling with uniform transport parameters was performed while the validation of transport parameters through modelling of present machines was still ongoing, so validated transport parameters were not available.

The modelling activity started with deuterium-only modelling (section 4.2.2), impurities are later added (section 4.2.2).

D-only modelling

In its earlier stage DTT will be equipped with a full tungsten wall; since the first divertor geometry is not defined yet, the studied divertor geometry is a plausible geometry, the one proposed for the FAST tokamak, reported in the last interim design report[4] and shown in figure 4.15a; the influence of possible divertor geometry on power exhaust will be investigated in section 4.2.3. Figure 4.15b shows the first wall as simulated in SOLEDGE2D-EIRENE; complete reflection of deuterium and impurities is set over the all wall (black lines) but on the absorbing surfaces (represented in red) that are the apertures that lead to the pump posed beyond the first wall. The albedo of the absorbing surfaces was set to match the target separatrix density; typical value is 0.92. When impurities are added, the albedo was set equal to deuterium. Puffing locations are shown in figure 4.15b, deuterium fuelling is located near the low field side mid-plane while two different locations were tested for impurity seeding: the dome and the low field side of the external divertor plate.

According to [5] and plasma parameters in table 4.3, the predicted cross-field heat flux decay length is: λ_q =1 mm, a narrow decay length given by the high field of the machine and comparable to the one predicted for ITER. The simple 2-point model [82] directly relates λ_q to the sum of heat diffusion coefficient for electrons and ions. By assuming λ_q =1 mm and $\chi_e = \chi_i = \chi$ the value for heat diffusion transport coefficient is set to χ =0.15 s/m^2. The particle diffusive transport coefficient was chosen as the typical value for ITER simulations: D =0.3 s/m^2. For this first scenario study, it has was chosen to keep all the transport parameters uniform over the entire plasma section. Simulations are performed with no drift included. Neutral species included in Eirene are atomic and molecular deuterium and impurities if seeding is inserted.

The scope of those simulations is determining the maximum amount of input power that can be transported from the core to the external wall, without exceeding the current maximum

Parameter	Value
R	2.11 m
a	0.64 m
R/a	3.3
Volume	29 m^3
q_{95}	3
I_P	5.5 MA
B_T	6.0 T
H_{98}	1
P_{in}	45 MW
$\langle n_e \rangle_{sep}$	$8 \times 10^{19} \mathrm{m}^{-3}$
λ_q	$\simeq$1 mm

Table 4.3: DTT full-power single-null scenario parameters. The scenario was later modified increasing the major radius to 2.19 m, the influence on power exhaust and power handling is negligible.

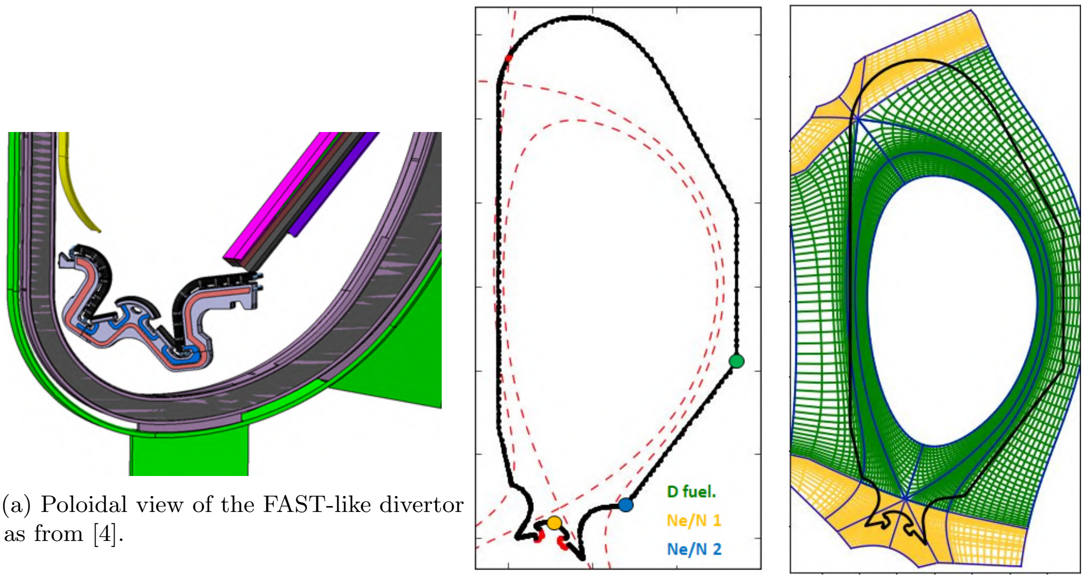

(a) Poloidal view of the FAST-like divertor as from [4].

(b) First wall; dots represent puff. locations, abs. surfaces are red.

(c) SOLEDGE2D-EIRENE grid; penalization technique extend it to the wall.

Figure 4.15: DTT divertor and first wall poloidal view as in the project and as simulated.

technological limit for tungsten divertor in steady-state conditions: 10 MW/m^2. They are also used as preliminary runs for seeded simulations. Puffing is set to 1.5×10^{22}D/s and albedo is adjusted to obtain the reference separatrix density: $\langle n_e \rangle_{sep} = 8.0 \times 10^{19} m^{-3}$. It was chosen to not use fixed albedo because one of the scopes of this project was to assess the requirement for divertor pumping, in doing so, using different pumping regimes is preferable; the same choice was made in the runs described in section 4.2.2.

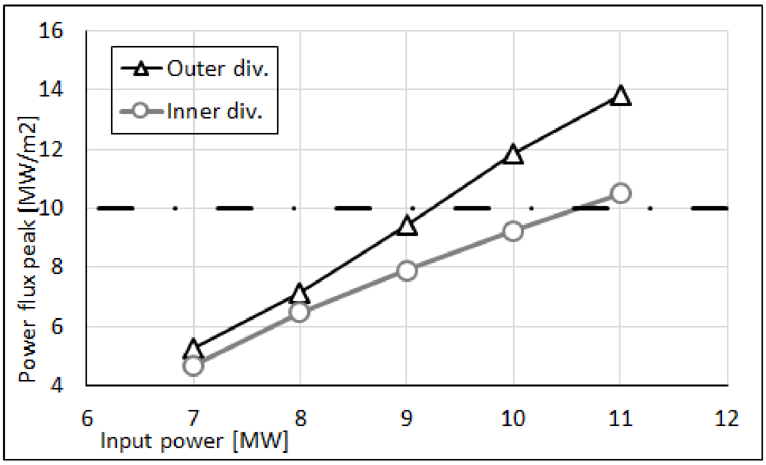

Figure 4.16: Maximum power flux to the outer and inner divertor in the input energy scan of D-only simulations. The imbalance between inner and outer target is caused by the different connection length to the inner and outer divertor.

Figure 4.16 shows the maximum power flux at the targets obtained in the P$_{sol}$ scan in pure deuterium. Results show the typical in-balance between inner and outer divertor power load, the latter always presenting higher power flux. For this reason, in this work, "attached" and "detached" conditions refer to the condition of the outer divertor plasma. Approximately 9 MW is the maximum input power that provides sustainable conditions at the outer divertor thus implying that, in the 45 MW reference scenario, the minimum radiated power to achieve a detached state is about 36 MW, corresponding to a radiated fraction of 80%, implying that this scenario can only operate in high radiation regimes.

Modelling with impurity seeding

Nitrogen and neon were tested as seeded impurities in the 45 MW scenario. Since SOLEDGE2D-EIRENE mesh is extended only a few cms inside the separatrix, the input power was set to 36 MW, assuming 9 MW radiated in the core. Deuterium puffing was kept constant ($\Gamma_D = 6.0 \times 10^{22}$D/s) while neon and nitrogen puffing rates were varied to compare Ne and N radiative cooling. Absorbing surface albedo was varied to match the scenario $\langle n_e \rangle_{sep}$.

Figure 4.17 shows the maximum power deposited to the outer target and the maximum temperature at the outer target in N and Ne cases. Results show that a certain degree of detachment can be achieved[2]. Figure 4.17 shows that sustainable conditions at the outer

---

[2] We do not discuss the most accurate definition of detachment or detachment degree [83]; in this case, we

divertor can be obtained with reasonable $\langle Z_{\mathrm{eff}}\rangle_{\mathrm{sep}}$, but also that with neon seeding lower $\langle Z_{\mathrm{eff}}\rangle_{\mathrm{sep}}$ is needed due to its higher cooling rate at high temperatures, see figure 4.18. With nitrogen seeding, a lower temperature can be achieved due to its higher cooling rate at low temperatures. The difference between neon and nitrogen performances is even larger when considering a fixed P_{aux}, in that case, $P_{In,N} > P_{In,Ne}$ since neon radiates more in the core; the same P_{In} was used in this study to avoid any further assumption. Higher radiated power fractions are radiated in neon cases than nitrogen cases, similarly to what was found in recent modelling on ASDEX-upgrade and ITER [84].

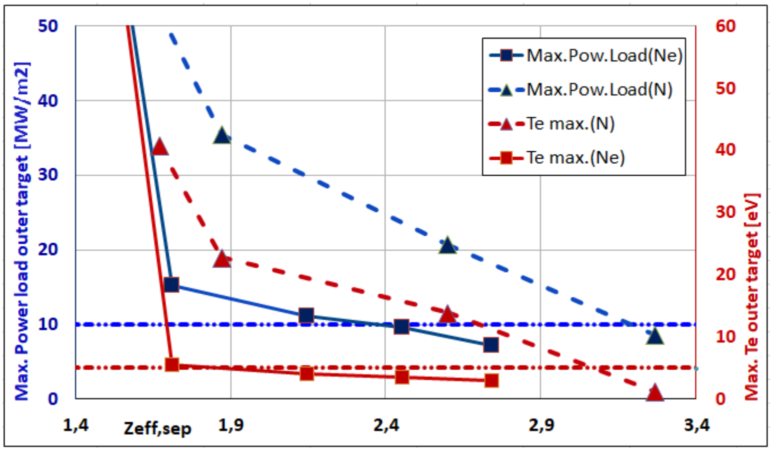

Figure 4.17: Maximum power deposit to and maximum electron temperature at the outer target in simulations using nitrogen or neon as seeded impurity.

Neutral pressure at the two main pumping system entrances present similar behaviours in all the above mentioned cases and do not depend on the seeded impurity but on detachment level only, better description will be given in the next section. Plasma and neutral distribution in the private region in the attached and detached scenario is fundamental for pumping system design.

The total power flux to the wall includes the radiative contribution; it contributes from 40% of the power flux to the divertor with deep detachment, to be irrelevant when plasma attaches.

An attached and a detached case (the first and last point in figure 4.17) were also modelled with neon seeding from the secondary seeding location. The output showed no sensible difference in terms of radiated power, impurity penetration, or power deposition when compared to the previous simulations where seeding was done from the dome. No preferential puffing location was found.

---

refer to it as the sudden drop of temperature and power flux caused by impurity radiation as the one shown in figure 4.17

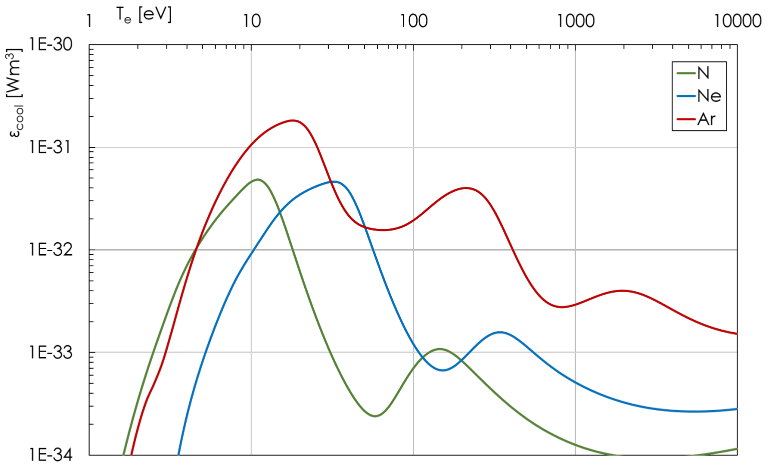

Figure 4.18: Cooling rates by different impurities as function of electron temperature; curves are calculated by using rate coefficients from coronal equilibrium of atomic reactions in ADAS database[2].

4.2.3 Modelling with validated transport parameters

In this section, the modelling of DTT with validated transport parameters is described. First the assumption of the modelling is described as well as the attempt to perform the edge modelling coherently with ongoing core and pedestal modelling; then, the effect of possibly uncertainty on transport parameters (described in chapter 3.1.6) are tested in DTT; the absolute performances of the FAST-like divertor are tested with neon and argon to compare the two impurities; lastly, the effect on power exhaust of possible divertor geometries is studied.

For this modelling activity, the last equilibrium for DTT single null full power scenario was used. The main difference with the equilibrium used in section 4.2.2 is that the major radius is increased to $R = 2.19$ (4% difference with respect to the previous equilibrium), no relevant difference on connection length or other power-exhaust-relevant parameters are found. Main plasma parameters of this equilibrium are listed in tables 3.1 and 3.3.

Modelling concept

The modelling activity with validated transport parameters is included in a more general modelling work whose aim is to obtain a coherent integrated core-pedestal-edge modelling. The coherency with pedestal modelling of plasma profiles obtained with validated transport parameters was already discussed in section 3.1.6. From the outcome of the modelling activity of section 4.2.2, it was chosen to set the pedestal density of the scenario to $\langle \mathrm{n_e} \rangle_{\mathrm{sep}} = 8.0 \times 10^{19} \mathrm{m}^{-3}$ which is a good compromise in order to obtain detached divertor plasma with reasonable impurity concentration.

Core modelling performed with JETTO[55] provides to edge modelling many input parameters as the integral of the particle flux from NBI absorbed by the plasma, which is shown as a function of the flux coordinated ρ in figure 4.19. Core modelling coupled with EPED profiles provided the transport parameters that were compared to those obtained with edge modelling. Lastly, it is possible to estimate the power radiated inside the separatrix from core modelling.

Edge modelling provides to core modelling estimation of neutral penetration and of the impurity concentration required to obtain sustainable power flux to the divertor.

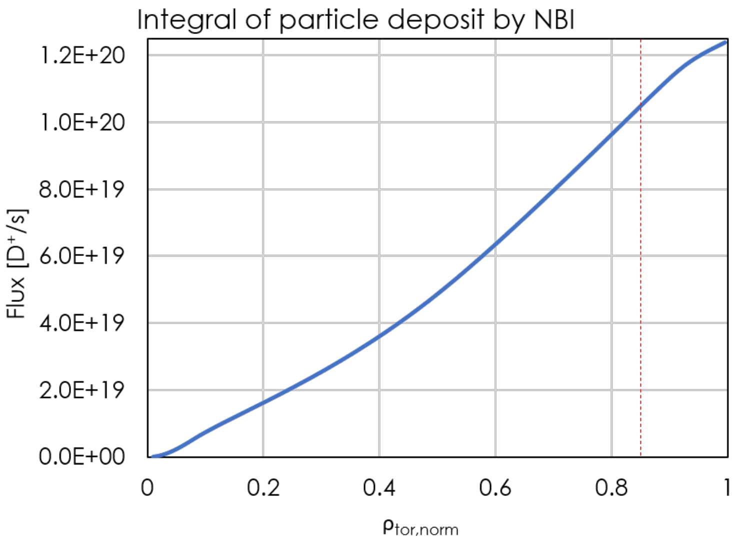

Figure 4.19: Integral of NBI particle deposition. The dashed red line represent the chosen SOLEDGE2D-EIRENE inner boundary flux coordinate, $\rho_{tor,norm} = 0.85$, where the inner boundary condition on flux particles is set $\Gamma_{D^+,in} = 1.05 \times 10^{20} D^+/s$

The estimation of power dissipation by impurity radiation within SOLEDGE2D-EIRENE depends on the considered scenario. It depends on the core concentration and on the element which is chosen as the main seeded impurity, it would also depend on divertor condition since tungsten concentration depends on sputtering which is highly influenced by divertor temperatures, tungsten sputtering is also influenced by the atomic number of the seeded impurity [85][86]. From available core-modelling results, 10 MW are estimated to be radiated inside SOLEDGE2D-EIRENE inner boundary which is set at $\rho_{torn,norm} = 0.85$ with the upper mentioned $\langle \mathrm{n_e} \rangle_{\mathrm{sep}}$ and $\langle \mathrm{Z_{eff}} \rangle_{\mathrm{sep}} \sim 2$ which is within the operative range of the machine.

An estimation of power dissipation by ELMs is still to be made for DTT. Generally, the power increasing the diamagnetic energy increases with the input power as it was found in chapter 3.2 and 3.1. It is also expected that the power should scale with the volume of the machine. For these reasons, it was assumed $P_{ELM} = 6\,\mathrm{MW}$, a better estimation will be made when modelling is available. According to equation 3.1, the nominal 45 MW of input power and the previous assumptions, on P_{ELM} and $P_{rad,in}$, the input power at SOLEDGE2D-EIRENE inner boundary is fixed to $P_{in} = 29\,\mathrm{MW}$ and will be the power input parameter used in all seeded cases, when deuterium-only runs are performed, the input power will be specified.

The grid was optimized so to obtain reasonable computational time and adequate spatial resolution (figure 4.20a). In figure 4.20c, shows typical grid radial extension at outer mid-plane with respect to the expected λ_q, density and temperature decay length are always larger [11]. Figure 4.20d shows the grid at the outer mid-plane, the length of the wall section where the grid is kept parallel to the wall is larger than four times the projection on the target along the magnetic surfaces of the predicted λ_q at mid-plane.

The space between the separatrix and the first wall on the low field side is reduced by the larger major radius of this scenario. The opening is still larger than three times longer than the density decay length in the SOL λ_n, so neutral flux outside the separatrix is still allowed even if reduced to that relative from the older equilibrium.

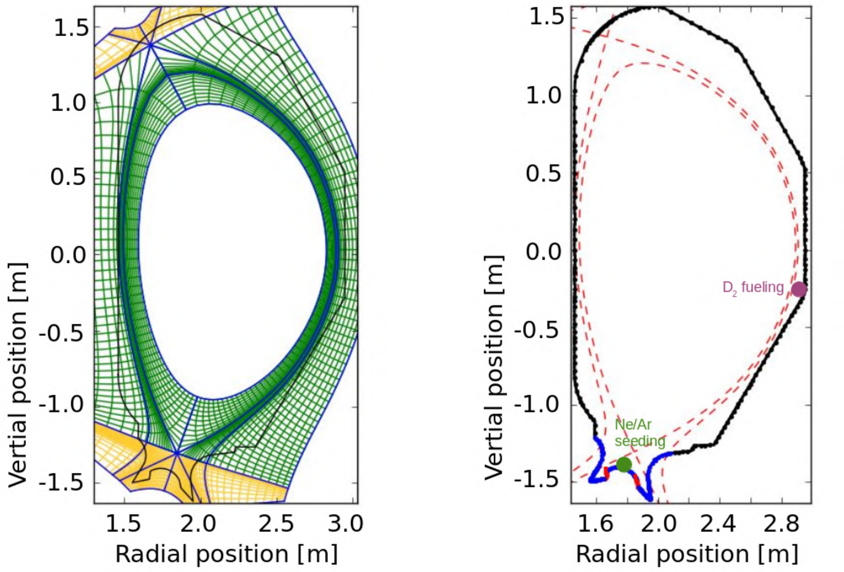

(a) SOLEDGE2D-EIRENE grid for DTT $R = 2.19$ SN equilibrium

(b) Pump surfaces and chosen fueling and seeding locations.

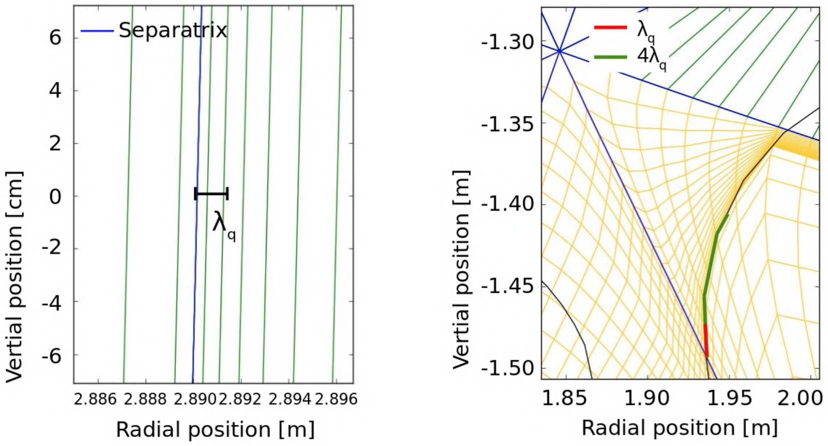

(c) Detail of outer mid-plane grid with respect to λ_q

(d) Detail of outer strike point grid with respect to λ_q

Figure 4.20: DTT grid and details

Optimization of puffing location

Figure 4.20b shows the pumping surfaces (red) and the puffing locations. Deuterium puffing is located at the outer mid-plane to optimize neutral penetrations, impurity seeding is made from the dome. A high neutral flux at the separatrix is required to sustain the pedestal (see [55]), edge modelling can compare different puffing locations, estimate neutral penetration and find the optimal puffing location. Starting from an attached D-only simulation with $\langle n_e \rangle_{sep} = 8.0 \times 10^{19} m^{-3}$ a scan on fueling rate was made from the high-field-side (HFS) and from the low-field-side (LFS). Figure 4.21 shows the estimated neutral penetration obtained when D_2 fueling is made from the LFS and the HFS. The picture also shows the linear fit of the two sets of data, the known term of the fits corresponds to the neutral flux given by recycling which is compatible between the two scans as it should be. LFS fueling clearly shows an advantage with a neutral penetration of 13% compared to the 3.6% of HFS fueling. Fueling from LFS also has the technological advantage of not requiring duct extension close to the central solenoid.

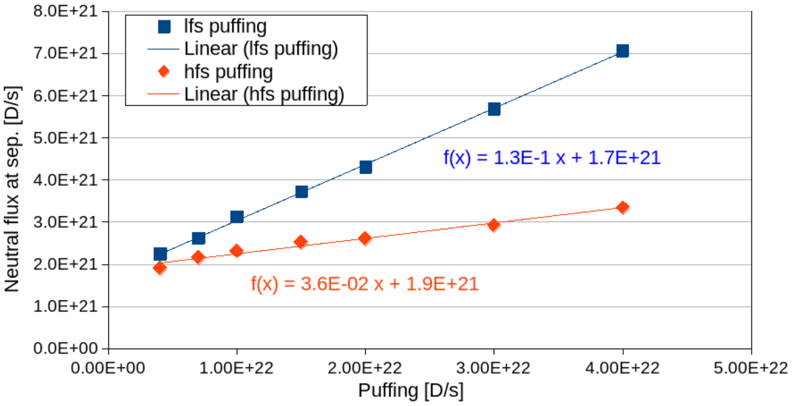

Figure 4.21: Neutral penetration across the separatrix when puffing is made from the low field-side or from the high field side, 13% of puffed particles cross the separatrix as neutral in the first case, only 3.6% in the second case; the flux of recycled particles is about 1.8×10^{21}D/s.

Effects of transport parameter variations

First, the effect of possible variations of transport parameters is studied. As discussed in section 3.1, one of the main uncertainty on transport parameters is the extension of pedestal parameters to the near-SOL. To produce plasma profiles that respect Eich scaling, it is necessary to extend the pedestal value of χ to the near-SOL. If far-SOL transport parameters were applied to the near-SOL, λ_q would be increased to several millimetres as in [63]. There is no scaling of particle decay length λ_D, so a parametric scan is needed to determine the effect of possible parameter variations. For this runs, a deuterium only simulations was used, the puffing was adjusted to so obtain $\langle n_e \rangle_{sep} = 5.0 \times 10^{19} m^{-3}$, the input power was fixed $P_{in} = 6.0\,\text{MW}$.

Figure 4.22a shows the transport parameter profiles that were used in this parametric scan; $D_{near-SOL}$ goes from 0.01 to 0.08 m^2/s, scanning over almost one order of magnitude. Figure 4.22b shows the electron density radial profiles at the outer mid-plane, while figures 4.22c and 4.22d show the outer target density and temperature. At the targets, two opposite effects take place when transport is reduced in the near-SOL. On one hand, particle transport reduction peaks particles profiles, tightening and increasing density profiles and recycling; on the other hand, the lower particle diffusion coefficient reduces the pseudo-convective term $(\Gamma_q, q-c)$ of the energy equation:

$$\Gamma q, q - c \propto D, \tag{4.10}$$

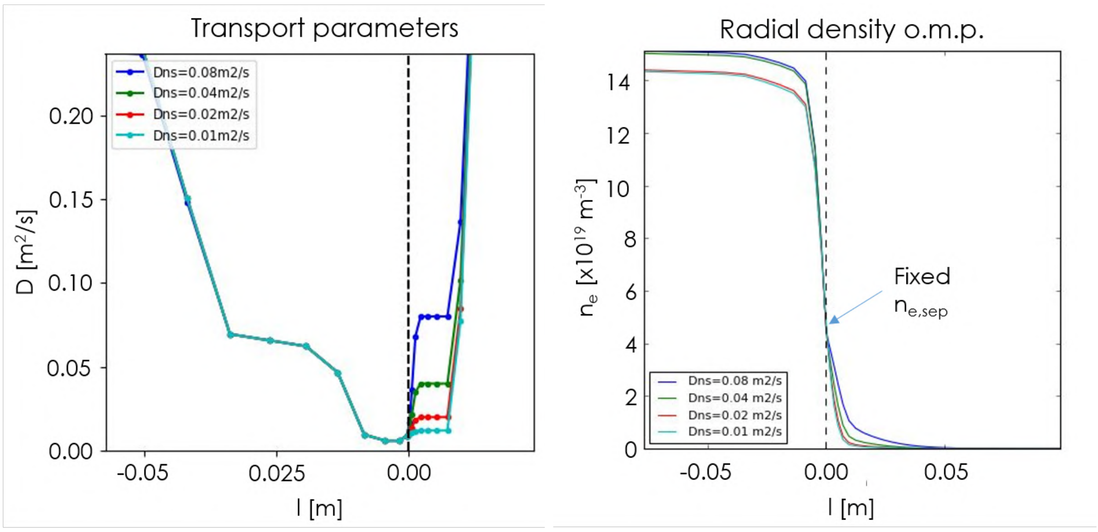

(a) Transport parameter

(b) Radial density profile

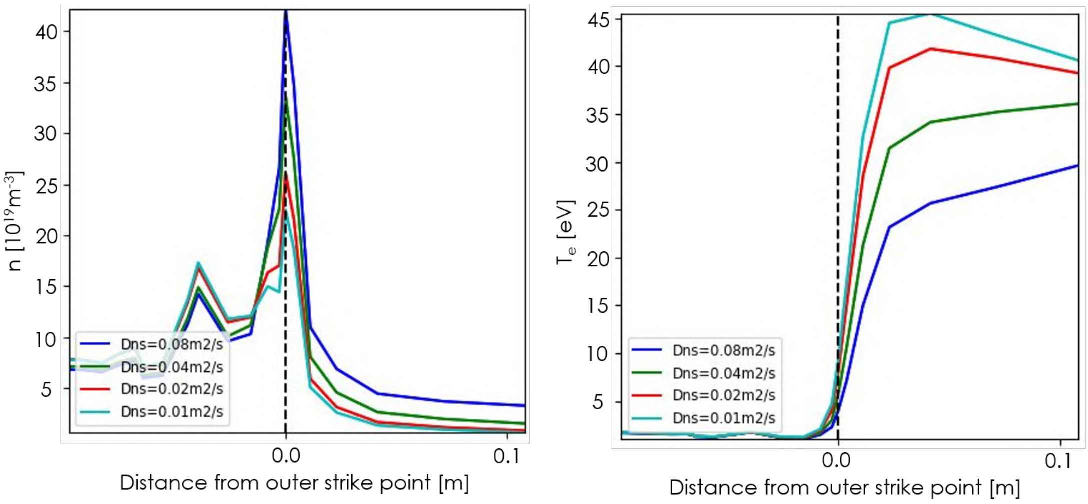

(c) Outer strike point density

(d) Outer strike point temperature

Figure 4.22: Near-SOL transport parameter scan. The case with lower D_{SOL} have higher target temperature, lower pumping and consequently lower puffing and pedestal top density.

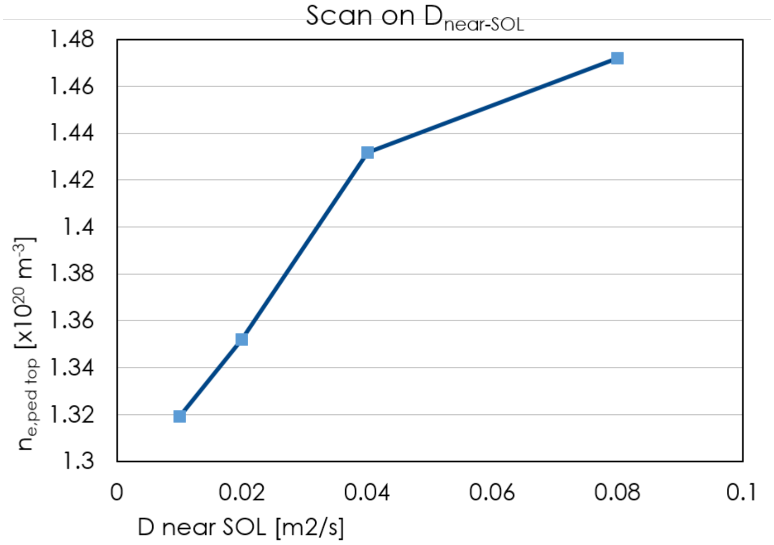

Figure 4.23: Density at pedestal top as function of particle transport parameter at near-SOL

energy flux profiles are tightened, the temperature increased and the density reduced for pressure conservation. From figures 4.22c and 4.22d it is clear that the second effect is dominant and that the lowest the particle transport coefficient, the more attached divertor plasma is. The different temperatures at the divertor target, and the consequent temperatures at the pump ducts, influence pumping. In the most attached cases, particle pumping is reduced, lower fueling is required to obtain the same $\langle \mathrm{n_e} \rangle_{\mathrm{sep}}$ and a lower neutral penetration on pedestal top density is obtained. Only a 10% variation of neutral penetration and n_e, pt is observed in this scan (see figure 4.23 from which implies that in this case $\mathrm{D}_{near-SOL}$ variation effect is negligible.

The figures also show that a factor 8 on $\mathrm{D}_{near-sol}$ only produces a factor 2 difference in terms of temperature and density profiles at the target. This result can be interpreted as a figure of merit of the validity of the approximations that were made selecting transport profiles.

Comparison between neon and argon seeding

In section 4.2.2, a comparison was made between neon and nitrogen cooling effectiveness which resulted in the heavier impurity producing the best cooling performances. In this section, cooling performances of neon and argon were tested to understand whether it is still the heavier impurity that has the best cooling performances, or if vice-versa argon radiation is peaked inside the separatrix.

Impurity seeding was set up to obtain total power radiation in SOLEDGE2D-EIRENE domain equal to 27 and 28 MW for both neon and argon. In both neon and argon cases, the outer divertor is detached (total radiated fraction is about 95%).

Pumping speed is set to 100 m^3/s, the nominal designed pumping speed of DTT. If the pumping speed is correctly matched, there is a one-to-one correspondence between separatrix density and fueling. A good estimation of fueling corresponds to a good estimation of neutral penetration and consequently of pedestal-top density. SOLEDGE2D-EIRENE can not operate yet with a fixed pumping speed on impurities, an albedo must be fixed at the beginning of the simulation. The albedo for impurities on the pumping surfaces is adjusted so to obtain a pumping speed on impurity equal to $20\,\mathrm{m^3/s}$.

Simulation were performed with a fixed electron density. Also in these simulations $\langle \mathrm{n_e} \rangle_{\mathrm{sep}} = 8.0 \times 10^{19} \mathrm{m^{-3}}$. The applied methodology is the best to compare different impurity seeding (or different geometries as in the next chapter), since possible differences in terms of power exhaust can not be imputed to density, particle pumping or fueling. This method is also extremely time demanding due to the necessity of tuning fueling and seeding to match both the radiated power and the electron density.

The impurity concentration required to achieve the target radiation is much higher in neon case than in argon case both in the $P_{rad} = 27\,\mathrm{MW}$ and the $P_{rad} = 28\,\mathrm{MW}$ case. Figure 4.24a shows the total impurity density ($n_{imp,tot}$) calculated summing over all the ionization states of neon or argon. Figure 4.24b show the impurity concentration calculated as the ratio between $n_{imp,tot}$ and deuterium density. Impurity density profiles are flat inside the separatrix since impurity sources are null a few cms inside the separatrix. The contribution to electron density given by the impurities is still much higher for neon given that $n_{Ne,tot}/n_{Ar,tot} \sim 4.5$ and that argon atomic number is only 1.8 times bigger than neon. This is clear also in Z_{eff} profiles that are shown in figure 4.24c.

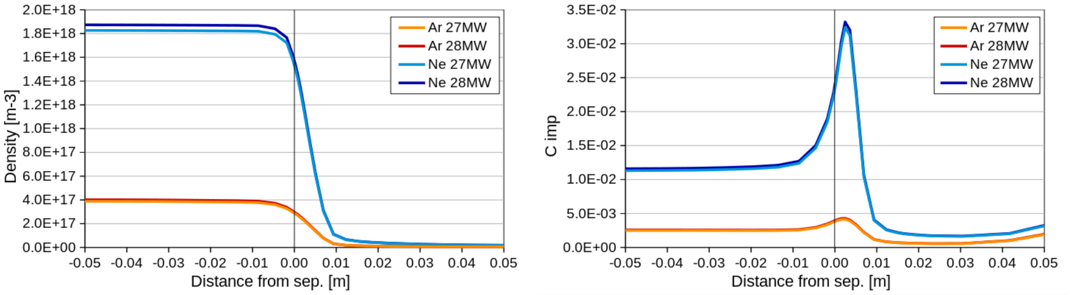

(a) Impurity density summed over all ionization state.

(b) Impurity concentration calculated as $n_{imp,tot}/n_D$.

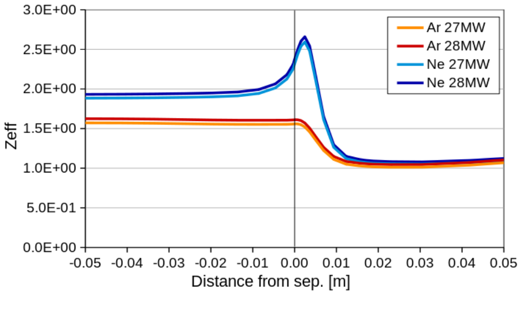

(c) Z_{eff} radial profile.

Figure 4.24: Impurity density concentration and Z_{eff} of neon and argon seeded simulations.

Analogously to section 4.2.2, it is found that the heavier impurity performs better in DTT conditions. This is not a general behaviour since impurity heavier than Ar (as for example Kr which is also considered for DEMO) could radiate mainly in the core reducing P_{SOL}, dedicated studies are needed. Ar cooling efficiency (figure 4.40) is not only higher in the temperature range typical of the core and the pedestal, but is also higher in the 1 to 20 eV range, this is why argon seeded case can radiate more close to the divertor target (figures 4.26c and 4.26d). The higher neon density required to reach the target density over-compensates the lower cooling efficiency of neon at the pedestal temperature of the pedestal and within the pedestal; consequently, the total power radiated by neon inside the separatrix is 8.2 MW while the power radiated in the argon seeded case is 5.4 MW. This is also shown in the radiation map along the separatrix in figures 4.26a and 4.26b which is much higher in neon case.

Those data also prove that with both Ne and Ar there is an impurity concentration range within concentration is high enough to obtain detached conditions at the divertor and low enough to not lower the power crossing the separatrix below the L-H transition threshold. The radiated power within the separatrix is about 15 MW for argon and 18 MW for neon, corresponding to about 30 MW and 27 MW crossing the separatrix. The L-H transition required power is between 15 and 20 MW according to current scalings as shown in figure 4.25. This claim will be tested when other indication of power radiation in the core will be available or additional information on electron and ion input power sharing.

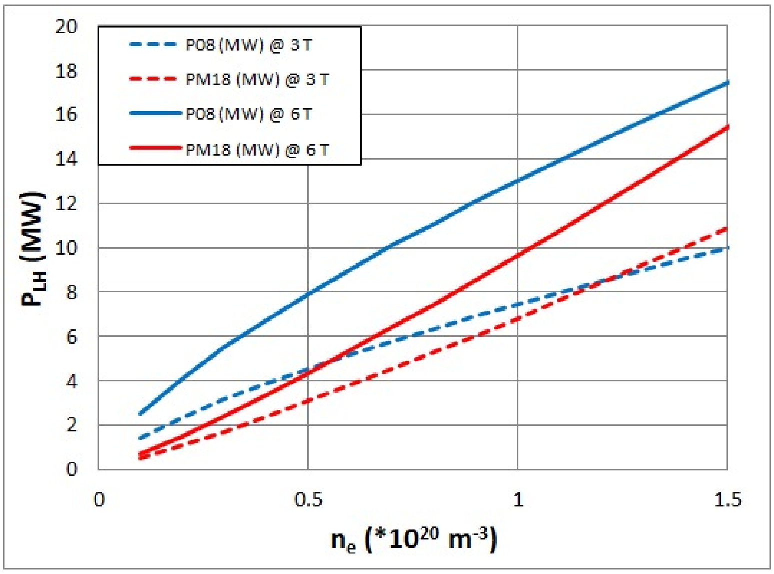

Figure 4.25: L-to-H transition threshold energy for DTT 3 T and 6 T scenario. Electron density refers to core average density which is assumed between $1.4 - 2.0 \times 10^{20}\text{m}^{-3}$

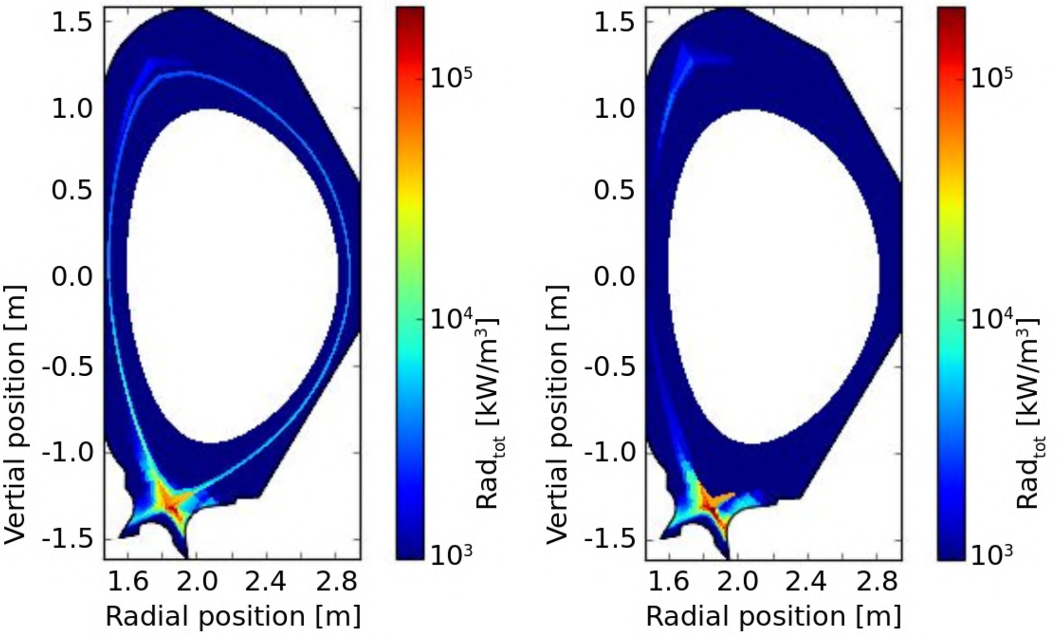

(a) Radiated power in neon seeded simulation with $P_{rad} = 28\,\mathrm{MW}$.

(b) Radiated power in argon seeded simulation with $P_{rad} = 28\,\mathrm{MW}$.

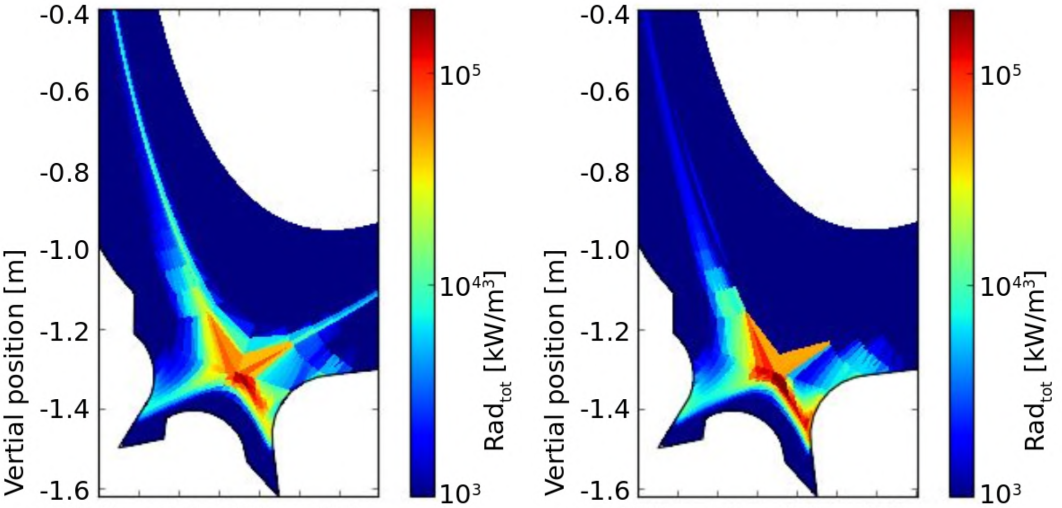

(c) X-point and divertor details of radiated power in neon seeded simulation with $P_{rad} = 28\,\mathrm{MW}$.

(d) X-point and divertor details of radiated power in argon seeded simulation with $P_{rad} = 28\,\mathrm{MW}$.

Figure 4.26: Radiation profile of neon and argon seeded simulations. The lower efficiency of neon requires higher impurity concentration than argon. Argon cooling rate is also much higher than neon in the 1 to 20 eV range (figure 4.40) and consequently has higher radiation close to the targets. The required neon density is much higher than argon that overcompensates the lack of cooling efficiency in the pedestal volume.

Divertor geometry influence on cooling and power load in DTT

In this section, the influence of divertor geometry on detachment onset in SN full-power DTT scenario is investigated. DTT first divertor design has not been finalized yet, it has already been decided that it will be made of tungsten monoblocks as in ITER. This work aims to test the effect of possible divertor geometry on power exhaust and impurity concentration required to obtain detached divertor plasma.

Divertor geometry has been proven to play a significant role in divertor plasma detachment in many existing machines, as for example DIII-D [87], JT-60U [88] and TCV [89]. The divertor geometry affects divertor neutral pressure, impurity content required for the detachment onset and maximum input power that allows detached condition at the divertor.

One of the main divertor geometrical characteristics is the connection length (L_c) between the mid-plane and the divertor. The 2-point-model (section 2.1.2) predicts the divertor plasma temperature to scale with a factor proportional to $L_c^{4/7}$ in deuterium-only plasmas. In seeded plasmas, temperature reduction may lead to an increase of seeded impurity cooling efficiency; the effect of divertor leg on detachment may scale with a higher power, although this must be evaluated case-by-case and impurity-by-impurity. Many different divertor plasma configurations such as the snowflake, X and Super-X divertor are studied to increase the connection length and favour detachment onset. With a fixed SN scenario, the connection length is limited by machine dimension and scenario characteristics, a limited range of connection lengths can be tested.

The principal effect of a closed divertor is to increase neutral compression in the divertor volume. The compression is mainly caused by the emission angle of recycled particles. As shown in figure 4.27. In a closed divertor configuration, recycled particles are emitted mostly towards the private region, while in open geometries a higher fraction of particles is recycled towards the main plasma. In standard divertor configurations, divertor closure is characterized by the angle β between the projection of the inner divertor leg and the divertor wall itself, the smaller β, the higher the divertor closure.

Recently in DIII-D an extremely closed divertor configuration, the small angle slot (SAS) divertor was conceptualized and successfully experimented with. This geometrical configuration guarantees sensible advantages in terms of power exhaust [90] [91] [92].

Limits to the divertor closure are posed by the technology that is used for the PFC and the engineering solutions required. First, the shaping of tungsten monoblocks has a lower limited curvature radius that limits possible divertor shaping [93]. Secondly, keeping constant all other parameters, a reduction of divertor aperture leads to a reduction of the grazing angle. The grazing angle is defined as the angle of impact between the magnetic field line and the target surface:

$$\alpha = \tan^{-1}\left(B_\theta / B_\varphi\right). \tag{4.11}$$

The Grazing angle can not be arbitrarily reduced, when grazing angle is reduced much below 3°, monoblock leading edges can be exposed to severe power fluxes and subsequent melting. In this case, the tilting of the monoblock is required, thus reducing the plasma wetted area. ITER operative grazing angle will be between $3 - 4.5°$ [94][95][96]. A higher divertor closure keeping the grazing angle constant is obtained by setting the wall farther away from the X-point, compatibly to the geometrical constraints of the vessel.

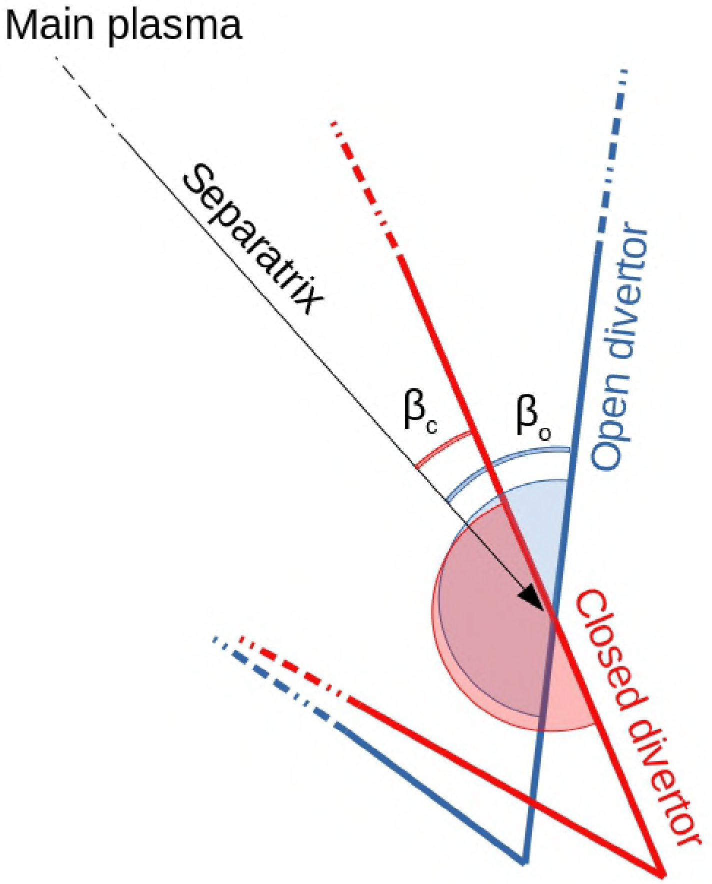

Figure 4.27: Sketch of the effect of divertor aperture: the black arrow represent the separatrix, and the two semicircles represent an approximation of the angular reflection probability of recycled particles on the wall, the blue and the red one representing the open and closed divertor case; β_c and β_o are the divertor aperture of the closed and open divertor respectively.

A scan was made on realistic divertor configurations for DTT, taking into account the above mention geometrical limits, with the scope of understanding the influence of realistic geometries on detachment onset. Geometrical characteristics of considered outer divertor geometries are listed in table 4.4. The scan has only been performed for the outer divertor since it is usually the most challenging in terms of power exhaust due to the usual position of the stagnation point that usually leads to approximately 2/3 of power crossing the separatrix to flow to the outer divertor and 1/3 to the inner one [11]. This asymmetry was also found in DTT in section 4.2.2 and in [97]. In work, in all of the considered geometries, the inner target is always detached when the outer target detaches. The inner target is similar to the FAST-like divertor geometry and has a grazing angle of 2°.

The following outer divertor geometries were defined according to two different needs: first, the inner side of the divertor target has to be at least within 6 cm from DTT vessel; secondly, a scan on grazing angle and divertor is performed. Three grazing angles were selected: $\alpha \simeq 1, 2, 3°$, as well as three divertor apertures: $\beta \simeq 19, 26, 34°$ and are labelled with an increasing number with the increasing divertor aperture and grazing angle as in table 4.4. The considered geometries which are shown in figure 4.28 have different connection lengths which are also listed in table 4.4. Geometry #3 was not simulated since an open divertor with $\alpha = 3°$ would have had an extremely short outer divertor and consequent disadvantages in terms of power handling. Geometry #7 has a divertor aperture $\beta = 23°$ to not exceed the boundary given by DTT vessel; a divertor with $\alpha = 3°$ and $\beta 19$ would have not fit into the vessel.

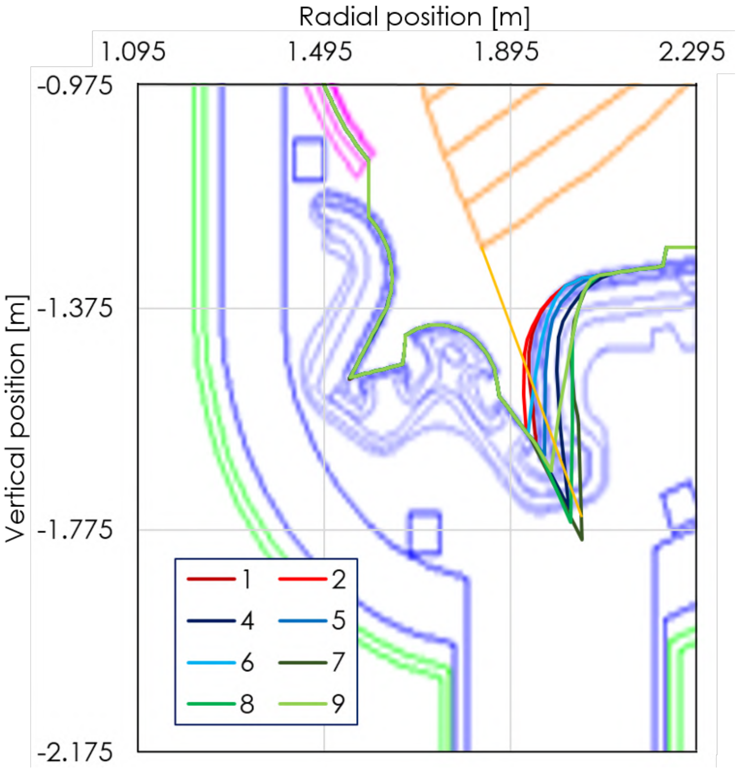

Figure 4.28: Considered divertor geometries and main DTT components such as vessel and magnetic coils.

Geom #	Pol. ang. [deg]	Graz. ang. [deg]	Conn. l [m]
1	19	1.1	21.1
2	26	1.1	20.7
3	-	-	-
4	19	2.0	23.5
5	26	2.0	22.3
6	34	2.1	21.6
7	23	2.9	24.4
8	26	3.0	24.0
9	34	3.0	22.9

Table 4.4: Characteristics of considered geometries. The connection length is calculated from the point 0.5 mm out of the separatrix at the outer mid-plane to the outer divertor target.

First, the eight geometries were tested in deuterium-only simulations, then impurity seeding was added. In full-power seeded simulations, the influence of different geometries is evaluated in detached conditions.

The geometries were first tested in deuterium-only cases with $P_{in} = 8\,\mathrm{MW}$, fixed pumping speed $v_p = 100\,\mathrm{m}^3/\mathrm{s}$; fueling was tuned to obtained $\langle \mathrm{n_e} \rangle_{\mathrm{sep}} = 8.0 \times 10^{19}\mathrm{m}^{-3}$ as in figure 4.29a. The effect of divertor closure can be estimated by studying the three geometries with grazing angle $\alpha \simeq 2$. Figures 4.29b-4.29d show that the most closed divertor (geometry #4) is detached while the most open divertors (geometry #5 and #6) are completely attached.

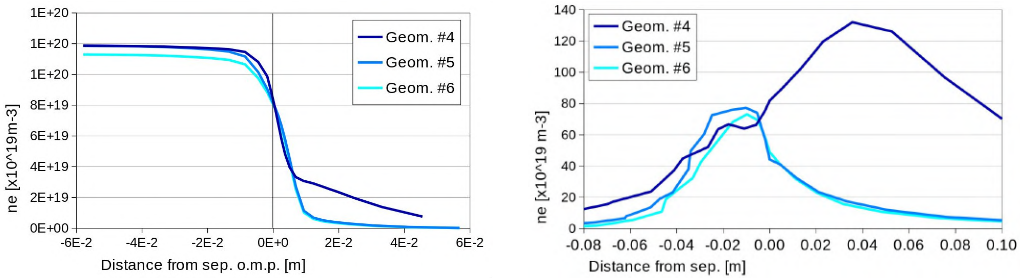

(a) Radial density profile at mid-plane.
(b) Electron density at outer divertor.

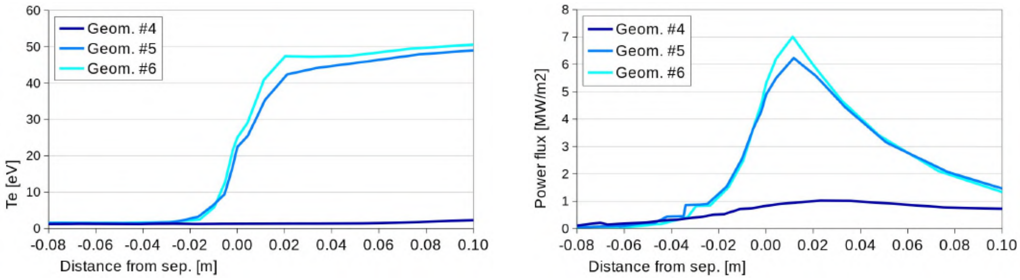

(c) Electron temperature at outer divertor.
(d) Power flux to the outer divertor.

Figure 4.29: Test of the three geometries with grazing angle $\alpha \simeq 2$ and different divertor closure: $\beta \simeq 19°, 26°, 34°$ for geometry #4, #5 and #6 respectively.

Closed divertor geometries also have longer connection lengths but connection length extension is responsible for only a fraction of the target temperature drop. With the 2-point model (section 2.1.2) it is possible to estimate the impact of the different connection lengths on the target temperature. According to the model, divertor temperature scales with $l^{-4/7}$, since no other parameter relevant to the 2-point model is different in the two simulations, the electron temperature drop at the target between geometry #6 and #5 given by the different connection lengths can be calculated as:

$$\Delta T = T_{\#6} - \left(\frac{l_{\#5}}{l_{\#6}}\right)^{-4/7} T_{\#6} = 0.02 T_{\#6} = 1\,\mathrm{eV}. \tag{4.12}$$

Equation 4.12 shows that, according to the 2-point model, the different connection length between geometry #6 and #5 is only 1.0 eV while the observed temperature difference is about 8 eV. Furthermore, the most closed geometry (#4) is completely detached.

To further stress the claim that that divertor closure is responsible for the temperature and power deposition drop observed in section figures 4.30a and 4.30b, two geometries with similar connection lengths and different divertor closure (and consequently different grazing angle) were compared, namely geometry #1 and #6. Again, it is evident that the higher the divertor closure, the lower the divertor temperature, the higher the divertor neutral pressure.

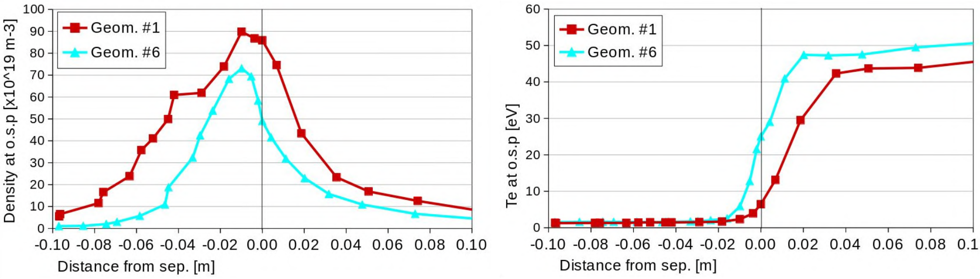

(a) Electron density at the outer target. (b) Electron temperature at the outer target.

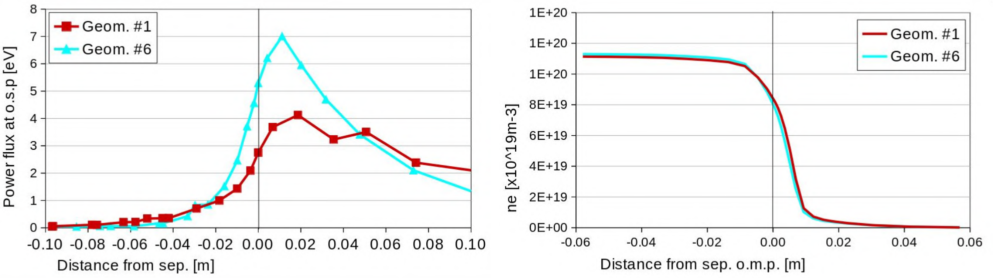

(c) Power deposition to the outer target. (d) Radial electron density profile at mid-plain.

Figure 4.30: Test of two geometries with similar connection length and different divertor aperture: $\beta = 19°$ for geometry #1 and $\beta = 34°$ for geometry #6. The two geometries also have different grazing angles, but this only impacts power deposition estimation.

After proving the effectiveness of the divertor closure in D-only cases, the effect of divertor geometries was tested with impurity seeding; neon was chosen as seeding impurity. Nitrogen was excluded because of the low DEMO relevance and argon was excluded for numerical reasons since it requires almost double the number of simulated species than neon.

The modelling concept with impurity seeding is the following. The input power is set to 29 MW as previously motivated, for simplicity the power is equally shared between electrons and ions. Since electron density at SOLEDGE2D-EIRENE inner boundary is higher than ion density, more sophisticated modelling would require unbalancing the input power share between electrons and ions to obtain the same temperature at the pedestal top. The simplistic assumption that was taken does not impact the comparison of different geometries.

All simulations started from attached conditions for reasons that will be explained in section 4.3; neon puffing is then slowly increased until detachment is reached. Once detachment is reached, different impurity radiation levels are simulated with each geometry. This methodology allows to obtain information on how much:

- divertor geometry affects the impurity concentration required to achieve detachment;
- divertor geometry affects impurity concentration in high radiation cases;
- divertor geometry affects impurity concentration in low radiation cases;
- is enrichment affected.

Using this methodology, when detachment is achieved, modelling is not steady-state, so the outcome may be slightly influenced by the velocity impurity seeding is increased in each simulation and by the peculiarly of each run, a margin of error must be considered when analysing the outcome of such simulations. To mitigate the cause of such uncertainty, neon seeding is increased very slowly to the run-time of the simulations, taking into account the typical penetration time of impurity in the pedestal:

$$\tau = \frac{(\Delta r)^2}{D} \approx 0.05\text{s} \tag{4.13}$$

where Δr is the radial distance across the magnetic surfaces and D is the particle transport parameter. The simulation run-time before detachment was reached after several second decimals in every geometry simulated.

Figure 4.31 shows the impurity concentration c_z at the pedestal top required to achieve detachment at the outer target. It must be stressed again that simulations were not steady-state at the detachment onset and that there are minor density differences within the runs. Impurity concentration was calculated as the ratio between neon and deuterium density at $\rho = 0.9$ surface (pedestal top):

$$c_z = \left\langle \frac{n_{Ne}}{n_D} \right\rangle_{\rho_{tor,norm}=0.9}, \tag{4.14}$$

this value was used as the figure of merit to compare the effect of divertor geometry on power exhaust and neutral compression.

Figure 4.31a shows the concentration required for detachment onset of each geometry; geometries are also grouped by grazing angle (same color scheme used in figure 4.28) and by divertor aperture angle. Neon concentrations are plotted in figure 4.31b, the figure shows a clear dependence of impurity concentration on connection length, with a 50% drop in minimum impurity concentration, proving the crucial role of connection length on detachment onset in seeded plasmas. It is thus crucial for the divertor geometry and/or the magnetic configuration to maximize the connection length to the outer target.

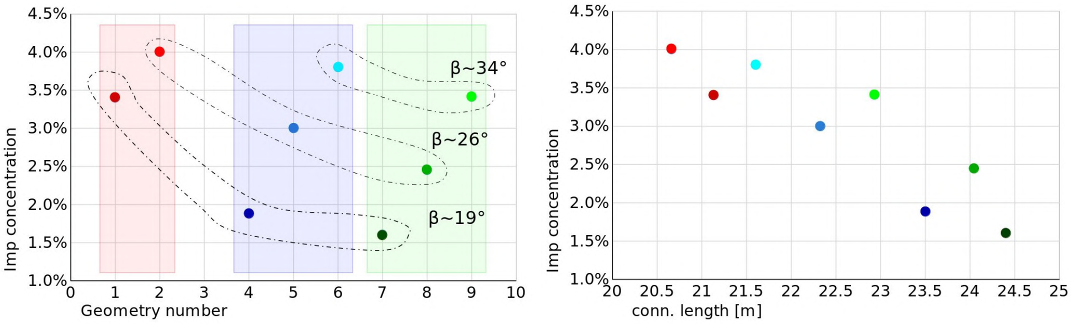

(a) Neon concentration at the pedestal top required to achieve detachment in each of the considered divertor geometry. AS in table 4.4 red, blue and green represent grazing angle of 1,2 and 3° respectively, divertor aperture indicated.

(b) Neon concentration at the pedestal top required to achieve detachment as function of divertor connection length. Connection length correlates with the required impurity concentration. Color scheme is the same used in figure 4.31a.

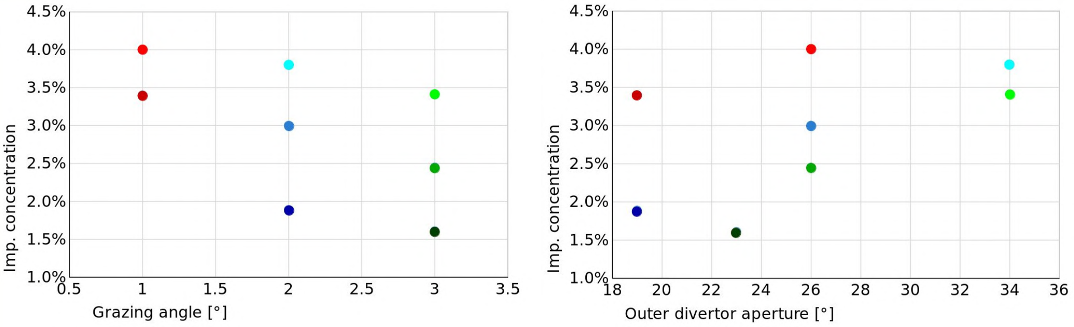

(c) Neon concentration at the pedestal top required to achieve detachment plotted with respect to the grazing angle.

(d) Neon concentration at the pedestal top required to achieve detachment plotted with respect to the divertor aperture.

Figure 4.31: Impact of divertor geometry on the concentration required for detachment onset, the same color scheme used in figure 4.28 was used.

Figure 4.31d shows that more closed divertor require lower impurity concentration to detach, although the effect given by the connection length must be taken into account. The decrease of minimum impurity concentration given by divertor closure can be deduced by comparing geometries with equal connection lengths: geometry #1 has a lower minimum impurity concentration than geometry #6, the same can be said for geometry #4 and #8. Divertor closure clearly plays a role in detachment onset, although slightly marginal compared to connection length.

On the contrary, grazing angle plays no role in detachment onset as is expected. As shown in figures 4.31c: the general lowering of concentration with the increasing of grazing angle is given by the longer connection length of higher grazing angle geometries. The only role of grazing angle is that of mitigating the power per area of surface, mainly in attached conditions. As previously discussed, the power deposition reduction given by a low grazing angle, is not straightforward since a lower grazing angle can lead to hot-spot melting and possible requirement of tilting of the tungsten tiles, which increases the grazing angle. In principle, If detachment is never lost the machine could work with arbitrarily low grazing angle due to the low power deposition by particles.

The scaling given by Goldston for divertor detachment[83][98], predicts the nitrogen concentration required to achieve detachment in a given machine:

$$c_N^{scaling} = \frac{1}{18.3} \frac{P_{sep}\,[MW]}{\langle B_p \rangle\,[T]\,(1+k^2)^{3/2}\, f_{GW,sep}^2} \times 4.0\,[\%] \tag{4.15}$$

In the scaling derivation, it is assumed that divertor plasma is not deeply detached[3]); scaling predictions can be compared to the result obtained with SOLEDGE2D-EIRENE modelling. To calculate the neon concentration required to achieve detachment according to Goldston, it needs to multiply the calculated c_N by a factor which is the ratio between the integrals of the cooling efficiencies of neon and nitrogen:

$$c_{Ne} = \frac{\int_{T_{tar}}^{T_{sep}} T_e \varepsilon_{Ne}}{\int_{T_{tar}}^{T_{sep}} T_e \varepsilon_N} c_N, \tag{4.16}$$

where $\varepsilon_{N/Ne}$ is the cooling efficiency of nitrogen/neon. Goldston scaling predicts $c_{Ne} \simeq 3\%$ which is in good agreement with the results found with SOLEDGE2D-EIRENE modelling. With longer and more closed divertors, the required concentration is lower than that of the scaling, shorter and more open divertor have the worst performances. Goldston scaling does not take into account divertor leg length.

After detachment is achieved, simulations are driven to different level of radiation: $P_{rad} = 26, 27, 28\,\mathrm{MW}$. Sustainable divertor conditions could hardly be achieved with a lower radiated power fraction. This result is confirmed by modelling with impurity seeding, but it could also be derived from deuterium-only modelling with simple considerations: when outer divertor is detached, inner divertor is deeply detached, thus the power deposition by particles to the inner divertor is negligible; in deuterium-only modelling the maximum input power to obtain detached

---

[3] Pressure conservation is assumed to derive the scaling, the assumptions hold if divertor plasma is not completely detached (i.e. $T_e \gtrsim 4\,\mathrm{eV}$

outer divertor is about 6 MW which corresponds to about 4 MW flowing to the outer divertor, thus meaning that $\max(P_{in} - P_{rad}) \simeq 4\,\mathrm{MW}$.

Figures 4.32a and 4.32b show the impurity concentrations required to obtained $P_{rad} = 28\,\mathrm{MW}$ and $P_{rad} = 27\,\mathrm{MW}$ respectively. The figures show a weak dependence of impurity concentration on divertor geometry. In this scan, the geometries are extremely different in terms of divertor aperture and connection length. They were proved to play a major role in plasma detachment in D-only simulations; nevertheless, in seeded plasma, the impurity concentration required in the different geometries are within $10 - 15\%$ difference which is considered negligible. With geometry #2 and $P_{rad} = 27\,\mathrm{MW}$ is not shown because it was not possible to obtain a detached simulation for this scenario.

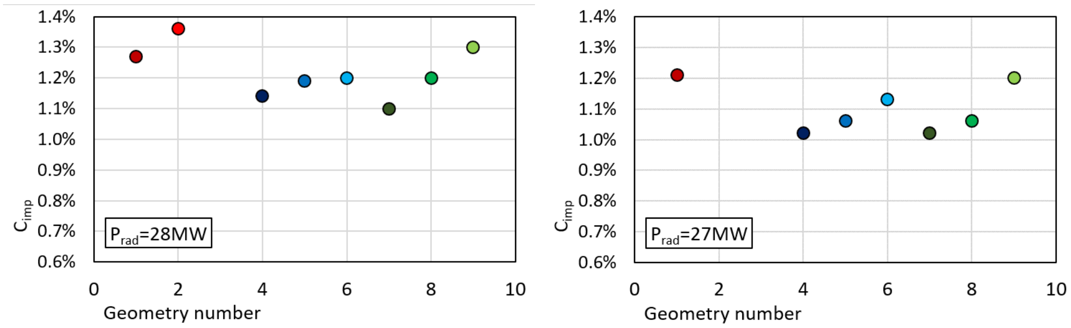

(a) Impurity concentration at the pedestal top for the scenario with $P_{rad} = 28\,\mathrm{MW}$.

(b) Impurity concentration at the pedestal top for the scenario with $P_{rad} = 28\,\mathrm{MW}$.

Figure 4.32: Impact of divertor geometry on impurity concentration

The weak dependence on divertor geometry can be explained considering that all the obtained scenarios are in deep detachment. The depth of the detachment generates a large low-temperature volume in front of the targets; in this volume, the neutrals are free to move and the enhancement on neutral compression given by divertor closure is lost. This behaviour is expected in all the scenarios in which there is strong X-point radiation and deep detachment. A graphical representation is given in figure 4.33 and 4.34 were the total radiation, electron temperature and neutral pressure of the scenario with $P_{rad} = 27\,\mathrm{MW}$ with geometry #6 and #4 are plotted. The electron temperature (figures 4.33b and 4.33b) shows that both the geometries are deeply detached. Since the radiation peaks at the X-point (figures 4.33a and 4.34a) and is lower close to the outer target, the connection length does not play a major role since the larger volume of geometry #7 is only partially exploited to radiate power. The consequence of the deep detachment is that neutral pressure is not affected by divertor closure as it would have been in an attached or partially detached scenario (figures 4.33c and 4.34c). Neutral compression in those deeply detached scenarios was mainly given by the upper component of the divertor that is indicated by the red arrow in figures 4.33c and 4.34c.

Lastly it can be observed that the neutral concentration is lower than that predicted by Goldston's scaling. This is given by the deep detachment state of the divertor plasma of these simulations. Goldston's scaling is valid until pressure is conserved along the magnetic field lines, this is not the case of these simulations that have a wide recombination zone in front of the targets where pressure is not conserved, plasma temperature is low and impurity cooling efficiency is high.

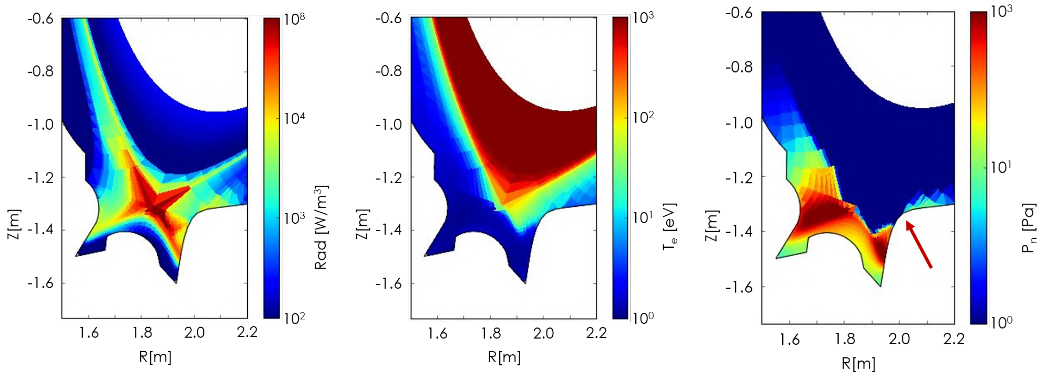

(a) Total radiation.

(b) Electron temperature.

(c) Neutral pressure.

Figure 4.33: Poloidal section of geometry #6 with $P_{rad} = 27\,\mathrm{MW}$

It was not possible to obtain partially detached scenario in which the role of divertor closure would have been more relevant, similarly to what was found in D-only simulations. A proof of this supposed behaviour is given by the impurity concentration that is required to detach the outer divertor plasma; in that case, moving from attached to detached divertor, connection length and divertor aperture were demonstrated to play a role. When I tried to obtained a partially detached simulation by reducing the impurity concentration the divertor plasma suddenly switched from deep detachment to attached. This is explained by considering the temperature dependence of neon cooling efficiency that generates a cascade effect: a lower neon concentration leads to the electron temperature increase that lowers neon cooling efficiency consequently increasing temperature. The effect of impurity cooling efficiency on simulation results is discussed in section 4.3.

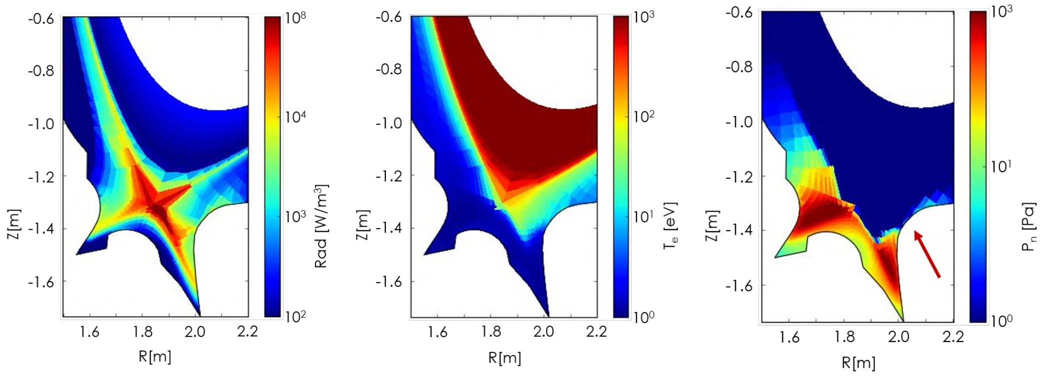

(a) Total radiation.

(b) Electron temperature.

(c) Neutral pressure.

Figure 4.34: Poloidal section of geometry #4 with $P_{rad} = 27\,\mathrm{MW}$

4.2.4 Other applications of DTT SOL and divertor modelling

In this section, analogously to section 4.1.4, the contribution of DTT edge and divertor modelling on the designing of the machine is described. First, the preliminary designing of DTT interferometer is described, then, the contribution of of edge modelling of ECRH duct designing is analysed.

DTT interferometer

[99] Interferometry is one of the most used techniques to measure line density on magnetically confined fusion experiment devices [100][101][101][102][103] due to the very simple relation between the phase shift of the laser beam crossing the plasma and the line integral density. The former is also associated with various measurement methods like high-frequency phase modulation and vibration compensation that considerably reduce measurement errors even at high time resolution. The main limitation of interferometry is related to the integral nature of the measurement which makes it difficult to use for detailed comparisons with the results of present 2D plasma modelling tools. To this end, multi-channel interferometers are normally used to provide local density evaluation by Abel inversion methods; this solution is always constrained by the number of ports available in fusion devices and the possibility to install mirrors inside the harsh vessel environment. Furthermore, the high number of components required by each optical channel limits the realization of numerous channels.

For the above reasons interferometers have never been considered to measure density in the divertor region of tokamak devices, where high spatial resolution is mandatory and in-vessel mirrors are typically required. On the other hand, in the divertor region, in particular around the X-point and along divertor legs, the plasma density is one of the most important parameters to compare with 2D modelling tools; the alternative Thomson Scattering measurement method is also difficult (not to mention its high cost).

Hence a novel interferometer based solution was proposed to measure the density in the divertor region of the DTT. As previously mentioned, DTT should be able to operate with ADCs) and liquid metal targets technologies with divertor conditions as close as possible to those foreseen on a fusion reactor. In both cases, ADCs and liquid metal targets, the achievement of plasma detachment is strongly correlated with the electron density along the divertor legs [104], as it is the raising of the MARFE at the X-point. These phenomena make density measurement in the divertor region fundamental in DTT and suggest an interferometric solution compatible with measurement requirements, device constraints and relatively easy implementation and maintenance.

A possible way to increase the number of line of sights (LOSs) has been previously found: a scanning technique [105] in which a single beam (or a few beams) is used to scans the plasma region. With this technique, a fraction of the often unused high time resolution is transformed in high spatial resolution. This solution solves the spatial resolution problem related to standard interferometers. The use of in-vessel mirrors with consequent high level of vibrations and uneasy alignment makes the standard Mach-Zehnder optical arrangement difficult. To answer this problem, the use of the dispersion interferometer (DI) scheme [106] was proposed. In this application, DIs presents the fundamental advantage against conventional ones without requiring alignment against a reference beam and without being insensitive to mechanical vibrations that would imply the need for a second shorter wavelength interferometer to measure path length variations. At the same time, the scanning scheme get rid of the duplication of nearly all optical components for measuring channel that is needed in standard DIs.

Interferometer details and components are described in [99]. Interferometers geometrical scheme inside and outside of DTT main chamber is shown in figure 4.35a, a detailed view of the divertor region is shown in figure 4.35a, again, the FAST-like divertor geometry was used in this scheme. The vertical LOSs of the interferometer intersect the main plasma, the X-point region and and below the dome, this is compatible with the insertion of the gaps for the passage of laser beams between the divertor mono-blocks. In figures 4.35c and 4.35d the positions of the mirrors under the targets (4.35c) and the behind dome (4.35d) are shown. Utilizing dedicated flipper mirrors the interferometer can switch between the two configurations thus allowing the measurement of the line density through the plasma only or plasma and divertor legs. In this way, the line density on divertor legs can be computed as the difference between the two measurements.

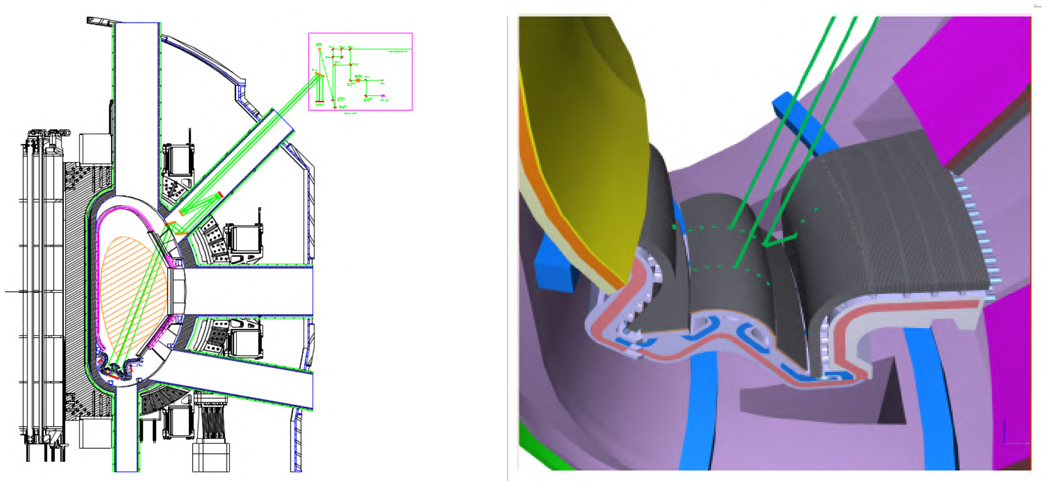

(a) asd

(b) asd

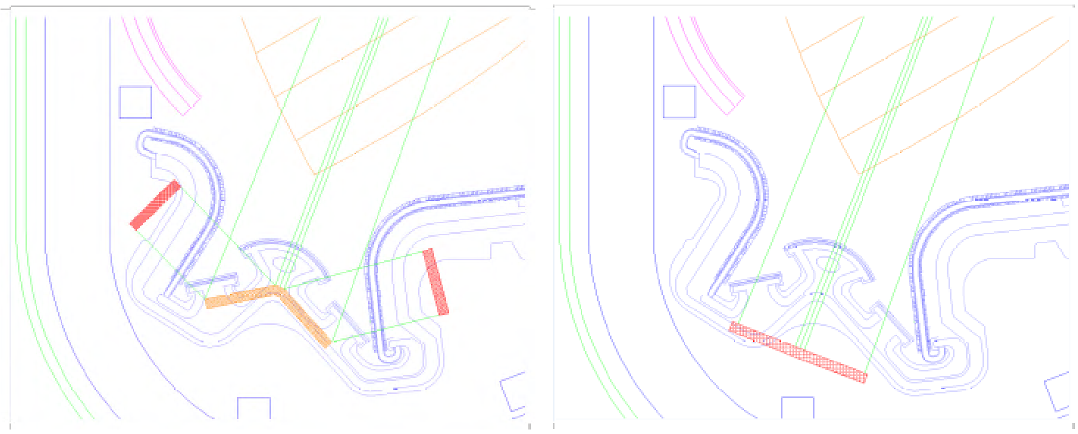

(c) asd

(d) asd

Figure 4.35: asd

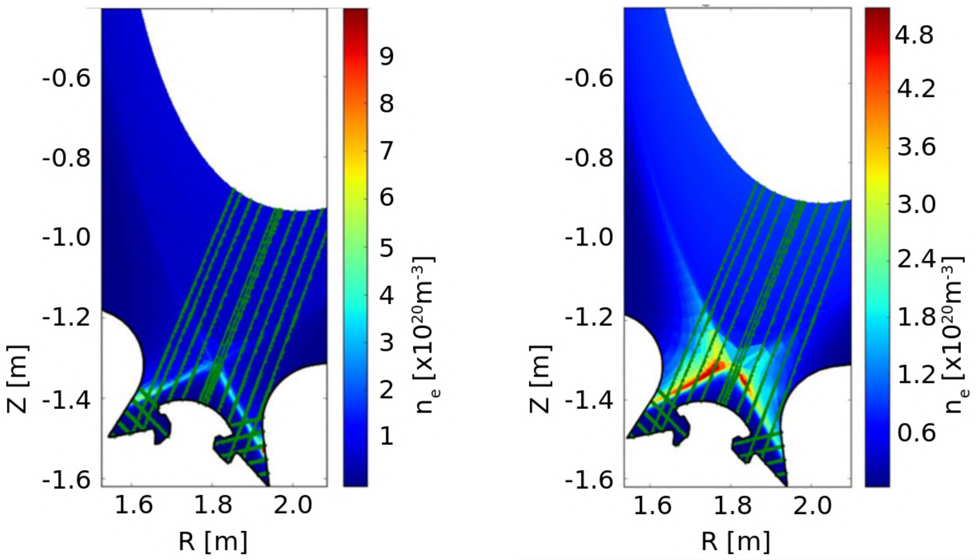

(a) 2D plot of electron density with partial detachment.

(b) 2D plot of electron density with deep detachment.

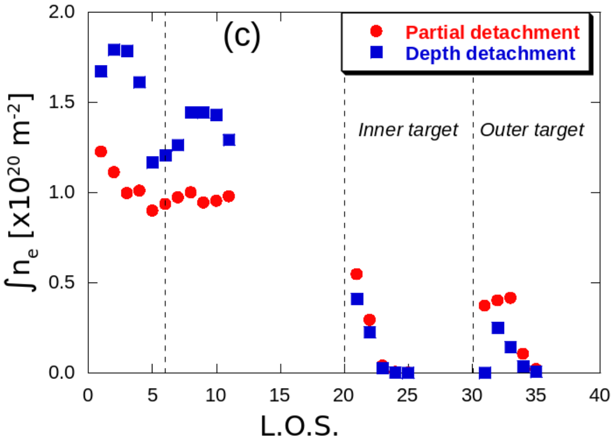

(c) Density line integrals computed along beam paths. Channels 1-10 on paths crossing plasma core, channels 21-35 on paths between dome and targets.

Figure 4.36: Modelling results and synthetic diagnostic data.

To assess the usefulness of the proposed interferometer in studying plasma edge, the difference in line density integrals of two different detachment conditions were compared, the expected line density measurement error was estimated. Divertor density has been evaluated with SOLEDGE2D-EIRENE edge modelling, with $P_{in} = 36\,\mathrm{MW}$ at the DTT medium operating density of $10^{20}\mathrm{m}^{-3}$ ($n/n_G \simeq 0.4$). SOLEDGE2D-EIRENE input parameters and the considered equilibrium, are those described in section 4.2.2 since validated transport parameters were not available at the time of this work. In figure 4.36 modelling results are shown in two detached conditions: partial detachment and deep detachment (figures 4.36a and 4.36b respectively). In figure 4.36c it is possible to see that the two detachment conditions provide quite different line integrals both along the path crossing the plasma core and the paths between dome and targets (the latter measure being computed by difference between the channels with optical path going to the mirrors under the targets and those going to the mirror under the dome). Considering a typical error in line integral of $2 - 5 \times 10^{18}\mathrm{m}^{-3}$; it is shown that the detachment states can be easily discriminated by the interferometer. No differences are detected by the inner divertor LOSs since deep detachment is achieved in both simulations.

The preliminary optical design of a dispersion interferometer shows the possibility to measure line density along divertor legs on the new Divertor Test Tokamak facility (DTT) with high spatial and time resolution. The proposed scheme combines the advantages of DIs and scanning interferometers. The system can switch between three different optical configurations to provide two different line density measurement and baseline evaluation/correction. Edge modelling shows the ability of the system to discriminate between different plasma detachment situations.

DTT ECRH

In this section, the application of edge modelling on the designing of ECRH ducts is described. ECRH will be the main auxiliary heating system in DTT[4]; the poloidal view of DTT ECRH heating system is shown in figure 4.37a;. Geometrically, from the plasma side, it consists of two ducts (the upper and the equatorial duct) that are joint beyond DTT external wall. ECRH ducts must be maintained in vacuum to operate correctly[107]; the vacuum is provided by a pumping system located beyond DTT external wall.

The scope of this work was to evaluate the effect on core and edge plasma of ECRH pumping system by simulating two different conditions: during steady-state ECRH operation and the transient given by the aperture of ECRH ducts. In both cases, it was decided to simulate the scenario in which ECRH pumping system could have the highest impact on DTT plasma, it will be named the *"worst-case scenario"*. The considered scenario is a high density detached scenario with $\langle \mathrm{n_e} \rangle_{\mathrm{sep}} = 8.0 \times 10^{19}$. The high-density scenario with detached divertor plasma was selected for this study because it requires the highest fueling rate. The fueling position was located at the outer mid-plane, close to the equatorial aperture, to obtain the highest neutral pressure in front of the aperture itself and consequently the highest pumping rate.

Neutral pressure at the outer mid-plane was taken from previous SOLEDGE2D-EIRENE simulations with the plasma characteristics listed above (see section 4.2.3). The Montecarlo code AVOCADO [72] utilizes the estimation of neutral pressure at the outer mid-plane provided by SOLEDGE2D-EIRENE simulations and the nominal pumping speed of ECRH pumps, to calculate the neutral pressure along ECRH ducts and the corresponding pumping speed at the

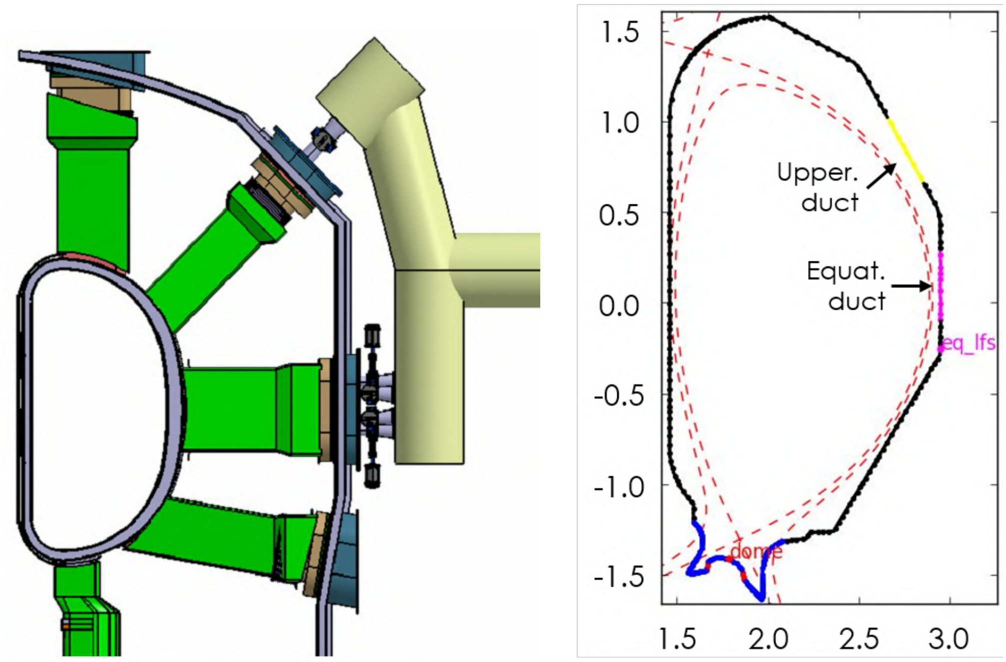

(a) DTT ECRH duct

(b) ECRH duct in SOLEDGE2D-EIRENE

Figure 4.37: ECRH in DTT and in SOLEDGE2D-EIRENE

	Total $[m^3/s]$	Upper duct $[m^3/s]$	Equat. duct $[m^3/s]$
C	58	15.5	43.5
$C_{aperture}$	1676.5	585.7	1090.9

Table 4.5: Neutral pressure in SOLEDGE2D-EIRENE and AVOCADO.

two DTT first wall aperture. The duct apertures are simulated in SOLEDGE2D-EIRENE by the yellow and pink surface in figure 4.37b.

Results of AVOCADO simulations in steady-state condition are shown in figure 4.38b; the reduced conductivity of ECRH guidelines at DTT outer wall causes a density drop and drastically reduces the effective pumping speed at DTT inner wall. The pumping speed (C) and conductance of inner wall duct ("C_{aperture}") aperture of four ECRH launchers calculated by AVOCADO is in table 4.5.

First, the steady-state condition is simulated. Even in the case of four ECRH launchers, pumping speed is limited to $58\,\mathrm{m}^3/\mathrm{s}$ in a region with low pressure, relatively high temperature and low density. Thus, when the pumping speed of table 4.5 is imposed at SOLEDGE2D-EIRENE boundary, the total deuterium pumped flux is in the order of 10^{20}D/s, as a comparison, the fueling flux required to sustain plasma density in this scenario is 7×10^{22}D/s. Since the pumped flux is more than two orders of magnitude lower than the fueling required to sustain the target plasma density, the impact of ECRH pumping is negligible in steady-state conditions.

The simultaneous opening of inner wall ECRH ducts is simulated. During DTT ramp-up,

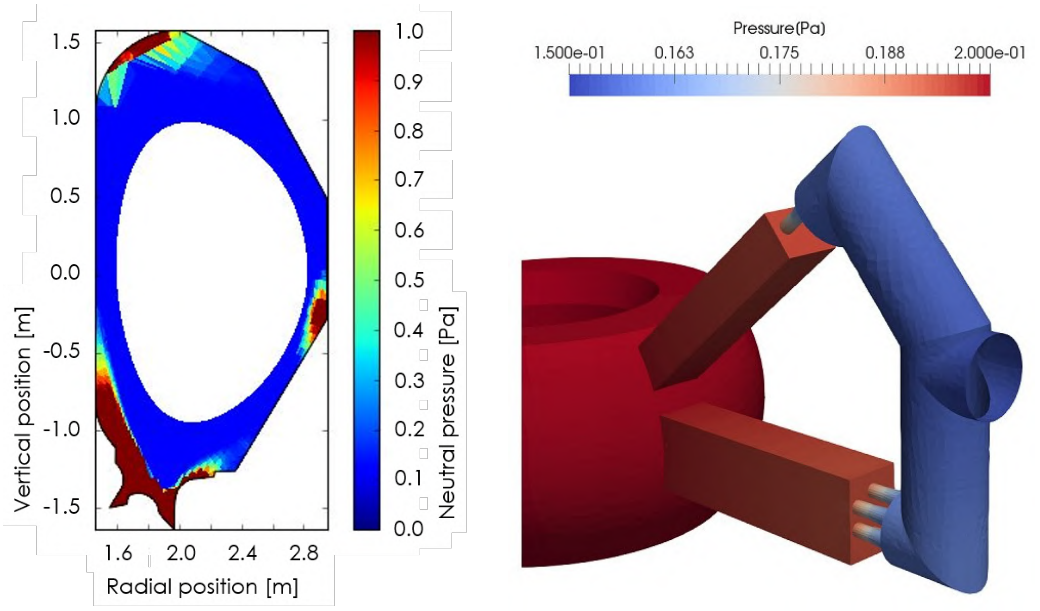

(a) Neutral pressure in considered DTT scenario.

(b) Pressure profile in ECRH ducts in steady-state conditions as from avocado simulations.

Figure 4.38: neutral pressure at DTT plasma edge and in one of the ECRH launchers.

before ECRH is launched into the plasma, the equatorial and upper duct of each launcher is opened. Assuming that before the opening $P_{ducts} \ll P_{main,chamber}$, the instantaneous pumping speed at the duct aperture is approximated equal to the duct aperture conductance (C_{aperture} in table 4.5); this approximation assumes that the flux of particles from the ducts to the main chamber is null.

A scan in pumping speed from the equatorial and upper duct was performed starting from the previously described scenario. Figure 4.39 shows the total calculated flux pumped from ECRH ducts as a function of total pumping speed; the total pumped flux is calculated as:

$$\Gamma_{\text{tot}} = \Gamma_{D,eq} + \Gamma_{D,up} + 2\left(\Gamma_{D2,eq} + \Gamma_{D2,up}\right). \tag{4.17}$$

The scan is effectively on pumping speed, but pumping speed at the two ducts was not imposed and is also an output of the simulations themselves. The boundary condition that was imposed at the absorbing surfaces (see figure 4.37b) is the albedo calculated as the reciprocate of the acceptance. The acceptance of the surfaces with n launchers was calculated as the ratio between the ducts area A_{duct} and the total toroidal projection of the absorbing surfaces in SOLEDGE2D-EIRENE of d_{duct} length:

$$a_n = n\frac{A_{duct}}{2\pi R_{wall} d_{duct}} \tag{4.18}$$

The choice of imposing the acceptance over the pumping speed was made to have the same albedo for both deuterium atoms and molecules.

In figure 4.39 the case with the higher pumping speed corresponds to the contemporary

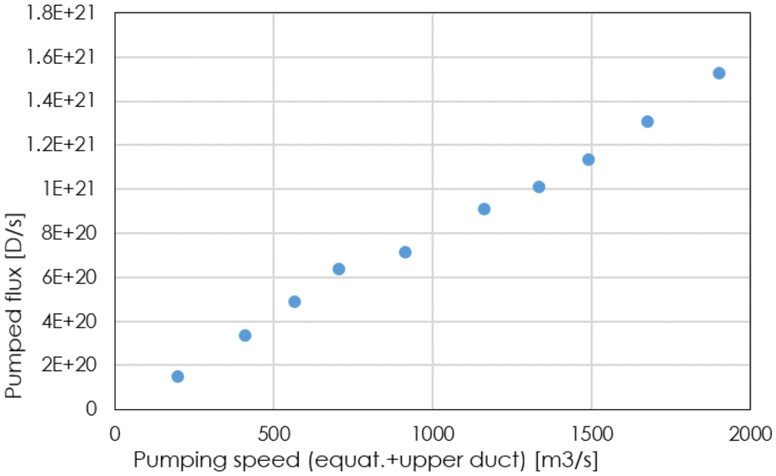

Figure 4.39: Pumped flux as function of total pumping speed from ECRH ducts.

aperture of both ducts of all of the four launchers. According to 4.18, acceptance of both surfaces was calculated as the ratio between the area of four aperture and the total toroidal area, the resulting total pumping speed is $1850\,\mathrm{m}^3/\mathrm{s}$, compatible to AVOCADO estimation ($C_{\text{aperture}} = 1677\,\mathrm{m}^3/\mathrm{s}$) that was made starting from uniform neutral density and temperature at the duct apertures. The pumped flux was estimated to be $1.55 \times 10^{21}\,\mathrm{D/s}$, still a factor 40 lower than the fueling flux.

From this result, it is concluded that even in the "*worst case scenario*" the contemporary aperture of all ECRH launchers cause a transitory absorption of particle which is negligible for the fueling and so could be successfully counteracted by the feedback system on fueling.

4.3 An hysteretic behaviour of cooling performances

In this section, the sensitivity of the modelling with impurity seeding, and the dependence of simulations outcome on initial conditions are analysed.

In deuterium-only simulations, edge modelling results generally reflect the behaviour described by the 2-point-model described in section 2.1.2; the system of the equation to be solved does not allow multiple solutions, it is generally true within the limits of the 2-point-model itself. When impurities are added to the system, there is no guarantee that the simulation that there is only a single solution for a given set of input parameters

Because of the non-linearity of the cooling rates of the principle seeding elements (see figure 4.40), the number of species and the subsequent complexity of the transport and cooling equations, it was decided to use SOLEDGE2D-EIRENE DTT cases to test the dependency of modelling results on initial conditions. Indications of possible dependency of edge simulations outcome on plasma initial conditions were found by Wigram [108] simulating long-leg ARC scenario. ARC is a high density, high field machine; DTT has similar characteristics and was chosen to investigate this phenomenon utilizing DTT full power equilibrium. For simplicity, transport parameters were assumed uniform and the same input parameters of section 4.2.2, the same first wall geometry and $R = 2.14$ equilibrium were used. The seeding impurity was neon.

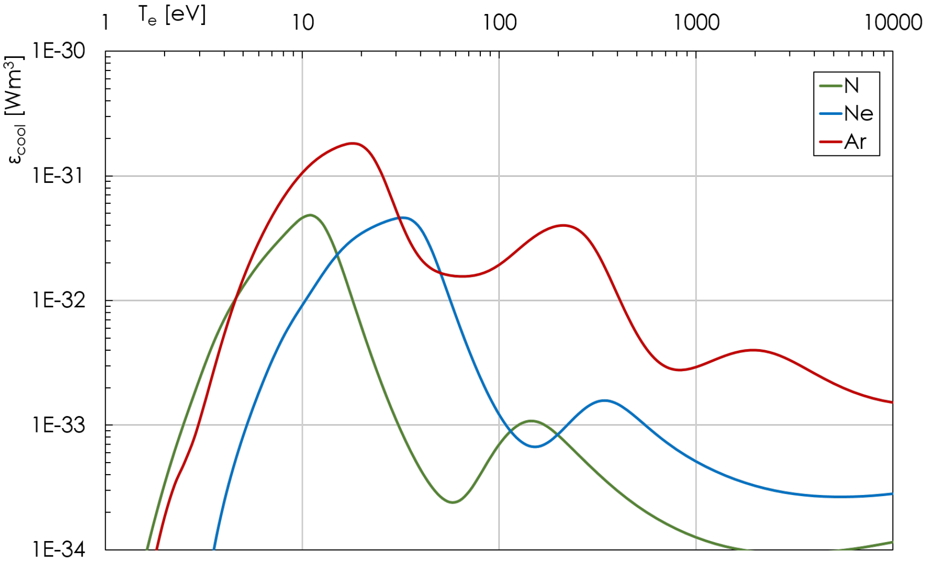

Figure 4.40: N, Ne and Ar cooling rates calculated from ADAS database [2]

The analysis was performed by slowly varying impurity influx, thus varying the impurity concentration in each simulation. The albedo of the absorbing surfaces is fixed to 0.92 for both D and Ne. In this analysis, it will be referred to *attached* and *detached* cases meaning attached and detached outer divertor plasma; inner divertor plasma was always detached in all cases considered.

The starting point is the detached reference case with P_{in}=36 MW, $\langle n_e \rangle_{sep} = 7.5 \times 10^{19} m^{-3}$, $\Gamma_D = 6.0 \times 10^{22}$D/s and $\Gamma_{Ne} = 1.5 \times 10^{21}$Ne/s (see figure 4.41a). Neon puffing is progressively reduced in various runs keeping constant all other parameters until complete attachment is

Run #	Γ_{Ne} $\times 10^{21}$Ne/s
1	1.5
2	1.3
3	1.1
4	0.9
5	0.7
6	0.55
7	0.9
8	1.1
9	1.3
10	1.5
11	1.7
12	2.1
13	2.5

Table 4.6: Main DTT parameters for the single null considered scenario

reached at the outer target figure 4.41b with $\Gamma_{\mathrm{Ne}} = 5.5 \times 10^{20}$Ne/s. Once a simulations converges to an attached condition Neon puffing is then increased in various other simulations to re-achieve detachment. Considered puffing values are in table 4.6. This study has the scope of understanding whether attachment and re-detachment do follow the same path or not, if not, it means that under certain conditions multiple solutions are allowed.

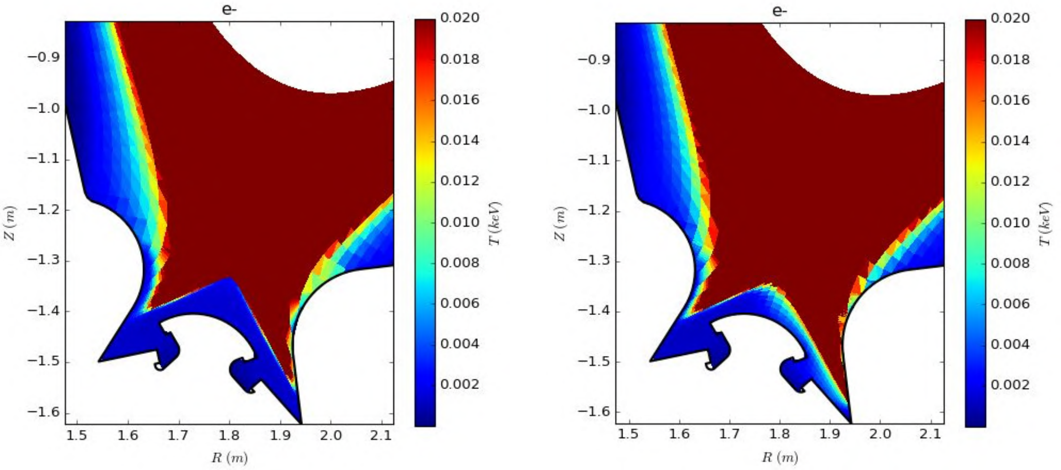

(a) Detached outer divertor case

(b) Attached outer divertor case

Figure 4.41: Electron temperature in divertor region saturated at 20 eV

Figure 4.42 shows simulation results; each point represent a run whose settings were previously described. It must be stressed that the points do not represent a transitory state, but are all converged simulations with different input parameters. Results of a simulation are used as the starting point of the following simulation with different input neon flux so to start with the divertor plasma condition found in the previous run.

Figure 4.42 shows the results of this seeded impurity scan. It displays an hysteretic-like behaviour of attachment and re-detachment. Figure 4.42a shows that, after attachment, much higher $\langle Z_{eff} \rangle_{sep}$ is needed to reduce the maximum power deposit to the outer divertor below the maximum power load that will be sustainable in DTT. The cycled is closed when detachment is achieved again with higher $\langle Z_{eff} \rangle_{sep}$ than that required to maintain detached conditions. It is possible to distinguish between a *cold branch* and a *hot branch* of the graph that are encountered when going from detachment to attachment and from attachment to detachment respectively. Similar behaviour was previously observed with the 2D edge code U-EDGE [108]. In that case, impurity concentration was calculated as a fixed fraction of main-plasma density; now, this behaviour can not be ascribed to this impurity treatment approximation that was used in that work.

The decreasing neon influx lowers the radiated fraction of input power, increases the power deposited to the outer target, increases the temperature in that region and lowers plasma density. Consequently, the neutral pressure at the entrance of the outer divertor pump is reduced (figure 4.42d) so much that almost no neutral gas is pumped from that surface. This is the explanation for the increase of electron density shown by the blue line in 4.42b. The decrease of electron density at the separatrix doesn't follow the same path because the outer target keeps being attached at a higher neon puffing rate after plasma attaches; thus, pumping from the outer target region is slowed (red line in figure 4.42d). Electron density decreases only due to the increase of pumping efficiency at the inner target absorbing surface (red line in figure 4.42c).

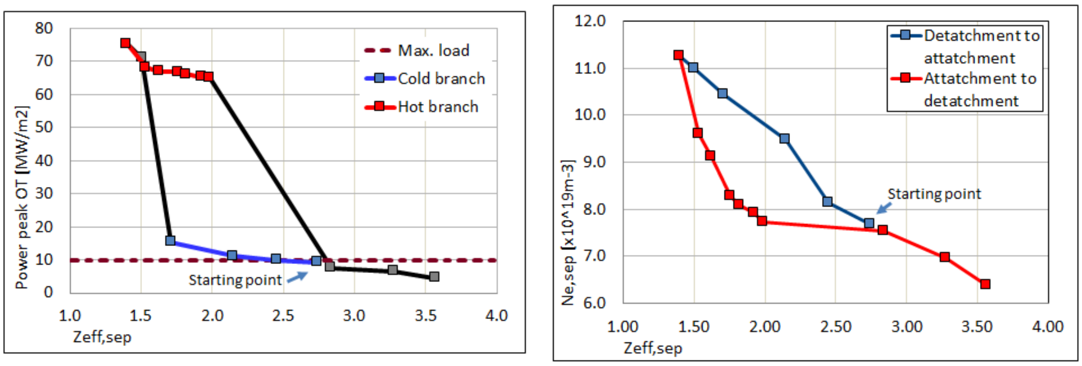

(a) Hysteretic-like behavior in Ne seeded simulations

(b) $\langle n_e \rangle_{sep}$ as function of $\langle Z_{eff} \rangle_{sep}$.

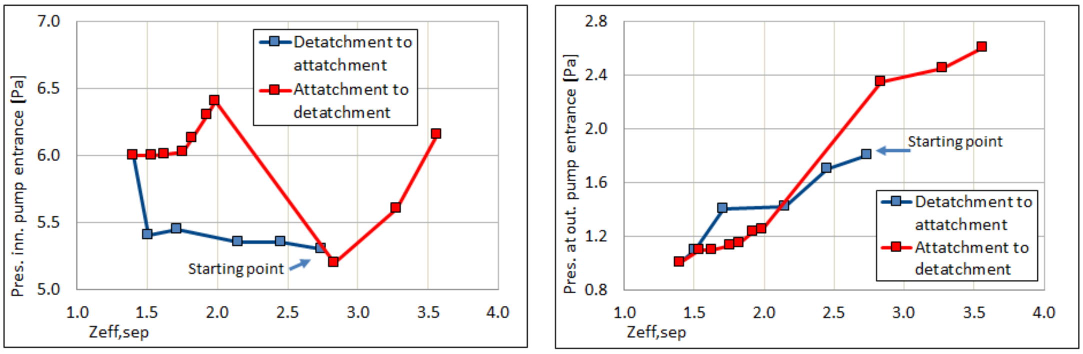

(c) Pressure at inner target absorbing surface.

(d) Pressure at outer target absorbing surface.

Figure 4.42: Hysteresys-like behaviour in seeded simulations.

There are two separate configurations: the first one where neutrals are almost equally shared between inner and outer divertor; the second one where, after attachment, high temperatures compress neutrals to the inner divertor, the amplitude of DTT dome and the position of the strike points enhances this difference. An explanation for this behavior can be derived from the figures 4.43 and 4.44 where neutral neon density, total neon density and total radiation due to neon are plotted in an attached and in a detached case respectively. The two outputs refer to simulations with the same neon input flux with the first being in the so-called *hot branch* and the second in the *cold branch*. In the attached case (4.43a), neutral neon particles moving to the outer divertor are immediately ionized, resulting in a net reduction of cross-field transport with respect to the lower temperature case where neutrals were abundant 4.44a. One of the reason why the total neon density (figures 4.43b and 4.44b) is much lower in the attached case is neon pressure conservation and the temperature difference between the two cases. Deuterium pressure conservation leads to the reduction of deuterium density, it consequently lowers the friction force between deuterium and neon.

Figure 4.40 shows a decrease of neon cooling efficacy with the increase of electron temperature. The drop of cooling efficacy after detachment requires a higher impurity content to achieve the same radiation fraction and generates the hysteresis. The high neutral compression given by the geometry of the machine can play a role in limiting neutral transport and enhancing the hysteresis but further studies are needed.

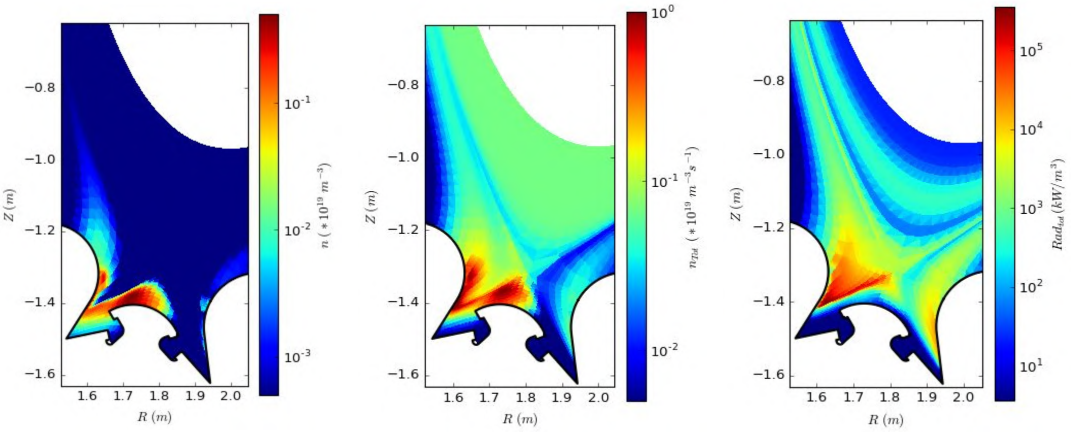

(a) Neutral Ne density (b) Total Ne density (c) Total Ne radiation

Figure 4.43: Attached outer target scenario

It becomes evident that at least two different equilibrium can be achieved even similar neon concentration: one with high temperature, low radiation, reduced transport and low neon density; the second is a high radiating, low temperature high neon density case. It is reasonable to conclude that the re-arrangement of neutral particles after detachment or attachment persists and generates this hysteretic-like behaviour explained in this section.

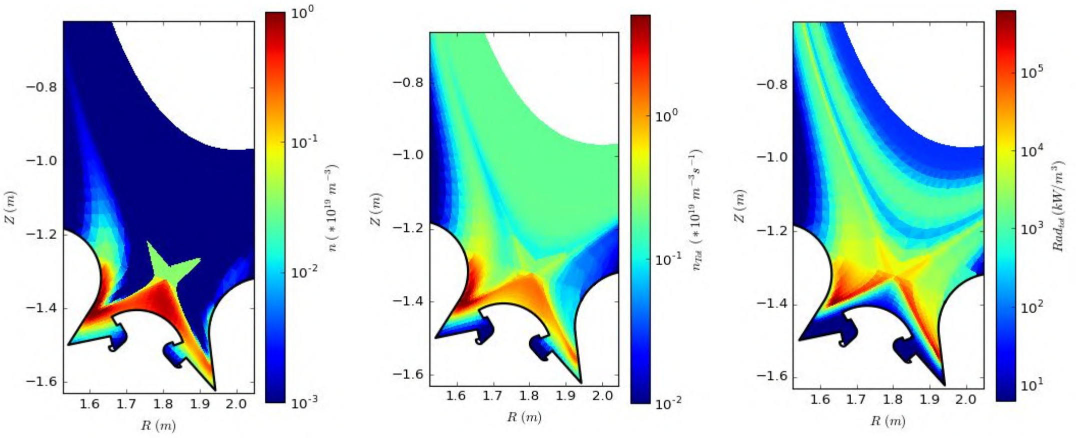

(a) Neutral Ne density

(b) Total Ne density

(c) Total Ne radiation

Figure 4.44: Detached outer target scenario

4.3.1 Mathematical analysis of the hysteretic behaviour

In this section, the output of SOLEDGE2D-EIRENE simulations are compared to the predictions given by simple 1D models. The 1D-edge model made by Kallenbach [109] starts from the assumption of the the two point model [11].

The heat flow along the field line causes a temperature drop as in the two point model:

$$q_{\parallel} = -k_0 T_e^{5/2} \frac{\partial T_e}{\partial l} \approx -2390 \frac{\mathrm{J}}{\mathrm{s\ m\ eV}^{7/2}} Z_{eff}^{-0.3} T_e^{5/2} \frac{\partial T_e}{\partial l}. \tag{4.19}$$

The approximation of thermal conductivity dependence on Z_{eff} is derived from experimental data. The heat flux along the field line is reduced by plasma radiation:

$$\frac{\partial q_{\parallel}}{\partial l} = -n_e^2 c_z L_z \left(T_e\right), \tag{4.20}$$

where $L_x\left(T_e\right)$ is the radiation function showed in figure 4.18. In Kallenbach's model, as in the 2-point model, the system is closed by pressure conservation:

$$n_e\left(l\right) T_e\left(l\right) = \text{const.} = n_{e,\mathrm{omp}} T_{e,\mathrm{omp}}. \tag{4.21}$$

The last two assumptions (equation 4.20 and 4.21) limits the validity of the model by neglecting all the pressure loss reactions, charge exchange and recombination. The model can be considered valid until partial detachment conditions are achieved; when complete detachment is achieved, temperature drops below 5 eV and recombination processes are dominant; thus it can be useful to study detachment threshold. This simplification allows an analytical solution for the system that is given by Post [110]. Given $n_{e,omp}$, $T_{e,omp}$, $n_{e,tar}$ and $T_{e,tar}$ plasma density and temperature at the outer mid-plane and at the target, the total radiation integrated along the field line is:

$$\begin{aligned} q_{rad} &= \left(q_{omp}^2 - q_{tar}^2\right)^{0.5} \\ &= n_{e,\mathrm{omp}} T_{e,\mathrm{omp}} \left(2 \int_{Te,tar}^{Te,omp} L_z\left(T_e\right) T_e^{0.5} k_0 c_z \mathrm{d}T_e\right)^{0.5} \\ &= n_{e,\mathrm{omp}} T_{e,\mathrm{omp}} \left(2 \int_{Te,tar}^{Te,omp} 2390 L_z\left(T_e\right) T_e^{0.5} Z_{\mathrm{eff}}^{-0.3} c_z \mathrm{d}T_e\right)^{0.5} \left(\mathrm{Wm}^{-2}\right). \end{aligned} \tag{4.22}$$

The total radiation estimated outside of the separatrix from the outer mid-plane to the outer target is than calculated multiplying by the area perpendicular to the field line:

$$P_{rad,out} = q_{rad,out} A = q_{rad,out} \cdot \left(2\pi R \lambda_{tar} \sin(\tan^{-1}(B_\theta / B_\varphi))\right), \tag{4.23}$$

where λ_{tar} is the typical power flux decay length at the target; $\lambda_{tar} = 6\,\mathrm{mm}$ in single-null DTT case with the input parameters used in section 4.2.3.

If impurity concentration and plasma density and temperature are fixed, q_{rad} is determined by the integral factor $L_z\left(T_e\right) T_e^{0.5}$, shown in figure 4.45 for neon, and the integration boundaries of such function.

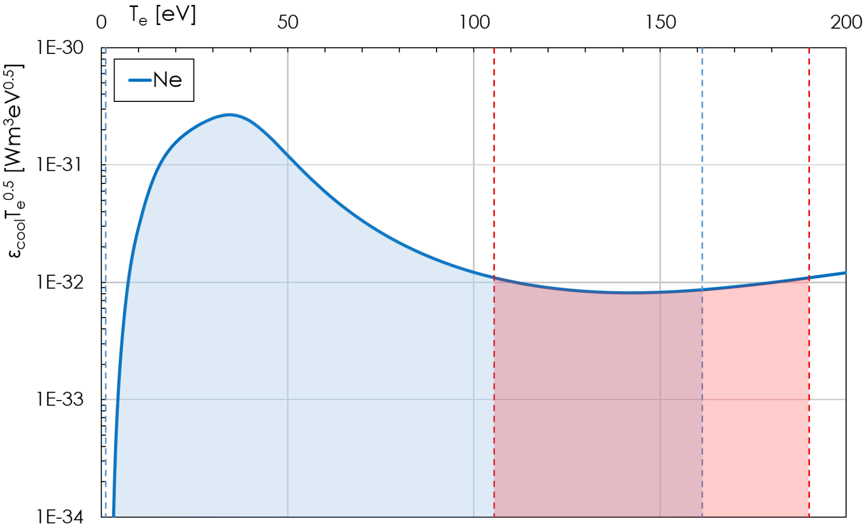

Figure 4.45: Integral factor $L_z(T_e)T_e^{0.5}$ for neon as function of temperature; integration boundaries of the attached and detached cases are shown in red and blue.

Starting from this assumptions and assuming constant Z_{eff} and c_z, Goldston derives his scaling of the impurity required to achieve detachment [111]. The scaling derivation do not take into account the effect of friction force between deuterium and impurities which can play a role in impurity confinement. this will also be a limit of the model presented below.

In this study, two neon seeded cases modelled with SOLEDGE2D-EIRENE are analysed using the model described above, both case have the same divertor geometry, geometry #5 in section 4.2.3, and the same input and transport parameters described in the same section. Both cases have similar impurity concentration but one is attached and the second is detached, so the first one is the upper mentioned *hot branch* and the latter in the *cold branch*. Z_{eff} and T_e poloidal projection is showed in figure 4.46; quantities are plotted along the field line, labelling with zero the point 1 mm outside of the outer mid-plane were negative X axis values are from the outer mid-plane to the outer target and positive x values go to the inner target.

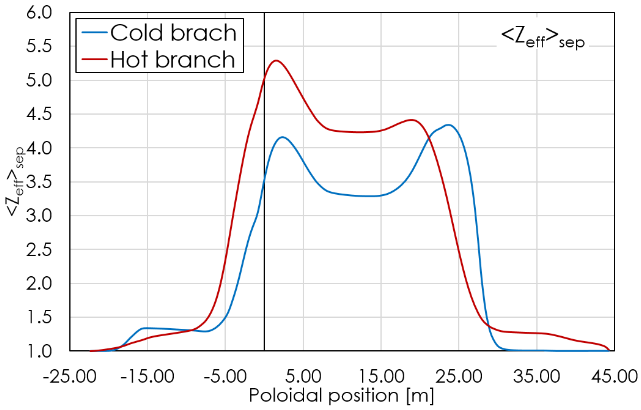

(a) Poloidal projection of Z_{eff}

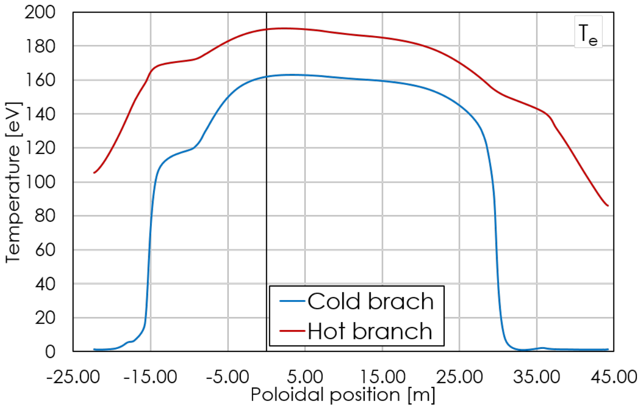

(b) Poloidal projection of T_e

Figure 4.46: Poloidal projection of quantities along the field line in the attached and in the detached case; position 0 m corresponds to the outer mid-plane, negative values of position coordinate correspond the section of the magnetic field line that leads to outer divertor, positive values lead to the inner divertor.

Radiation at the outer (and in this specific case also inner) target in the attached and detached case is obviously very different, given the similarity of c_z and Z_{eff}, the difference is sustained by the different integration boundaries of the cooling factor which are 1 to 162 eV and 105 to 190 eV respectively.

The total radiation at the inner and outer divertor were calculated according to equation 4.22 and 4.23 to compare the radiation estimated with this model to the more precise estimation of SOLEDGE2D-EIRENE. Considering the simplicity pf the model, there is a good agreement between the model predictions and SOLEDGE2D-EIRENE. The main difference between the two estimation is that of the radiated power of the detached case, the deeply detached case has a large low density radiating zone where pressure is not conserved, this leads to the under-estimation of total radiation by the 1-D model.

Figure 4.45 also shows the integration intervals of equation 4.22 for the outer divertor. Starting from the attached case, if impurities are added to the system, the target temperature (lower boundary) and the mid-plane temperature (upper boundary) are reduced almost equally according to equation **??**. In that temperature range, the red integral is almost unchanged if the integration boundaries are both lowered, radiation in increased only by the increase of impurity concentration, not also by the increase of cooling efficiency. It's only when the impurity concentration is high enough to lower the target temperature to 50/60 eV there is a strong increase of cooling efficiency that lowers that lowers the electron temperature, causing a chain-effect that leads to detachment. This explains why in no neon seeded simulations the electron temperature at the target was in the $10 - 50$ eV range. On the contrary, if the starting condition is a detached plasma, part of the edge plasma has electron temperature in the highly efficient (in terms of plasma radiation) temperature range $10\,\mathrm{eV} < T_e < 50\,\mathrm{eV}$; the cooling efficiency in this temperature range is more than one order of magnitude higher than in the attached plasma temperature range, thus a much lower impurity concentration is required to radiate the same power which can be radiated in the attached case. The integral below the blue line is nine times larger than that below the red line in figure 4.45, by neglecting, this proves that even a much lower impurity concentration in detached state can radiate more than a higher one in attached condition.

This simple model and a linear scaling is now used to estimate the impurity concentration required to reach *detachment-to-attachment* threshold starting from the detached case and *attachment-to-detachment* threshold from attached case. It will be demonstrated that there is one concentration to reach the threshold starting from the detached case and a much higher one starting from attached case and that, within the limits of the model, the predicted concentrations are also found with SOLEDGE2D-EIRENE.

The power deposited to the outer target can be calculated with a simple energy balance consideration.

$$P_{tar} = P_{sep,OT} - P_{rad,OT} = 2/3\left(P_{in} - P_{rad,in}\right) - P_{rad,OT}, \tag{4.24}$$

where P_{in} is the input power at $\rho_{tor,norm} = 0.85$, $P_{rad,in}$ is the radiated power between $\rho_{tor,norm} = 0.85$ and the separatrix, $P_{rad,OT}$ is the power radiated at the outer target and it was assumed that 2/3 of the power crossing the separatrix goes to the outer target and 1/3 to the inner target.

From deuterium-only simulation it is estimated that the maximum input power so to obtain detached conditions at the outer divertor is about 6 MW thus implying that the maximum power flux to the outer divertor is 4 MW. In the two analysed cases $P^{det}_{rad,in} =$ and $P^{att}_{rad,in} =$. According to equation 4.22, in the two *zero cases*, attached and detached, $P_{rad,OT}$ can be calculated as:

$$\begin{aligned} P^{det,0}_{rad,OT} &= n_{e,\mathrm{omp}} T^{det,0}_{e,\mathrm{omp}} \left(2 \times 2390 \int_{1.5}^{162} L_z\left(T_e\right) T_e^{0.5} Z_{\mathrm{eff},0}^{-0.3} c_z^0 \mathrm{d}T_e\right)^{0.5} \\ P^{att,0}_{rad,OT} &= n_{e,\mathrm{omp}} T^{att,0}_{e,\mathrm{omp}} \left(2 \times 2390 \int_{105}^{190} L_z\left(T_e\right) T_e^{0.5} Z_{\mathrm{eff},0}^{-0.3} c_z^0 \mathrm{d}T_e\right)^{0.5} \end{aligned} \tag{4.25}$$

In equation 4.25 I'm assuming that there is no correlation between inner and outer divertor temperature, in reality there is due to the energy conductance along the magnetic field lines. This is the same assumption made by Goldston and is required to keep the model simple.

Assuming that $c_z \propto Z_{\mathrm{eff}}$ and assuming that around the considered impurity concentration c_z profiles with respect to temperature scale linearly,thus assuming that in the two cases $\left(\frac{c_z^{att/det}}{c_{z,0}^{att/det}}\right)$ in independent on temperature, $P_{rad,OT}\left(c_z\right)$ is calculated as:

$$\begin{aligned}
P_{rad,OT}^{det,0} &= n_{e,\mathrm{omp}} T_{e,\mathrm{omp}}^{det,0} \left(\frac{c_z^{det}}{c_{z,0}^{det}}\right)^{0.35} \left(2 \times 2390 \int_{1.5}^{162} L_z\left(T_e\right) T_e^{0.5} (c_z^{0,det})^{0.7} \mathrm{d}T_e\right)^{0.5} \\
&= P_{rad,OT}^{det,0} \times \left(\frac{c_z^{det}}{c_z^{0,det}}\right)^{0.35} \\
P_{rad,OT}^{att,0} &= n_{e,\mathrm{omp}} T_{e,\mathrm{omp}}^{att,0} \left(\frac{c_z^{att}}{c_{z,0}^{att}}\right)^{0.35} \left(2 \times 2390 \int_{105}^{190} L_z\left(T_e\right) T_e^{0.5} (c_z^{0,att})^{0.7} \mathrm{d}T_e\right)^{0.5} \\
&= P_{rad,OT}^{att,0} \times \left(\frac{c_z^{att}}{c_z^{0,att}}\right)^{0.35}
\end{aligned} \tag{4.26}$$

Substituting 4.26 in equation 4.24, equation 4.27 is obtained:

$$\begin{aligned}
\frac{2}{3}\left(P_{rad,in}^{det,0}\right)\left(\frac{c_z^{det}}{c_z^{0,det}}\right) + P_{rad,OT}^{det,0}\left(\frac{c_z^{det}}{c_z^{0,det}}\right)^{0.3} &= \frac{2}{3}P_{in} - P_{max,tar} = 15.3MW \\
\frac{2}{3}\left(P_{rad,in}^{att,0}\right)\left(\frac{c_z^{att}}{c_z^{0,att}}\right) + P_{rad,OT}^{att,0}\left(\frac{c_z^{att}}{c_z^{0,att}}\right)^{0.3} &= \frac{2}{3}P_{in} - P_{max,tar} = 15.3MW
\end{aligned} \tag{4.27}$$

By solving the two equation in 4.27 for the unknowns c_z^{det} and c_z^{att}, the following values are obtained:

$$\begin{aligned}
c_z^{det} &\sim 1.5\%, \\
c_z^{att} &\sim 5\%.
\end{aligned} \tag{4.28}$$

With SOLEDGE2D-EIRENE modelling it was found that $c_z^{att}(soledge) \sim 3.5\%$ and $c_z^{det}(soledge) \sim 1\%$ The two values are compatible to those derived with the methodology presented above (equation 4.28).

This model has some limitation which are:

- c_z^{det} is overestimated because the simulation that was used to derive it was in deep detachment state, since this model has all the limits of the original Goldston's scaling, it underestimates the radiation in this state;
- the model relies on the assumption that in detached state, the integral within the red lines in figure 4.45 is almost constant until detachment is achieved. The assumption is good due to the flatness of $\varepsilon_{cool} T_e^{0.5} inthe 70 - 200\,\mathrm{eV}$ range, but integral increases. The assumption that was made leads to the over-estimation of c_z^{att}.

The model reproduces the hysteretic behaviour that was observed in SOLEDGE2D-EIRENE and can give an estimation of the impurity concentration required to obtain detachment from attached state or vice-versa when modelling these scenarios.

Chapter 5

Modelling of liquid metal divertor surfaces

In this chapter, the implementation of a self-consistent model for the simulations plasma facing components (PFCs) made of liquid metal is described.

The model has been developed to described a capillary porous system (CPS) as plasma facing components [112], but other similar plasma facing components such as liquid metal pool [113] or liquid metal vapor box [40](which were described in section2.3) can also be modelled with minor adjustments; in fact, in section 5.3 a vapor box configuration is simulated.

The model is *self-consistent* meaning that liquid metal temperature, evaporation and sputtering are not fixed in the simulation as they often are in liquid metal PFC models[45]. On the contrary, the only input in this model are the geometrical characteristic of the PFC, PFC material, liquid metal element and coolant temperature. Liquid metal temperature, evaporation and sputtering flux are results of the simulation itself and are self consistent with particle and power flux calculated by SOLEDGE2D-EIRENE.

As described in section 2.3, the most promising elements to be used as liquid metal PFC are lithium and tin, a mixture of the two has been proposed as well[114]. Both lithium and tin have been implemented in the model but only lithium has been tested in SOLEDGE2D-EIRENE; implementation of tin would have required the definition of bundles to lower the amount of simulated ions and have a reasonable amount of species in the simulations. To prevent misinterpretation, from know on, it will be referred to liquid metal meaning lithium even if also tin has been numerically implemented in the model.

In section 5.1 the physical analysis that allowed the numerical implementation of the liquid metal target model is presented; the test of the model outside of SOLEDGE2D-EIRENE is described in section 5.2; in section 5.3 the model has been applied to DTT cases, it was compared with previous modelling, lastly predictive simulations of possible geometrical solutions have been performed.

5.1 Liquid target model

The numerical model was implemented to be able to reproduce the behaviour of a plasma facing component made of capillary porous system; a sketch poloidal section of the component as it is modelled is represented in figure 5.1.

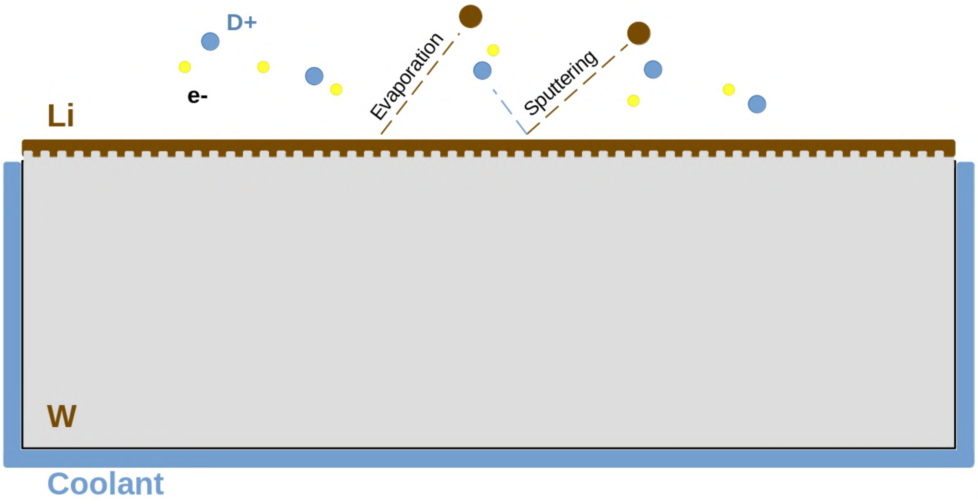

Figure 5.1: Sketch of modelled used to describe the capillary porous system.

Capillary porous system liquid metal PFC are generally made of a tungsten alloy covered by by lithium or tin on the plasma-exposed side. The porosity of the tungsten prevents major liquid metal spray of drop emission.

Tungsten porous surface is kept wet thanks to the capillary system inside the slab that connects a liquid metal reservoir to the plasma-facing surface [115]. Such technology keep the surface wet even when the emitted flux is of the order of 10^{24}part/m^{2}s [39], although, in this work, the porous surface is always assumed to be wet, so no limit to the emission rate are imposed; on the other hand, the model can predict the liquid metal emission by evaporation and sputtering and so define an operative range in terms of plasma temperature and flux to the wall which is compatible to the technological limits on lithium emission.

Due the need of a simple 2D heat transport model, the reservoir and the capillary system that connects the reservoir to the porous surface are not included in the model and were consequently not represented in figure 5.1. The reservoir and the capillary system alter the thermal conductivity inside tungsten slab. Nevertheless, the inclusion in the thermal model of the internal capillary system would have required a much more complex heat transport code and would have required a 3D treatment of thermal diffusion which is normally done by dedicated codes. The simple approximation of heat diffusion through a tungsten slab that is made in the model is very general, efficient under a computational point of view and extremely flexible to size modification. When particular CPS is modelled, the dimensions of the target can be adapted to match the temperature profiles obtained with more complex codes. Also the cooling scheme in the model can be adapted to describe the cooling scheme of the CPS by adapting boundary conditions. For example, the limiter CPS tested in FTU was cooled only from the side opposite to the plasma-facing one. In that case the boundary condition and the two sides would have been null thermal flux through the boundary and not fixed temperature like in the case which are described in the sections below.

The main physical plasma-liquid metal layer interaction to be modelled are: heat deposition, liquid metal particle evaporation, sputtering by deuterium and impurities and redeposition of impurities on the liquid metal layer.

The implementation of a model for the self consistent simulation of liquid metal plasma facing component in SOLEDGE2D-EIRENE requires 3 steps:

- A model for the calculation of evaporated particles
- A model for the calculation of sputtered particle flux
- A model for thermal diffusion in the plasma facing component

Sections 5.1.1, 5.1.2 and 5.1.4 describe those three steps respectively.

5.1.1 Evaporation model

When heat is deposited to a liquid lithium surface, an amount of lithium evaporates from the surface. The evaporated flux can be estimated with the Langmuir evaporation law [116]:

$$\Gamma_{evap}^{Li} = \frac{p_{Li} - p_a}{\sqrt{2\pi m_{Li} k_B T_{surf}}}, \tag{5.1}$$

where p_a is the ambient pressure, m_{Li} is lithium mass, and T_{surf} is the surface temperature in Kelvin.
p_{Li} is lithium vapor pressure, the pressure of the vapor cloud formed in front of liquid lithium layer. A good estimation of lithium vapor pressure in given by equation 5.2 derived in [117]:

$$\ln\left(p_{Li}\right)[Pa] = 26.89 - \frac{18880}{T_{surf}} - 0.4942\ln\left(T_{surf}\right). \tag{5.2}$$

Figure 5.2 shows the evaporation rate calculated with the Langmuir evaporation law and the estimation of lithium vapor pressure.

The validity range in terms of surface temperature of equation 5.1 goes from the melting point $T_m = 454\,\mathrm{K}$ to the boiling point $T_m = 1603\,\mathrm{K}$[1], with that implying that $\Gamma_{evap}^{Li} = 0$ if $T_{surf} < T_m$. This is also the operative window of a liquid lithium plasma facing component that is about 1200 K. As a comparison, tin operative range goes from 505 to 2875 K and is twice as large as lithium one in terms of temperature; this is the advantage of tin over lithium as liquid metal PFC.

One of the phenomena that may occur in a liquid lithium PFC is the formation of lithium hydride (LiD) in the liquid metal layer. LiD is formed due to the elevate chemical affinity of lithium and hydrogen. Since LiD vapor pressure is much lower than pure lithium vapor pressure, lithium hydride may drastically reduce the net vapor pressure of the mixture, thus reducing the net evaporation rate[118].

---

[1] Langmuir evaporation law better reproduce experimental data when $T_{surf} \leq 1450\,\mathrm{K}$

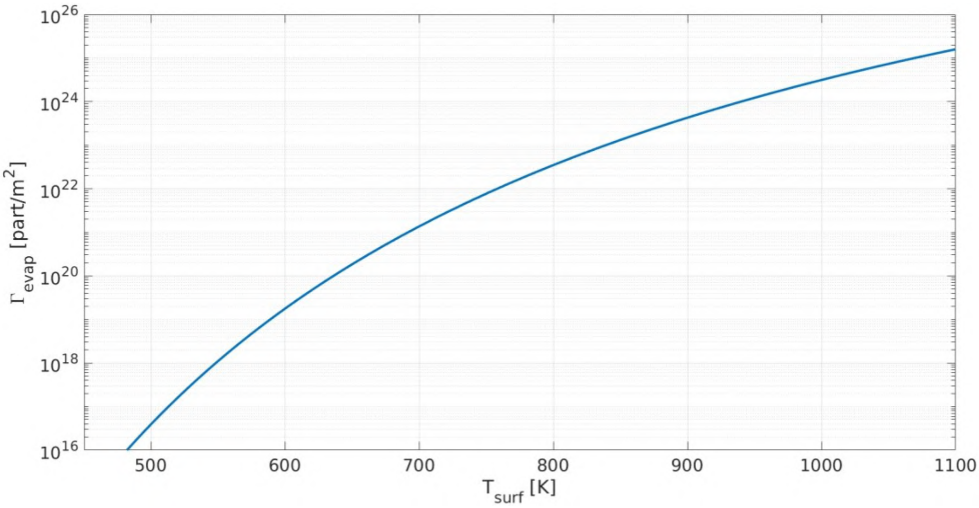

Figure 5.2: Lithium evaporation as function of temperature calculated with equation 5.1

The dissociate temperature of LiD is estimated between 900 and 1000 K[119], so it should not play an important role beyond that temperature range; on the other hand, it could drastically affect evaporation rate below 900 K.

A possible solution for the estimation of lithium evaporation with considering lithium hydrate contribution is proposed by Abrams. [120] (p.26). This solution consist is re-scaling p_{Li} by a factor proportional to the LiD concentration β, such that $p_{Li+LiD} = p_{Li}$ if $\beta = 0$ and $p_{Li+LiD} = p_{LiD}$ if $\beta = 1$:

$$p_{Li+LiD}\left(\beta\right) = p_{Li}\left(1-\beta\right)^{\gamma}, \tag{5.3}$$

where $\gamma = 0.705$ is an experimental fitting parameter.

The solution proposed by Abrams has been implemented in this model; although, since it required the knowledge of LiD concentration which is unknown for future machine and divertor-like plasma, β has been kept equal to 0 for simplicity in all of the simulations presented in this chapter. The approximation $\beta = 0$ is good when target $T_{tar} > 1000K$ because LiD dissociation occurs at that temperature and D is released from the target. The estimation of β will be crucial when validating the code against experimental data if the target is colder than the dissociative temperature if LiD.

5.1.2 Sputtering model

When a particle hits a surface with a kinetic E_{in} that is higher that a threshold energy E_{th} (typical of the surface itself), one or more particle can be emitted from the surface, the process is suppressed below the threshold energy.

This process is called sputtering; sputtering yield is defined as:

$$Y = \frac{\text{Emitted particle flux}}{\text{Impinging particle flux}}. \tag{5.4}$$

Physical sputtering

Physical sputtering of lithium particles by deuterium bombardment is given by the *one-on-one* interaction of a deuterium and a lithium particle. The sputtering yield of a deuterium particle with energy E_{in} which impact on a surface with binding energy E_{th} can be estimated by the Bohndansky-Eckstein[121][122] model:

$$Y(E_{in}) = a s_n^{KrC} \frac{\left(\frac{E_{in}}{E_{th}} - 1\right)^{\mu}}{\lambda + \left(\frac{E_{in}}{E_{th}} - 1\right)^{\mu}} \tag{5.5}$$

where s_n^{KrC} is the nuclear stopping power of the material and a, λ and mu are parameters typical of the projectile-target combination that are derived experimentally.

In this model, equation 5.5 has been implemented assuming the kinetic energy of deuterium particles as the particle acceleration in the Debye sheath[123]:

$$E_{in} = \frac{1}{2}\left[\ln\left(2\pi\frac{m_e}{m_D}\right) - 1\right] T_e \tag{5.6}$$

From equation 5.5 it is possible to derive that physical sputtering does not have a strong dependency on particle energy if $E_{in} \gg E_{th}$ and has a stronger dependency when the two variables are of a similar order of magnitude. In lithium case, according to equation 5.6, sputtering yield dependency is mostly independent of plasma temperature when $T_e \gtrapprox 100\,\mathrm{eV}$.

In this model the dependence on incident angle of the sputtering yield is missing but can be implemented if experimental data are available.

Thermal sputtering

Thermal sputtering is a collective phenomena that is observed when target material temperature is close to the melting temperature; it is even more pronounced if the surface is liquid. Thermal sputtering has been observed in for lithium and tin [124][125]

Thermal sputtering is a collective phenomena, meaning that it can not be described as a particle-particle interaction, but rather as a multi-particle interaction. Collective interaction are favourite when molecular bounds are weakened as in melting point proximity or in liquids.

Thermal sputtering can be estimated considering adatoms which are formed on the surface. Adatoms are atoms in an excited state do not have enough energy to escape the surface, lattice etc. Clearly, the bounding energy in a surface with many excited atoms is reduced with respect to the ground state condition.

An estimation for the sputtering yield from adatom formation is given in [126]:

$$Y_{\mathrm{adatom}}(T) = \frac{Y_{ad}}{1 + A\exp\left(\frac{E_{ad}-E_D}{k_B T_{surf}}\right)}, \tag{5.7}$$

where E_{ad} is the adatom surface binding energy, E_D is the activation energy and Y_{ad} and A are experimental data fitting parameters. For liquid lithium, the value assumed were those calculated by Abrams [120]: $Y_{ad} = 2.9$, $A = 9.6 \times 10^{-6}$ and $E_{ad} - E_D = 0.7\,\mathrm{eV}$. Equation 5.7

shows no direct dependency of adatom sputtering on impinging particle energy

Figure 5.3 shows the adatom sputtering yield calculated according to 5.7 in the operative temperature range of a liquid lithium PFC. Y_{adatom} is higher than 1 in this operative range while physical sputtering from $50 - 100$eV deuterium particles is normally one order of magnitude lower according to equation 5.5 thus meaning that adatom sputtering is the primary sputtering source.

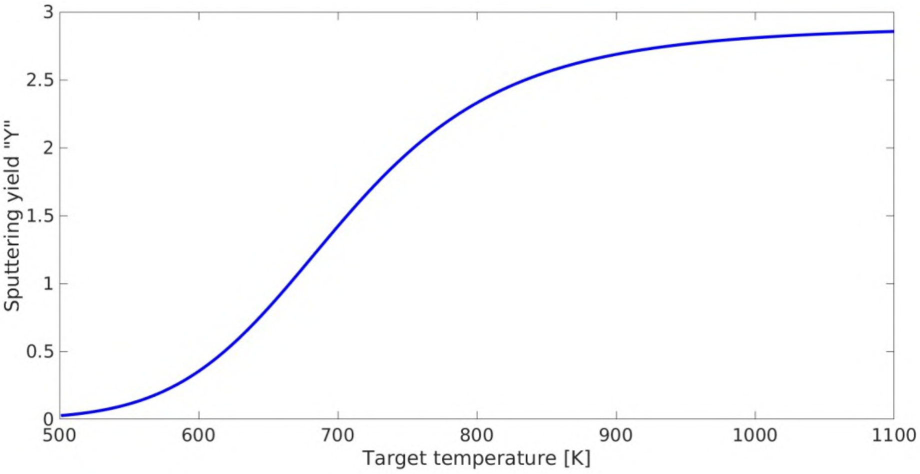

Figure 5.3: D on Li sputtering yield as function of liquid target temperature.

Chemical sputtering

Sputtering is also influenced by the presence of LiD in the lithium layer as it is for evaporation. There are two reasons for this behaviour. First, LiD has a higher surface binding energy than pure lithium, thus reducing lithium sputtering yield. Second, when a considerable quantity of deuterium is deposited in the layer, the energy of the impinging deuterium particles is more likely to be transferred to the deuterium particle in the liquid metal layer due to mass similarity; this preferential sputtering effect also reduces the sputtering yield.

Lithium sputtering yield by deuterium bombardment was calculated with the code TRIM as a function of LiD concentration (β) by Abrams.

A function $f(\beta)$ is defined to fit TRIM data and reproduce the decay of sputtering yield with LiD concentration:

$$f(\beta) = \frac{1}{10^{\beta*1.651}}; \tag{5.8}$$

the function is equal to 1 when pure lithium surface is considered.

5.1.3 Surface emitted particle flux

The total emitted particle flux is calculated as the sum of evaporation rate, physical sputtering and thermal sputtering taking into account the contribution to the reduction of evaporated and sputtered flux given by LiD formation. The total calculated lithium emission rate implemented in the model is:

$$\Gamma_{Li}\left(T_{surf},\Gamma_{D^+},\beta,E_{in}\right)=\frac{p_{Li+LiD}\left(T_{surf},\beta\right)-p_a}{\sqrt{2\pi m_{Li}k_B T_{surf}}}+ \\ +\Gamma_{Li}^{in}f\left(\beta\right)\left[a s_n^{KrC}\frac{\left(\frac{E_{in}}{E_{th}}-1\right)^{\mu}}{\lambda+\left(\frac{E_{in}}{E_{th}}-1\right)^{\mu}}+\frac{Y_{ad}}{1+A\exp\left(\frac{E_{ad}-E_D}{k_B T_{surf}}\right)}\right] \tag{5.9}$$

Both sputtered and evaporated particles are emitted in SOLEDGE2D-EIRENE with a cosine-like distribution; this is a common assumption for evaporated particles, but is also solid for sputtered particles as confirmed by TRIM code.

5.1.4 Heat transport model

As described in section 2.3, the most promising type of liquid metal plasma facing component consists of a porous tungsten block covered on the plasma-facing side by the liquid metal itself. Assuming this technology, the heat transport model in the liquid metal PFC is modelled as pictured in figure 5.4. The power flux from the plasma is deposited on the liquid metal layer, it diffuses through the tungsten block and flows to the cooling pipes. In this approximation the cooling is made at the lower three sides of the block by imposing a fixed temperature equal to the temperature of the coolant immediately out of the block itself as in picture 5.4. The heat transport model is a 2D poloidal model, assuming toroidal symmetry.

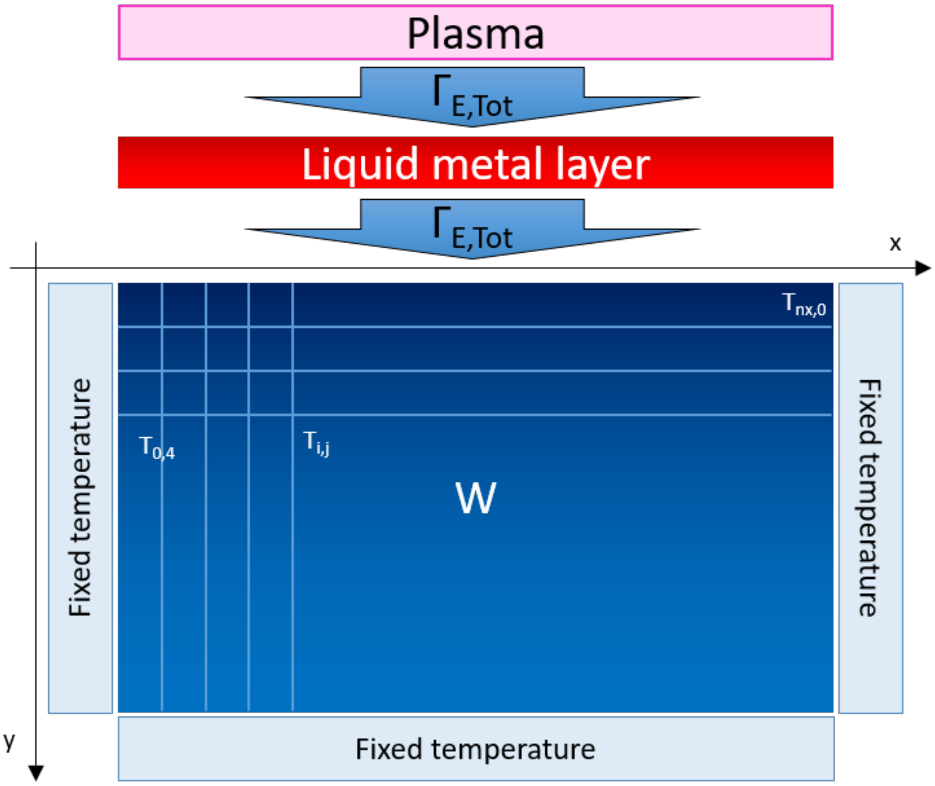

Figure 5.4: Thermal conductivity model of liquid lithium target.

The thermal diffusion model is based on the energy conservation equation:

$$\rho c_p \frac{\partial T}{\partial t} - \nabla \cdot (k \nabla T) = \dot{q}_V, \tag{5.10}$$

where $\dot{q}_V$ is the volume heat source while ρ, c_p, and k are three coefficient that are typical of the considered material and are the material density, thermal capacity and thermal conductivity respectively.

In steady state condition, with no volume energy sources and assuming toroidal symmetry, equation 5.10 becomes the Poisson equation 5.11

$$\frac{\partial^2 T}{\partial x^2} + \frac{\partial^2 T}{\partial y^2} = 0 \tag{5.11}$$

To solve equation 5.11 with the upper mentioned boundary conditions, the target area is discretized in $nx \times ny$ nodes with $i = 1, ..., nx$ and $j = 1, ..., ny$ labelling the x and y axis respectively, with $T_{i,j}$ being the approximation of temperature at position $(x = (i-1)\,dx, y = (j-1)\,dy)$ as shown in figure 5.4. A second grade discretization of the second derivatives of equation 5.11 is used, the central finite difference approximation:

$$\frac{T_{i-1,j} - 2T_{i,j} + T_{i+1,j}}{dx^2} + \frac{T_{i,j-1} - 2T_{i,j} + T_{i,j+1}}{dy^2} = 0 \qquad i = 2, nx-1; j = 2, ny-1, \tag{5.12}$$

which is true for every node which is not at the boundary of the PFC. Equation 5.12 describes a system of $nx \times ny$ unknowns and $(nx-1) \times (ny-1)$ equations.

Outside of the three side of the PFC not facing the plasma, fixed temperature is imposed (Dirichlet boundary conditions). Equation 5.12 can also be extended to the nodes at these three boundaries by substituting the temperature out of the PFC with the cooling temperature T_{cool} which is a known term:

$$\left.\begin{array}{lll} T_{i-1,j} = T_{cool} & \text{if} & i = 1 \\ T_{i+1,j} = T_{cool} & \text{if} & i = nx \\ T_{i,j+1} = T_{cool} & \text{if} & j = ny. \end{array}\right\} \text{ Known terms} \tag{5.13}$$

At the liquid metal boundary, we want to impose fixed heat flux perpendicular to the wall as boundary condition, the heat flux being the output of SOLEDGE2D-EIRENE simulations which is obviously not constant on the x axis. I will refer to this quantity as $\Gamma_{E,\perp}$.

Imposing power flux at the upper boundary means imposing equation 5.14:

$$k_W \frac{\partial T}{\partial y} = -\Gamma_{E\perp}, \tag{5.14}$$

taking positive the energy flux perpendicular to the wall $\Gamma_{E\perp}$, k_W is the 1D heat conduction coefficient for tungsten, and the positive direction of y axis is from the liquid metal surface going inside the tungsten block.

To implement such boundary condition, the *ghost boundary method* has been used. The method is the following. Nodes at the liquid metal boundary are labelled with $j = 1$, by assuming that equation 5.14 is true a bit inside and outside the domain, the domain can be fictionally extended to $j = 0$. The second grade discretization (a second grade discretization was also used for the second derivatives of the Poisson equation) of equation 5.14 calculated at $j = 1$ at position the $x_i = nx \times (i-1)$:

$$\frac{T_{i,2} - T_{i.0}}{2dy} = -\frac{\Gamma_{E\perp}(x_i)}{k_W}. \tag{5.15}$$

By assuming that the Poisson equation is also true a little bit outside of the domain (i.e.$j = 0$), the following system of equations is obtained:

$$\begin{cases} T_{i,0} = T_{i+2} + 2\frac{\Gamma_{E\perp}(x_i)}{k_W}dy & \text{CFD first derivative at } (x_i, 0) \\ \frac{T_{i-1,1} - 2T_{i,1} + T_{i+1,1}}{dx^2} + \frac{T_{i,0} - 2T_{i,1} + T_{i,2}}{dy^2} = 0 & \text{CFD Poisson equation at } (x_i, 0) \end{cases} \tag{5.16}$$

By substituting $T_{i,0}$ in the second equation of 5.16, equation 5.17 is obtained:

$$-2\left(\frac{1}{dx^2} + \frac{1}{dy^2}\right)T_{i,1} + \frac{T_{i-1,1}}{dx^2} + \frac{T_{i+1,1}}{dx^2} + 2\frac{T_{i,2}}{dy^2} + 2\frac{\Gamma_{E,\perp}(x_i)}{k_W dy} = 0. \tag{5.17}$$

Equation 5.17 differs from 5.12 from the lack of term $\frac{T_{i,0}}{dy^2}$, the factor 2 in red and the known term $2\frac{\Gamma_{E,\perp}(x_i)}{k_W dy}$ in green.

Equation 5.17 consists of nx equations. Equation 5.12 extended with 5.13 and 5.17 consists of a system with $nx \times ny = n_{nodes}$ equations with $nx \times ny = n_{nodes}$ unknowns, the unknowns being $T_{i,j} \forall (i, j)$.

Nodes can be mapped in a single dimension array

$$T_{i,j} = T_z \qquad z = 1, n_{nodes} \tag{5.18}$$

The system of n_{nodes} equations can be written as:

$$\left[\hat{M}\right][T] = [b] \quad \text{with } [T] = T_{1,\dots,n_{nodes}} \tag{5.19}$$

with $\left[\hat{M}\right]$ being a $n_{nodes} \times n_{nodes}$ interaction matrix and $[b]$ being the matrix of the known terms (n_{nodes} length).

Mapping z as follows (from left to right and from up to down in figure 5.4):

$$z = i + (nz - 1)\, j, \tag{5.20}$$

the $\left[\hat{M}\right]$ matrix is filled as follows according to 5.12, 5.13 and 5.17:

$$\begin{cases} M_{z,z} = -2\left(\frac{1}{dx^2} + \frac{1}{dy^2}\right) & \forall \quad (i, j) \\ M_{z,z+1} = M_{z+1,z} = \frac{1}{dx^2} & \forall \quad i \neq nx \\ M_{z,z-1} = M_{z-1,z} = \frac{1}{dx^2} & \forall \quad i \neq 1 \\ M_{z,z+nx} = M_{z+nx,z} = \frac{1}{dy^2} & \forall \quad j \neq 1, ny \\ M_{z,z+nx} = M_{z+nx,z} = \frac{2}{dy^2} & \text{if} \quad j = 1 \\ M_{z,z-nx} = M_{z-nx,z} = \frac{1}{dy^2} & \forall \quad j \neq 1 \\ M = 0 & \text{elsewhere} \end{cases} \tag{5.21}$$

while the $[b]$ array is filled as:

$$\begin{cases} b_z = 0 & \forall \quad (i \neq 1, nx) \cup (j \neq ny) \\ b_z = -\frac{T_{cool}}{dx^2} & \text{if} \quad ((i = 1) \parallel (i = nx)) \cup (j \neq 1, ny) \\ b_z = -\frac{T_{cool}}{dy^2} & \text{if} \quad j = ny \cup (i \neq 1, nx) \\ b_z = -T_{cool}\left(\frac{1}{dx^2} + \frac{1}{dy^2}\right) & \text{if} \quad (i = 1 \parallel i = nx) \cup (j = ny) \\ b_z = -2\frac{\Gamma_{E,\perp}(x_i)}{k_W\, dy} & \text{if} \quad (j = 1) \cup (i \neq 1, nx) \\ b_z = -2\frac{\Gamma_{E,\perp}(x_i)}{k_W\, dy} - T_{cool} & \text{if} \quad (j = 1) \cup (i = 1, nx) \end{cases} \tag{5.22}$$

If the heat diffusion parallel to the liquid metal surface is neglected, the perpendicular flux to the liquid metal layer (SOLEDGE2D-EIRENE output) is equal to the perpendicular heat flux to the tungsten target, so $\Gamma_{E\perp}$ the array $[b]$ is the power flux perpendicular to the wall calculated by SOLEDGE2D-EIRENE. The approximation of neglecting parallel heat flux diffusion in the liquid metal is a good approximation given the extremely limited height of the liquid metal surface.

Temperature at the target, is found by inverting equation 5.19:

$$[T] = \left[\hat{M}^{-1}\right][b]\,. \tag{5.23}$$

As shown in figure 5.5, k_W depends on target temperature, thus, also the term $\frac{\Gamma_{E,\perp}(x_i)}{k_W\, dy}$ depends temperature which is a result of the calculation. For this reason, is is needed to solve equation 5.23 assuming an initial value of surface temperature T_{surf} then recalculating $[b]$ from the previous calculation of $[T]$.

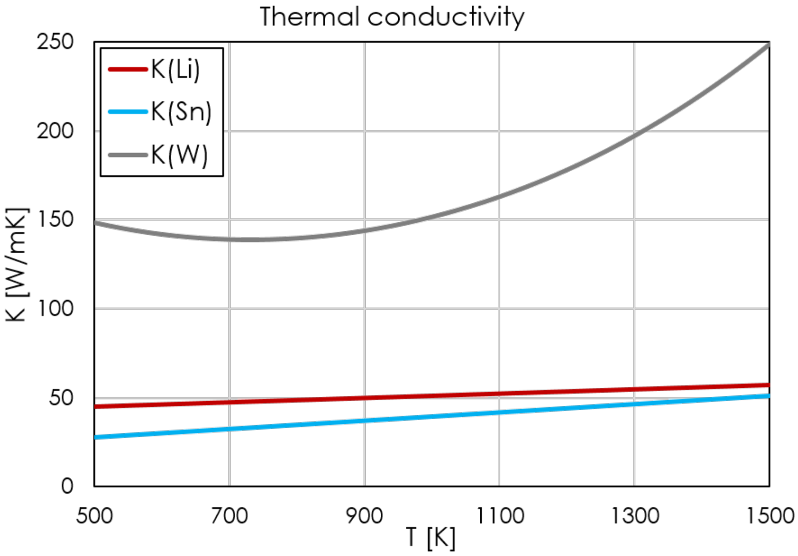

Figure 5.5: Thermal conductivity of liquid metals and tungsten as from [3] and (ADD quatation) respectively.

Fortunately, in the considered temperature range, $k_W(T)$ does not have a strong dependence on temperature, as shown in figure 5.5 so not many iterations are needed. For simplicity, it was decided to start from a uniform $T_{surf} = 700\,\text{K}$. Assuming the same input power that is assumed in figure 5.8a, the surface temperature is calculated using the previously described model and results with $1, 10, 100$ and 1000 iterations were compared. Figure 5.6 shows the difference of target temperature profiles between the single iteration case and and the other three cases; differences are minimal, it clearly shows that convergence is clearly achieved even with only 10 iterations. That is the number of iterations that has been implemented in the model.

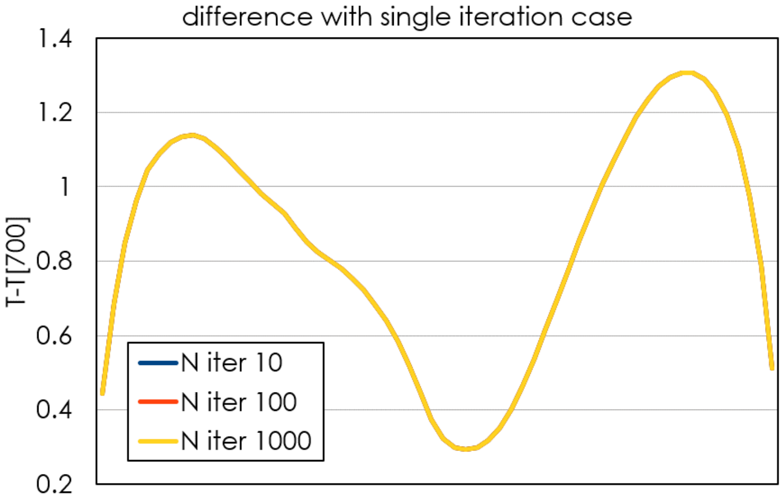

Figure 5.6: Iteration required for surface temperature calculation.

Finally, liquid metal temperature at $x = x_i$ is calculated using heat diffusion equation:

$$T_{LM}\left(x_i\right) = T_{i,1} + \frac{\Gamma_{E,\perp}\left(x_i\right)}{k_{LM}\left(T^*\right)} d_{LM}, \tag{5.24}$$

Where $k_{LM}\left(T^*\right)$ is the thermal conductivity of the liquid metal at $T = T^*$ with T^* being the temperature at the middle of the liquid metal layer depth. Again, in iteration is needed due to the dependence of this factor on temperature.

5.1.5 Model implementation in SOLEDGE2D-EIRENE

The model implementation in SOLEDGE2D-EIRENE is described in picture 5.7. Before EIRENE is called, STYX, the ensemble of routines that interface SOLEDGE2D to EIRENE, is called. One of the things that is done by STYX is calculating plasma fluxes to the wall and initialing EIRENE surfaces.

In STYX it is check if there is any liquid metal PFC, if so, it checks whether EIRENE has already been called or not. Before the first EIRENE iteration the characteristics of each liquid metal PFC are read and allocated (width, T_{cool}, number of discretization elements, liquid metal width), liquid metal surfaces are ordered clockwise on each liquid metal PFC. Since the first iteration of EIRENE is called before SOLEDGE2D, at the first EIRENE iteration, the last value of lithium recycling coefficient at the wall calculated in the previous run is used.

The heat diffusion calculation is not called in every EIRENE call by default, infact, the user

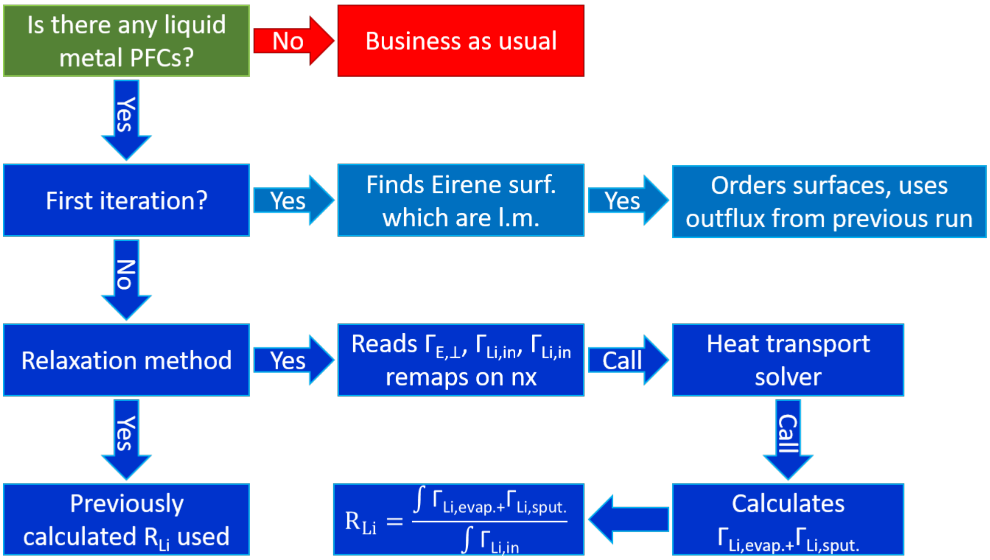

Figure 5.7: Implemented model flowchart.

can select the number of EIRENE call in between every call of the heat diffusion model.

When the heat diffusion model is the be called, STYX reads output from the last SOLEDGE2D and EIRENE iterations, reading perpendicular energy, and particle flux of deuterium and lithium (sputtering of heavier impurities has not been implemented yet). Fluxes are re-mapped over the selected discretization of the liquid metal PFC (the typical spatial discretization of the PFC is largely more detailed that the typical SOLEDGE2D-EIRENE surface length). Matrix $\left[\hat{M}\right]$ and $[b]$ are calculated, equation 5.23 is solved iteratively.

The sputtering and evaporation modules are called and the recycling coefficient of the liquid metal PFC is calculated as:

$$R_{Li-Li} = \frac{\int \Gamma_{sputt.} + \Gamma_{evap.}}{\int \Gamma_{Li,in}}, \tag{5.25}$$

where

$$\Gamma_{Li,in} = \Gamma_{in}\left(Li^{n}\right) + \Gamma_{in}\left(Li^{+1}\right) + \Gamma_{in}\left(Li^{+2}\right) + \Gamma_{in}\left(Li^{+3}\right) \tag{5.26}$$

5.1.6 Considered collisions

The implemented collisions for lithium are:

- $e^-, Li \rightarrow e^-, Li^+, e^-$ Electron impact ionization
- $e^-, Li+ \rightarrow e^-, Li^{2+}, e^-$ Electron impact ionization
- $e^-, Li^{2+} \rightarrow e^-, Li^{3+}, e^-$ Electron impact ionization
- $e^-, Li+ \rightarrow Li$ Recombination
- $e^-, Li^{2+} \rightarrow Li^+$ Recombination
- $e^-, Li^{3+} \rightarrow Li^{2+}$ Recombination

- $e^-, Li \rightarrow e^-, Li^*$ Electron impact excitation
- $e^-, Li^+ \rightarrow e^-, Li^{+,*}$ Electron impact excitation
- $e^-, Li^{+2} \rightarrow e^-, Li^{+2,*}$ Electron impact excitation

data are taken from ADAS database [2].

Elastic collisions between Li and Li or D and Li atoms have not been implemented yet. This approximation was also taken in [113]. Elastic collisions may play an important role in power dissipation only when lithium density are extremely high, especially closed divertor geometries like the vapor box configurations[127]. Lithium collisions with deuterium particles have been implemented in similar model such as Eunomia [44]. The implementation of such collisions is foreseen as a future development of this model; the relevance of such collisions may be tested against experimental data from existing machines which already test liquid metal PFC such as the linear machine MAGNUM-PSI[38][128].

5.2 Model test: dry run

Before being implemented in SOLEDGE2D-EIRENE, the model has been tested using two different SOLEDGE2D-EIRENE outputs on an analogous external script to test the model and to understand its limits. The two cases are an attached and a partially detached case. Figure 5.8a shows the temperature pattern of the attached case, while figure 5.8b shows the partially attached one. The target has been chosen to be 25 cm long.

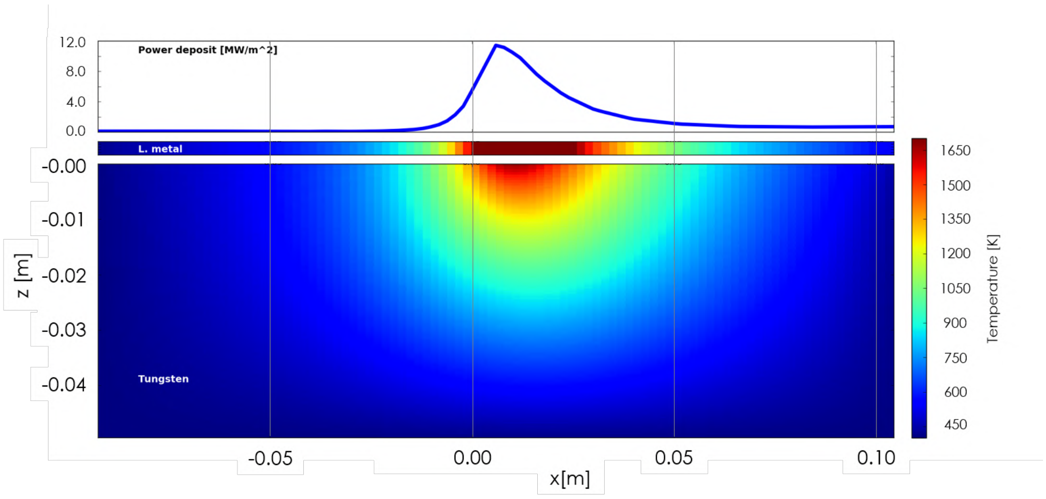

(a) Usage of attached conditions as input for thermal conduction model

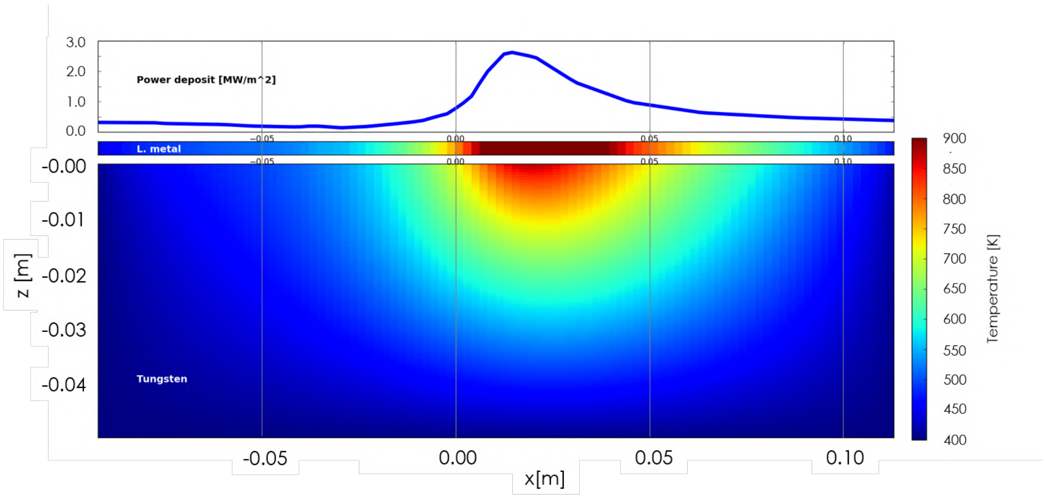

(b) Usage of detached conditions as input for thermal conduction model

Figure 5.8: Results of test of thermal conductivity model

As figure 5.8b shows, in attached cases, when heat flux is well above 10 MW/m^2, liquid metal layer temperature are above the threshold limit for the model imposed in section 5.1.

5.3 Application to SOLEDGE2D-EIRENE

The model was implemented and tested on SOLEDGE2D-EIRENE with the aim of studying the effect of liquid metal divertor in DTT.

Previous modelling of possible LMD geometry was made by Pericoli[47] with the edge code TECXY; in section 5.3.1, SOLEDGE2D-EIRENE liquid metal tool has been tested against TECXY simulations; then, in section 5.3.2 the model has been applied to study the effects of LMD implementation in DTT.

5.3.1 Comparison with previous modelling

Modelling of possible DTT liquid metal divertor solutions had been made by Pericoli [46][47]. Figure 5.10 shows the simplified geometry used for DTT modelling with TECXY. The geometry is rather simple, it uses al the available space in the vessel, the grazing angle is very large since the first wall is almost perpendicular to the poloidal projection of the magnetic field lines. The same geometry used in TECXY was used in SOLEDGE as shown in figure 5.9b

In the article, λ_q is set to be equal to 3 mm and transport parameters are uniform. Also in this modelling activity, uniform transport profiles are used $\chi = 0.3\,\mathrm{m}^2/\mathrm{s}$, $D = 0.1\,\mathrm{m}^2/\mathrm{s}$, $\nu = 1.0\,\mathrm{m}^2/\mathrm{s}$ to obtain the same λ_q. Transport coefficient were kept uniform of the all simulation domain.

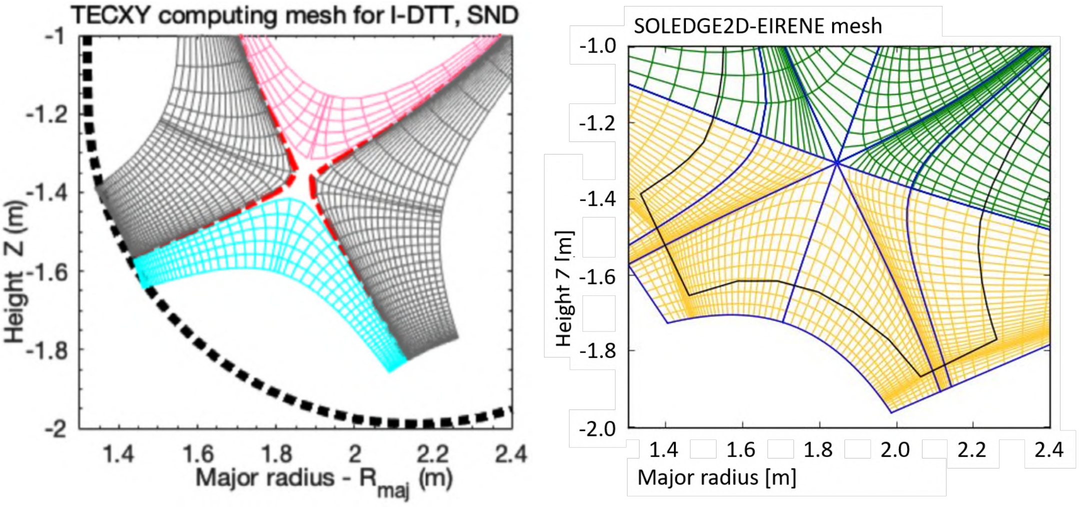

(a) Detail of TECXY geometry from in [47]

(b) Detail of SOLEDGE2D-EIRENE.

Figure 5.9: Considered liquid metal divertor geometries

In figure 5.10, the full wall geometry implemented in SOLEDGE is shown; the puffing and pumping location are in red, and the inner and outer liquid lithium targets are in green and blue respectively. We should note that the liquid metal surface is very large for this specific case, about $2.6\,\mathrm{m}^2$ for the inner divertor target and $3.3\,\mathrm{m}^2$ for the outer target.

The same input power was imposed (35MW), lithium is emitted by the liquid metal surfaces and absorbed by the tungsten surfaces were lithium particles ”stick”, deuterium puffing is set to obtain $\langle \mathrm{n_e} \rangle_{\mathrm{sep}} = 1 \times 10^{20} \mathrm{m}^{-3}$.

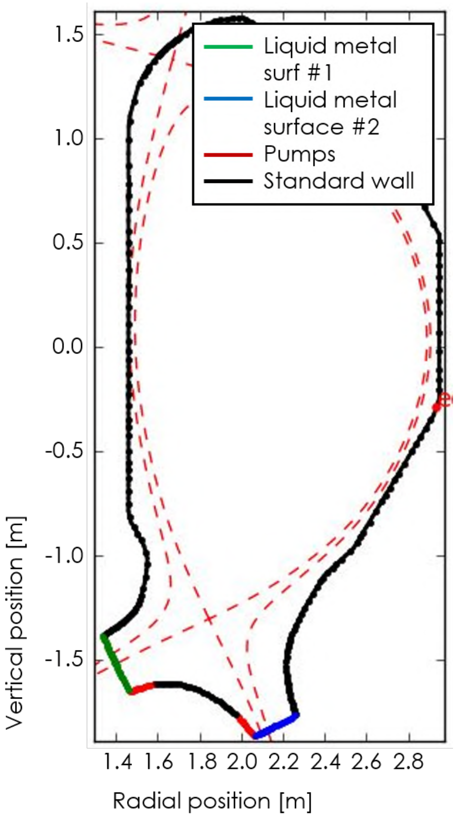

Figure 5.10: Divertor geometry in SOLEDGE2D-EIRENE made to reproduce TECXY DTT geometry studied by Pericoli.

Code	$n_{e,sep}$ $\times 10^{20} m^{-3}$	$n_{Li,sep}$ $\times 10^{19} m^{-3}$	c_{Li} %	P_{rad} MW
TECXY	1	0.25	2.5	19.6
SOLEDGE2D	1	2.4	24	11

Table 5.1: Main DTT parameters for the single null considered scenario

Table 5.1 shows the value of some "key parameters" in TECXY and SOLEDGE2D-EIRENE simulations. Similarly to Pericoli, the inner and outer divertor plasma are attached and the power flux to the divertor target is not sustainable in such condition. He concluded that heavier impurities were required to obtain sustainable conditions at the divertor and simulated argon seeded cases to obtain sustainable divertor condition and lower plasma dilution. Qualitatively similar results were found by SOLEDGE modelling of D-Li plasma, modelling with seeded impurities is not discussed in this work. TECXY simulation found a relatively low fuel dilution ($\sim 5\%$) as shown in table 5.1. In SOLEDGE case, the plasma dilution is even higher. Lithium concentration is caused by the strong lithium source at the target, the source is stronger in SOLEDGE case because the power deposition to the target is higher since the radiated power is lower in SOLEDGE case. This generates the quantitative difference between the two code outputs.

It is observed that the total radiation in TECXY case is higher even though lithium concentration is lower. The explanation for this difference was found analysing the total radiation D-only cases. Deuterium radiation is mainly given by the neutral specie, and is very high compared to what is normally observed when modelling present machines. TECXY D-only modelling predicts about 10MW radiated by deuterium in D-only DTT scenario with $\langle n_e \rangle_{sep} = 1 \times 10^{20} m^{-3}$ almost 1 order of magnitude higher than what was observed in modelling of present machines (sections 3.2 and 3.1). The overestimation of neutral radiation is given by the fluid treatment of neutrals which is generally not accurate due to the high temperature neutral which are inserted in the system, SOLEDGE evaporated neutrals are instead inserted with wall temperature distribution. What was directly observed for deuterium also happens for lithium and leads to the overestimation of plasma radiation.

The extreme fuel dilution was also found to be a major problem for liquid lithium plasma facing components also in [129] [113] and it is given by the elevate lithium evaporation rate. In the next section I analyze how and how much plasma dilution could be reduced and if it could be compatible to fusion-relevant plasmas.

5.3.2 Study on possible DTT liquid metal divertor geometry

Geometries and input parameters

The divertor geometry that was designed is an extremely closed one and is shown in figure 5.11a, it will be referred to this geometry as the standard liquid metal divertor geometry. The proposed divertor is 10 cm within the geometrical boundaries of the vessel, so there is space for tiles and cooling ducts. The closed and long divertor geometry is though to optimize impurity compression, reduce fuel dilution and plasma cooling. The lithium wetted surface is much lower than in the case analysed in the previous section, about $1.1\,m^2$ for the inner and $1.3\,m^2$ for the outer divertor, the idea was to reduce lithium emission (and consequently plasma dilution) by limiting the wetted zones only to the areas surrounding the strike points. It will be shown that those geometrical choices could successfully contain plasma dilution. Since this kind of divertor would not be made of tungsten monoblocks, the is no lower limit of the curvature radius of the targets. Both Inner and outer divertor plates, green and blue in figure 5.11a, have a grazing angle of 3°, a slightly more close divertor would have been obtained if the grazing angle was reduced to 2°. Both inner and outer divertor target are entirely considered liquid metal divertor surfaces in the simulations.

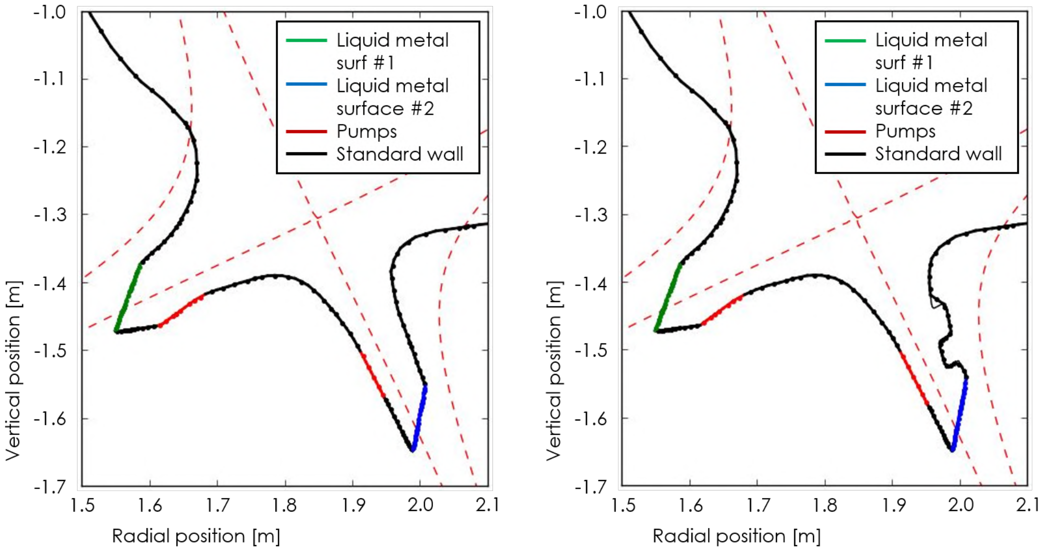

(a) Possible liquid metal divertor geometry within geometrical limits of DTT vessel.

(b) Possible vapor-box-like geometry within the geometrical limits of DTT vessel.

Figure 5.11: Considered liquid metal divertor geometries

Figure 5.11b shows the vapor-box-like geometry that will be analysed as an alternative geometry to the standard one later in this section; The geometry is the same as in figure 5.11a but the outer divertor is even more closed by a vapor-box-like structure that helps increasing neutral compression and inevitably takes some of the power flowing from the main plasma.

Both geometries have a dome in order to increase neutral compression in the divertor volume. Pumping surfaces are shown in red. Divertor and first wall can be *"hot walls"* or *"cold walls"*. When a lithium particle in-pings on a *hot wall*, typically $T_{wall} \gtrsim 300\,\mathrm{K}$, the particle is reflected, on the contrary, when it hits a *"cold wall"* ($T_{wall} \lesssim 300\,\mathrm{K}$), the particle sticks to the surface that in practice works as a pumping surface for lithium. The divertor walls, represented in black in figure 5.11, are always considered *hot walls* due to the high heat deposition from particles, radiation and conduction. The first wall (not represented in the picture) could be actively cooled or not, so both *hot* and *cold wall* conditions were tested.

The simulated liquid lithium target depth is 8 cm, similarly to tungsten monoblocks, the depth of the liquid lithium layer is assumed to be 2 mm. The poloidal length is about 11 cm for the inner target and 9 cm for the outer target. The cooling temperature imposed at the three sides of the target not exposed to the plasma is 320 K ($\sim 50\,\mathrm{C}^{\circ}$) a typical cooling water temperature. The 2D grid for solving the heat transport equation in the target is a 60×40 grid for both inner and outer divertor.

The transport parameters obtained in section 3.1 were used in this work so to have a realistic heat flux decay length and particle transport.

Input power scan

An input power scan was performed with the standard divertor geometry with two main objectives:

- Find the maximum input power which can sustained by this liquid metal PFC configuration and compare it that of the standard tungsten wall;
- Estimate plasma dilution inside the separatrix given by lithium influx.

The simulations of this input power scan are unseeded and will be compared to tungsten-wall cases with deuterium-only simulated in chapter 4.2.3.

In a liquid lithium target, similarly to a carbon wall and differently to a tungsten one, there is almost no limit on plasma temperature in front of the target. In a metal machine the maximum target temperature is approximately 5-10eV to limit tungsten sputtering because only a minimum tungsten concentration is allowed in the plasma core. One of the technical limits is the maximum power flux peak that can be sustained by these targets which is about . The second operational limit is the target temperature: if the target exceeds the boiling temperature (1615 K) the lithium influx is not controlled and bubbles formation or spray may occur. Lastly, the implemented sputtering model and the thermal conductivity of lithium have a upper limit for their validity which is about 1400 K, this is not a technical limit for the target, but is a limit above which simulations outcome may be less reliable.

The simulations are performed assuming the first wall to be hot, so lithium particles impacting on the first wall (not made of lithium) are reflected. The pumping of lithium is made by the pumping surfaces as much as for deuterium. As in chapter 4.2.3 deuterium pumping speed was set to $100\,\mathrm{m}^3/\mathrm{s}$. The albedo on pumping surfaces for lithium was set to obtain an effective lithium pumping speed of $20\,\mathrm{m}^3/\mathrm{s}$, this values is arbitrary and is taken with the assumptions that the pumping system would extract a certain fraction of lithium and not only deuterium. This is an approximation since in a liquid metal environment pumps won't be available and the metal collected at the wall would be recirculated to the CPS.

In the power scan, the input power was varied from $P_{in} = 8.5\,\mathrm{MW}$ to $P_{in} = 16\,\mathrm{MW}$. The power is equally shared between electrons and ions.

In figure 5.12 the profiles at the target obtained with the power scan are shown. Figures 5.12b, 5.12c and 5.12d show inner target electron density, temperature and power deposition; figures 5.12e, 5.12f and 5.12g show the same parameters at the outer target.

The inner target is detached in the $P_{in} = 8.5\,\mathrm{MW}$ case. With the increase of input power, target temperature and power deposition increase at both inner and outer target, until with $P_{in} = 16.0\,\mathrm{MW}$ the critical value of $15\,\mathrm{MW/m}^2$ is reached. Although this kind of targets could sustain a transitory power flux higher $15\,\mathrm{MW/m}^2$, this can be considered as the steady state limit. With the increase of the deposited power flux and the consequent increase of target temperature, the sputtering and evaporation rates of lithium increases; lithium concentration increases with higher input power (figure 5.13e). This is the self regulating mechanism of liquid metal targets: when power flux is increased, the target element concentration in the plasma is increased, thus increasing power radiation and partially reducing the power deposited to the targets. The mechanism has some limits which are of opposite nature for lithium and tin: in

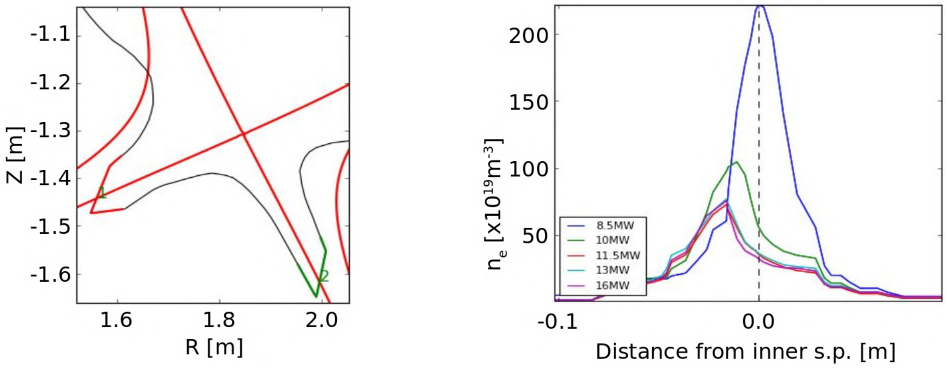

(a) DIvertor geometry view.

(b) Electron density at inner target.

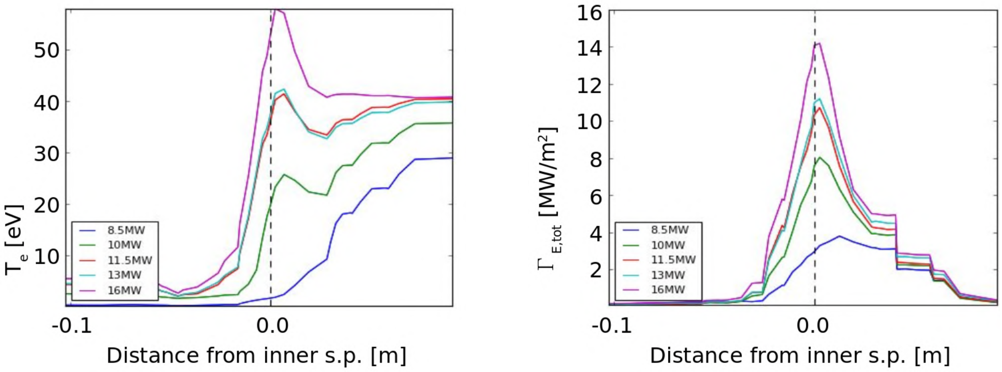

(c) Electron temperature at inner target.

(d) Power deposition at inner target.

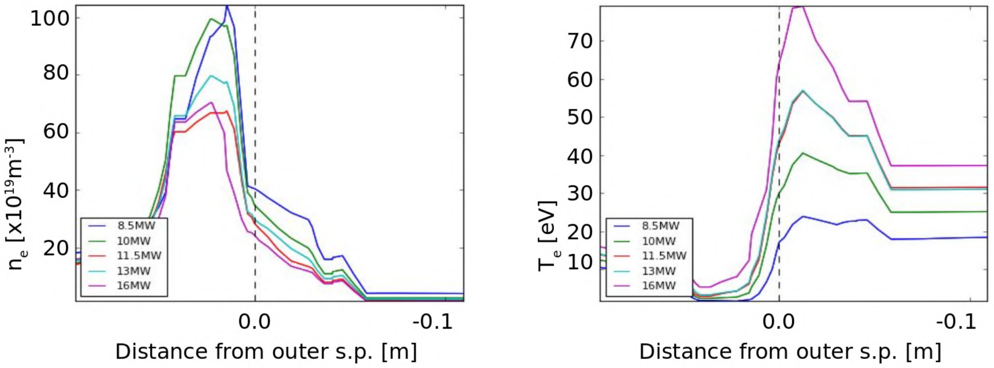

(e) Electron density at outer target.

(f) Electron temperature at outer target.

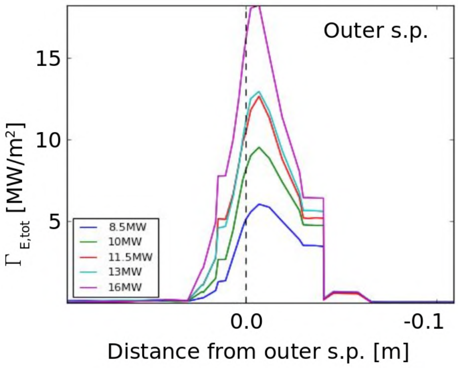

(g) Power deposition at outer target.

Figure 5.12: Electron density, temperature and power deposition to the inner and outer target.

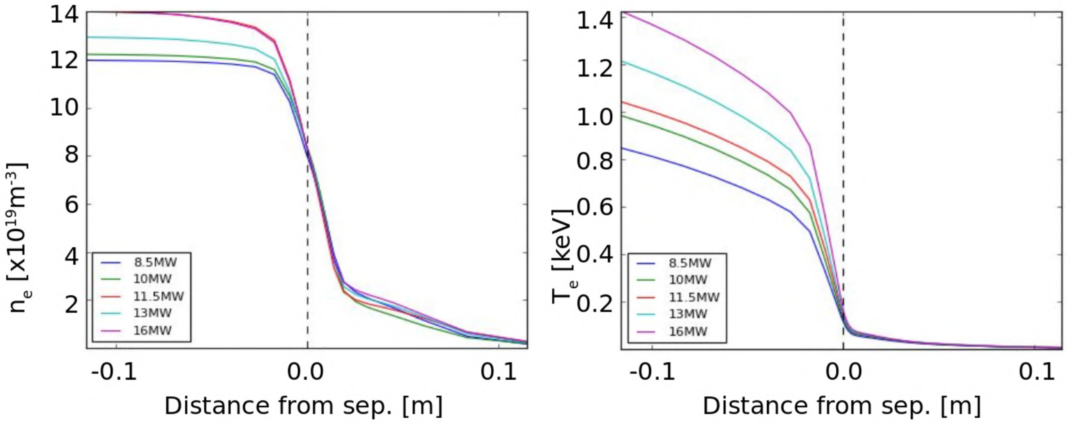

(a) Electron density profiles at mid-plane.

(b) Electron temperature profiles at mid-plane.

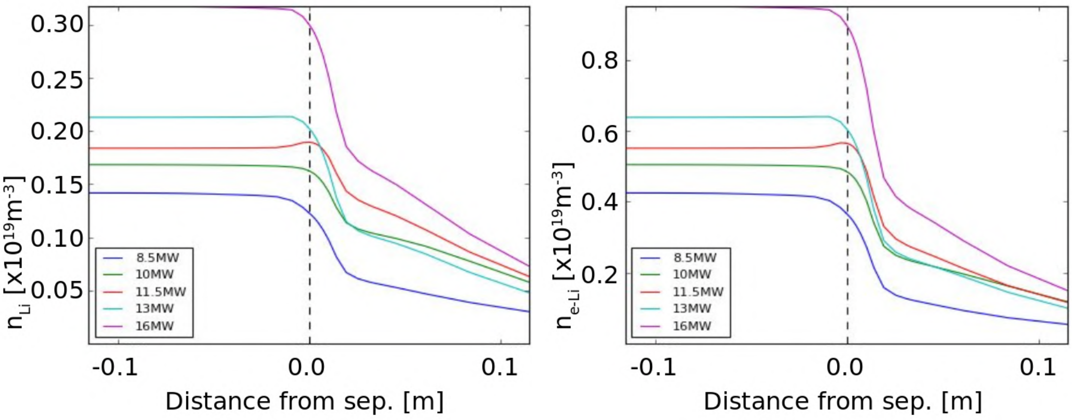

(c) Lithium density profiles at mid-plane.

(d) Electron density given by lithium.

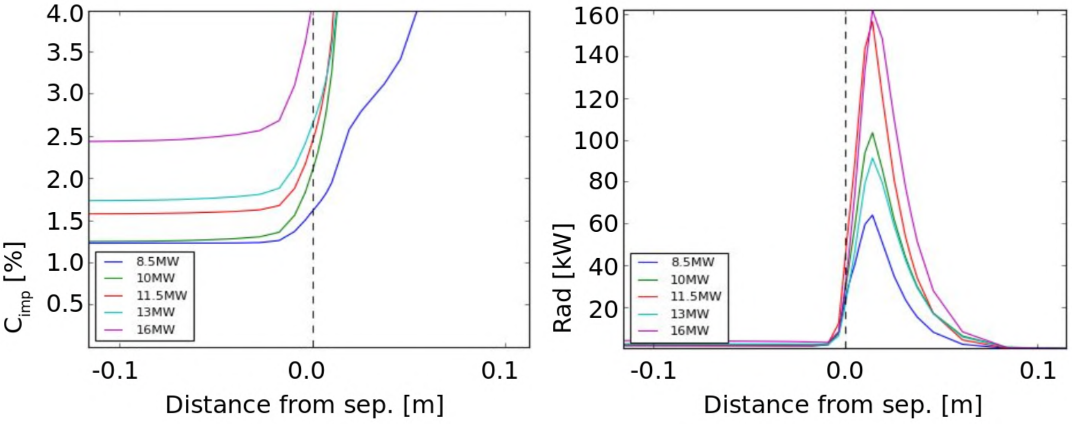

(e) Lithium concentration profile at midplane.

(f) Radiation profile at mid-plane.

Figure 5.13: Main parameter profiles at mid-plane for the performed input power scan.

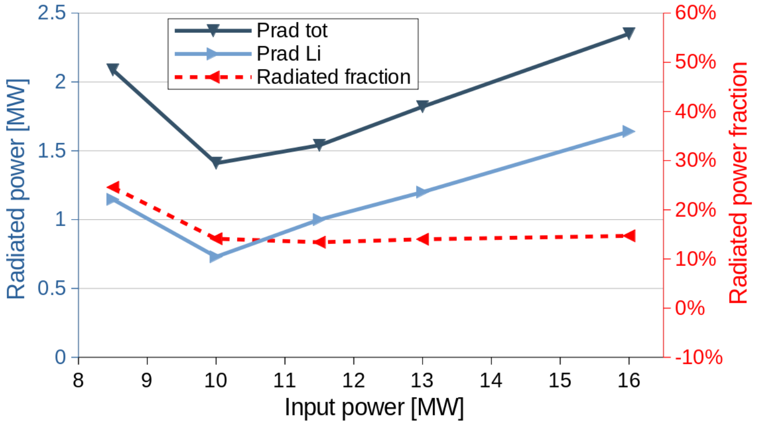

Figure 5.14: Total radiated power, power radiated by lithium and total radiated power fraction for simulation of the input power scan.

lithium case the limited cooling efficiency can not increase radiated power enough so to reduce power flux to the targets below the nominal limit (figure 5.12g); for tin, the elevate Z of the material can increase radiation inside the separatrix, thus reducing core performances. Lithium concentration and core radiation are not a concern since core radiation is almost null and lithium concentration is only 2.5% in the maximum input power case. The contribution to n_e given by lithium is consequently negligible as well (figure 5.13d).

Figure 5.14 shows the total power dissipated in each of the simulations as well as that dissipated only by lithium radiation, the difference between the two lines is deuterium radiation. Lithium radiation is obviously higher than deuterium one, but they are in the same order of magnitude, while in the cases analysed in sections 4.2.2 and 4.2.3 deuterium radiation was negligible, not because deuterium radiation was lower in those cases, but because neon and argon radiation was much higher due to their higher cooling efficiency. When input power is increased, radiated power fraction is always very low but in the $P_{in} = 8.5 MW$ case where the inner target is detached. this is due to the fact that lithium cooling efficiency is very low when $T_e > 50\,\mathrm{eV}$, lithium radiation in fact is almost null in the core (figure 5.13f and 5.15) and is concentrated in the SOL and in the divertor region in front of the targets. Radiated power if figure 5.14 is not a monotonous decreasing function of input power because of the feedback mechanism described in the previous paragraph; radiation is high in the detached case(8.5 MW), decreases with the increasing of plasma temperature (10-11.5 MW) and increases again when lithium concentration rapidly increases (13 and 16 MW) due to target heating. The total radiated power fraction instead is constant in all cases with both inner and outer divertor attached, thus meaning that the fraction of power deposited to the target is also constant, this is a further proof that the feedback mechanism of lithium radiation can partially mitigate power flux to the divertor.

When input power is increased to $P_{in} = 16\,\mathrm{MW}$, the maximum input power to the outer target reaches the technical limit of $\sim 15\,\mathrm{MW/m^2}$ (figure 5.12g), while electron temperature at the target is lower than 100 eV (figure 5.12f, while there is no major concern for the inner target. Figure 5.16 shows the inner and outer target average temperatures for each simulation. The average temperature is not a simple average over the liquid metal surface whose value would

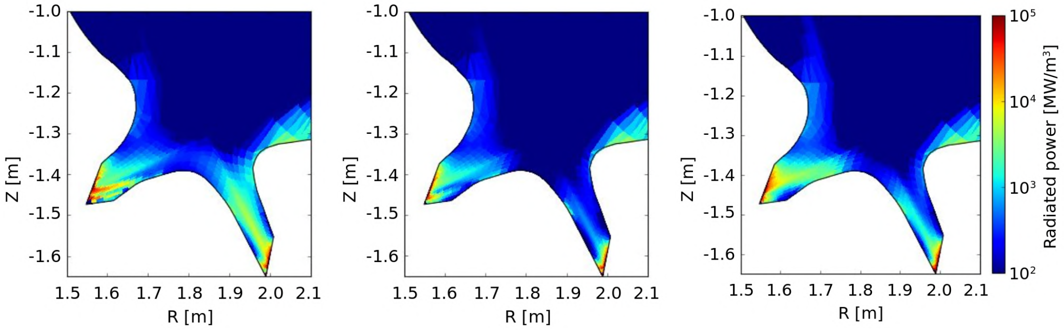

(a) Power radiated in the divertor region for the P_{in} = 8.5 MW case.

(b) Power radiated in the divertor region for the P_{in} = 10.0 MW case.

(c) Map of power radiated in the divertor region for the P_{in} = 13.0 MW case.

Figure 5.15: 2D view of radiated power. Radiation is high in the detached case due to high cooling efficiency (5.15a), is reduced when plasma attaches (5.15b) and increases again with the increase of lithium concentration (5.15c)

depend on target extension, but it is instead calculated as the average temperature seen by in-pinging deuterium particles:

$$\langle T \rangle_{tar} = \frac{\sum \Gamma_D(l) T(l)}{\sum \Gamma_D(l)}, \tag{5.27}$$

with a weight given by deuterium flux, so it is not much different from the maximum target temperature. In the $P_{in} = 16$ MW case, the limit target temperature ($T_{lim} = 1605$ K) is almost achieved by the average target temperature calculated with equation 5.27 and it is locally obtained.

In the $P_{in} = 16MW$ case, average net lithium flux from the target calculated as:

$$\left\langle \Gamma^{net} \right\rangle_{tar} = \langle \Gamma_{evap} + \Gamma_{sputt} - \Gamma_{in} \rangle_{tar} = 3 \times 10^{23} \text{Li/sm}^2. \tag{5.28}$$

This value is within the tested technological limits of existing capillary porous systems[39].

In sections 4.2.3, it was demonstrated that, for DTT single-null scenario using the validated set of transport parameters, a similar connection length and a tungsten wall with deuterium only plasma, the maximum input power to obtain sustainable conditions at the outer divertor was $P_{in} \simeq 8$ MW. With a liquid lithium wall the maximum input power is doubled. The 8 MW difference is only partially given by lithium radiation which only radiates about 1.7 MW in the $P_{in} = 16.0$ MW case. The maximum input power difference between the two divertor types is mainly due to the capability of liquid lithium to sustain high electron temperature in front of the targets (figures 5.12c and 5.12f) without damaging the divertor structure, without polluting and diluting the main plasma 5.13e and without radiating in the main plasma 5.13f.

For these reasons, liquid lithium divertor are a valuable solutions for power exhaust in future machine and their test and implementation could bring major advantages with respect to conventional tungsten divertors. In the next paragraphs it will be briefly discussed how some minor adjustments could increase even more the performances of such divertor.

Better performances and higher maximum input power (possibly up to $P_{in} = 20$ MW) could have been achieved: by reducing the grazing angle or by using smaller targets. By reducing the

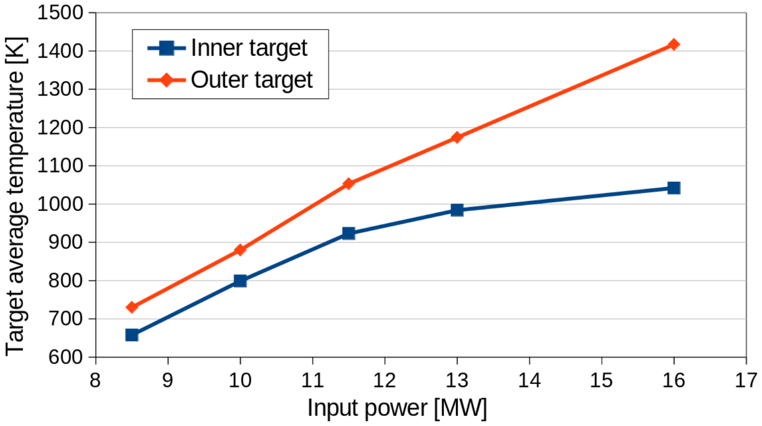

Figure 5.16: Average temperature at the inner and outer target.

grazing angle, the consequent reduction of the power flux per unit of area (for example by a factor ∼ 2/3 if the grazing angle was reduced to 2°) would have lowered the target temperature which was proven in the previous section to be the major limitation to liquid metal targets. Since temperature is the limit of these targets, the definition of an optimal grazing angle would be of major importance to estimate the power exhaust performances those targets; in this preliminary study, the grazing angle was set to 3° to test the target under geometrical condition which are analogous to future ITER divertor and also DTT divertor which is expected to operate with a grazing angle of 2/3°. Furthermore, by keeping the same connection length and reducing the grazing angle, the divertor closure would have been enhanced, with consequent benefits on power dissipation by radiation.

By reducing the size of the targets (both in length and depth) or the position of the cooling pipes, the maximum target temperature would have been reduced. Although, this could be seen more as a numerical trick than a physical solutions. Elevate temperature gradients in tungsten could lead to damaging or cracking of the alloy. These kind of phenomena are not treated in this work, but in future target designing, the size of tungsten targets must take into account both the constructive limits given by tungsten structure and the consequent expected power flux profiles. In this modelling we have been extremely cautious using target dimension which are comparable to current tungsten monoblocks, it was proven that liquid metal PFC could be made smaller than monoblocks due to their higher thermal conductivity [29]. When comparing SOLEDGE2D-EIRENE simulations to the experimental data the modelled target depth should be adapted to match the cooling scheme of the PFC which is experimented. Lastly, the introduction in the model of heat flux conduction parallel to the target surface could reduce the target temperature peak.

Although minor adjustments may increase the maximum input power, impurities are needed for full power scenario. To simulate seeded scenarios, it is needed to implement seeded impurities sputtering since medium Z impurities such as neon or Argon normally have a sputtering yield much higher than deuterium and lithium. The implementation of sputtering by medium Z impurities is needed to correctly evaluate total lithium content.

Effect of vapor box divertor and wall temperature on power exhaust and impurity concentration

The vapor-box-like divertor geometry shown in figure 5.11b was tested as a more closed geometry alternative to the standard one shown in figure 5.11a. The vapor box[127] should allow a higher neutral compression in the divertor area and higher cooling effectiveness. The study of a closed divertor geometry like the vapor box geometry fully utilize SOLEDGE2D-EIRENE capability of extending plasma domain to the wall. The studied geometry is not a completely closed vapor box like that proposed by Schwartz [128], but is an adaptation to the shape of DTT vessel and the shape of magnetic surfaces of DTT single-null reference scenario. The magnetic surfaces which are intersected by the two closures that make the vapor-box structure are spaced at mid-plane about 5.5 and 7.5 mm apart (about three and four times the expected $lambda_q$) outside of the separatrix, the closure next to the liquid metal target being the closer to the separatrix. In the standard divertor case the distance between the divertor closure and the separatrix was about 6 times λ_q. The basic idea is to have progressively closer closures so to spread the power coming from the main plasma that does not flow directly to the main target. The liquid metal target has the same dimension and characteristics of the standard geometry case. The inner target remains the same.

A case analogous to the $P_{in} = 11.5\,\mathrm{MW}$ one simulated in the previous section was used for the vapor-box-like geometry to test the effect of the geometry on power exhaust and impurity content in the core.

The comparison between the case with standard divertor and with vapor-box-like divertor is shown in figure 5.17. Power deposition to the target (figure 5.17a) is compatible to the standard divertor case; this result is obtained with an impurity concentration in the core four times lower than in the standard divertor case (figure 5.17b. The enrichment factor, calculated as the radio between impurity flux to the divertor and impurity concentration in the core is twice as big for the vapor box geometry, thus implying that impurities are confined to the divertor twice better than in the standard geometry.

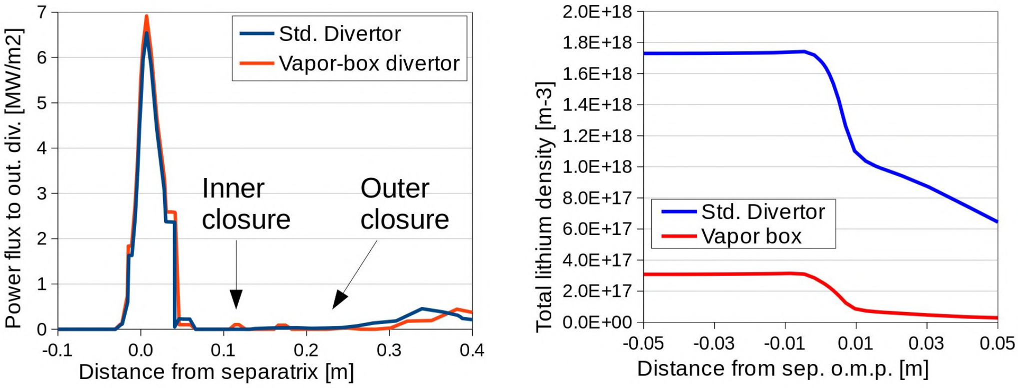

(a) Power flux to the outer divertor.

(b) Lithium density at outer mid-plane.

Figure 5.17: Comparison between standard and vapor-box-like divertor in a $P_{in} = 11.5\,\mathrm{MW}$ case. The power flux is always below $1\,\mathrm{MW/m^2}$ in both closures because particle flux is negligible

Figure 5.18 show the deuterium density and electron temperature at the outer divertor in the vapor-box-like geometry case simulated. The two peaks on electron temperature (figure 5.18b) corresponds to the two closures of the vapor-box configuration. The power flux to the closures (figure 5.17a) is in both cases below 1 MW/m^2 which can easily be sustained by a actively cooled standard tungsten block. The condition is sustainable because deuterium particle flux to the closures is negligible with respect to the flux to the liquid metal target. This condition must be satisfied when designing a vapor box divertor geometry.

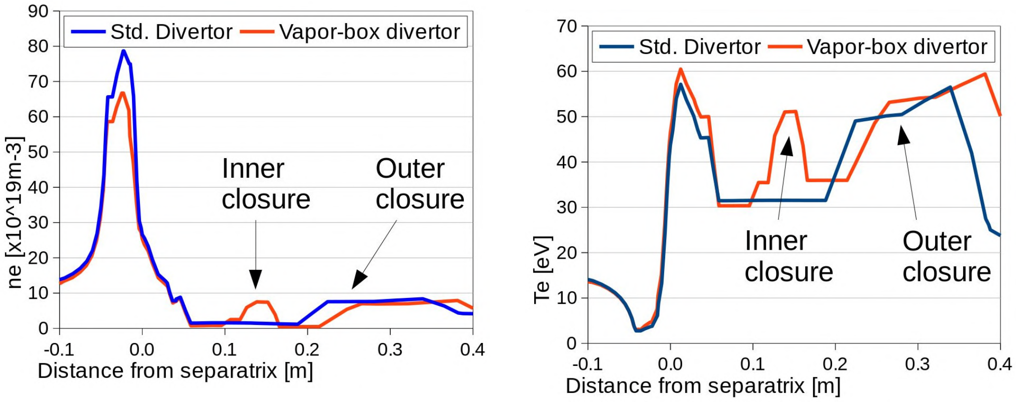

(a) Total lithium concentration at outer mid-plane.

(b) Electron temperature at the outer target.

Figure 5.18: Particle and power flux to the outer target and electron temperature at the target in the vapor-box-like simulation. The positions of the first and second closure are indicated in the pictures.

The vapor box configuration is not particularly suitable for this specific configuration in DTT because of the magnetic surface shapes that limit divertor closure. A longer divertor geometry as the X-divertor or the super-X divertor would better suite a test of closed liquid metal divertor. These geometries would allow higher divertor closure by exploiting the flux compression area along the divertor leg. Nevertheless, even this single null configuration has the ability of drastically reducing impurity content in the core increasing the enrichment by a factor 2, without obtaining relevant power fluxes to the vapor-box closures. The effect of a closed liquid metal divertor geometry would be even more pronounced in detached conditions where neutral impurity flux to the main plasma must be limited.

In the previous simulations it was assumed that the first wall of DTT was a *hot wall* meaning that first wall temperature was high enough to reflect in-pinging lithium particles. To make the comparison between hot and cold wall, the same vapor-box geometry simulation of the previous case was modelled with cold first wall; the divertor area and the vapor-box is still considered hot due to the high power flux received by both particles and radiation. For the *cold wall* case, lithium pumping was neglected since lithium absorption by the wall already serve this purpose.

Figure 5.19 shows the comparison between the two cases. Lithium concentration is reduced in the main plasma by a factor four, as shown in the figure. This has almost no impact on power exhaust (figures 5.19b and 5.19c because lithium radiation is negligible due to the low lithium concentration in the plasma.

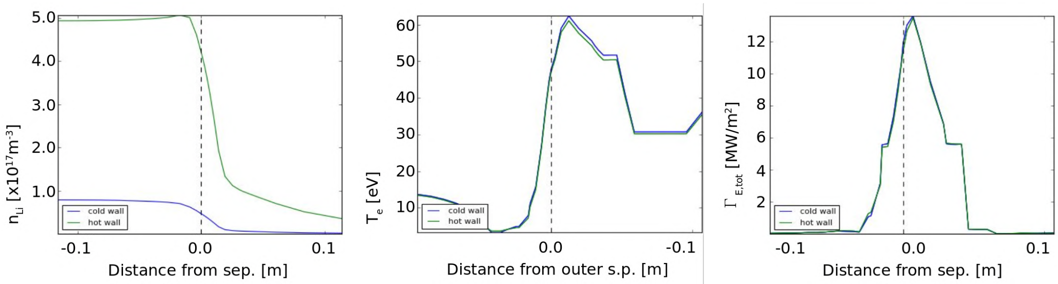

(a) Lithium density at outer midplain

(b) Electron temperature at outer target

(c) Total power flux to the outer target.

Figure 5.19: Comparison between a vapor-box divertor with a cold and a hot first wall, with a cold wall lithium density in the main plasma is reduced by a factor 4.

5.4 Future studies

The study of liquid metal surface as possible alternative divertor solutions with SOLEDGE2D-EIRENE will continue both on the experimental and modelling side.

The model should be tested against experimental data to learn how to match those data and if changes to the code are required. Experiments ongoing at MAGNUM-PSI on liquid metal targets[27][38] are ideal to test the code against experimental data. Experiments coupled with modelling could also help understand and estimate some of key values included in the model like the effect of lithium hydrate (β parameter in the model) and estimate heat transport in a complex system such as the porous systems which are used as liquid metal PFCs. Experiments for testing of a vapor-box-like structure at MAGNUM-PSI have also been proposed [128], the penalization technique implemented in SOLEDGE2D-EIRENE could perfectly match the modelling requirements of such experiments.

The study of the relevance and possible inclusion of other collision in the simulation (such as D-Li collisions) could be made with both experimental and modelling approach.

Possible implementation of tin as liquid metal PFC component in SOLEDGE2D-EIRENE is subordinate to the definition of bundles and subsequent validation against experimental data.

The impact of reactor-relevant medium-Z impurities such as neon and argon will be studied by implementing the relative sputtering reactions. Due to its high cooling efficiency at high plasma temperature and the capability of lithium of liquid metal divertor to resist high electron temperatures, argon could be ideal for liquid metal divertors, but the combined effect of lithium and argon should be first evaluated with this kind of modelling.

Chapter 6

Conclusions

This thesis presents the work carried out during the three years of my PhD. Power exhaust mitigation is one of the major challenges for future reactor-relevant machines such as DEMO. In the path (”iter” in Latin) to DEMO, the experimentation of ITER highly-radiative baseline scenario, equipped with a standard single-null divertor with tungsten monoblocks, will test standard divertor solution under fusion-relevant conditions. To mitigate the risk that this scenario will not be suitable when extrapolating from ITER to DEMO, current and future fusion machines will study alternative solutions alongside ITER. Two of the devices that will play a major role in testing plasma scenarios that can be scaled to DEMO, are DTT and JT-60SA. The main goals of my PhD activity were modelling of edge plasma of these two tokamaks, studying their characteristics defining scenario characteristics and proposing possible improvements.

The modelling activity began from the analysis of current experiments using SOLEDGE2D-EIRENE. This analysis was divided into the modelling of W-wall machines for transport parameters definition towards DTT modelling and the modelling of C-wall JET discharges to identify transport and plasma-wall interaction parameters to model JT-60SA equipped with carbon wall.

The modelling of C-wall JET discharges began by identifying a pulse that could be considered relevant for the determination of JT-60SA transport parameter determination. I identified a pulse with a similar magnetic field, q, plasma density and plasma volume. I determined transport coefficients by comparing modelling output with experimental data such as the density at mid-plane from Thompson scattering, total and line radiation from bolometer and spectroscopy. The analysis of carbon line emission also allowed the validation of the model utilized for carbon sputtering evaluation. I found no need to add carbon recycling factor to reproduce carbon emission data, since the Bohdansky sputtering model could correctly estimate carbon content.

Similarly to what I did for C-wall modelling, I derived a homogeneous set of transport parameter profiles for DTT by modelling four different JET discharges with ILW. I derived the transport profiles by successfully comparing simulation results with experimental data like electron temperature and density at mid-plane from Thompson scattering (and their fit made with EPED at 95% of ELM cycle), radiative emission from bolometry, line emission from spectrometer and plasma density and temperature in the divertor region from Langmuir probes measurements. I proved that to set of transport profiles is compatible with those obtained by

SOLPS-ITER modelling from the same pulses. I also compared the transport parameters to those obtained from C-MOD modelling with SOLEDGE2D-EIRENE which were compatible with those obtained with JET simulations. The transport profiles for DTT modelling were defined by scaling the transport profiles derived from this modelling activity by a numerical factor, derived by the 2-point model, which takes into account the scenario differences between DTT and JET or DTT and C-MOD.

I modelled JT-60SA fully inductive low-density full-power scenario using the transport profiles that were derived from the modelling activity on JET equipped with C-wall. First I proved that the minimum electron density to obtain sustainable conditions at the divertor target was $\langle \mathrm{n_e} \rangle_{\mathrm{sep}} = 2.0 \times 10^{19}\mathrm{m}^{-3}$. I estimated that the maximum auxiliary input power that gave sustainable power flux to the outer divertor in the unseeded scenario was $P_{aux,max} \simeq 21\,\mathrm{MW}$. I found that argon provided better cooling performances than neon and I estimated that, with the plasma purity foreseen, the maximum input power was 33 MW for argon and 30 MW for the neon seeded scenario. The scenario with 41 MW of input power (full-power) was sustainable only if the condition on plasma purity was relaxed from $\eta = 0.8$ to $\eta = 0.7$.

I used plasma and neutral density, temperature and radiative emission of attached and detached plasma simulations with neon, argon or without impurity seeding to test the effectiveness of the JT-60SA divertor spectrometer to identify divertor plasma state.

By using the transport parameters validated against experimental data, I found an operative range of plasma parameters for the DTT full-power single-null scenario, which allows operating in h-mode with detached divertor plasma. I demonstrated that Argon gives the best cooling performance compared to neon and nitrogen since it requires lower impurity concentration and Z_{eff} to obtain sustainable conditions at the divertor plates. I proved that, with a separatrix density $\langle \mathrm{n_e} \rangle_{\mathrm{sep}} = 8 \times 10^{19}\mathrm{m}^{-3}$ detachment could be achieved with reasonable $\langle \mathrm{Z}_{eff} \rangle_{sep}$. I analyzed the impact of deuterium fueling of neutral penetration and found an optimal fueling position. I performed a scan on possible outer divertor geometries, compatible with DTT design, to test the capability of connection length and divertor closure to facilitate detachment onset. I demonstrated that, in D-only scenarios, both divertor characteristics highly influence detachment onset, with divertor closure playing a major role. After having added impurity seeding to the modelling, divertor closure played and divertor connection length still played a relevant role in facilitating detachment transition. When I compared the impurity concentration required to achieve similar power dissipation by radiation in different divertor geometries, I proved that the tested divertor geometries don't play a relevant role in confining the impurities to the divertor region. This behaviour was due to the depth of the achieved plasma detachment that lowers neutral confinement in the divertor region. Plasma and neutral profiles of attached and detached seeded simulations were successfully used as a test for the capability of the DTT divertor interferometer to distinguish between the two plasma states. I analyzed the impact of ECRH duct aperture on plasma density, proving that the additional pumping given by the simultaneous opening of all the ECRH ducts could be counterbalanced by a feedback system on the fueling rate.

I found a hysteretical-like behaviour of cooling performances simulating seeded discharges. A scan on impurity seeding was performed for a DTT case starting from detached plasma condition, reducing the impurity content until attachment and hereafter, increasing them again until detachment onset. I proved that attachment and re-detachment do not follow the same path, meaning that different impurity concentrations are required to move from attachment to detachment and from detachment to attachment. This behaviour is mainly due to the different electron temperatures typical of the two plasma states which imply higher or lower cooling efficiency of the seeding impurities. I also proved that some other factors, like neutral compression and pressure conservation, also played a role in the onset of the hysteretical behaviour.

Liquid metals are proven to be a valuable alternative divertor configuration to standard tungsten divertor for power exhaust mitigation in fusion-relevant machines; their possible experimental test is considered in the DTT project. Towards possible implementation in a fusion-relevant machine, careful modelling should be performed to study the advantages and disadvantages of liquid metal divertors. To do so, I added to SOLEDGE2D-EIRENE a self-consistent model that simulates heat transport and particle emission in a CPS-based actively cooled liquid metal PFC. The model calculates the power and particle flux to the liquid metal target and heat dissipation through the PFC, calculates the temperature profile of the liquid metal surface and in the CPS accordingly to the power flux, cooling temperature and CPS dimensions. This tool also takes into account target composition and temperature to calculate particle evaporation rate and sputtering yield by taking into account physical, thermal and chemical contributions to sputtering. I tested this model on the DTT single-null scenario with lithium as the liquid metal element. I proved that in unseeded simulations the input power could be raised to $P_{in} = 16\,\mathrm{MW}$ still obtaining sustainable conditions at the divertor targets, which is twice the maximum input power for D-only cases with tungsten monoblocks. It was proven that the major advantage of LMDs is the ability to sustain high electron temperatures and power fluxes without excessively diluting the main plasma or radiating in the main plasma itself. A passive feedback system that reduces power deposition by increasing lithium content was found, although power radiation by lithium was found to play a minor role in making the gap in power exhaust capabilities between scenarios with LMD and those with a metallic wall. In DTT single-null scenario, impurity seeding is needed to obtain sustainable conditions at the divertor targets. I proved that both the vapour-box divertor and the cold wall conditions could help reduce even more lithium concentration in the plasma core and increase plasma purity, which is a crucial parameter for future reactors. Possible seeded impurities could enhance lithium sputtering, divertor geometry and first wall temperature control could help reduce lithium concentration in such regimes. A closed geometry as the vapour box helps the detachment onset, an input power scan could confirm this hypothesis with or without impurities.

Bibliography

[1] Q Wu and al. Energy consumption transition and human development. *Monash University*, 2010.

[2] The-ADAS-Project. Open-adas database. `https://open.adas.ac.uk/`. Version 2.1.

[3] G. Giordanengo and et al. Thermal conductivity of liquid metals and metallic alloys. *Journal of Non-Crystalline Solids*, 250-252:377–383, 1999.

[4] R. Martone and al. eds. *DTT Divertor Tokamak Test facility Interim Design Report: A milestone along the roadmap to the realisation of fusion energy.* 2019.

[5] T. Eich and al. Scaling of the tokamak near the scrape-off layer H-mode power width and implications for ITER. *Nuclear Fusion*, 53(9), sep 2013.

[6] T. Eich and et. al. Turbulence driven widening of the near-sol power width in asdex upgrade h-mode discharges. *Nuclear Fusion*, 60, 2020.

[7] JT-60SA Research Unit. JT-60SA Research Plan. 2020.

[8] Smil V. *Energy Transitions: Global and National Perspectives.* 2016.

[9] IEA. *Energy access outlook 2017: from poverty to prosperity.* Tech. rep., International Energy Agency, Paris, France.

[10] IEA, Paris. World gross electricity production by source. 2019.

[11] P. Stangeby. *The Plasma Boundary of Magnetic Fusion Devices.* 2000.

[12] H. Bufferand and al. Near wall plasma simulation using penalization technique with the transport code SOLEDGE2D-EIRENE. *Journal of Nuclear Materials*, 438(SUPPL), 2013.

[13] H. Bufferand and al. Numerical modelling for divertor design of the WEST device with a focus on plasma-wall interactions. *Nuclear Fusion*, 55(5), may 2015.

[14] G. Ciraolo and et al. Investigation of edge and sol particle flux patterns in high density regimes using soledge2d-eirene code. *Contributions to Plasma Physics*, 54:432–436, 2014.

[15] S.I. Braginskii. Transport processes in plasma. *Reviews of plasma physycs*, 1:205–311, 1965.

[16] V.M. Zhdanov. Transport processes in multicomponent plasma. *Taylor Francis,*, 2002.

[17] H. et al. Bufferand. Three-dimensional modelling of edge multi-component plasma taking into account realistic wall geometry. *Nuclear Materials and Energy*, 18:82–86, 2019.

[18] V. Rozhansky and et al. New b2solps5.2 transport code for h-mode regimes in tokamaks. *Nuclear Fusion*, 49(2):025007, jan 2009.

[19] X. Bonnin and et al. Presentation of the new solps-iter code package for tokamak plasma edge modelling. *Plasma Fusion Res.*, 11, 2016.

[20] G.D. Porter and et al. Uedge simulation of edge plasmas in diii-d double null configurations. *Physics of Plasmas*, 17, 2010.

[21] A.V. Chankin and et al. EDGE2d-EIRENE modelling of near SOL e r: possible impact on the h-mode power threshold. *Plasma Physics and Controlled Fusion*, 59(4):045012, mar 2017.

[22] S. Wiesen and al. On the role of finite grid extent in solps-iter edge plasma simulations for jet h-mode discharges with metallic wall. *Nuclear Materials and Energy*, 17:174–181, 2018.

[23] D. et al. Reiter. The eirene and b2-eirene codes. *Fusion Science and Technology*, 47:172–186, 2005.

[24] D. Reiter. The data file amjuel additional atomic and molecular data for eirene. Version January 13, 2020.

[25] The data file HYDHEL:. The data file hydhel: Atomic and molecular data for eirene based upon: “elementary processes in hydrogen-heliumplasmas. Version January 13, 2020.

[26] J.H. You. European demo divertor target: Operational requirements and material-design interface. *Nuclear Materials and Energy*, 9:171–176, 2016.

[27] T.W. Morgan and al. Liquid metals as a divertor plasma-facing material explored using the pilot-PSI and magnum-PSI linear devices. *Plasma Physics and Controlled Fusion*, 60(1):014025, oct 2017.

[28] G. Pintsuk and al. High heat flux testing of newly developed tungsten components for west. *Fusion Engineering and Design*, 173:112835, 2021.

[29] S. Rocella and al. Cps based liquid metal divertor target for eu-demo. *Journal of Fusion Energy*, 39, 2020.

[30] H. Zohm and et al. 57(8):086002, jun 2017.

[31] B.N. Sorbom and et al. Arc: A compact, high-field, fusion nuclear science facility and demonstration power plant with demountable magnets. *Fusion Engineering and Design*, 100:378–405, 2015.

[32] J.W. Coenen and al. Liquid metals as alternative solution for the power exhaust of future fusion devices: status and perspective. *Physica Scripta*, T159:014037, apr 2014.

[33] M.A. Jaworski and al. Liquid-metal plasma-facing component research on the national spherical torus experiment. *Plasma Physics and Controlled Fusion*, 55(12):124040, nov 2013.

[34] S. V. Mirnov, E. A. Azizov, V. A. Evtikhin, V. B. Lazarev, I. E. Lyublinski, A. V. Vertkov, D. Yu. Prokhorov, and T. K. Soboleva. Perspectives of the lithium capillary-pore system application in fusion: Experiments with lithium limiter on t-11m tokamak. *AIP Conference Proceedings*, 875(1):83–88, 2006.

[35] G. Mazzitelli and al. FTU results with a liquid lithium limiter. *Nuclear Fusion*, 51(7):073006, may 2011.

[36] R Kaita and al. Surface treatment of a lithium limiter for spherical torus plasma experiments. 3 2001.

[37] G. G. van Eden and al. Self-regulated plasma heat flux mitigation due to liquid sn vapor shielding. *Phys. Rev. Lett.*, 116:135002, Apr 2016.

[38] P. Rindt and et al. Power handling and vapor shielding of pre-filled lithium divertor targets in magnum-PSI. *Nuclear Fusion*, 59(5):056003, mar 2019.

[39] P. Rindt and al. Using 3d-printed tungsten to optimize liquid metal divertor targets for flow and thermal stresses. *Nuclear Fusion*, 59(5):054001, mar 2019.

[40] R.J. Goldston and al. The lithium vapor box divertor. *Physica Scripta*, T167:014017, jan 2016.

[41] M.A. Jaworski and al. Thermocapillary and thermoelectric effects in liquid lithium plasma facing components. *Journal of Nuclear Materials*, 390-391:1055–1058, 2009. Proceedings of the 18th International Conference on Plasma-Surface Interactions in Controlled Fusion Device.

[42] D.N. Ruzic and al. Lithium–metal infused trenches (LiMIT) for heat removal in fusion devices. *Nuclear Fusion*, 51(10):102002, aug 2011.

[43] M. Poradziński and al. Integrated core-sol-divertor modelling for demo with tin divertor. *Fusion Engineering and Design*, 124:248–251, 2017. Proceedings of the 29th Symposium on Fusion Technology (SOFT-29) Prague, Czech Republic, September 5-9, 2016.

[44] R. Chandra. Simulation of neutral lithium atoms in magnesium-psi using eunomia. *Master thesis*, 2017.

[45] L. Balbinot. Simulation of lithium cooling and transport in magnum-psi using b2.5-eunomia coupled codes. *Master thesis - University of Padua*, 2018.

[46] V. Pericoli Ridolfini and et al. A comparative study of the effects of liquid lithium and tin as demo divertor targets on the heat loads and sol properties. *Physics of Plasmas*, 26:012507, 01 2019.

[47] V. Pericoli Ridolfini and et al. Comparison between liquid lithium and liquid tin targets in reactor relevant conditions for demo and i-dtt. *Physics of Plasmas*, 27:112506, 11 2020.

[48] A. Gallo and al. Impact of the plasma geometry on divertor power exhaust: experimental evidence from TCV and simulations with SolEdge2d and TOKAM3x. *Plasma Physics and Controlled Fusion*, 60(1):014007, oct 2017.

[49] G. Ciraolo and al. H-mode west tungsten divertor operation: deuterium and nitrogen seeded simulations with soledge2d-eirene. *Nuclear Materials and Energy*, 12:187–192, 2017. Proceedings of the 22nd International Conference on Plasma Surface Interactions 2016, 22nd PSI.

[50] D. Galassi and al. Numerical investigation of optimal divertor gas baffle closure on TCV. *Plasma Physics and Controlled Fusion*, 62(11):115009, sep 2020.

[51] R. Ambrosino. Dtt - divertor tokamak test facility: A testbed for demo. *Fusion Engineering and Design*, 167:112330, 2021.

[52] X. Bonnin and D. Coster. Full-tungsten plasma edge simulations with solps. *Journal of Nuclear Materials*, 415(1, Supplement):S488–S491, 2011. Proceedings of the 19th International Conference on Plasma-Surface Interactions in Controlled Fusion.

[53] S. Gao and al. Tungsten divertor plasma simulation with bundled charge state model by solps-iter on east. *AIP Advances*, 11(2):025233, 2021.

[54] M Greenwald and al. A new look at density limits in tokamaks. *Nuclear Fusion*, 28(12):2199–2207, dec 1988.

[55] I Casiraghi and al. First principle-based multi-channel integrated modelling in support of the design of the divertor tokamak test facility. *Nuclear Fusion*, 61, 2021.

[56] H. Zohm. Edge localized modes (ELMs). *Plasma Physics and Controlled Fusion*, 38(2):105–128, feb 1996.

[57] A.W. Leonard. Edge-localized-modes in tokamaks. *Physics of Plasmas*, 090501(21):105–128, Sep 2014.

[58] L.L. Lao and al. Reconstruction of current profile parameters and plasma shapes in tokamaks. *Nuclear Fusion*, 25(11):1611–1622, nov 1985.

[59] S. Brezinsek and et al. Study of physical and chemical assisted physical sputtering of beryllium in the JET ITER-like wall. *Nuclear Fusion*, 54(10):103001, sep 2014.

[60] S. Brezinsek and et al. Beryllium migration in JET ITER-like wall plasmas. *Nuclear Fusion*, 55(6):063021, may 2015.

[61] K. Krieger and al. Beryllium migration and evolution of first wall surface composition in the jet ilw configuration. *Journal of Nuclear Materials*, 438:S262–S266, 2013. Proceedings of the 20th International Conference on Plasma-Surface Interactions in Controlled Fusion Devices.

[62] S. Wiesen and al. Modelling of plasma-edge and plasma–wall interaction physics at JET with the metallic first-wall. *Physica Scripta*, T167:014078, feb 2016.

[63] E. Kaveeva and al. SOLPS-ITER modelling of ITER edge plasma with drifts and currents. *Nuclear Fusion*, 60(4):046019, mar 2020.

[64] V Kotov, D Reiter, R A Pitts, S Jachmich, A Huber, and D P Coster and. Numerical modelling of high density JET divertor plasma with the SOLPS4.2 (b2-EIRENE) code. 50(10):105012, sep 2008.

[65] G. Rubino and al. Assessment of scrape-off layer and divertor plasma conditions in jt-60sa with tungsten wall and nitrogen injection. *Nuclear Materials and Energy*, 26:100895, 2021.

[66] C. Meineri and al. Preliminary assessment of neon impact on dtt power exhaust with alcator c-mod transport coefficients. *Offshore Mediterranean Conference*, pages OMC–2021–191, 2021.

[67] S. Saarelma and al. Integrated modelling of h-mode pedestal and confinement in JET-ILW. *Plasma Physics and Controlled Fusion*, 60(1):014042, nov 2017.

[68] J. Garcia and et al. Physics comparison and modelling of the JET and JT-60u core and edge: towards JT-60sa predictions. 54(9):093010, aug 2014.

[69] H. Kawashima and et al. Evaluation of heat and particle controllability on the jt-60sa divertor. *Journal of Nuclear Materials*, 415(1, Supplement):S948–S951, 2011. Proceedings of the 19th International Conference on Plasma-Surface Interactions in Controlled Fusion.

[70] H. Kawashima and et al. Simulation of radiative divertor plasmas by ar seeding with the full w-wall in jt-60sa. *Contributions to plasma physics*, 56:778–783, 2016.

[71] R. Zagorski and et al. Numerical analyses of jt-60sa scenarios with the corediv code. *Nuclear Fusion*, 56:016018, Jan 2016.

[72] E. Sartori et al. Avocado: A numerical code to calculate gas pressure distribution. *Vacuum*, 90:80–88, 2013.

[73] G. Giruzzi and al. Advances in the physics studies for the JT-60sa tokamak exploitation and research plan. *Plasma Physics and Controlled Fusion*, 62(1):014009, oct 2019.

[74] M. Valisa and al. Physics requirements for the vuv survey spectrometer intended for the divertor radiation monitoring on jt-60sa. *Contribution to 46th EPS Conference on Plasma Physics*, 2020.

[75] W. Biel and al. Design of a high efficiency extreme ultraviolet (xuv) overview spectrometer system (hexos) for plasma impurity studies in the stellarator experiment wendelstein 7-x. *Review of Scientific Instruments*, 75, 10 2004.

[76] T. Nakano and al. Volume recombination of c4in detached divertor plasmas of JT-60u. *Nuclear Fusion*, 47(11):1458–1467, oct 2007.

[77] B. Zaniol and al. Measurements of cv flows from thermal charge-exchange excitation in divertor plasmas. *Physics of Plasmas*, 8(10):4386–4389, 2001.

[78] E. Havlíčková and al. Numerical studies of effects associated with the super-x divertor on target parameters in mast-u. *Journal of Nuclear Materials*, 438:S545–S549, 2013. Proceedings of the 20th International Conference on Plasma-Surface Interactions in Controlled Fusion Devices.

[79] H. Reimerdes and al. Power distribution in the snowflake divertor in TCV. *Plasma Physics and Controlled Fusion*, 55(12):124027, nov 2013.

[80] G. Di Gironimo and al. Improving concept design of divertor support system for fast tokamak using triz theory and ahp approach. *Fusion Engineering and Design*, 88(11):3014–3020, 2013.

[81] *Fusion Engineering and Design*, 88(11):1677–1681, 2013.

[82] V. Kotov and D. Reiter. Two-point analysis of the numerical modelling of detached divertor plasmas. *Plasma Physics and Controlled Fusion*, 51(11):115002, oct 2009.

[83] R. Goldston and et al. A new scaling for divertor detachment. *Plasma Physics and Controlled Fusion*, 59(5), mar 2017.

[84] E. Sytova and et. al. Comparing N versus Ne as divertor radiators in ASDEX upgrade and ITER. *Nuclear Materials and Energy*, 19:72–78, 2019.

[85] A. Huber and al. Peculiarity of highly radiating multi-impurity seeded h-mode plasmas on JET with ITER-like wall. *Physica Scripta*, T171:014055, jan 2020.

[86] M Bernert and al. Power exhaust by sol and pedestal radiation at asdex upgrade and jet. *Nuclear Materials and Energy*, 12:111–118, 2017. Proceedings of the 22nd International Conference on Plasma Surface Interactions 2016, 22nd PSI.

[87] H.Q. Wang and al. Effects of divertor geometry on h-mode pedestal structure in attached and detached plasmas in the DIII-d tokamak. *Nuclear Fusion*, 58(9):096014, jul 2018.

[88] N. Asakura and al. Role of divertor geometry on detachment and core plasma performance in jt60u. *Journal of Nuclear Materials*, 266-269:182–188, 1999.

[89] R.A. Pitts and al. Divertor geometry effects on detachment in tcv. *Journal of Nuclear Materials*, 290, 03 2001.

[90] H.Y. Guo and al. Small angle slot divertor concept for long pulse advanced tokamaks. *Nuclear Fusion*, 57(4):044001, feb 2017.

[91] R. Maurizio and al. Numerical assessment of the new v-shape small-angle slot divertor on DIII-d. *Nuclear Fusion*, 61(11):116042, oct 2021.

[92] M.W. Shafer and al. Dependence of neutral pressure on detachment in the small angle slot divertor at diii-d. *Nuclear Materials and Energy*, 19:487–492, 2019.

[93] R.A. Pitts and al. Physics conclusions in support of iter w divertor monoblock shaping. *Nuclear Materials and Energy*, 12:60–74, 2017.

[94] R.A. Pitts and al. Physics basis for the first iter tungsten divertor. *Nuclear Materials and Energy*, 20:100696, 2019.

[95] J.P. Gunn and al. Surface heat loads on the ITER divertor vertical targets. *Nuclear Fusion*, 57(4):046025, mar 2017.

[96] J.P. Gunn and al. Thermal loads in gaps between iter divertor monoblocks: First lessons learnt from west. *Nuclear Materials and Energy*, 27:100920, 2021.

[97] L. Balbinot and al. Development of DTT single null divertor scenario. *Nuclear Materials and Energy*, 27:100952, 2021.

[98] H. Henderson and al. An assessment of nitrogen concentration from spectroscopy measurements in the jet and asdex upgrade divertor. *Nuclear materials and Energy*, 18:147–152, 2019.

[99] L. Balbinot and al. Dispersion scanning beam medium infra-red interferometry for divertor plasma density measurement in DTT. *Journal of Instrumentation*, 15(02):C02028–C02028, feb 2020.

[100] G. Braithwaite and al. Jet polari-interferometer. *Review of Scientific Instruments*, 60(9):2825–2834, 1989.

[101] D.K. Mansfield and al. Multichannel far-infrared laser interferometer for electron density measurements on the tokamak fusion test reactor. *Appl. Opt.*, 26(20):4469–4474, Oct 1987.

[102] D. J. Bamford and al. Co2 laser-based dispersion interferometer utilizing orientation-patterned gallium arsenide for plasma density measurements. *Review of Scientific Instruments*, 84(9):093502, 2013.

[103] P. Innocente and S. Martini. A two color multichord infrared interferometer for rfx. *Review of Scientific Instruments*, 63(10):4996–4998, 1992.

[104] C.S. Pitcher and P.C. Stangeby. Experimental divertor physics. *Plasma Physics and Controlled Fusion*, 39(6):779–930, jun 1997.

[105] A. Canton and al. Two-color medium-infrared scanning interferometer for the frascati tokamak upgrade fusion test device. *Appl. Opt.*, 45(36):9105–9114, Dec 2006.

[106] T. Akiyama and al. Dispersion interferometer using modulation amplitudes on LHD. *Review of Scientific Instruments*, 85(11):11D301, 2014.

[107] S. Garavaglia et al. Progress of dtt ecrh system design. *Fusion Engineering and Design*, 168:112678, 2021.

[108] M. Wigram and al. UEDGE modelling of detached divertor operation for long-leg divertor geometries in ARC. *Contributions to Plasma Physics*, 58(6-8):791–797, jul 2018.

[109] A Kallenbach and al. Impurity seeding for tokamak power exhaust: from present devices via ITER to DEMO. *Plasma Physics and Controlled Fusion*, 55(12):124041, nov 2013.

[110] D. Post and al. Calculations of energy losses due to atomic processes in tokamaks with applications to the international thermonuclear experimental reactor divertor. *Physics of Plasmas*, 2(6):2328–2336, 1995.

[111] R J Goldston, M L Reinke, and J A Schwartz. A new scaling for divertor detachment. *Plasma Physics and Controlled Fusion*, 59(5):055015, mar 2017.

[112] I. Lyublinski and al. Protection of tokamak plasma facing components by a capillary porous system with lithium. *Journal of Nuclear materials*, 463:1156–1159, aug 2015.

[113] G. Nallo and al. Self-consistent modelling of a liquid metal box-type divertor with application to the divertor tokamak test (dtt) facility: Li vs. sn. *Nuclear Fusion*, 59, 03 2019.

[114] D. Ruzic and al. Investigation of tin-lithium eutectic as a liquid plasma facing material. *APS Division of Plasma Physics Meeting*, 2016.

[115] M.L. Apicella et al. Preliminary analysis on a liquid lithium limiter in capillary porous system (cps) configuration in view of a “litization” experiment on ftu tokamak. *Fusion Engineering and Design*, 75:351–355, 11 2005.

[116] Langmuir I. The condensation and evaporation of gas molecules. *Proceedings of the National academy of sciences*, 3(3), 1917.

[117] Richard E Honig. Vapor pressure data for the solid and liquid elements. *RCA review*, 23(12):567, 1962.

[118] E.E. Shpil’rain and al. *Thermophysical Properties of Lithium Hydride, Deuteride and Tritide*. Springer Science and Business Media, 1987.

[119] D.A. Johnson and al. Metals and chemical change. *Royal Society of Chemistry*, 59(5):167, 2002.

[120] T.W. Abrams. Erosion and re-deposition of lithium and boron coatings under high-flux plasma bombardment. *Princeton, NJ : Princeton University*, 2015.

[121] J. Bohdansky and al. A universal relation for the sputtering yield of monatomic solids at normal ion incidence. *Nuclear Instruments and Methods in Physics Research Section B: Beam Interactions with Materials and Atoms*, 2(1):587–591, 1984.

[122] W. Eckstein and R. Preuss. New fit formulae for the sputtering yield. *Journal of Nuclear Materials*, 320(3):209–213, 2003.

[123] Naval Research laboratory, Washington DC. *NRL Plasma Formulary*. 2016.

[124] R. Doerner, S. Krasheninnikov, and K. Schmid. Particle-induced erosion of materials at elevated temperature. *Journal of Applied Physics*, 95:4471–4475, 04 2004.

[125] T.W. Morgan, D.C.M. van den Bekerom, and G. De Temmerman. Interaction of a tin-based capillary porous structure with iter/demo relevant plasma conditions. *Journal of Nuclear Materials*, 463:1256–1259, 2015. PLASMA-SURFACE INTERACTIONS 21.

[126] R. Doerner, M. Baldwin, S. Krasheninnikov, and K. Schmid. High temperature erosion of beryllium. *Journal of Nuclear Materials - J NUCL MATER*, 337:877–881, 03 2005.

[127] R.J. Goldston and al. Recent advances towards a lithium vapor box divertor. *Nuclear Materials and Energy*, 12:1118–1121, 2017. Proceedings of the 22nd International Conference on Plasma Surface Interactions 2016, 22nd PSI.

[128] J.A. Schwartz and et al. Physics design for a lithium vapor box divertor experiment on magnum psi. *Nuclear Materials and Energy*, 18:350–355, 2019.

[129] G.F. Nallo and al. Modeling the lithium loop in a liquid metal pool-type divertor. *Fusion Engineering and Design*, 125:206–215, 2017.